A COMPUTATIONAL AND EXPERIMENTAL INVESTIGATION INTO THE PERFORMANCE OF INDUSTRIAL REFRIGERATION HELICAL OIL SEPARATORS

A thesis presented for the degree of Doctor of Philosophy

By

Lewis Brown, BEng (Hons)

Department of Mechanical and Aerospace Engineering

University of Strathclyde

Glasgow

July 2013

Signed:

Date: 24/07/2013

Abstract

An oil separator is a key component in an industrial refrigeration system as it prevents the compressor discharge oil creating a liquid film on the internal walls of the heat exchangers which leads to a reduction in efficiency of the system and increased operating costs. The Henry Technologies helical oil separator operates in refrigeration systems globally yet there is currently no available data on the performance of the unit. In this investigation the performance of the helical separator has been captured for a range of operating conditions using a custom built test facility. An assessment has also been made to determine the ability of current state-of-the-art computational models to predict the performance of the separator.

The computational modelling approach used in this study was the Euler-Lagrange, which requires the solution of the continuous gas phase prior to the injection of the dispersed liquid phase. A Perspex replica of the helical separator being investigated was used to carry out LDA velocity component measurements and produce laser sheeting images which could be used to validate the single phase computational model. The unsteady nature of the swirling flow field in the separator, as a result of the PVC, required the implementation of the advanced LES turbulence model with high order discretization schemes.

Separation efficiency and pressure drop measurements have also been obtained for various gas and liquid flow rates at 0 BarG and 3 BarG working pressures which clearly demonstrate that as the gas flowrate and operating pressure decreases the separation efficiency also decreases. The flow regime at the inlet to the separator consists of a heavily stratified liquid film with an annular dispersed droplet mist. Since the DPM model only models the trajectories of droplets; experimental data was obtained which characterised the performance of the separator subject to a droplet only mist with the liquid film being extracted and quantified just upstream of the inlet. The Malvern Spraytec laser diffraction apparatus was employed to determine the droplet size and distribution entering and leaving the separator allowing a grade-efficiency curve to be produced for the unit.

Using the size, distribution, liquid flowrate and separation efficiency of the separator for the droplet mist only condition the DPM model was used to simulate the droplet trajectories with the validated single phase gas flow model. The droplet breakup and liquid

film models were explored to determine the optimum modelling criteria which could predict the droplet separation efficiency obtained through the experimental testing.

Using the information obtained through the experimental testing, computational simulations and the theory presented within the literature for droplet separation, design improvements have been suggested for the Henry Technologies separator. These include increasing the discharge flowrate through the no mesh separator, assessing a unit with a tangential inlet and compressed helix, designing a wire mesh attachment for the separator inlet and a swirl generator to be located in the centre tube. All design improvements resulted in increased separation efficiency but were coupled with an increase in pressure drop.

Contents

List of Figures

List of Tables

Acknowledgments

Nomenclature

Main Symbols

a   Inlet Height, Speed of Sound

A   Area

b   Inlet Width

B_L Beam Waist Diameter before Expansion

C_c Cunningham Correction Factor

C_D Drag Coefficient

d_{50} Cut Size Diameter

d_d Droplet Diameter

d_f Fringe Spacing

D   Diameter

D_{Tij} Turbulent Diffusion

E_w Beam Expansion Ratio

Eu   Euler Number

f   Frequency

f_D Doppler Shift Frequency

f_μ Near Wall Damping Function

F_C Centrifugal Force

F_D Drag Force

F_{ij} Production by System Rotation

F_L Focal Length

F_s Frequency Shift

g   Gravity

G   Refraction Correction Factor, Convolution Kernel

H   Height

I_r Relative Turbulence Intensity

k   Turbulent Kinetic Energy

K   Splashing Parameter

l_m Mixing Length

L   Length

$\dot{m}$ Mass Flowrate

n   Normal Vector

Oh	Ohnesorge Number
P	Pressure
ΔP	Pressure Drop
P_{ij}	Stress Production Term
P_k	Rate of Production of Turbulent Kinetic Energy
$\dot{Q}$	Volume Flowrate
r	Radius
r_a	Position of Measurement Volume
r_c	True Measurement Radius
r_i	Inner Radius of Cylindrical Chamber
r_o	Outer Radius of Cylindrical Chamber
Re	Reynolds Number
S	Surface Area, Source Term
S_{ij}	Strain Rate
Stk	Stokes Number
Sw	Swirl Number
t	Time
t_w	Window Thickness
T_{int}	Integral Time
u,v,w	Velocity in the x, y and z coordinates
u',v',w'	Velocity Fluctuations in the x, y, z coordiantes
u_τ	Friction Velocity
U	Total Velocity
We	Weber Number
x,y,z	Cartesian Coordinates
Δx	Fringe Spacing
x_a	Location of Measurement Volume in Absence of a Window
x_c	Corrected Position of Measurement Volume
y^+	Dimensionless Wall Coordinate
Y_M	Compressible Turbulence to the Overall Dissipation Rate

Greek Symbols

α	Angle Relative to Normal

α_d	Volume Fraction of Dispersed Phase
β	Direction of Particle Motion
Γ	Diffusion Coefficient
δ	Kronecker Delta
Δ	Differential, Filter Length Scale
ε	Dissipation of Turbulent Kinetic Energy
ϵ_{ij}	Dissipation
ζ	Normally Distributed Random Number
η	Efficiency Parameter
η_f	Refractive Index of Fluid
η_f	Refractive Index of Window
θ	Intersection Angle of Laser Beam
κ	Von Karman Constant
λ	Wavelength, Molecular Mean Free Path
μ	Dynamic Viscosity, Molecular Viscosity
ν	Kinematic Viscosity
ν_{eff}	Effective Viscosity
ν_t	Turbulent Viscosity
ξ	Pressure Drop Coefficient
ρ	Density
σ	Surface Tension
τ	Shear Stress
ϕ	Any Variable
ϕ_{ij}	Pressure Strain
χ	Mass Fraction
ψ	Inertial Separation Parameter

Subscripts

d	Droplet
f	Film
g	Gas
i,j,k	Cartesian Notation
in	Inlet
l	Liquid

n	Normal Component
o	Outlet
s	Static
Sa	Sauter
SGS	Sub-Grid Scales

Abbreviations

BSA	Burst Spectrum Analyser
CFD	Computational Fluid Dynamics
CPU	Central Processing Unit
DNS	Direct Numerical Simulation
DPM	Discrete Phase Model
DRW	Discrete Random Walk
FVM	Finite Volume Method
GEC	Grade Efficiency Curve
HFC	Hydroflurocarbon
LDA	Laser Doppler Anemometry
LES	Large Eddy Simulation
PISO	Pressure-Implicit with Splitting of Operators
PMT	Photo Multiplier Tube
POE	Polyolester
PVC	Precessing Vortex Core
RANS	Reynolds Averaged Navier Stokes Equation
RMS	Root Mean Square
RNG	ReNormalisation
RSM	Reynolds Stress Model
SGS	Sub-Grid Scales
SIMPLE	Semi-Implicit Method for Pressure Linked Equations
TAB	Taylor Analogy Breakup

Chapter 1 Introduction

1.1 Background

Industrial refrigeration systems are used to control the temperature in the food, chemical, process, manufacturing, construction and indoor recreational winter sports industries. The typical operating temperatures of an industrial refrigeration system extend down to -60° or -70°C, with temperatures below this range being catered for in the cryogenics industry. The efficiency and reliability of the refrigeration plant is affected by the presence of oil which is needed to provide lubrication, sealing and cooling to the compressor. During the refrigerant vapour compression process, the lubricant oil becomes entrained within the gas flow and exits through the compressor discharge line. On entering the condenser the oil dissolves into the liquid refrigerant during the condensation process the oil deposits on the internal walls of the heat exchanger held in place due to the high surface tension and viscosity of the lubricant. Oil still entrained within the refrigerant is carried through the system to the evaporator. It is in the evaporator that the heat is removed from the region to be cooled and during the vaporisation of the refrigerant the oil may leave the heat exchanger as a liquid mist but can also build up on the internal tube walls. The amount of oil present in refrigeration systems typically varies between 0.5-8% mass fraction and can have an extremely detrimental effect on the thermal capacity of the evaporator including; increasing the two-phase flow pressure drop, reducing the log mean temperature difference, preventing the entire volume of refrigerant from evaporating, increasing the boiling temperature of the refrigerant, reducing the heat transfer coefficient of the evaporator.

It is clear that oil present in the rest of the refrigeration system, in particular the heat exchangers, is undesirable and detrimental to the overall system performance. At high vapour qualities, the presence of oil lowers the heat transfer coefficients by up to 90% (Thome, 2004). Therefore in order to prevent oil carryover the entrained oil in the compressor discharge has to be controlled. This is achieved by installing an oil separator in the compressor discharge line which removes much of the oil from the refrigerant vapour and returns it to the compressor crankcase where it originated.

To ensure the oil removal process from the refrigerant is efficient requires identifying and understanding the design elements which govern the separator performance. Not only will

a highly efficient separator ensure optimum system performance, it also important in terms of productivity, reliability, operational costs, competitive advantage and the highly topical environmental impact of energy consumption. As a result separator manufacturers need to be able to determine the performance of their units to ensure a high level of oil separation is being achieved. Coupled with the separation efficiency of a separator is the pressure drop through the unit. It is pressure drop within the separator that relates directly to the operating costs of the entire refrigeration system. The oil separator in an industrial refrigeration system in some cases can account for up to 10% of the overall system pressure loss under typical operating conditions.

The main aim of this thesis is to assess the abilities of the current mathematical models to determine the performance of a droplet separator and therefore assess the possibility of being used as a design tool. This will be carried out using the Henry Technologies helical oil separator as part of an EPSRC Industrial Case Award with the University of Strathclyde. Currently no publically available research exists in specific relation to this range of oil separators; the work presented within this thesis aims to fill the knowledge gap in this regard. Henry Technologies currently hold a significant portion in the industrial refrigeration oil separator market selling in excess of 17,800 separators in 2012 of which 7,400 were of the helical variant. In order for Henry to remain competitive in the separator market requires a detailed analysis of the current helical separator in terms of the separation efficiency and pressure drop which characterise the overall performance of the unit. Once a detailed understanding of how the current unit performs design modifications can be explored and tested. These modifications will be based on theoretical predictions and separation performance enhancement recommendations previously published in the literature. For a redesigned separator to be successful in relation to the standard helical separator it would need to include one or more of the following modifications; improved separation efficiency, lower pressure drop, reduced cost of manufacture.

1.2 Industrial Refrigeration Cycles

Three main refrigeration cycles are employed in the industrial refrigeration sector; the cycle choice is dependent on the thermodynamic limitations associated with specific operational, economic and legal needs of the application. The Vapour Compression Cycle (VCR) governs the industries described previously which can provide cooling down to -70°C. The Gas Refrigeration Cycle caters for the cryogenic range which allows for the liquefaction of gases

and the Absorption Refrigeration Cycle is principally operated where waste heat is available for use in the generation of a vapour. Cascade and Multistage cycles also exist as variants to the three main cycles when there is a need for moderately low temperatures and high efficiency but come with extra capital cost and complexity.

The basis of the VCR, the environment where the helical separator is most often used, can be described by examining the process which originated as the ideal Carnot Refrigeration Cycle but due to theoretical impossibilities the conditions for its implementation do not exist due to thermodynamic irreversibilities, design margins and physical restraints. As a result the Carnot Cycle is modified to the Actual Vapour Compression Cycle which describes the process of heat removal from a warm medium. The process outlined below is summarised in the schematic and Temperature-Entropy diagram shown in Figure 1.1.

1. (1-2) The refrigerant begins as a saturated vapour and undergoes compression to a high pressure through the compressor to produce a superheated vapour. This also results in an increase in temperature.

2. (3-4) The superheated vapour then undergoes condensation producing a saturated liquid through the condenser. This allows the heat to be dumped to the surroundings by an external medium, usually air or water, being blown over the condenser coils by a fan.

3. (5-6) The saturated liquid is then expanded through an expansion valve resulting in a sudden reduction in pressure. This results in the flash evaporation of part of the liquid refrigerant. This process known as the auto-refrigeration effect, which causes the liquid-vapour mixture to achieve a temperature lower than the temperature of the region to be cooled.

4. (7-8) The liquid-vapour mixture is then expanded through the evaporator causing the liquid part of the mixture to be evaporated thus removing the heat from the enclosed space. The warm air in this region is circulated by a fan thus increasing the heat transfer process. The heat absorbed is then disposed of by the condenser. The cycle is closed with saturated vapour returning to the inlet of the compressor.
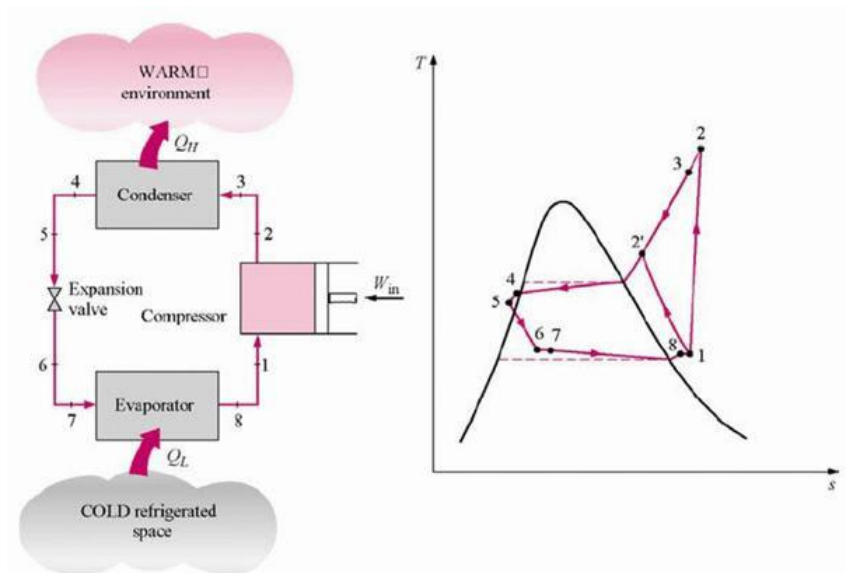
Figure 1.1: Actual Vapour Compression Refrigeration Cycle and T-s Diagram (Cengel & Boles, 2010)

The Coefficient of Performance (COP) is a measure of the efficiency of a refrigeration system and is defined by equation 1.1;

$$COP = \frac{Refrigeration\ Effect}{Work\ Required} = \frac{Q}{W_{in}} \qquad (1.1)$$

which for the Actual VCR given in Figure 1.1 becomes;

$$COP = \frac{h_8 - h_7}{h_2 - h_1} \qquad (1.2)$$

Q represents the heat extracted from the cold medium, W_{in} is the work supplied to the system from the compressor and h is the enthalpy at a particular point in the process. The COP is related to the temperature of the refrigerant in the cycle which is defined by the temperatures of the warm and cold mediums and the temperature difference, ΔT, required across the heat exchanger surfaces as given by the T-s diagram in Figure 1.2.
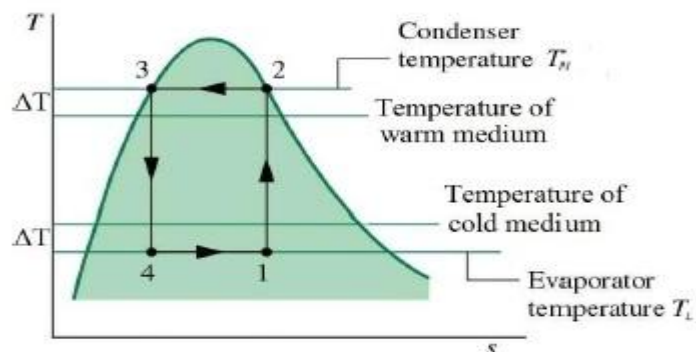
Figure 1.2: Heat Exchanger Temperature Difference T-s Diagram (Cengel & Boles, 2010)

4

It should now be clear that any factor which affects the heat transfer capabilities of the evaporator and condenser will result in a negative impact on the efficiency of the refrigeration cycle as defined by equation 1.1. Such factors include altered flow regimes over the heat exchanger surfaces, altered thermal properties of the refrigerant and of course fouling due to deposition, all of which can occur due to the presence of oil in the refrigeration system. Based on this it is critical for efficient system operation that the oil levels present are carefully managed through the installation of an oil separator to remove the oil before entering the heat exchangers.

1.3 Gas Liquid Separation

Gas or vapour-liquid separation takes place not only in the industrial refrigeration sector but several other industrial applications including oil refineries, compressor systems, gas pipelines and natural-gas processing plants. For the majority of these sectors the separation takes place under the influence of gravity and the devices are known as 'knock-out' drums/pots or 'flash' drums. These separators usually have large internal volumes to allow the incoming mixture velocity to be significantly reduced and cater for high dispersed phase volume fractions, in excess of several per cent, where the majority of droplets are larger than 500 μm. For applications where the droplet size is dominantly in the order of a few microns then demisting meshes or pads are used but are only suitable for low dispersed flow volume fractions and are not suitable for dealing with slug flow type conditions. Demisters cause the small entrained droplets to agglomerate until they grow to a size which allows them to be gravitationally separated from the vapour stream.

The intermediate droplet size range, 10-300 μm, is catered for by a cyclonic type separator which currently plays a critical role in the oil and gas industries where space is at a minimum therefore the large expensive gravity separators are being replaced by more compact and efficient gas-liquid separators. The use of a multi-stage separation process is often used in industry to cater for large volumetric concentrations of entrained liquid. Such assemblies consist of a liquid hold-up drum similar to the aforementioned gravity separators upstream and then a singular or bank of cyclone separators downstream.

A good example of a multi-mechanism separator is the standard Henry Technologies helical oil separator is shown in Figure 1.3. The internal geometry of the unit contains mechanisms which combines the processes found in a gravitational separator, a demisting mesh and a cyclonic type of separator. A number of empirical models exist relating to the separation

efficiency and pressure loss within a cyclone type geometry which have been rigorously tested. These models will be used as an initial basis for estimating the theoretical performance of the helical oil separator as presented in Chapter 2.

Figure 1.3: Henry Technologies Helical Oil Separator

1.4 Main Project Objectives

The objectives of this study are concerned with assessing the capabilities of the currently available mathematical models to predict the performance of a droplet separator. In doing so validation data was obtained from the helical oil separator through experimental testing within the Department of Mechanical and Aerospace Engineering laboratories in the University of Strathclyde. To allow the necessary parameters to be measured a custom test facility had to be designed, built and commissioned. The validation process was subdivided into two main categories; single phase flow analysis and two phase flow analysis. In addressing the former a Perspex replica of the helical oil separator was used to obtain Laser Doppler Anemometry (LDA) measurements within the main body of the separator. The data obtained could then be manipulated to assess the single phase models using Computational Fluid Dynamics (CFD) simulations ensuring the gas phase flow was accurately modelled since this has a direct consequence on the droplet separation efficiency. The assessment of the two phase flow included obtaining separation efficiency, pressure loss, droplet size, distribution and flow regime data under a range of controlled conditions. The data could

then be used to assess the currently available models for droplet separation performance prediction.

The project objectives are summarised as follows;

1. Obtain velocity component measurements within a specially manufactured Perspex replica of the helical oil separator using LDA. The data obtained can then be compared with the single phase flow simulation to validate the model results.

2. Using the custom built test facility obtain quantitative data of the separation efficiency and pressure drop of the helical oil separator over a range of discharge gas volume flowrates and liquid fractions for a range of operating pressures. This will be carried out using air as the working gas and a POE refrigerant lubricant as the dispersed phase.

3. Obtain quantitative data on the droplet size and distribution at the inlet and outlet of the separator and quantify the fraction of liquid film versus droplet mist entering the separator over the range of conditions tested. This data will provide the separation efficiency of the unit subject to a droplet only flow which can then be compared directly with the discrete phase data obtained computationally.

4. Assess the ability of the currently available computational models to predict the gas flow field within the separator and then implement the Discrete Phase Model (DPM) to determine the separation performance of the separator and compare with the performance data obtained experimentally.

5. Determine the potential of using the validated modelling approach to predict droplet separation enhancement modifications and present a redesigned separator based on the findings from the performance assessment of the current unit and the recommendations presented within the relevant separation technology literature.

1.5 Thesis Outline

The second chapter of this thesis presents background information on the operating and two phase flow conditions which exists within gas-oil separators. Leading on from this an assessment of the literature will be presented to justify the need for carrying out this work by identifying the different separation mechanisms which exist and the flow conditions which dictate the choice of separator. Furthermore the theoretical models available for separator performance predictions and the current state of the art for computational

modelling of a droplet separator under both single and two phase flow conditions will be explored. This review aims to highlight the gaps which exist within the literature and how the work presented within this investigation aims to fill some of these voids.

Chapter 3 describes the process involved for experimentally measuring the gas flow velocities within the separator geometry using LDA and how the data can then be used to validate the single phase computational model through direct comparison of the velocity components at various locations within the separator volume.

Chapter 4 presents the design, operation and data acquired from the performance testing of the helical oil separator. The overall separation efficiencies for the standard unit and a modified separator unit are given as well as the associated pressure drop values. The droplet size and distribution at the inlet and outlet of the separators are measured using a laser diffraction technique which allows a grade efficiency curve characterising the performance of the units to be produced.

Chapter 5 uses the validated single phase flow model to provide an assessment of the available models within the discrete phase modelling (DPM) approach to be assessed and a procedure for predicting the separation efficiency of the separators to be determined.

Chapter 6 describes the possible design changes to the current helical separator and uses the DPM model to predict the potential improvements in performance which are then compared with the experimental data. In doing so provides an assessment of the proposed modelling approach as a potential tool for future separator design improvements.

Finally, in Chapter 7 the conclusions drawn from this thesis are presented and recommendations given for future work.

Chapter 2 Background and Literature Review

2.1 Introduction

2.1.1 Separator Description

A droplet separator in a very generic sense is a device used to retain droplets which are entrained within a continuous phase gas flow. As a preamble of how the helical unit operates as a droplet separator a description from the Henry Technologies product catalogue provides an indication of the basic separation mechanisms that require to be considered within the literature for this study;

"Upon separator entry, refrigerant gas containing oil in aerosol form encounters the leading edge of the helical flighting. The gas/oil mixture is centrifugally forced along the spiral path of the helix causing the heavier oil particles to spin to the perimeter, where impingement with a screen layer occurs. The screen layer functions as both an oil stripping and draining medium. Separated oil flows downward along the boundary of the shell through a baffle and into an oil collection chamber at the bottom of the separator. The specially engineered baffle isolates the oil chamber and eliminates oil re-entrapment by preventing turbulence. The virtually oil free refrigerant gas then exits through a second screen fitting just below the lower edge of the helical flighting. A float activated oil return needle valve allows the separated oil to return to the compressor crankcase or oil reservoir. There is a permanent magnet positioned at the bottom of the oil collection chamber to capture any system metal debris, which could impair the operation of the needle valve. With proper selection, an oil separation efficiency of 99% can be achieved."

From the preamble it is evident that the helical unit employs gravitational, centrifugal and impingement based mesh filtration to remove the entrained droplets from the refrigerant gas flow therefore these will be explored in detail in the forthcoming sections.

2.1.2 Separator Operating Conditions

The helical oil separator operating in a refrigeration system is subject to a wide range of fluid conditions based on a number of factors, including; the refrigerant gas, the system operating pressure and temperature and the oil carryover rate from the compressor crank case. The range of industrial refrigerants used in refrigeration systems have a density range from 12 kg/m^3 for R134 (Ammonia) up to 188 kg/m^3 for R404a (HFC) and depending on

which gas the system is operating with dictates the flow regime which exists within the inlet pipe as can be seen from the Baker flow pattern map (Baker, 1954) shown in Figure 2.1.
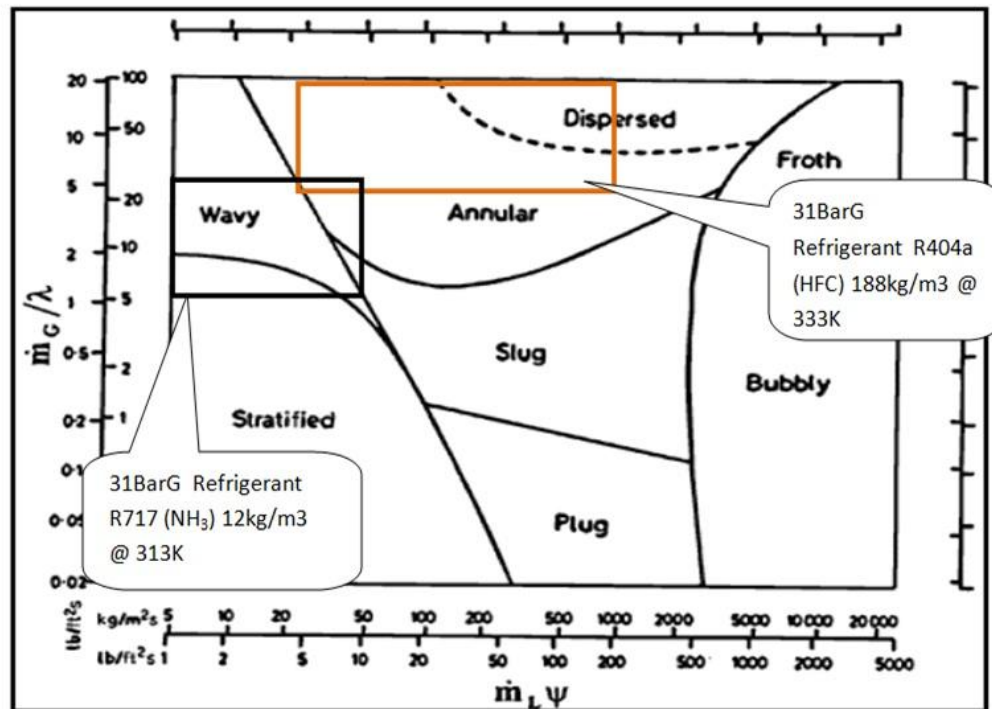
Figure 2.1: Baker Flow Regime Map with Plant Operating Conditions

As can be seen from the flow regime map, when ammonia is the working fluid the flow entering the separator is stratified/wavy indicating that the majority of the liquid flow will be a wall based film with only a small proportion present as a droplet mist. On entry to the separator the liquid film will drain down the cylindrical walls, creating a film on the internal wall mesh, and gather in the oil collection chamber where it is returned to the compressor. At the other end of the extremity is the HFC refrigerant which results in a dispersed/annular flow where there will be a proportion of the fluid as a liquid film round the internal surface of the pipe with a highly dense droplet mist present in the core of the pipe. When this type of flow regime exists at the entrance of the helical separator the separation process becomes far more complex due to the fluid mechanics associated with a droplet-film based flow. The complexities arise from the fact that there are a number of physical processes taking place in a swirling flow environment including droplet impact onto the liquid films, generation of droplets from the films and the draining of liquid films passing through the separation volume, which will all have a contributing effect on the performance capabilities of the separator. Therefore to fully analyse the separation process in the helical separator

and allow a computational model to be developed requires exploring these phenomenon in detail.

The flow regimes presented in Figure 2.1 are for a single working pressure of 31 BarG over a 20 degree temperature range, however the separator being investigated here is capable of working over a 0-31 BarG range between 263-403 K. Beyond this are separators used in CO_2 systems which operate at pressures around 100 BarG across a temperature range 228-423K where the flow regime entering the separator will be different from those at the lower pressure. As the working pressure of the system increases the degree of liquid entrainment also increases which is one of the driving factors for the existence of different flow regimes. This is due to the decrease in surface tension with increase in pressure or temperature causing the liquid film layers to break-up resulting in high droplet content. Also the mean droplet size produced increases with increasing pressure which is coupled with a change in the droplet size distribution which can be derived from the Harwell method (Hoffmann & Stein, 2008). The increase in droplet concentration due to an increase in pressure is also associated with the decrease in density ratio which reduces the inertia of the droplets relative to the gas.

The droplet size range which is believed to exist in the discharge line of the compressor is in the sub 10 micron range. Droplet sizes of this order are representative of an aerosol and are notoriously difficult to separate. Therefore, separation mechanisms which are able to remove sub 10 micron droplets will be investigated in detail.

The specific requirements of the industrial environment where the refrigeration system is to operate, in terms of compressor size, has a direct implication on the size of oil separator to be installed. For the helical oil separator Henry Technologies offer units capable of handling volume flowrates ranging from 1.3 to 159.8 m^3/hr. This extensive volume flowrate range, which spans two orders of magnitude, presents issues relating to geometrical scaling effects as well as scaling effects associated with the fluid conditions which the unit operates.

The other driving factor which governs separator design is the pressure drop across the unit, since a high pressure drop requires the system to deliver a greater amount of power which in turn increases the energy consumption leading to an increased cost for the plant operator and increased CO_2 emissions. However a low pressure drop is usually

contradictory to good separation efficiency due to physical mechanisms i.e. an increase of separation efficiency can result in an increased pressure drop. It is due to this relationship that a trade-off needs to be established to allow an efficient separator to be designed which is not detrimental to the overall energy consumption of the plant.

2.1.3 Literature to be Explored

To allow the helical unit to be compared to other types of separators a general background to droplet separators will be presented. The main mechanisms which promote droplet separation will be examined as well as their design and application. Such mechanisms include gravitational, inertial and filtration all of which are included in the helical separator volume. A review of the theoretical models which govern the selection of droplet separators will be presented with a detailed investigation on the removal of droplets in the sub 10 micron range. A critique will then be given of the pressure drop across a droplet separator and methods of reduction. Finally an assessment of the different numerical approaches to modelling the single phase and two-phase flow inside a droplet separator will be examined. A particular focus will be given to the accurate modelling process for swirling type flows which govern centrifugal separation. The models which capture accurately droplet mechanics under these flow conditions including droplet wall interactions and the effects of a liquid film will also be examined.

2.2 General Droplet Separation Mechanisms

There are three main categories into which separators belong namely electrostatic precipitation, diffusional deposition and inertial separation (Burkholz, 1989). The first category classifies the separation of droplets from the continuous gas phase through the presence of an electrical field. Diffusional deposition, also known as Brownian motion, is governed by the thermal motion of very small droplets, usually in the sub-micron range, this mechanism occurs when small particles collide with the gas molecules. The resulting collisions cause the sub-micron particles to deviate from the fluid flow path around objects like wire strands of a mesh increasing the likelihood of the object striking the surface and becoming separated. Finally inertial separation relies on the momentum of the particles. The design of electrostatic precipitators and diffusional filters each have one common design and geometry whereas inertial separators are available with a wide variation in their construction and setup of impact surfaces for droplet removal.

Given the description presented at the start of this chapter which highlights the separation mechanisms employed by the helical oil separator, the focus of this review is restricted to inertial based separation processes.

2.3 Inertial Separation

The type of inertial separation mechanism used for droplet removal is governed by the droplet diameter size and distribution of the incoming flow, since the forces which are imparted on a 1 μm droplet are quantitatively different from those on a 50 μm droplet. The separation units themselves can be subdivided into cyclones, wave-plate separators, packed bed, wire and fibre filters and scrubbers which all have varying capital and operational costs as well as separation efficiencies. Included within the inertial separation category is gravitational settling, although the size range of droplets for gravity to influence their motion exceeds 300 μm (Fewel & Kean, 1992). The low velocities required for gravitational separation to take effect necessitate the requirement for a very large vessel and result in a costly vessel in terms of production and available space, although the internals are very simplistic. Devices that use gravity as the sole separation mechanism are generally called knock-out drums and are typically used for bulk separation only as a primary stage separator and are not recommended for applications where high separation efficiency is required. As a result separation enhancement techniques need to be employed to transport the droplets to a surface and cause them to deposit there, from which they can agglomerate and discharge in the form of larger droplets, films or sheets. To allow inertial separation to occur a body for the droplets to impact on needs to be located within the gas stream in the form of a wire or fibre, or in the case of cyclones and wave plate separators, a surface which causes the gas flow to change direction. Large droplets having a large inertia will deviate from the gas streamlines and impact on the collection surface, small droplets will follow the streamlines of the gas flow without any deviation therefore avoiding impaction on the collection surface. For the case of intermediate sized droplets they can only partially follow the streamlines and therefore eventually deviate into the collection surface. Thus dependent on the particle size and distribution feeding a droplet separator the separation efficiency can vary from 0% for the extremely small droplets up to 100% for large droplets.

The type of inertial separator chosen is governed mainly by the droplet size which is feeding the unit. In the case of centrifugal separators, where the flow is subject to forces which are

multiple times greater than gravity, the droplet size for high separation is within the 10-300 µm region dependent on the size of the device, (Perry & Green, 1984). Inertial impaction as employed by mist eliminator pads removes droplets in the region of 1-5 µm. The typical design of this separation mechanism is a series of fibres or intertwined mesh strips housed in a containing vessel which must be large enough so that the continuous phase velocity is significantly low to prevent the agglomerated liquid droplets becoming re-entrained in the flow. Inertial impaction is also the main separation mechanism in a filter vane separator which consists of a series of baffle plates within a vessel. The main difference between a filter vane separator and a mist eliminator is that the former can operate at higher gas velocities due to the separated liquid being able to drain away more effectively thus reducing the probability of re-entrainment. However the limiting droplet diameter is in the region of 10 µm due to the size of the gaps between the baffle plates. In the work carried out by Fewel and Kean they state that the most common use for a vane separator is to modify an already existing mist eliminator where the gas velocity exceeds the design velocity (Fewel & Kean, 1992). The final method of separation, liquid/gas coalesce cartridges, can separate out droplets down to 0.1 µm whilst being able to maintain high gas velocities. The features of this separator include that of mist eliminator pads and filter vane separators combined. This separation technique is usually found downstream of a knock-out drum and is not designed to remove large volumes of liquid. The liquid/gas mixture flows through a tightly packed fibre bundle with a wrap on the outer which enhances the separated liquid to drain away.

The various inertial separation mechanisms described above are summarized in Table 2.1 in terms of the droplet size which can be separated by each technique.

Separation Mechanism	Limiting Droplet Size
Gravitational (Knock-out Drum)	300µ
Centrifugal	8-10µ
Mist Eliminator Pad	1-5µ
Filter Vane	10µ
Liquid/Gas Coalescer	0.1µ

Table 2.1: Summary of Inertial Separation Mechanisms

2.3.1 Gravitational Separation

The principles governing gravitational separation are conceptually simple since droplets are acted on by three forces; gravity, buoyancy and drag. The resultant of these forces dictates the direction of motion therefore the primary goal in a gravity separator design is to size the vessel such that the latter two forces succumb to the former causing the droplet to become separated from the flow (Jekel, et al., 2001). A typical gravitational separator is shown in Figure 2.2.
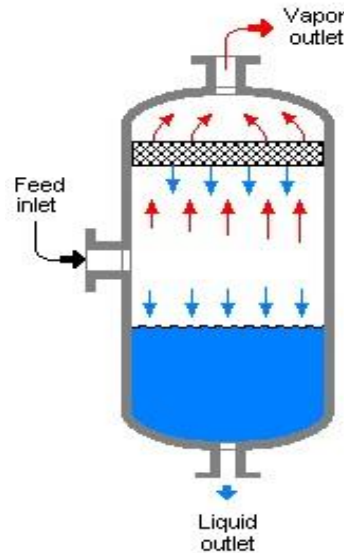
Figure 2.2: Vertical Gravitational Separator

The concept of terminal velocity is a key factor in gravitational separation and is defined as the velocity at which the vertical component of the drag force exactly counteracts gravity therefore the body will fall at a constant velocity since there is no overall net force and hence no acceleration. Therefore the terminal or suspending velocity, U_t, of the droplet is defined in equation 2.1 (Souders & Brown, 1934).

$$U_t = \frac{2gd_d(\rho_l - \rho_g)}{3C_D\rho_g} \qquad (2.1)$$

where g is the gravitational acceleration, d is the droplet diameter, ρ_l and ρ_g are the droplet and gas densities respectively and C_D is the drag coefficient for a smooth sphere based on the droplet Reynolds number which is defined as;

$$Re = \frac{\rho_g|U_d - U_g|d_d}{\mu_g} \qquad (2.2)$$

where U_d is the droplet velocity and U_g is the gas velocity. The value of C_D can be estimated using the following (Bird, et al., 1960);

$$C_D = \frac{24}{Re} \quad Re < 1 \tag{2.3}$$

$$C_D = \frac{18.5}{Re^{\frac{3}{5}}} \quad 1 < Re < 500 \tag{2.4}$$

$$C_D \approx 0.44 \quad 500 < Re < 2 \times 10^5 \tag{2.5}$$

Vertical gravitational separation is the simplest case since all the motion is in a singular plane therefore in order for separation to occur the gas velocity must be less than the droplet terminal velocity. For low velocities and when the Reynolds number is less than 1 such that equation 2.3 applies then Stokes law is satisfied where;

$$U_{t(Stk)} = \frac{gd^2 \Delta\rho}{18\mu_g} \tag{2.6}$$

It is reported that in the ASHRAE Refrigeration handbook of 1998 a recommendation for the sizing of low-pressure vertical separators is presented (Jekel, et al., 2001). For a given refrigerant, temperature and vertical separation distance the maximum allowable steady vapour flow is given. A method for estimating the vertical separation distances required is shown in Table 2.2 (Jekel, et al., 2001).

Vertical Separating Distance (mm)	Critical Parameters	Temperature (°C)				
		10	-6.67	-23.33	-40	-56.67
254	Vertical Vapour Velocity (m/s)	0.15	0.21	0.31	0.48	0.8
	Droplet Size (μm)	81	92	104	122	147
	Vertical Travel (mm)	2.03	4.06	8.64	21.3	59.2
610	Vertical Vapour Velocity (m/s)	0.64	0.87	1.3	2.0	3.3
	Droplet Size (μm)	296	317	355	405	472
	Vertical Travel (mm)	32.3	61.2	133	320	884
914	Vertical Vapour Velocity (m/s)	0.71	0.99	1.4	2.2	3.5
	Droplet Size (μm)	334	364	398	444	508
	Vertical Travel (mm)	39.6	78.0	163	378	1010

Table 2.2: Critical Droplet Sizes and Maximum Vertical Travel for Recommended Vertical Vapour Velocities

From Table 2.2 it can be seen that at a temperature of -56.67°C, vapour velocity of 0.8 m/s and a droplet size of 147 μ m the maximum vertical travel required is 59.2 mm whereas the vessel height is 254 mm meaning the vessel is oversized whereas at the same temperature for a vapour velocity of 3.5 m/s and a droplets size of 508 μm the maximum travel is 1010 mm with an available vertical separation distance of only 914 mm therefore the vessel is undersized. It is also reported that other approaches are more fundamental for vertical gravity separators by first calculating the terminal velocity of the required droplet size then setting the vapour velocity to between 75% and 90% of that value (Jekel, et al., 2001).

In the case of horizontal gravity separators the carrier gas flows predominantly in the horizontal direction with the droplets settling in the vertical direction, as a result the droplets have velocity components in both directions making the analysis more complex. As a result the droplet residence time, τ, is of significant importance and is defined as;

$$\tau = \frac{L}{U_{va,x}} \tag{2.7}$$

where L is the length of the vessel in the x-direction between inlet and exit and $U_{va,x}$ is the vapour velocity in the x-direction. For a droplet to be separated it must fall from its position in the vapour flow to either the liquid surface or internal wall of the vessel within the residence time described in equation 2.7. Therefore the vertical distance travelled by a droplet becomes;

$$\Delta y = \tau U_t \tag{2.8}$$

It is recommend that horizontal separators should have inlet and exits separated by a horizontal length at least equal to that of the vertical height and that anything beyond this length will increase the residence time therefore allowing larger vapour velocities to be handled (ASHRAE, 1998). However in the case of very small droplets where Stokes law applies the residence time needs to be very large which in turn means extremely long horizontal lengths or extremely low settling velocities. It is the former reason that gravity separators are rarely used in applications where high separation efficiency is required since the physical size and cost of horizontal gravity separators is too great for many industrial situations.

In relation to the Henry Technologies separator under investigation the residence time for a droplet is enhanced by the inclusion of the helical path. This forces the bulk flow to descend

round the helix ensuring there are at least one and a half revolutions of the geometry before entering the centre tube of the geometry. This prevents the gas from short circuiting the separator by flowing vertically downwards and then upwards through the outlet. This increase in residence time will allow time for the smaller droplets to transit to the cylindrical walls and adhere to the descending liquid film therefore improving the overall separation efficiency.

2.3.2 Impingement and Impaction Separation

A comprehensive approach to droplet separation based on an inertial separation parameter Ψ is presented by Burkholz (Burkholz, 1989). The fundamentals of this parameter are based on the Stokes number which defines the ability of a droplet to deviate from the streamlines of the flow and impact on a surface. The inertial separation parameter therefore acts as a method of defining the separation efficiency of a droplet. The calculation of inertial separation must start from a given gas flow field and is dependent on the tendency of a mass, in this case in the form of a droplet, to deviate from the streamlines of the continuous flow and impact on a surface thereby becoming separated from the flow. This is the fundamental concept which governs particle and droplet separation in mesh filters and cyclones and therefore requires an extensive review. It is the consequence of inertial separation which leads to the removal of the entrained oil from the refrigerant gas flow within a helical oil separator.

To determine whether a suspended droplet will deviate from the streamlines of the carrier gas a force balance on the droplet has to be examined. This requires the centrifugal and gravitational acceleration forces, the pressure gradient and frictional drag forces all to be accounted for. When dealing with cyclonic separation it is only the former force which needs to be considered due to the large density difference between the continuous phase and dispersed phase, the high velocities of the droplet and gas and the rapid changes in direction of the streamlines (Hoffmann & Stein, 2008). However when examining wire filter based separation all the forces need to be considered; Burkholz demonstrates the effect of inertial separation on a single wire fibre of a mesh screen by assuming it to be a simple cylinder (Burkholz, 1989), Figure 2.3.
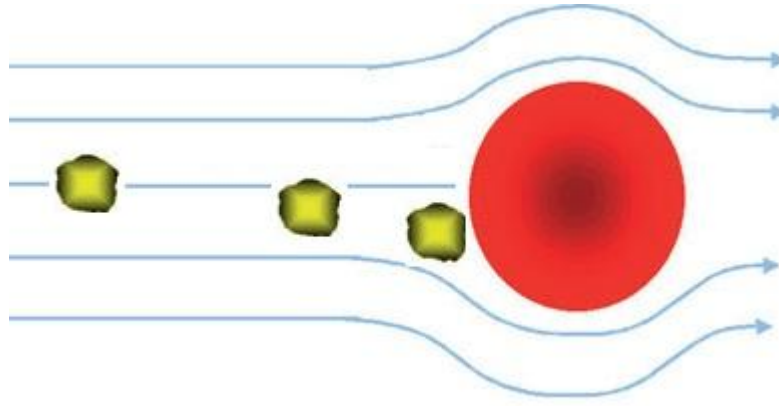
Figure 2.3: Inertial Separation

The inertial separation parameter Ψ, a dimensionless number grouping together the basic parameters which contribute to inertial separation (D_f, ρ_l, d, ΔP, ρ_g, μ_g) was first recognized in 1931 by Albrecht and Sell for determining the effects of a single fibre in a wire mesh, but can also generalised to account for all types of separation equipment as shown by (Burkholz, 1989).

$$\Psi = \frac{1}{4}\left(\rho_l \rho_g^{-\frac{1}{3}} \mu_g^{-\frac{4}{3}}\right)\left(\Delta P^{\frac{2}{3}} D^{-\frac{2}{3}} d^2\right) \tag{2.9}$$

Burkholz demonstrated that equation 2.9 could be written as (Burkholz, 1989);

$$\Psi = Stk_B Re_g^{\frac{1}{3}}\left(\frac{Eu}{2}\right)^{\frac{2}{3}} \tag{2.10}$$

where Stk_B is the Stokes number applied by Burkholz which only accounts for the liquid density rather than the density difference and Eu is the Euler number which represents the pressure drop coefficient;

$$Eu \equiv \frac{\Delta P}{\frac{1}{2}\rho_g u_g^2} = \xi \tag{2.11}$$

Assuming that any acceleration on the droplet can be neglected then the behaviour of a droplet at any location in a trajectory can be described by balancing the inertial and frictional forces;

$$m\frac{d\overrightarrow{u_l}}{dt} = C_D \frac{\rho_g}{2}\left(\overrightarrow{u_l} - \overrightarrow{u_g}\right)\left|\overrightarrow{u_l} - \overrightarrow{u_g}\right|\frac{\pi}{4}d^2 \tag{2.12}$$

where u_l is the liquid droplet velocity, u_g is the gas velocity, m is the droplet mass and $\frac{d}{dt}$ the time derivative, with the arrows denoting a vectorial equation and the straight brackets representing absolute values. Thus equation 2.12 becomes;

$$\frac{d\vec{u_l}}{dt} = \frac{18\mu}{\rho_l d^2}\left(\vec{u}_l - \vec{u}_g\right)$$
(2.13)

Equation 2.13 combined with equation 2.9 can be solved in a two dimensional x-y coordinate system to calculate inertial separation for different flow fields (Burkholz, 1989). An approximate formula for the fractional separation efficiency of a single fibre, assumed to be a single cylinder, with Re>50 was presented by Loffler and Muhr in 1972 where the effects of the boundary layer on the cylinder has been accounted for as shown in equation 2.14 below (Burkholz, 1989);

$$\eta_{Inertia} = \Psi^3/\left(\Psi^3 + f_1\Psi^2 + f_2\Psi + f_3\right)$$
(2.14)

with;

$f_1 = -0.0133 lnRe + 0.931$

$f_2 = 0.0353 lnRe - 0.36$

$f_3 = -0.0537 lnRe + 0.398$

The accuracy of equation 2.14 above 10% is $\pm 1\%$. To account for the effects of interception, which occurs when a droplet following a streamline passes within a distance equal to the radius of the target fibre, thus just causing the droplet to be retained. Interception happens mainly at low Reynolds numbers and the interception efficiency is calculated from;

$$\eta_{Interception} = \left\{\left(1 + \frac{d}{D_f}\right)ln\left(1 + \frac{d}{D_f}\right) - \frac{1}{2}\left(1 + \frac{d}{D_f}\right) + \frac{1}{2}\left(1 + \frac{d}{D_f}\right)^{-1}\right\}/La$$
(2.15)

where;

$$La \approx 2 - lnRe \ \ for \ Re < 1$$
(2.16)

2.3.3 Wire Mesh Filtration

The theory discussed in the previous section with respect to the inertial separation parameter and single cylinder separation efficiency can be related to the actual performance of a wire mesh separator. The inertial separation parameter indicates that the pressure drop is proportional to the size of the target fibre, for the separation of a particular limiting droplet size. Based on this knowledge it is advantageous to the overall performance of the separator if the impacting wire diameter is kept as small as possible. One of the governing parameters for the separation and pressure drop of a filter is based on its overall onflow area. The relative onflow area, p, is defined as the ratio of the open cross-sectional area to total onflow cross-sectional area through equation 2.17;

$$p = \frac{LD_f}{F} \qquad (2.17)$$

where L is the total wire length and F is the overall onflow area. Based on equation 2.17, taking each mesh layer, n, as a separate opportunity for a droplet to be removed and assuming that no re-entrainment takes place and that the events at each layer are considered as individual entities then the efficiency of a mesh screen with n layers is;

$$\eta_{Filter}(n) = 1 - (1 - \eta_{Filter}(0)p)^n \qquad (2.18)$$

A key parameter in determining the performance of any separator is the limiting droplet diameter often referred to as the cut size or d_{50} cut-point diameter and is defined as the droplet size that is separated with an efficiency of 50% (Hoffmann & Stein, 2008). For a knitted wire mesh filter the limiting droplet diameter is;

$$d_{50} = 8(fGH)^{-\frac{1}{3}} D_f^{\frac{2}{3}} v_0^{-\frac{2}{3}} S^{-\frac{1}{3}} \rho_l^{\frac{1}{3}} \qquad (2.19)$$

where;

$$d_{50} = \rho_l^{\frac{3}{2}} \rho_g^{\frac{1}{2}} \mu_g^{-2} \qquad (2.20)$$

where G is the ratio of filter mass/filter volume, f is an empirical correction factor (0.8-1.0) and H is the filter thickness.

The pressure drop can also be obtained for a wire mesh filter assembly using equation 2.21. The losses are attributed with the complex path the gas flow has to make through the wire mesh screen and is defined as;

$$\Delta P = fG\left(\frac{H}{D}\right)\left(\frac{\rho_g}{\rho_l}\right)v_g^2 \tag{2.21}$$

The helical separator consists of a single layer mesh screen comprising 60 strands per inch (0.16 mm diameter wires, 0.263 mm aperture, 39% open area) at the entrance to the centre tube and on the cylindrical wall of the main separation space. Given the conditions which the separator operates inertial separation is the dominant mechanism for the mesh screens therefore the method presented above can be used to determine the fractional efficiency and pressure drop for these components. Using this method the d_{50} value for the mesh and associated pressure drop were found to be 6.3 microns and 15 Pa respectively for a single layer mesh screen subject to a flow field at atmospheric pressure.

2.3.4 Centrifugal Separation

The indicated principle separation mechanism within the helical oil separator is through the generation of a centrifugal force as stated in the description of the product by Henry Technologies. Therefore an in-depth examination of the literature relating to centrifugal separation, generated through cyclonic type geometry, is required in order to allow a performance assessment of the separator to be carried out.

The ability to use the generation of a centrifugal force to promote particle separation was first proposed by Gustaf De Laval in 1877 (Gupta, et al., 1984). Since then extensive research has been carried out in order to improve the efficiency of particle removal through experimental testing, empirical derivations and more recently computational simulations. The most commonly used geometrical configuration to exploit the centrifugal force is the cyclone separator which has been optimised through numerous investigations (Shepherd & Lapple, 1939), (Ter Linder, 1953), (Stairmand, 1951) with the Stairmand design being referred to as the "High Efficiency Stairmand Cyclone." A typical cyclone configuration with the gas flow path from inlet to outlet is shown in Figure 2.4. In the central core region a quasi-forced vortex exists where the tangential velocity is proportional to the radius in the outer region a quasi-free vortex exists where the tangential velocity is a constant. The particle removal process is initiated with the flow entering the separator tangentially through the inlet chute. This imparts a spinning motion on the flow directing the particles

to be separated radially outwards towards the cylindrical wall. As the gas flow swirls, it is transported axially downwards in the outer part of the separation space to below the entrance level of the centre tube, or vortex finder as it is referred to in cyclone geometries. Within this region the gas flow is slowly forced towards the centreline of the geometry transitioning the axial movement to be in the upward direction. The vortex motion continues down the geometry towards the base until all the flow is in the upward direction allowing the gas to exit the cyclone geometry. The particles which collide with the cylindrical walls of the separator, as a result of the centrifugal flow field, are transported down the internal surfaces under gravity and are collected in the lower region of the separator geometry often referred to as the dust hopper (Hoffmann & Stein, 2008).
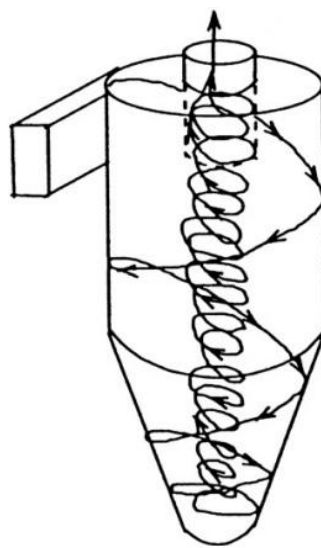
Figure 2.4: A Typical Tangential Inlet Cyclone with Cylindrical Coordinate System

Due to the compact nature, absence of moving parts, low cost of manufacture and lack of requirement for regular maintenance and replacement of components the cyclone separator has been and still is a popular choice of separator in industry for the removal of a dispersed phase; solid or liquid; from the continuous phase; either gas or liquid. This has led to a very diverse range of applications within industry and has resulted in a number of researchers experimentally studying the behaviour of the fluid flow within the geometries hence there is a large amount of data available characterising the performance of cyclones. Early cyclone literature contains reports on observations relating to performance and optimisation based on an understanding of the gas flow patterns inside a cyclone from physical measurements, knowledge of centrifugal acceleration and Stokes law. The combination of these methods provides a detailed understanding of the carrier gas and

droplet motion inside a cyclone geometry. Later literature connects these early observations about specific elements of cyclone performance with theory, semi-empirical models and most recently mathematical models that are solved using CFD with an ever increasing demand for computational advancements to allow an accurate solution which can describe the phenomenon which exists in practice. Empirical models have been derived which describe the flow characteristics within cyclones which in turn can lead to theoretical predictions of the separation efficiency and pressure drop for the overall geometry. The vast majority of these empirical models are formulated for solid particle separation from a gas stream in a cylinder on cone cyclone geometry with a tangential inlet, like that shown in Figure 2.4; however there are models available to describe the effects of droplets in "Demisting cyclones."

The liquid droplets entering a demisting cyclone are normally greater in size and not porous unlike the particles feeding gas-solid cyclones, therefore making separating the dispersed phase easier (Hoffmann & Stein, 2008). Within the upstream pipework leading to the separator the small droplets can coalesce into larger drops, where the driving force for this physical process is dictated by the surface tension of the liquid. Once in the main separation volume the droplets are directed towards the walls of the cylindrical body through centrifugal forces and form a liquid film. The liquid film contains a much larger mass of fluid which is not easily removed or re-entrained back into the gas phase, unlike gas-solid cyclones. Gas-liquid cyclones are also less prone to 'plugging' due to the agglomeration of solid particles through being tacky or statically charged and are less prone to erosion in comparison to gas-solid units. As a result the designs of gas-liquid cyclones have a greater amount of scope therefore are commonly found with a range of different internal features including; coalescing mats, anti-creep skirts, close-fitting vanes and isolation disks, to name a few, all of which exist to some degree within the Henry Technologies helical separator.

With regards to the design and mode of operation, droplet cyclones correspond generally pretty well to the well-known and thoroughly investigated dust cyclones (Burkholz, 1989). However, the low pressure conditions which exist within the cyclone geometry can lead to creeping flows which transport the collected droplets as a liquid film to the exit tube therefore certain design modifications need to be implemented to prevent this phenomenon occurring, this will be discussed further later on. Even with the strong similarities which exist between dust and droplet cyclone separators, there still exists very

24

few investigations which have been published on droplet separation in cyclones (Burkholz, 1989); although this citation is over twenty years old the author believes it to still be valid. This is attributed to the difficulty associated with measurements of the droplet sizes formerly encountered in similar gas-droplet investigations. Nevertheless the only difference between droplet and solid particulate cyclones is in the method of the dispersed phase removal. The mechanisms of separation are the same therefore the laws which govern the separation of dust particles can also be applied to droplet separation. As a result the following section will investigate in detail the empirical models available to predict the separation efficiency and pressure drop for cyclone dust collectors so that the most effective models can be used to help predict the performance of the helical oil separator being investigated in this project.

As described previously the mechanism which leads to the separation of the dispersed phase in a cyclone separator is by a centrifugal force which is produced through the generation of an intense vortex flow either via a tangential inlet into the main separation space or by axial guide vanes inducing the swirling motion. The outlet of a cyclone acts as a sink for the gas flow and forces the gas to be drawn radially inwards towards the axis of the cyclone producing a Rankine vortex. The presence of a Rankine vortex has been acknowledged and investigated by a number of researchers (First, 1949)**,** (Reydon & Gauvin, 1981)**,** (Zhou & Soo, 1990)**,** (Fraser, et al., 1997)**.** The flow in the main body of a cyclone is typically turbulent characterized by a Reynolds numbers in the region of $\sim 10^{5}$ particularly in the boundary layers on the internal surfaces and in the centre core of the geometry. It has been reported that the flow in the central region of the cyclone, where there is a low pressure core, as rotating like a solid body with a high level of turbulence and transient nature (Ter Linden, 1949). Within the central core the existence of the flow contraction for the gas exit tube and the sharp edge associated with this feature generates pressure losses and flow instabilities such as a precessing vortex core (PVC) (Abdullah, 1996).

The flow field within a cyclone is generally described in terms of the Reynolds number as described in equation 2.2, where the characteristic length is the diameter of the main cyclone cylindrical body, and a geometric swirl parameter which measures the ratio of angular to axial momentum (Cortes & Gil, 2007). The swirling flow results from a tangential velocity component being imparted on the flow on entry into the cylindrical body of the

cyclone usually through a tangential duct. The swirl number has been defined as a non-dimensional number which represents the axial flux of swirl momentum by the product of axial momentum and equivalent nozzle radius (Gupta, et al., 1984);

$$S_w = \frac{G_\theta}{G_z \frac{D_o}{2}} \tag{2.22}$$

where G_θ is the axial flux of swirl momentum given as;

$$G_\theta = \int (\rho uw + \rho \overline{uw})r^2 \, dr \tag{2.23}$$

which includes the z-θ direction turbulent shear stress term where u and w are the velocity components in a cylindrical polar coordinate system. G_z describes the axial flux of axial momentum;

$$G_z = \int \{(\rho w^2 + \rho \overline{w^2}) + (P - P_\infty)\}r \, dr \tag{2.24}$$

which includes the z direction turbulent normal stress term and the pressure term. Due to the complex nature of the flow in a cyclone and the variation in axial flowrate with axial position other velocity parameters are required to obtain the local values for S_w. As a result simplifications are required to produce a generic swirl number for the cyclone geometry (Hoekstra, et al., 1999) which reduce to;

$$S_w = \frac{\pi D_o D}{4 A_{in}} \tag{2.25}$$

where A_{in} is the cross-sectional area of the inlet duct to the cyclone. Industrial gas cyclones generally operate with a S_w between 1.5 and 4.0 (Hoekstra, et al., 1999). The swirl number for the helical separator was computed to be 4.65 which would indicate that the geometrical configuration of the helical unit should exhibit some of the flow characteristics of a cyclone.

The main focus of research into cyclone separators has always centred on understanding the driving factors leading to enhanced separation efficiency and a reduced pressure drop. These factors are determined mainly by the interactions between the physical and geometric design of the cyclone, the phases subject to separation and the environment in which it is installed. Since the introduction of the first cyclonic separator in the latter part of the 19th century, extensive work has been carried out to gather experimental data on the flow characteristics and at the same time develop theoretical models (Cortes & Gil, 2007).

2.3.4.1 Velocity Profile Data

The velocity profile within a cyclonic geometry is characterized by the axial, radial and tangential components of which the latter dominates and is directly related to the amount of centrifugal force which is applied to the flow field (Ter Linder, 1953). A typical profile for the tangential velocity component is where the tangential velocity increases from the centreline of the geometry to a maximum value at the edge of the forced vortex then decreases from this point to the cylindrical wall (Stairmand, 1951). Early experimental flow investigations within cyclones were carried out using a Pitot tube to determine the velocity profiles and pressure drop. A glass cyclone model with a variable inlet vane was investigated with the results showing that the tangential velocity distribution in the flow region below the vortex finder could be described by the relationship;

$$ur^n = constant \tag{2.26}$$

where the vortex exponent, n, is prescribed a value of 0.5 (Shepherd & Lapple, 1939). A similar piece of work was carried out where the three velocity components were measured along with the total and static pressures (Ter Linden, 1949). The inlet velocity and static pressure were 10.7 m/s and 90 mm H_2O gauge respectively with an atmospheric discharge; the results of the investigation are given in Figure 2.5.
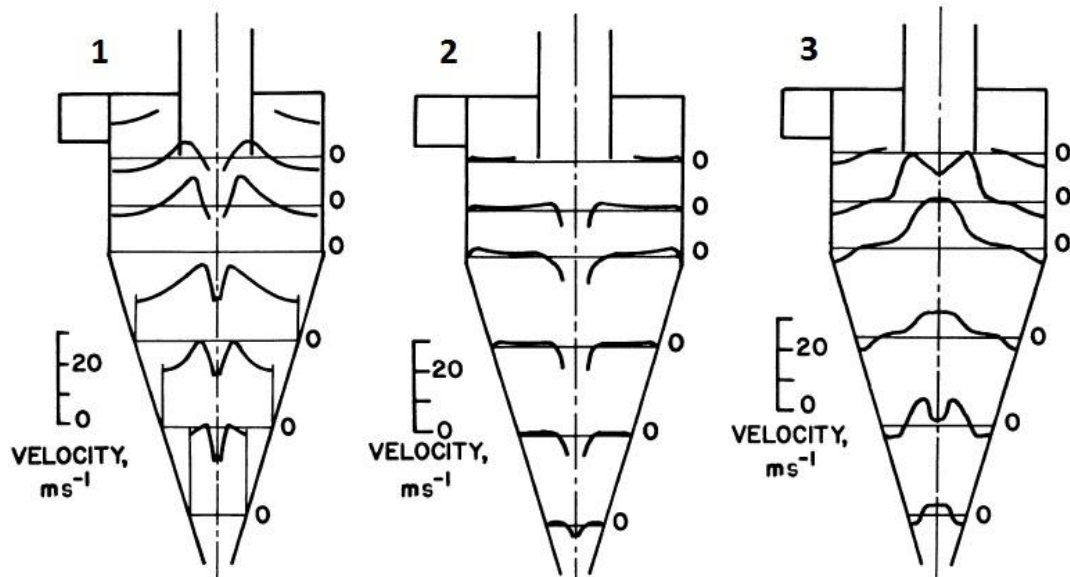
Figure 2.5: 1-Tangential 2-Radial 3-Axial Velocity Profiles in a Cyclone Separator (Ter Linden, 1949)

27

The first image shown in Figure 2.5 displays the tangential velocity profile which shows an increase from the cylindrical wall to the perimeter of the centre tube. This is governed by the free vortex flow in this outer region where the vortex exponent in equation 2.26 is prescribed a value of 1 denoting the complete conservation of angular momentum as a result of the high shearing action. At the core of the cyclone there is a point of inflection in the velocity profile after which their magnitude reduces dramatically in the vortex core which is governed by the forced vortex flow with the vortex exponent taking on a value of -1 demonstrating solid body rotation with no shearing. Based on this and the information from experimental studies on the range of values for n suggests that the conditions within a cyclone tend to that of free vortex flow where the conservation of angular momentum holds true. The second image displays the radial velocity profile where in the outer region of the cyclone this component is almost constant. Towards the core of the cyclone there is a change in direction of the radial component from a positive direction towards the cylindrical wall in the outer region to a negative direction towards the cyclone centreline in the forced vortex region. The final image shows the axial component where at the wall of the cyclone the flow is downward, which transports the collected particles to the base of the separator. On the other hand the axial velocity in the core region of the cyclone is in the upward direction with an inverted W-shaped velocity profile occurring below the entrance of the centre tube. The nature of the axial velocity profile is due to the presence of the precessing vortex core (PVC) which oscillates around the centreline of the geometry.

Amongst the early experimental techniques for measuring the velocity patterns inside a cyclone separator is the use of hotwire anemometry which has the advantage of a very good time resolution and physically being smaller in size than a Pitot tube. However both these techniques require a physical presence in the flow field which can alter the natural path of the fluid and neither has the ability to determine the direction of the velocity. The various issues that result from these intrusive techniques is mainly due to attenuation of swirl and inconsistent readings near the centreline due to the (PVC) (Peng, et al., 2002) (Cortes & Gil, 2007). The development of the non-intrusive optical laser based technique, Laser Doppler Anemometry (LDA), has been successfully employed in recent years (Abdullah, 1996), (Hoekstra, et al., 1999), (Zhou & Soo, 1990), (Hsieh & Rajamani, 1991). LDA requires the addition of small seeding particles which follow the gas flow faithfully the only drawback being that these particles may be segregated inside the volume leaving a void at the centreline where the time resolution is limited due to the PVC and sometimes

can result in no measurements at all (Cortes & Gil, 2007). There is also the issue of beam misalignment due to the curvature of the cylindrical wall (Hoffmann & Stein, 2008). In the majority of cases however the time-averaged velocity component measurements are obtained successfully along with information on the degree of turbulence within the flow and the effect of any periodic fluctuations.

From this review of acquiring velocity component measurements within a cyclone separator, where the flow field is swirling, it is apparent that to avoid any interference with the flow a non-intrusive measurement technique such as LDA should be used. The typical characteristics of each velocity components have also been identified therefore providing an indication of the types of profiles which might be expected when obtaining measurements from the helical separator.

2.3.4.2 Pressure Drop

The effects of pressure drop in cyclones are mainly due to the three factors; vortex energy, solid loading and wall-friction, with the principal case being the vortex energy (Gil, et al., 2002). The pressure drop in strongly swirling flow situations contain special fluid mechanics effects which lead to results which contradict intuition from regular swirl free flow phenomenon resulting in some confusion in the cyclone literature. The pressure drop in a cyclone is a combination of the static and dynamic pressure between the inlet and outlet ducts and is represented by equation 2.27 as described by (Ogawa, 1984);

$$\Delta P = \Delta P_s + \rho \frac{U_{in}^2}{2} \qquad (2.27)$$

The pressure loss in a cyclone has been studied very closely by a number of workers, (Shepherd & Lapple, 1939), (Ter Linden, 1949), (Stairmand, 1949) with the most commonly used pressure drop relationship shown in equation 2.28;

$$\frac{\Delta P}{\rho U_{in}^2} = f\left(\frac{U_{in}D}{v}\right) \qquad (2.28)$$

The dimensionless group on the right hand side of equation 2.28 is the well-recognised Reynolds number; in general if the value of this parameter is $\approx 10^5$ or greater than the inertial forces dominate the viscous ones and equation 2.28 can be reduced to equation 2.11, the Euler number. As a result of this simplification the pressure drop for any given cyclone is purely a function of geometry and solids loading. Dealing with the latter point the

pressure drop coefficient is usually broken down into two factors; a particle free loss, ξ_g, and a particle laden loss, ξ_s, the product of which is the overall Euler number. A summary of the various models in order to determine the value of ξ_g , are presented (Cortes & Gil, 2007). One of the most simple, yet effective empirical models for determining the pressure drop with the assumption that the particle loading is very low applies (Shepherd & Lapple, 1939);

$$\xi = K \frac{ab}{D_o^2} \qquad (2.29)$$

where K is a constant which is prescribed a value of 16 for standard tangential inlet cyclones and 7.5 for inlet vane units where the inner wall of the tangential entry extends past the cyclone inner wall to a point halfway opposite the wall. This model was compared with other models, (Stairmand, 1949), (Alexander, 1949), and found to give results as good as the more complicated calculation methods, (Leith & Mehta, 1967), even though equation 2.29 only includes the cross-sectional area of the inlet and the diameter of the outlet.

The mechanisms which contribute to the pressure drop in a cyclone at first seem perplexing as they are contrary to intuition; that is cyclone pressure drop decreases with an increase in wall friction, concentration of the dispersed phase and the length of the cyclone body. The main contributor to the pressure loss is due to the viscous dissipation of the kinetic energy term, $\frac{1}{2}\rho v_t^2$, in the vortex finder. For example, increasing the wall friction factor causes greater losses in the separation volume, however this also causes a reduction in the tangential component of the velocity, v_t, which in turn means there is a reduction in losses in the vortex finder. Inside the vortex finder the tangential velocity is naturally greater and since the kinetic energy contains the square of this velocity component then there will be an increase in the dynamic pressure and hence a reduction in the pressure drop as a result of increased wall friction (Hoffmann, et al., 1992).

Since the pressure drop in a centrifugal separator can be costly in terms of performance if it is high, extensive research has been done in order to find methods of reducing it. Amongst the attempts was the introduction of both straight and curved flow straightening vanes above and below the entry to the outlet duct (Shepherd & Lapple, 1939). In doing so they found that the vanes positioned within the cyclone had a positive effect in reducing the pressure drop whilst those situated one diameter downstream of the exit had no noticeable

effect. A deswirl device has been trialled in the outlet duct of a standard Stairmand cyclone 5 diameters downstream of the entrance to the vortex finder (Browne & Strauss, 1977). Tests were carried out with four different blade configurations; 2, 4, 8 and 16, and discovered that a pressure drop reduction of over 22% could be achieved from the 8 blade configuration without a detrimental effect to the efficiency of the unit.

A pressure drop reduction of 33% was achieved by inserting a central body at the central axis of the cyclone. The effect of this body forced the maximum swirl velocity to migrate towards the wall. This resulted in a reduction in the swirl and axial velocity components in the core with an increase in the total and static pressure (Zhou & Soo, 1990).

A more detailed study was carried out recently on the effects of flow rectifying equipment on the dynamics of the vortex and the separation efficiency in a reverse-flow centrifugal separator (Hoffmann, et al., 2006). An important observation made by the authors was that the presence of the swirl at a static pressure tapping will give a higher static pressure at the wall than the cross-sectional average. To attempt to compensate for this the outlet pressure tapping was placed a meter downstream of the gas outlet so that the intensity of the swirl was given a chance to dissipate, however this makes it more likely for the measured pressure drop to appear lower than it actually is. The results from their investigation showed that the installation of the rectifying vanes under the gas outlet reduces the pressure drop by up to 30%, but also has a detrimental effect on the separation efficiency.

2.3.4.3 Separation Efficiency

The mechanics of a cyclone which have been discussed to this point only partially describe the operation of the device as a whole; the main purpose of any centrifugal separator is to separate the dispersed phase from the continuous phase through the generation of forces with the resultant transporting them to the cylindrical wall. The forces which dominate in a centrifugal device are of course the centrifugal forces and the drag forces; however there are also interactions between particles and the wall and between individual particles which are often neglected in the literature due to the lack of understanding of their effects on the separation process (Cortes & Gil, 2007). The centrifugal force given in equation 2.30 is an inertial based force which acts to move the particulate phase towards the wall of the separation vessel;

$$F_C = \frac{\pi d^3}{6}(\rho_d - \rho_g)\frac{u^2}{r} \qquad (2.30)$$

The drag force given in equation 2.31, based on Stokes law for a spherical particle, opposes the motion of particles in the radial direction results from the continuous phase attempting to cause the particles to follow in the direction of the main stream flow direction;

$$F_d = 3\pi d_d \mu v \qquad (2.31)$$

where v is the radial velocity component (m/s). Based on equation 2.30 and equation 2.31 it can be seen that dense particles with a large diameter at a small radius with a high swirl velocity will produce a large centrifugal force and hence enhance the separation efficiency. For a particle to move towards the wall and be collected then $F_c > F_d$, however when $F_c < F_d$ then the particle will move to the vortex finder and become entrained within the inner vortex. In the case where the centrifugal force equals the drag force then there is a 50% chance of the particle being collected and a 50% chance it will become part of the inner vortex (Wang, et al., 2003).

The ability of a centrifugal separator to collect the dispersed particles from the continuous flow is measured by its collection efficiency, η, defined as the fraction of the inlet flow rate of solids separated in the main body. The particle size distribution (PSD) in a separator usually has a wide range therefore the collection efficiency is given for indefinitely small intervals, producing a continuous function η(x) defined as the grade-efficiency of the separator. This data can then be plotted graphically producing a grade efficiency curve which has a characteristic sigma shape upon which the d_{50} cut size is defined; the particle diameter which is separated half the time (Cortes & Gil, 2007). A typical grade-efficiency curve (GEC) is shown in Figure 2.6.
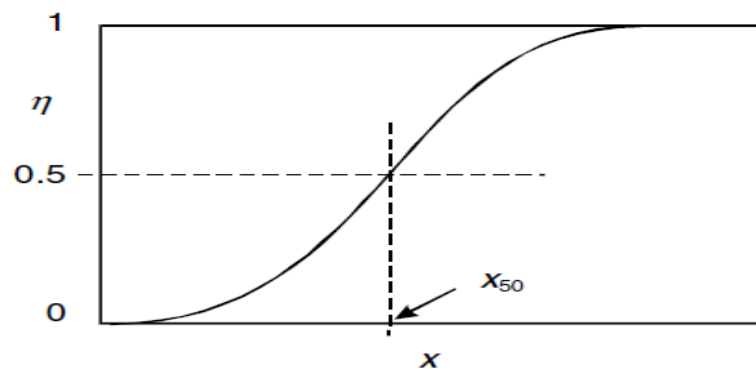
Figure 2.6: Typical Grade Efficiency Curve showing d_{50} Cut Point (Hoffmann & Stein, 2008)

The characteristic S-shaped GEC given in Figure 2.6 indicates the probability of separation of all particle sizes with the gradient of the curve indicating how sharp the cut off of separated particles will be. A GEC is produced as a result of data from experimental testing or computational modelling such that the efficiency for a particular particle diameter can be described by;

$$\eta_d(d) = \eta_d \frac{f_s(d)}{f_{inj}(d)} = 1 - (1 - \eta_d)\frac{f_e(d)}{f_{inj}(d)} = 1 - (1 - \eta_d)\frac{dF_e(d)}{dF_{inj}(d)} \qquad (2.32)$$

where η_d is the partition function which divides the droplets in a given size range into the separated and escaped flow streams. The subscripts s, inj and e denote the fraction separated, injected and escaped respectively.

Early empirical models for the prediction of cyclone separation efficiency are based on much idealized arrangements of particle forces and velocities which ignore the chaotic nature of the flow due to the turbulent fluctuations and vortex structure instabilities which exist in practice yet some models produce successful results. There are two modelling approaches for cyclone separators presented in the literature; the equilibrium orbit model and the time-of-flight model. The equilibrium orbit model is defined whereby a particle rotating on the circumference of the control surface (CS), $\frac{D_o}{2}$, experiences a force balance between the centrifugal force and the inward drag force with the former being proportional to the mass of the particle, d^3, and the latter is proportional to d. This implies that the large particles will be easily centrifuged to the cyclone wall whereas the small particles will be dragged into the core region and carried out of through the exit tube. The particle size where the force balance is equal will just orbit the circumference of the CS and stand a 50% chance of being captured hence this defines the cut size of the separator. The time-of-flight model is defined by the migration of the particle to the wall and ignoring the inward gas velocity with the posed question of-whether a particle which is injected at any lateral position in the inlet has time to reach the cylindrical wall and be collected before it reaches the base of the cyclone (Hoffmann & Stein, 2008). Hybrids of these two classical modelling approaches have also been presented in the literature.

The equilibrium orbit model based on the force balance on a particle, is obtained by equating equation 2.30 and equation 2.31 to give the cut size of the separator theoretically where the density difference between the two phases is neglected, is given as;

$$d_{50} = \sqrt{\frac{v_{rCS} 9 \mu D}{\rho_d v_{\theta CS}^2}} \tag{2.33}$$

where v_{rCS} and $v_{\theta CS}$ are the radial and tangential velocities at the control surface respectively. From the determination of the d_{50} cut size a GEC can be determined (Hoffmann & Stein, 2008) which takes the form;

$$\eta(d) = \frac{1}{1 + \left(\frac{d_{50}}{d}\right)^{6.4}} \tag{2.34}$$

The exponent of 6.4 given in equation 2.34 produces good results for smooth, well-designed laboratory cyclones, however for large scale, refractory-lined units and poorly designed small-scale cyclones the exponent can be reduced to a value between 2 and 4.

The time of flight model, proposed by Rosin et al. in 1932 who compared the time required for a particle injected at any location in the inlet to reach the wall versus the time actually available for this, denoting the d_{50} as the smallest particle size which can traverse the entire inlet jet before reaching the bottom of the cyclone whilst ignoring the inward gas velocity. The geometrical configuration of the separator used by Rosin et al. when investigating the time of flight model was cylindrical and later a conical type separator geometry was investigated (Hoffmann & Stein, 2008). More recently this model has been applied to an inline rotary-flow cyclone with successful results (Ramachandran, et al., 1994). The total time taken for a particle to reach the bottom of the separator is dependent on the diameter of the cylindrical body, D, the number of spiral turns the particle completes in the geometry, N_s, and the gas inlet velocity, v_{in};

$$Residence\ Time = \frac{\pi D N_s}{v_{in}} \tag{2.35}$$

where N_s can be calculated from equation 2.36 based on previous findings as a function of the inlet velocity;

$$N_s = 6.1(1 - e^{-0.066 v_{in}}) \tag{2.36}$$

from this the droplet cut size can be obtained for the time of flight model as;

$$d_{50} = \sqrt{\frac{9 b \mu}{\pi N_s v_{in} (\rho_d - \rho_g)}} \tag{2.37}$$

A hybrid model which combines the features of the equilibrium-orbit and the time-of-flight models was developed which considers both particle migration from the outer to the inner vortex and the radial movement to the separator wall (Dietz, 1981). The cyclone was divided into three separate regions; the entrance region, the down-flow region and the up-flow region. A proposal was made where there was an interchange of particles between the latter two regions, however it was also assumed that turbulence produces a uniform radial concentration profile for uncollected particles within each region. This model assumes that the particle concentration changes discontinuously across the boundary between the two regions. This is not physically possible and the approach of considering the transport of particles to be the net result of two opposing fluxes does not correctly reflect the physical exchange process. This idea was further developed but included a fourth region at the bottom of the separation space where the separated particulate phase is collected, where the effect of re-entrainment can be included (Mothes & Loffler, 1988). A more important factor however is the consideration of a finite turbulent diffusivity in both the upward and downward flow, avoiding the discontinuities of the Dietz model.

The time of flight model has been shown to produce successful results for hybrid type separators (Ramachandran, et al., 1994). Since this model is purely based on the fluid properties and geometrical parameters, without the requirement for local velocity information, the author will use this to estimate the d_{50} values for the helical oil separator. In applying the maximum and minimum velocities at the inlet to the separator operating at atmospheric pressure the time of flight model predicts the cut size of the helical separator to be 10.7 microns for a 100% discharge flowrate and 39.3 microns for a 25% discharge flowrate. These d_{50} predictions demonstrate the limitations of the cyclonic separation which are expected from the helical separator and identify a droplet size range to focus on for separation efficiency enhancement.

2.4 Liquid Film and Droplet Separation Phenomenon

2.4.1 Solid versus Liquid Separation

The literature reviewed up to this point is applicable to the separation of both solids and liquids from gas flows, however the Henry Technologies helical separator is required to separate only liquid in the form of a film and droplets from the gas stream. Although the mechanisms which result in the dispersed phase being separated are similar for solids and liquids, the difference in physical properties and particle dynamics are somewhat different

and it is the purpose of this section to explore this since each state poses its own unique problems and advantages.

2.4.2 Inlet Conditions

The effectiveness of all separators depends largely upon the size of the dispersed phase which needs to be removed. Gas-liquid centrifugal separator performance is highly dependent on the flow regime; droplet size and distribution; and liquid loading in the upstream pipework. Gardner and Owen describe the differences between the behaviour of liquids and solids in relation to separation devices and conclude that in the majority of cases the drops of liquid entrained in a gas flow are relatively coarse (Gardner & Owen, 1997). The flow regime describes how the two phases, liquid and gas, are distributed within the internal cross-section of the pipe. Being able to predict the flow regime in the horizontal pipework leading to the separator inlet allows for a better understanding of the mechanisms required to achieve a high level of separation since a heavily stratified liquid film will become quickly separated under the influence of gravity in comparison to an annular flow regime containing a core of sub-micron droplets. The range of flow regimes which can exist in horizontal pipelines are shown in Figure 2.7.
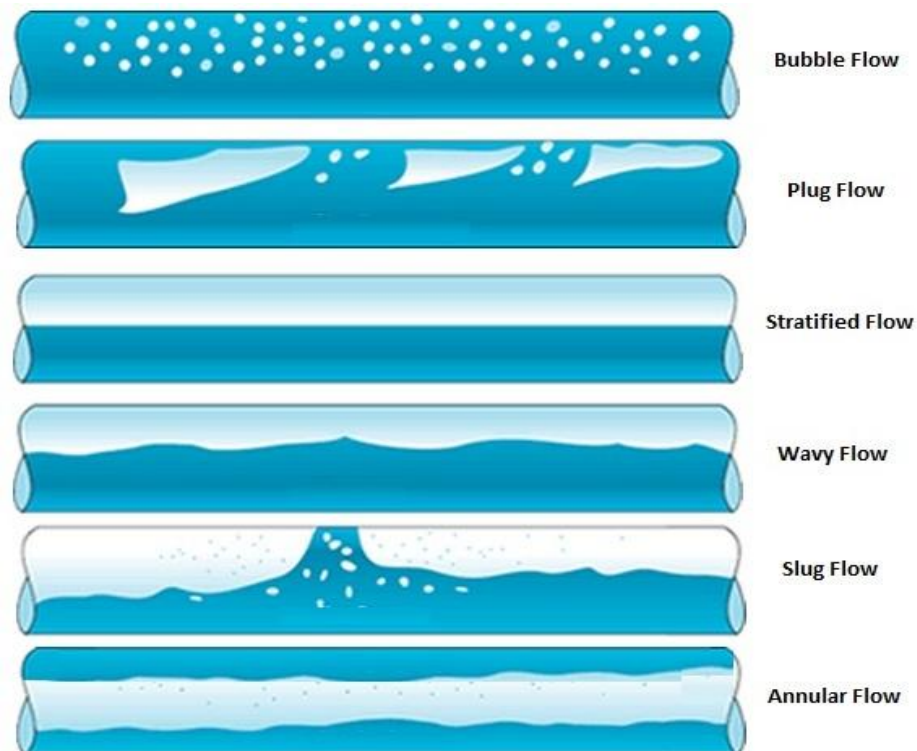
Figure 2.7: Horizontal Pipeline Flow Regimes

The flow regimes can be described as follows;

1. Bubble Flow: Small gas bubbles are distributed continuously throughout the liquid volume concentrated in the upper region of the pipe due to their lower density in comparison to the liquid. This is a high liquid volume fraction regime.

2. Plug Flow: The pockets of gas present in the bubble flow regime grow in size and form larger voids in the liquid flow leaving a thicker liquid film along the bottom of the pipe. This occurs when the relative gas flowrate is increased.

3. Stratified Flow: A distinct boundary exists between the two phases with the gas occupying the upper region which usually occurs for low flowrates of both phases although the relative gas velocity is higher.

4. Wavy Flow: Waves begin to form on the surface of the stratified liquid film as the relative gas velocity increases.

5. Slug Flow: A further increase in gas velocity beyond that of wavy flow causing the gas to occupy a larger volume in the upper pipe region and greater disturbances in the liquid layer, this is a highly transient regime.

6. Annular Flow: The gas phase is dominant in this regime and forces the liquid to produce an annular film with a small volume of liquid suspended in the gas flow as droplets. A further increase in the gas flowrate will result in an isolated dispersed droplet flow.

Predictions of which flow regime will exist in the pipeline have been investigated. In 1954 Baker produced a flow regime map for flows in pipelines based on the mass velocities of the gas and liquid phases (Thome, 2004). This was combined with two additional parameters which account for fluid property corrections with respect to air and water at the conditions which Baker obtained the data. These parameters and their dependency on pressure and temperature allow different operating conditions to be accounted for. The gas phase parameter is defined as;

$$\lambda_B = \left(\frac{\rho_g}{\rho_{air}} \frac{\rho_d}{\rho_{water}} \right)^{\frac{1}{2}} \qquad (2.38)$$

and the liquid phase parameter is;

$$\psi_B = \left(\frac{\sigma_{water}}{\sigma}\right)\left[\left(\frac{\mu_d}{\mu_{water}}\right)\left(\frac{\rho_{water}}{\rho_d}\right)^2\right]^{\frac{1}{3}} \qquad (2.39)$$

where $\rho_{water} = 1000\frac{kg}{m^3}$, $\rho_{air} = 1.23\frac{kg}{m^3}$, $\mu_{water} = 0.001\frac{kg}{ms}$ and $\sigma_{water} = 0.072\frac{N}{m}$.

Further investigations have been carried out by Mandhane et al. who produced their own flow pattern map and suggested that no significant improvement was found by including the effects of the physical properties of the fluids using the previously suggested parameters (Mandhane, et al., 1974). In the work of Taitel and Dukler several empirical parameters were included to determine the flow regime including the Martinelli parameter, the gas Froude number and two additional parameters which they introduced (Taitel & Dukler, 1976). The inclusion of the gas Froude number has also been employed by petroleum companies for their own flow regime maps (B.V, 2002).

The diameter of the inlet pipe for a particular gas/liquid flowrate is the driving factor for the velocity of the flow therefore influencing the size and distribution of the droplets entering the separator, which in turn will dictate the efficiency of the unit and the pressure drop. The volume fraction of droplets contained within an annular flow regime can vary from zero to a value close to unity with the droplets being able to deposit on the wall whilst the disturbance waves on the liquid film can become sheared off into droplets thus becoming entrained in the annular flow. As a result it is important to firstly be able to quantify the volume fraction ratio of droplets to liquid film entering the separator and secondly to determine the size and distribution of the droplets. A detailed review of droplet size measurements is presented by Simmons and Hanratty who use a Malvern Spraytec particle sizer to determine the drop size distributions in a horizontal pipe (Simmons & Hanratty, 2001). The laser beam from the Malvern instrument was directed through glass windows giving access to the flow section. Minimal contamination of the windows by incoming droplets was achieved by placing the windows some distance away from the flow and minimising the size of the openings at the test section. The work also presents a film removal method where the flow passes through a porous section and the liquid film which is travelling with a lower velocity than the gas and droplets is forced through the pores due to the pressure in the pipe. Burkholz also presents a device to drain the liquid film from a horizontal pipe flow called a 'Schalkragen'. The mechanism consists of a circular baffle, flanged into the piping equipment with a liquid film outlet as an oblique trough underneath the piping which is connected through drainage slits (Burkholz, 1989).

2.4.2.1 Inlet Geometry

The geometrical configuration of the inlet to the cylindrical separator can be tangential, scroll, helicoidal, axial or in the case of the Henry helical separator; radial for ease of manufacture. A typical cyclone design employs a rectangular cross-sectional tangential inlet chute or a 180° scroll wrap around inlet (Cortes & Gil, 2007). The more complex scroll and helicodial designs are most often used in high capacity applications for high particulate loading since the additional costs can be justified to prevent excessive erosion of the vortex finder by the incoming inlet flow and also reduce the pressure drop by reducing the constriction effect (Shepherd & Lapple, 1939). An adjustable inlet vane is shown to have an increase in pressure drop with increased constriction (Shepherd & Lapple, 1939). A computational investigation has been carried out into the effects of varying the rectangular section inlet duct of a tangential inlet cylinder-on-cone cyclone (Elsayed & Lacor, 2011). It was found that the maximum tangential velocity in the cyclone decreases with increasing inlet dimensions however the pressure drop also decreases as a result. The effects of changing the inlet width is more significant than changing the inlet height particularly for the d_{50} value with the optimum ratio of width to height being 0.5-0.7.

2.4.2.2 Inlet Droplet Size Estimation

The droplet size feeding a gas-liquid separator is highly dependent on the upstream pipework conditions since this controls factors such as the shear rate; which is a function of the pipe diameter, gas velocity and the fluid physical properties, which govern the generation and deposition of droplets. The average drop size entering the separator under mist-annular flow conditions can be calculated using the Harwell correlation (Hoffmann & Stein, 2008). This correlation applies to steady state flow conditions and is considered to be accurate and robust since it was developed and validated with steam-water, air-water and other fluid data (Hoffmann & Stein, 2008)). The original Harwell method contains a term dependent on the volumetric concentration of droplets and one which is independent, determining the droplet concentration is difficult therefore this term will not considered in the calculation. The resulting mean drop size is conservative which is acceptable since larger droplets are most easily separated. The Harwell method produces the Sauter mean droplet diameter $\langle x_{Sa} \rangle$, which is defined as the mean of the diameter of a sphere that has the same volume to surface area ratio as the droplet of interest;

$$\langle x_{Sa} \rangle = 1.91 D_{in} \frac{Re^{0.1}}{We^{0.6}} \left(\frac{\rho_g}{\rho_l} \right)^{0.6} \qquad (2.40)$$

where Re is the gas phase Reynolds number defined in equation 2.2 and We is the droplet Weber number defined as;

$$We = \frac{\rho v_{in}^2 D_{in}}{\sigma} \qquad (2.41)$$

where D_{in} is the internal diameter of the inlet pipe, v_{in} is the mean gas velocity in the inlet pipe, ρ_g and ρ_l are the gas and liquid phase densities and σ is the interfacial surface tension of the liquid.

The more meaningful volume-average drop diameter can be determined from the Sauter diameter which is more useful for separation studies which is given as;

$$\langle x \rangle_{med} = 1.42 x_{Sa} \qquad (2.42)$$

Applying the Harwell correlation to the flow conditions which exist at the entrance to the helical oil separator at atmospheric pressure it is found that the Sauter mean droplet diameter and the volume-average droplet diameter are in the range 17-78 microns and 24-111 microns respectively for recommended operational flowrate range of the helical unit at atmospheric pressure.

2.4.3 Liquid Entrainment

Re-entrainment of the liquid film in both the inlet pipe and walls of the separator is a very complex phenomenon which occurs when the relative velocity between the gas and liquid phase exceeds the critical value dependent mainly on the physical properties of the latter phase. Very little work is available in the literature examining liquid film re-entrainment from gas-liquid separators and there are only empirical and semi-empirical correlations available to calculate it which are all based on the average height of the liquid film (Brigadeau, 2007). There are different mechanisms associated with the entrainment of a liquid film from the wall dependent on the two phase flow regime. A summary of the four basic mechanisms for liquid film entrainment into a gas flowing co-currently in the upper region of the pipe when the flow regime is a wavy liquid film as shown in Figure 2.8, (Ishii & Grolmes, 1975).
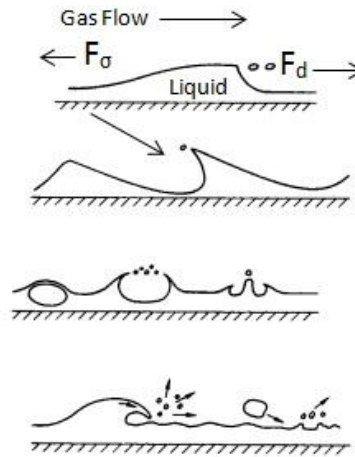
Figure 2.8: Entrainment Mechanisms for Concurrent Gas Liquid Flow

The first mechanism in Figure 2.8 shows entrainment by droplets being sheared from a roll wave which is associated with high Reynolds number flows. The second mechanism shows entrainment due to the gas flow undercutting a wave crest which is likely to occur for low Reynolds number flows. The third and fourth mechanisms shows the effect of liquid entrainment due to bubble burst on the surface or splashing due to droplet impingement onto the surface, these two mechanisms are less applicable to gas-liquid separation than the former two.

The film Reynolds provides a method of differentiating between the different regimes;

$$Re_l = \frac{\rho_l u_l \delta_l}{\mu_l} \tag{2.43}$$

where δ_l is the thickness of the film and the other parameters are the same as equation 2.2 with the subscripts referring to the properties of the liquid film. The inception of entrainment is argued to be dependent on the liquid film Reynolds number up to a certain point and also has a lower limit (Ishii & Grolmes, 1975). Below the lower limit entrainment is unlikely to occur except when the gas velocity is very high; in this case a liquid-film Weber number correlation can be applied to correlate entrainment (Austrheim, 2006). In the case of intermediate to high liquid film Reynolds number entrainment occurs due to shearing of the flow as a result of roll-wave formation. The onset of roll-wave entrainment is described through the force balance between the drag force due to the high shear flow of the gas on the liquid wave crest and the surface tension force acting to hold the film together, therefore when the drag force was greater than or equal to the force due to surface tension then roll wave entrainment will occur.

The onset of roll wave entrainment can be described through the following relationships;

$$\frac{\mu_l \mu_g}{\sigma} \sqrt{\frac{\rho_g}{\rho_l}} \geq 11.78 N_\mu^{0.8} Re_l^{-\frac{1}{3}} \ for \ N_\mu \leq \frac{1}{15} \tag{2.44}$$

$$\frac{\mu_l \mu_g}{\sigma} \sqrt{\frac{\rho_g}{\rho_l}} \geq 1.35 Re_l^{-\frac{1}{3}} \ for \ N_\mu \geq \frac{1}{15} \tag{2.45}$$

where N_μ is a viscosity number used to describe the droplet disintegration in the gas flow through the ratio of viscous forces due to the internal flow to the surface tension forces;

$$N_\mu = \frac{\mu_l}{\sqrt{\rho_l \sigma \sqrt{\frac{\sigma}{g \Delta \rho}}}} \tag{2.46}$$

Using these correlations the efficiency of a gas-liquid cyclone separator, which is limited by re-entrainment, becomes a function of the drag and surface tension forces such that the efficiency can be determined (Austrheim, 2006);

$$\eta_{entr}(a) = f \left(\frac{\frac{\mu_l \mu_g}{\sigma} \sqrt{\frac{\rho_g}{\rho_l}}}{N_\mu^a Re_l^{-\frac{1}{3}}} \right) \tag{2.47}$$

the right hand side of equation 2.47 is defined as the re-entrainment number with the exponent a optimized by Ishii and Grolmes, and Austrheim, with the latter finding 0.4 to be the optimal value. In a geometry where the wall liquid film is swirling round the wall rather than draining down the wall due to the gravitational pull the g term in equation 2.46 needs to be substituted with the centripetal acceleration of the film, $u_{\theta,l}^2/R$. The tangential component of the liquid film velocity is determined by taking the cosine of the absolute liquid film velocity. This can be expressed as (Austrheim, 2006);

$$u_{l,\theta} = \sqrt{\frac{f_{g,i} \rho_g u_{g,\theta}}{f_{l,w} \rho_l}} \tag{2.48}$$

where $f_{g,i}$ and $f_{l,w}$ represent the friction factors between the gas and liquid film surface and the liquid film and wall respectively and are defined as;

$$f_{g,i} = 0.005 \left(1 + 300 \frac{\delta}{R} \right) \tag{2.49}$$

$$\sqrt{f_{l,w}} = KRe_l^m \qquad (2.50)$$

where K=3.73 and m=-0.47 for 2<Re_l<100 or K=1.96 and m=-1/3 for 100<Re_l<1000. The liquid film thickness can be calculated as;

$$\delta = \frac{\dot{Q}cos^2\alpha}{\pi D u_{l,\theta}} \qquad (2.51)$$

As was previously mentioned at the low Reynolds number entrainment limit a liquid film Weber number can be used to determine the onset of entrainment along with an additional correlation parameter, S;

$$We = \frac{\rho_g u_g^2 \delta}{\sigma} \qquad (2.52)$$

$$S = \frac{u_g u_l}{\sigma} \qquad (2.53)$$

which for gas velocities greater than 25 m/s the critical value of the Weber number where the onset of entrainment happened became independent of S for S>5, whilst for lower values it became dependent on S.

Although the concept of liquid entrainment will not take place under the conditions which are to be explored in this investigation for the helical oil separator they will occur at higher operating pressures similar to those which the separator will experience in practice therefore are worthy of discussion.

2.5 Computational Modelling

The approach for carrying out a computational investigation of the helical oil separator is based on the assumption that the flow field which will exist within the main separation volume will exhibit characteristics which are similar to that of a typical cyclone separator. This can be assumed due to the path which the flow must take between the inlet and outlet of the geometry resulting in a swirling motion of the flow and hence generating a centrifugal force. From this connection it is necessary to assess the literature available which explores the requirements for the accurate numerical modelling of a cyclone separator.

The first step in the modelling study of a cyclone separator is to obtain the solution to the continuous phase flow field within the geometry. This is most commonly carried out using a

well-established CFD code such as Fluent, CFX and Star-CD to name but a few. These solvers have been extensively used and validated for the purpose of analysis and design for a wide range of fluid flow case studies. The fundamental concept in all of the available packages is through the solution of the Navier-Stokes equations which govern fluid flow. Due to the complexity associated with the turbulent nature of most industrial flow cases a time-averaged form of the basic Navier-Stokes equations are solved since the computational time and effort associated with Direct Numerical Simulation (DNS) would be colossal. The time averaging process which assumes that the instantaneous velocity appearing in the original equations can be represented by a mean component and a fluctuating component (i.e. u=U+u') results in additional unknown Reynolds Stress terms being formed which must be modelled. It is the aim of the turbulence closure models to represent the Reynolds Stresses in a form which captures the true underlying physics of the turbulent flow.

2.5.1 Turbulence Modelling

CFD solves the governing Navier Stokes equations for fluid flow using numerical approaches such as the finite volume method. In a complex flow situation like that in a centrifugal separator where the flow is strongly swirling, three dimensional and with high streamline curvature the direct solution of the governing equations would require an extremely fine computational grid consisting of multiple millions of nodes. For the direct simulation of the highly turbulent flow within a centrifugal separator this is not yet possible due to the vast amount of computational time and memory required. In order to overcome this difficulty mathematical models have been developed which can mimic the fluctuating velocity field within a turbulent flow called turbulence models. This leads to the Reynolds-averaged Navier-Stokes (RANS) equations. This idea was first presented by Boussinesq in 1877 who suggested the concept that the Reynolds stresses might be proportional to the mean rate of deformation which led to the introduction of the eddy viscosity concept (Versteeg & Malalasekera, 2007).

The accuracy of the turbulent model is dependent on how well the differential equations describe the transport of the fluid properties. The greater the number of differential equations that are solved by the turbulence model the more accurate the solution, however this increase in accuracy comes at a cost in terms of computational time and memory. A trade-off has therefore been established in terms of accuracy and resources. Researchers have devoted a great deal of time examining the available turbulence models

from the basic mixing length model of Prandtl; the most commonly used two-equation k-ε model through to the more complex multi-equation Reynolds Stress Transport Model (RSM) and the Large Eddy Simulation (LES) models. The aim of this section is to review the most commonly used models in complex swirling flow situations such as that present in a centrifugal based separator.

2.5.1.1 Standard k-ε Model

The two equation k-ε turbulence model based on the gradient diffusion hypothesis to relate the Reynolds stresses to the mean velocity gradients and the turbulent viscosity is the most popular model in engineering flow problems due to how well it has been validated. Launder and Spalding provide a detailed review of tests they carried out on the model (Launder & Spalding, 1974). The turbulent viscosity is obtained from the product of the turbulent velocity and length scale. The solution of the transport equation for the turbulent kinetic energy, equation 2.54, gives rise to the turbulent velocity while the turbulent length is estimated from the turbulent kinetic energy and the solution of the transport equation for its rate of dissipation, equation 2.55.

$$\frac{\partial}{\partial t}(\rho k) + \frac{\partial}{\partial x_j}(\rho U_j k) = \frac{\partial}{\partial x_j}\left(\frac{\mu_t}{\sigma_k}\frac{\partial k}{\partial x_j}\right) + P_k - \rho\varepsilon \tag{2.54}$$

$$\frac{\partial}{\partial t}(\rho\varepsilon) + \frac{\partial}{\partial x_j}(\rho U_j\varepsilon) = \frac{\partial}{\partial x_j}\left(\frac{\mu_t}{\sigma_\varepsilon}\frac{\partial\varepsilon}{\partial x_j}\right) + \frac{\varepsilon}{k}(c_{\varepsilon 1}P_k - c_{\varepsilon 2}\rho\varepsilon) \tag{2.55}$$

The assumption for the k-ε model is that the turbulent viscosity is related to the turbulent kinetic energy and its rate of dissipation through;

$$\mu_t = \rho c_\mu \frac{k^2}{\varepsilon} \tag{2.56}$$

The empirical constants C_μ, C_1, C_2, σ_k, σ_ε are prescribed the numerical values 0.09, 1.44, 1.92, 1.0, 1.3 respectively (Launder & Spalding, 1972). The production term denoted P_K in the turbulent kinetic energy and dissipation equation is defined as;

$$P_k = -\rho\overline{u_i u_j}\frac{\partial u_j}{\partial x_i} \tag{2.57}$$

The first application of the standard k-ε to a centrifugal separation situation was the simulation of a cyclone using Computational Fluid Dynamics (CFD) (Boysan, et al., 1982). Since this pioneering work many researchers have carried out studies of cyclone separators

using this model however the results produced have been found to be inadequate for flows containing swirl with high streamlined curvature with the results describing excessive levels of turbulent viscosity and unrealistic tangential velocity distributions (Griffiths & Boysan, 1996). The reason for these inaccuracies lies with the k-ε models inability to account for the extra strains caused by the high streamlined curvature, intense swirl and excessive recirculation present in centrifugal separators (Hanjalic, 1999). The results from the numerical model were validated with experimental data obtained by Hsieh and Rajamani using Laser Doppler Anemometry (LDA) and it was discovered that the turbulence in centrifugal separators is too anisotropic to treat with a standard k-ε model and a higher order model such as the RSM is required to give reasonable velocity predictions (Narasimha, et al., 2007). Three simple assumptions, which are the key to the failure of the standard k-ε model to predict the flow field in centrifugal separators, are highlighted as follows; the convection and diffusion of turbulent kinetic energy are almost negligible; the eddy viscosity is isotropic; and the turbulent length scale is proportional to the normal distance from the wall (Abdujelala & Lilley, 1984).

2.5.1.2 Modified k-ε Model

To account for the anisotropic nature of the turbulent flow within centrifugal separators work has been carried out by a number of researchers to modify the standard k-ε model to allow it to capture the characteristics associated with a strongly swirling flow field. The results obtained from the standard k-ε model have been compared with that of an anisotropic model consisting of the k-ε model and the Prandtl mixing length model combined (Meier & Mori, 1999). With the addition of the Prandtl model the turbulent anisotropy is introduced along with other components of the Reynolds stresses;

$$\left(\mu^{(t)}\right)_{\theta,\theta} = \left(\mu^{(t)}\right)_{z,\theta} = \left(\mu^{(t)}\right)_{r,\theta} = \left(\mu^{(t)}\right)_{in} + \bar{\rho}r^2l^2\left\{\left[\left(\frac{\partial(\overline{v_r})}{\partial r}\right)^2 + \left(\frac{(\overline{v_r})}{r}\right)^2 + \left(\frac{\partial(\overline{v_z})}{\partial z}\right)^2\right] + \right.$$

$$\left. \frac{1}{2}\left\{\left[r\frac{\partial}{\partial r}\left(\frac{(\overline{v_\theta})}{r}\right)\right]^2 + \left(\frac{\partial(\overline{v_r})}{\partial z} + \frac{\partial(\overline{v_z})}{\partial r}\right)^2 + \left(\frac{\partial(\overline{v_\theta})}{\partial z}\right)^2\right\}\right\}^{1/2} \tag{2.58}$$

where $\left(\mu^{(t)}\right)_{in}$ is the turbulence associated with the inlet to the cyclone body and is defined by;

$$\left(\mu^{(t)}\right)_{in} = \bar{\rho}(\bar{k})_{in}^{1/2}\frac{D_h}{10} \tag{2.59}$$

and l is the Prandtl mixing length which is given a value of 0.034 (Meier & Mori, 1999).

The results of this study concluded that the standard isotropic model failed to predict the swirling flow whereas the modified model successfully predicted the flow and the phenomena associated with geometries exhibiting high streamline curvature.

The RNG variant of the k-ε model, based on ReNormalization Group Theory, was explored by Griffiths and Boysan which included the effect of rotation in the calculation of the turbulent viscosity (Yakhot & Orszag, 1986). The analytical derivation results in a model with additional terms in the transport equations from that of the standard k-ε variant and different numerical constants, the enhanced turbulent kinetic energy and dissipation rates with the Renormalization group theory applied are shown in equation 2.60 and equation 2.61;

$$\rho \frac{Dk}{Dt} = \frac{\partial}{\partial x_i}\left(\alpha_k \mu_{eff} \frac{\partial k}{\partial x_i}\right) + P_k - \rho\varepsilon \qquad (2.60)$$

$$\rho \frac{D\varepsilon}{Dt} = \frac{\partial}{\partial x_i}\left(\alpha_\varepsilon \mu_{eff} \frac{\partial \varepsilon}{\partial x_i}\right) + C_{1\varepsilon}\frac{\varepsilon}{k}P_k - C_{2\varepsilon}\rho\frac{\varepsilon^2}{k} - R \qquad (2.61)$$

where α_k and α_ε are the inverse effective Prandtl numbers for k and ε and have been prescribed a value of 1.393 for high Reynolds number flows. The modified model constants are 1.42, 1.68 and 0.0845 for $C_{1\varepsilon}$, $C_{2\varepsilon}$ and C_μ respectively. The inclusion of an analytical expression for the turbulent Prandtl number in addition to having an extra R_ε term, equation 2.62, in the dissipation rate equation allows the RNG model to show substantial improvements over the standard k-ε model where the geometry contains strong streamline curvature, turbulent vortices and highly rotational flow.

$$R_\varepsilon = \frac{C_\mu \rho (Sk/\varepsilon)^3 (1-\frac{Sk/\varepsilon}{4.38})}{1+0.012(\frac{Sk}{\varepsilon})^3}\frac{\varepsilon^2}{k} \qquad (2.62)$$

The effects of swirl in the mean flow on the turbulent viscosity is also accounted for in the RNG model and is defined in terms of the turbulent viscosity before the swirl modification and is a function of the swirl constant, the swirl number and the ratio of turbulent kinetic energy to its rate of dissipation.

The performance of the RNG model to predict the axial and tangential velocity in a gas cyclone has been evaluated (Hoekstra, et al., 1999). However despite the extra terms and modified constants in this model in comparison with the standard k-ε model it was still

found that both models were unable to predict realistic velocity distributions, when compared with LDA data, and they concluded it to be unsuitable for cyclone flow. The RNG k-ε model has been employed to simulate the effect of turbulence and pressure drop and found it to yield a reasonably good prediction with only a 14-18% deviation from the measured value for the pressure drop and is preferred in comparison to the more complex RSM model in terms of CPU time limitations (Gimbun, et al., 2005).

A modification to the length scale in a swirling flow field by introducing the swirl Richardson number, Ri, was proposed by Bradshaw in 1971 (Abdullah, 1996). The Richardson number is dependent on the turbulent kinetic energy, the rate of dissipation, swirl velocity and streamline curvature;

$$Ri = \frac{k^2}{\varepsilon^2} \frac{u}{r^2} \frac{\partial(ru)}{\partial z} \qquad (2.63)$$

The last term in equation 2.63 represents the swirl gradient which allows for the mixing length to increase or decrease as the gradient becomes positive or negative hence allowing for the anisotropy of turbulence which is not included in the standard k-ε model. The addition of the Richardson number to the rate of dissipation equation is shown in equation 2.64. An additional term is also present in this equation, c, which was found to have an optimum value of 0.2.

$$\frac{\partial}{\partial t}(\rho\varepsilon) + \frac{\partial}{\partial x_j}(\rho U_j \varepsilon) = \frac{\partial}{\partial x_j}\left(\frac{\mu_t}{\sigma_\varepsilon} \frac{\partial \varepsilon}{\partial x_j}\right) + \frac{\varepsilon}{k}[c_{\varepsilon 1}P_k - c_{\varepsilon 2}(1 - cRi)\rho\varepsilon] \qquad (2.64)$$

This modified form of the k-ε model has been applied to a cyclone separator in order to assess how well the Richardson number could predict the velocity distributions and concluded that the results obtained were in better agreement with the experimental results from LDA measurements, but still require further improvements in order to make them acceptable for design purposes (Fraser, et al., 1997).

2.5.1.3 Reynolds Stress Model

The Reynolds Stress Model (RSM) is the most complex of the classic turbulence models since the eddy-viscosity hypothesis used in the k-ε model is discarded and the RSM closes the RANS equations by solving the individual transport equations for the Reynolds stresses along with an equation for the dissipation rate. This requires the solution of the six independent Reynolds stresses shown in equation 2.65, therefore in a 3 Dimensional flow

simulation a solution obtained from the RSM requires an additional seven transport equations to be solved.

$$\frac{\partial}{\partial t}\left(\rho \overline{u_\iota u_J}\right) + \frac{\partial}{\partial x_k}\left(\rho u_k \overline{u_\iota u_J}\right) = P_{ij} + F_{ij} + D_{Tij} + \phi_{ij} - \varepsilon_{ij} \qquad (2.65)$$

where P_{ij} is the stress production term, F_{ij} is the rotation production term, D_{Tij} is the turbulent diffusion term, ϕ_{ij} is the pressure strain term and ε_{ij} is the dissipation term respectively given as;

$$P_{ij} = -\rho \left(\overline{u_\iota u_k}\frac{\partial u_j}{\partial x_k} + \overline{u_J u_k}\frac{\partial u_i}{\partial x_k}\right) \qquad (2.66)$$

$$F_{ij} = -2\rho \Omega_k (\overline{u_J u_m}\varepsilon_{ikm} + \overline{u_\iota u_m}\varepsilon_{jkm}) \qquad (2.67)$$

$$D_{Tij} = -\frac{\partial}{\partial x_k}\left[\rho \overline{u_\iota u_J u_k} + \overline{p(\delta_{kJ}u_\iota + \delta_{\iota k}u_J)}\right] \qquad (2.68)$$

$$\phi_{ij} = \overline{\left(\frac{\partial u_\iota}{\partial x_J}\frac{\partial u_J}{\partial x_\iota}\right)} \qquad (2.69)$$

$$\varepsilon_{ij} = -2\mu \overline{\frac{\partial u_\iota}{\partial x_k}\frac{\partial u_J}{\partial x_k}} \qquad (2.70)$$

Although the RSM can depict the effects of streamline curvature, swirl, rotation, and rapid changes in strain to a higher degree than the previous models which have been examined the accuracy of the results is still limited by the closure assumptions adopted to model the terms in the Reynolds stress transport equations. The modelling of the pressure-strain and dissipation rate, equation 2.69 and equation 2.70, create particular challenges and are often the reason for the short-fall in the accuracy of the RSM predictions (ANSYS, 2009).

Hoekstra et al. are amongst the many researchers who have carried out studies to evaluate the performance of the RSM in comparison with the two equation k-ε and its variants in predicting the gas flow field in a centrifugal separator (Hoekstra, et al., 1999). These authors compared the predicted axial and tangential velocities of the k-ε model, the RNG-k-ε model and the Reynolds stress transport model, with that of LDA measurements and found that the k-ε and the RNG variant predicted unrealistic velocity distributions. The RSM gave results which were in reasonable agreement with the LDA data, although some

discrepancies were found which require further improvement of this model. A similar investigation concluded that the results from the CFD simulations produced the general trend of that from the experimental data, with the k-ε model predicting a higher rotational flow while the RSM predicted a large decay in the intensity of the tangential and axial velocities (Erdal & Shirazi, 2004). These authors also found that both turbulence models failed to predict the finer details in the up-flow region of the separator and the local axial velocity profiles.

The exact form of the RSM in literature involving swirling flow is not constant and researchers have presented different manipulations of what they believe to be the best model to mimic the flow patterns captured by experimental measurements (Murphy, et al., 2007). These authors also examined the effects of omitting the wall reflection terms from the simulation and found that the results obtained were generally in agreement with the data from experiments.

Slack et al. modelled a conventional high efficiency Stairmand cyclone, applied an unstructured mesh and solved the simulation with the RSM and the more complex Large Eddy Simulation (LES) turbulence models (Slack, et al., 2000). From this investigation they concluded that the steady state simulation using the RSM on a fairly course unstructured mesh provides a computationally inexpensive method for determining the time-averaged flow in a centrifugal separator, with the results being in excellent agreement with that of the experimental measurements. The LES model in this study did however reveal the presence of time dependent vortex oscillations which potentially create an impact on the separation efficiency, but at a much greater computational cost. The performance of the RSM and LES turbulence models in a cyclone separator has also been evaluated and concluded that the RSM results were not as representative as the LES data (Shalaby, et al., 2005). They observed that the tangential velocity profiles of the RSM demonstrating solid body rotation reaching too far towards the external walls of the cyclone. The LES model produced very encouraging results with the conclusion that this model is a better alternative to the more conventional turbulence model.

2.5.1.4 Large Eddy Simulation

Large Eddy Simulation (LES) is the intermediate stage for the simulation of turbulence ahead of RANS but just short of DNS in terms of the fraction of the resolved scales. The difficulty in the simulation of turbulence is attributable to the difference in length scale

between the smallest and largest of the turbulent eddies and the behaviour associated with each. The largest eddies are comparable in size to the characteristic length of the mean flow and are anisotropic with their behaviour being dictated by the flow geometry, boundary conditions and body forces. The smaller eddies on the other hand are almost isotropic and have generic behaviour, particularly at high Reynolds numbers. The LES model computes the effects of turbulence by directly simulating the large eddies and using a more compact model to capture the less erratic small eddies. LES makes use of a spatial filtering mechanism, in place of the more traditional time-averaging approach, in order to separate out the larger eddies from the smaller ones. In one dimension the filter velocity can be defined as;

$$\bar{u_\iota} = \int G(x,x)\, u_i(x) dx \tag{2.71}$$

where G(x, x') is the filter function. The function is large where G(x, x') is less than the filter width Δ, a length scale, over which the averaging is performed. Eddies that are larger than Δ are defined as "large eddies" and those that are smaller are "small eddies". To classify the size of the eddies two convolution filters are employed for the spatial filtering. For a cut-off length $\bar{\Delta}$ these are the box or top-hat filter and the Gaussian filter respectively with the former being most commonly used in the finite volume method for LES (Versteeg & Malalasekera, 2007);

$$G(x_i) = \begin{cases} \frac{1}{\Delta_i} & |x_i| \leq \frac{\Delta_i}{2} \\ 0 & |x_i| > \frac{\Delta_i}{2} \end{cases} \tag{2.72}$$

$$G(x) = \left(\frac{\gamma}{\pi\Delta^2}\right)^{\frac{1}{2}} exp\left(\frac{-\gamma|x|^2}{\Delta^2}\right) \tag{2.73}$$

where G is the convolution kernel and γ is a numerical constant taken to be 6. Applying the top-hat filter function, equation 2.72, the filtered form of the governing Navier-Stokes equations can be derived. The filtered form of the equations govern the evolution of the large scale eddies while the effect of the small scale eddies appear in the Sub Grid Scale (SGS) stresses are modelled by;

$$\tau_{ij} = \overline{u_\iota u_J} - \bar{u_\iota}\bar{u_J} \tag{2.74}$$

The models used are based on the eddy-viscosity hypothesis and assume proportionality between the anisotropic part of the SGS stress tensor whose purpose is to remove the energy from the resolved scales into the sub grid scales (Smagorinsky, 1963). The equation relating the turbulent shear stresses to the strain rates is;

$$\tau_{ij}^{sgs} = -\mu_t \left(\frac{\partial \overline{u_i}}{\partial x_j} + \frac{\partial \overline{u_j}}{\partial x_i} \right) \qquad (2.75)$$

In recent years the application of LES to resolve the flow in centrifugal separators has been made possible due to advances in computational software and memory. A study has been carried out on hydrocyclones using the RNG k-ε model, the Reynolds Stress model and the Large Eddy Simulation model to determine the air-core dimension which is the key to predicting the mass split between the underflow and overflow (Delgadillo & Rajamani, 2005). These authors produced velocity profiles at various axial locations for the three turbulence models, compared them with experimental data and concluded that the LES captures the dynamics of the flow which allow the accurate prediction of the velocity profiles therefore the extra computational power and effort required to solve this model is justified. The only downfall of the LES model is the prediction of the near wall regions where it fails to accurately predict the flow pattern; this is overcome by using the renormalization of the subgrid scales which include the effects of molecular viscosity.

Shalaby carried out a detailed study on the use of LES to simulate cyclone separators by firstly validating the model in a straight square channel then proceeding to compare it to the standard k-ε model and the Reynolds Stress model (Shalaby, 2007). The conclusions from the study stated that the k-ε model produced weak results for cyclone flow while the RSM investigation results were not as good as the LES data at agreeing with experimental data.

2.5.2 Multiphase Modelling

The second key factor when carrying out a Computational Fluid Dynamics (CFD) analysis on a centrifugal based separator, which has a continuous phase and a dispersed phase, is to choose the multiphase flow model which calculates the droplets trajectories within the computational domain. The information from these calculations will determine whether a droplet will become separated within the geometry or carried over and exit with the continuous gas flow. As the flow field within the separator is turbulent in nature the particle trajectories will be affected by the random fluctuations and eddies hence the

model calculations must account for these effects if realistic results are to be obtained. There are two main approaches which can be used in order to simulate the dispersed flow; the Eulerian method and the Lagrangian method. The Eulerian method treats the dispersed phase as a continuum and solves the transport equations for the phase concentrations and since each of the flow variables are a function of space and time they are represented as fields. This approach is suitable when the particle loading is fairly high and when it is not necessary to extract particle impact information at the boundaries. An attempt to develop an Eulerian formulation that could better account for the behaviour near an obstructing surface wall was carried out with the aim to define a particle-wall rebounding layer in which the collision process had a significant effect on incoming particles (Tu, et al., 1996).

2.5.2.1 Lagrangian Modelling

The Lagrangian method tracks individual particles over small time steps as they pass through the computational domain where the mass and momentum equations for each particle are based on the average properties of that particle. The conservation equations for the particles are ordinary differential equations which govern the change of mass and momentum since each individual particle has its own position in space and is individually tracked. Each of the governing equations contains terms which account for the interaction of the particle with the continuous phase. In one-way coupling simulations it is assumed that the particles have no effect on the fluid flow: the flow field is obtained before the trajectories are calculated. Two-way coupling simulations are required when the particles do affect the flow solution: the overall computation then becomes an iterative process. For the majority of cases of solid particle or liquid droplet separation the loading is small therefore it can be safely assumed that the presence of particles does not affect the flow field allowing the one-way coupling approach to be adopted (Elsayed & Lacor, 2013). The two main factors to consider when using the Lagrangian particle tracking approach are the forces to include in the particle equations of motion and the method which accounts for the velocity fluctuations.

The prediction of a particle's trajectory is obtained by integrating the force balance in the Lagrangian reference frame. This force balance equates the inertia of the particle with the other forces acting on the particle through the flow field. Therefore for a spherical particle the equations of motion in the x-direction are;

$$\frac{dx_d}{dt} = u_d \qquad (2.76)$$

$$\frac{du_d}{dt} = F_D(u - u_d) + \frac{g_x(\rho_d - \rho_g)}{\rho_d} + F_x \qquad (2.77)$$

where F_x is an additional acceleration term and $F_D(u-u_d)$ is the drag force per unit droplet mass where;

$$F_D = \frac{18\mu}{\rho_d d_d^2} \frac{C_D Re}{24} \qquad (2.78)$$

with u representing the fluid phase velocity, u_d is the particle velocity, μ is the molecular viscosity of the gas, ρ_g is the gas density, ρ_d is the density of the droplet and d_d is the droplet diameter. Re is the relative Reynolds number of the particle and C_D is the drag coefficient.

The last term in equation 2.77 denotes any additional forces which may arise due to special circumstances such as: the virtual mass associated with fluids which are more dense than the particulate phase; the force due to a rotating reference frame; the thermophoretic force which is the result of a temperature gradient in the fluid; Brownian force which affects sub-micron droplets; Saffman's lift force which is generated as a result of shearing in the fluid. Further details of each additional force term can be found in the Fluent User's Guide along with the relevant equations for each term (ANSYS, 2009). A study was carried out which concluded that many of the additional forces produce negligible effects and in the case of droplet separator modelling the only term deemed worthy of inclusion is the Saffman lift force (Meng & van der Geld, 1991).

The prediction of dispersed phase motion in turbulent flow fields is complex due to the effects of the turbulence on particles being significant; except for droplets which are greater than the length of the turbulent scale which are unresponsive to velocity fluctuations (Crowe, et al., 1998). The droplets equation of motion require both the instantaneous droplet and fluid velocities at that instant in time but generally the fluid phase equations are time averaged therefore the instantaneous velocity component information is unavailable. However the fluid velocity can be viewed as;

$$u = \bar{u} + u \qquad (2.79)$$

where the mean component is obtained from the solution of the time averaged fluid phase equations. The fluctuating part is obtained through a stochastic tracking procedure which predicts the turbulent dispersion of the particles through an integration of the trajectory equations for individual particles using equation 2.77 along the path of the particle. The various potential paths due to the droplet encountering different eddies are averaged out by releasing enough droplets into the domain to account for the random droplet dispersion. The lifetime of the eddy is taken to be equal to the Lagrangian integral time scale, T_L, which is usually deduced from the Eulerian properties by;

$$T_L = \frac{\ell}{\sqrt{k}}$$

(2.80)

where ℓ denotes the Eulerian length scale and k is the turbulent local energy, where the former is defined as;

$$\ell = \int_0^\infty R_E dr$$

(2.81)

where R_E is the Eulerian correlation function of the fluctuating velocities. Measurements of this function are much easier to carry out than for the Lagrangian function so data for Eulerian flow properties are readily available. A range of schemes have been proposed in the literature to simulate particle dispersion due to turbulence (Crowe, et al., 1998). In the discrete random walk (DRW) model available in Fluent the fluctuating velocity components are discrete piecewise constant functions of time. The interaction of a particle with a series of discrete fluid phase turbulent eddies is simulated through the DRW where each eddy is characterised by a Gaussian distributed random velocity fluctuation u', v', w' and a time scale τ_e.

The concept of the random fluctuating velocity components being isotropic and obeying a Gaussian probability distribution has been proposed (Gosman & Ioannides, 1981), such that;

$$u = \varsigma\sqrt{\overline{u^2}}$$

(2.82)

where ς is a normally distributed random number and

$$\sqrt{\overline{u^2}} = \sqrt{\overline{v^2}} = \sqrt{\overline{w^2}} = \sqrt{\frac{2k}{3}}$$

(2.83)

The characteristic lifetime of the eddy is defined as a constant;

$$\tau_e = 2T_L \qquad (2.84)$$

or as a random variation about T_L;

$$\tau_e = -T_L \ln(r) \qquad (2.85)$$

where r is a uniform random number between 0 and 1. Equation 2.85 yields a more realistic description of the correlation function in comparison to equation 2.84. The transit time for a droplet to cross an eddy is defined as;

$$t_{cross} = \tau ln\left[1 - \frac{L_e}{\tau|u-u_d|}\right] \qquad (2.86)$$

where τ is the droplet relaxation time, $|u-u_d|$ is the magnitude of the relative velocity and L_e is the eddy length scale;

$$L_e = \frac{C_L^{\frac{3}{4}} k^{\frac{3}{2}}}{\varepsilon} \qquad (2.87)$$

with C_L taking on a value of 0.15 for the k-ε and its variants and 0.3 for the RSM.

Improvements have been proposed by a number of studies to the original proposal of Gosman and Ioannides which include; a technique to avoid the step change in velocity when a particle passes from one eddy to the next; a simpler technique for selecting the fluctuation velocity of the eddy; a group modelling scheme where the volume occupied by the particle grows with time due to diffusion (Crowe et al., 1998).

Other stochastic flow models exist where the trajectory of the fluid particle and the discrete phase particle are generated simultaneously and Probability Density Function propagation models where the turbulent dispersion of the particles about a mean trajectory is calculated using statistical methods; this is known as particle cloud tracking. Although other models exist the eddy interaction model described above is the most popular and has been widely used in the literature for the modelling of particle separation.

2.5.2.2 Dispersed Phase Fate

Once the dispersed phase has been released into the computational domain prior to reaching a boundary, liquid droplets can coalesce or breakup. Since the volume fraction of

the droplet phase is low in this investigation, $\alpha_d = \frac{m_d}{\rho_d}$, where α_d<0.0008, the probability of droplet coalescence or droplet bounce off one another is extremely low. This is due to the fact that for two particles to collide they must be located in the same continuous phase cell (O'Rourke & Amsden, 1987), which for such a low value of α_d is highly unlikely. The generation of secondary droplets within the domain can occur mainly due to three mechanisms; breakup caused by interaction with the continuous phase, breakup by droplets impinging on a liquid film present on a surface and breakup of the surface liquid film due to interfacial shear stresses. The possibility of breakup is determined through the Weber number of the droplets, equation 2.88, for the first two cases and the Weber number of the film, equation 2.89 for the latter case.

$$We_d = \rho_g\left(u_g - u_d\right)^2 \frac{D_d}{\sigma} \tag{2.88}$$

$$We_f = \rho_g\left(u_g - c_w\right)^2 \frac{\delta}{\sigma} \tag{2.89}$$

where D_d is the droplet diameter, σ is the interfacial surface tension of the droplet, δ is the film thickness and c_w is the wave velocity of the liquid film. For breakup to occur, the critical values for We_d and We_f are 13 and 1.5 respectively (Jia, et al., 2007).

There are various droplet breakup models available, two of which are: the widely used Taylor Analogy Breakup (TAB) model (O'Rourke & Amsden, 1987) and the wave model (Patterson & Reitz, 1987). The TAB model is recommended for injections where the Weber number is less than 100 and where the spray penetrates at a low velocity into a standard atmosphere. For applications out with these criterions the wave model is more applicable, in particular for high speed fuel injection application such as an internal combustion engine (Adbelghaffar, et al., 2011). The TAB will be explored in further detail since it is most suited to the low Weber number and low velocity flows within the helical oil separator.

The basis of the TAB model lies with the analogy between an oscillating and distorting droplet and a spring mass system. As a droplet becomes distorted and grows to a critical point where the parent droplet breaks up into a number of smaller child droplets the drag coefficient also changes which requires the incorporation of an additional model. The governing equation for droplet break-up is given as;

$$F - kx - d_d \frac{dx}{dt} = m_d \frac{d^2x}{dt^2} \tag{2.90}$$

where F is the external force on the droplet and x is the displacement of the droplet equator from its spherical (undisturbed) position. The coefficients of this equation are determined from Taylor's analogy;

$$\frac{F}{m_d} = C_F \frac{\rho_g u^2}{\rho_d r_d}$$
$$\frac{k}{m_d} = C_k \frac{\sigma}{\rho_d r_d^3} \tag{2.91}$$
$$\frac{d_d}{m_d} = C_d \frac{\mu_d}{\rho_d r_d^2}$$

where m_d is the mass of the droplet, ρ_g and ρ_d are the gas and droplet densities respectively, u is the relative velocity of the droplet, r_d is the undisturbed droplet radius, σ is the droplet surface tension and μ_d is the droplet viscosity. The numerical constants C_F, C_k and C_d are 1/3, 8 and 5 respectively. When the value of x is greater than the product of C_b and r, where C_b is 0.5, the droplet is assumed to breakup. The energy of the large droplets is equal to the energy of all sub-droplets after the breakup. The energy of the parent droplet is given as;

$$E_{parent} = 4\pi r_d^2 \sigma + K \frac{\pi}{5} \rho_d r_d^5 \left[\left(\frac{dy}{dt} \right)^2 + \omega^2 y^2 \right] \tag{2.92}$$

where K is of the order 10/3, $y = \frac{x}{C_b r_d}$ and ω is the droplet oscillation frequency defined as;

$$\omega^2 = C_k \frac{\sigma}{\rho_d r_d^3} - \frac{1}{t_d^2} \tag{2.93}$$

with t_d denoting the time associated with the droplet motion. The resulting energy of the child droplets is given as;

$$E_{child} = 4\pi r^2 \sigma \frac{r_d}{r_{d32}} + \frac{\pi}{6} \rho_d r_d^5 \left(\frac{dy}{dt} \right)^2 \tag{2.94}$$

where r_{d32} is the Sauter mean radius of the droplet size distribution and can be determined through equating equation 2.92 and equation 2.94 by setting y=1 and $\omega^2 = \frac{8\sigma}{\rho_d r_d^3}$:

$$r_{d32} = \frac{r_d}{1 + \frac{8Ky^2}{20} + \frac{\rho_d r_d^3 (dy/dt)^2}{\sigma} \left(\frac{6K-5}{120} \right)} \tag{2.95}$$

The number of child droplets produced can be easily obtained once the size has been determined through the conservation of mass. The normal velocity component of the parent droplet is imposed upon the child droplets through the TAB model with the velocity at the equator of the parent droplet defined as dx/dt=C$_b$r$_d$(dy/dt). The resulting normal velocity of the child droplets is given as;

$$u_{normal} = C_v C_b r_d \frac{dy}{dt}$$ (2.96)

where C$_v$ is of the order 1. Further information of the breakup associated with the TAB model can be found in the theory guide (ANSYS, 2009). An investigation has been carried out into the performance of cyclone separators in oil injected compressor systems and found that by applying the TAB model produced results which were within 10% error of the experimental data whereas without the use of this model the performance of the separator was over-predicted by up to 40% at the lower end of the inlet velocity range (Gao, et al., 2012).

When a droplet comes in contact with one of the surfaces in the domain it is important to have suitable boundary conditions to allow the droplet trajectory calculations to be either terminated or continued. The correct application of solid wall boundary conditions allows the performance of a separator to be accurately modelled. The available droplet-wall interaction boundary condition types available include; reflect, liquid-film, liquid-jet, trap and escape.

The wall reflect boundary condition can be described in terms of restitution coefficients for a particular dispersed phase material Figure 2.9. Restitution coefficients range from 0 to 1, where a value of 1 implies that a droplet retains all of its normal and tangential momentum after impact. Based on the particle velocity ratio a measure of the momentum exchange on impact is determined and therefore can lead to an improvement in separation efficiency or be a detriment depending on the outcome. Bhasker carried out an investigation into the performance of a cyclone separator used in a Circulating Fluidized Bed Combustion (CFBC) where the discrete phase model was applied with ash as the particulate phase (Bhasker, 2002). The coefficient of restitution on the solid walls was prescribed a value of 0.7 which was deemed to give a realistic prediction of three different particle sized groups of ash; 10 microns, 100 microns and 1000 microns. Elsayed and Lacor have studied the effect of vortex finder dimensions on the performance of nine cyclone separators using the DPM

model and applied a coefficient of restitution of 1.0 which assumes a perfect elastic collision (Elsayed & Lacor, 2013). In the work carried out by Gao et al. they make use of the reflect boundary condition but do not explicitly state the restitution coefficient (Gao, et al., 2012).
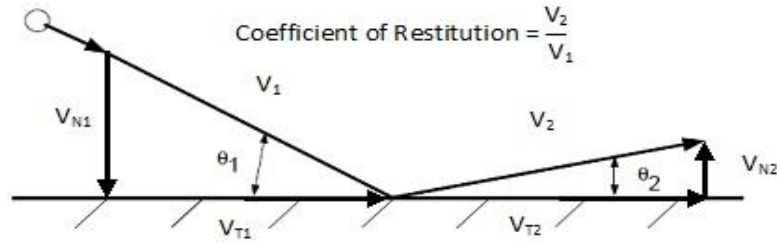
Figure 2.9: Reflect Wall Boundary Condition Notation

One liquid-film model in particular was specifically designed for simulating internal combustion engines but can be used to model any liquid droplet impinging on a boundary surface and forming a liquid-film. The model can be divided into four sub-sections: the initial interaction with the solid surface to create a liquid-film, subsequent droplet tracking on the surface, and calculation of the variables associated with the liquid film and how coupling affects the gas phase. When a droplet impacts on the surface there are four fates for the droplet; stick, rebound, spread and splash, (Bai, et al., 2002), with both stick and spread resulting in droplet deposition on the impact surface. When the impingement energy of the droplet is low the rebound criteria is applied and the droplet bounces off the film. The transition between deposition and rebound is given as;

$$stick \rightarrow rebound \rightarrow spread\ 1 \leq We_{im} = \frac{\rho_d d_d v_{2n}^2}{\sigma} \leq 5 \qquad (2.97)$$

The velocity of the droplet in the rebound regime is determined from equation 2.98 for small particles bouncing on a wetted surface, where the subscript 1 refers to the incoming droplet, 2 refers to the droplet after impact, n is the normal velocity component and t is the tangential component;

$$v_{1t} = \frac{5v_{2t}}{7}, v_{1n} = -ev_{2n} \qquad (2.98)$$

where e is a restitution coefficient which can be determined by equation 2.99 (Bai, et al., 2002);

$$e = 0.993 - 1.76\theta_1 + 1.56\theta_1^2 - 0.49\theta_1^3 \qquad (2.99)$$

where θ_1 defines the impact angle of the impinging droplet as shown in Figure 2.9. The criterion between droplet deposition and splash on a rough surface was investigated and found to obey the following relationship (Mundo, et al., 1995);

$$deposition \rightarrow splash\ K = OhRe^{1.25} \approx 57.7 \qquad (2.100)$$

where K is a dimensionless parameter for impingement expressed in terms of Reynolds and Ohnesorge numbers with the latter defined as the ratio of the square root of the Weber number to the Reynolds number. When a droplet impacts on a wetted surface and splashes the ratio of mass which is splashed to the incident mass is given by;

$$r_m = 0.2 + 0.9R(0,1) \qquad (2.101)$$

where R(0,1) is a random number distributed uniformly between 0 and 1. The resultant droplet size and number of droplets ejected from the liquid film are given as;

$$D_{d1} = \frac{C_w}{D_{d2}} \qquad (2.102)$$

$$N_{eject} = 0.187We_{im} - 4.45 \qquad (2.103)$$

where $C_w = \left(\frac{r_m}{N_{eject}}\right)^{\frac{1}{3}}$ satisfying the conservation of mass. This liquid film model has been applied to study the performance of wave plate separators, with and without hooks, for steam-water separation in a turbine (Jia, et al., 2007). Under the typical flow conditions for this application the breakup of droplets by impingement on the liquid film was the dominant mechanism of secondary droplet generation and good agreement was found with experimental data with the maximum errors being of the order of only 1-2%.

2.5.2.3 Eulerian Modelling and Comparison with Lagrangian

A multiphase model for cyclone separators using CFD based on the mixture model has been presented which is a simplified Eulerian approach to two phase flow modelling (Brennan, et al., 2007). The mixture model solves only the equations of motion for the mixture. The assumption attached to this model is that the primary phase is the continuous fluid phase and solves transport equations for the volume fractions of each of the dispersed phases in the mixture. It also assumes that the slip velocities can be modelled algebraically without having to solve the momentum equations for the dispersed phase and that the forces due

to the stress tensors are negligible in terms of their effect on the slip velocity in comparison to the hydrodynamic and gravitational forces. These authors enhance the standard mixture model by including the effects of granular viscosity, pressure and drag laws; these terms all require the granular temperature. The results from this CFD simulation gave a good prediction of the cyclone efficiency curve therefore showing good promise as a cyclone design tool.

A more advanced model for capturing two phase flow phenomenon is the Volume of Fluid (VOF). This method has been applied to determine the flow regimes for water-air and gas-oil liquid-vapour mixtures and compared them with experimental data taken from the Baker chart (De Schepper, et al., 2008). The VOF method employs a single set of conservation equations which are shared by both the continuous and dispersed phases, while the volume fraction for each of the phases is tracked in each cell throughout the computational domain. As a result the most common applications of the VOF model is in stratified and free-surface flows. This investigation is the first to be carried out in which gas-oil-liquid vapour flow regimes have been simulated and the results were shown to be in good agreement with the expected flow regime according to the Baker chart.

A similar study was carried out to model the gas-liquid-solid flow in a hydrocyclone (Wang, et al., 2003). The authors use a combination of the RSM, stochastic Lagrangian model and the VOF model to satisfactorily describe the flow field and performance of a standard hydrocyclone. The VOF model can be used to simulate two or more immiscible fluid phases where the position of the interface between the fluids is of interest. The motion of the particles as they travel through the continuum are described by the Lagrangian multiphase flow model wherein the stochastic tracking of the particles and the turbulent dispersion are predicted through integrating the particle trajectory equations for each particle, using the instantaneous fluid velocity along each particles trajectory. The volume percentage of the solid phase was less than 10% therefore it was reasonable to ignore the effect of the solid phase on the liquid phase and the interaction between the particles, this has been widely applied to dilute flows. The single phase flow computational results obtained by Wang et al. were compared with the experimental measurements of Hsieh and Rajamani and a good agreement was found (Wang, et al., 2003), (Hsieh & Rajamani, 1991).

2.6 Summary

Having carried out a review of the literature relating to dispersed phase separation it is clear that there has been an extensive amount of research work carried out in this field. It is therefore worthwhile at this stage to summarise what is currently known and from this highlight the knowledge gaps which exist and how the work carried out in this investigation aims to fill some of the voids.

Droplet separation predominantly occurs due to inertial forces experienced by the droplet within the flow field. For droplets in the 300+ micron range this occurs mainly through gravitational separation. For droplets of 10 microns and greater they are separated by exploiting the centrifugal force generated through a cyclonic geometry. For droplets below 10 microns wire mesh pads and coalescing cartridges are required where the droplet laden flow passes through a complex path of wire mesh strands and fibres resulting in separation due to impingement and impaction. It is therefore apparent that the performance of a separator is directly dependent on the droplet size which exists at the inlet; therefore knowledge of this is required to accurately select the correct separation mechanism for the application.

The Henry Technologies helical oil separator is a complex device which employs a hybrid of gravitational, inertial, filtration and centrifugal separation mechanisms to remove liquid droplets and film from the gas flow. As far as the author can tell from the investigated literature a separator which comprises all of these mechanisms within a singular geometry where the gas-liquid-droplet mixture enters the geometry through a radial inlet has never been examined before. However the available empirical models can be used to provide an indication of the expected performance parameters of the helical separator for a range of operating conditions based on the individual separation mechanisms, but cannot be used to provide an accurate overall separation efficiency or pressure drop. It is on this basis that experimental testing is required to provide exact data to characterise the performance of the unit.

The numerical modelling of the gas-particle flow within centrifugal separation mechanisms, in particular the cyclone separator, has been examined in great detail within the literature and found to produce successful results. The majority of the studies concluded that because the flow is strongly swirling it is extremely complex and leads to difficulties associated with the computational modelling. However with the advancement in

computational power and memory the application of advanced turbulence models, in particular the RSM and LES, the flow field can be determined with growing levels of accuracy. The use of the DPM model has also shown to produce successful results to capture the separation efficiency for the geometries. There are however only a limited number of investigations which have been carried out to explore gas-droplet separation and in particular for geometry which is a hybrid of multiple separation mechanisms. Therefore this investigation aims to explore the capabilities of the current numerical models to predict the separation performance of a gas droplet separator thus attempting to bridge the knowledge gap using the experimental data for validation.

Having validated the computational model for the current helical separator geometry, some of the performance enhancement features which are presented with in the literature, such as an increased gas velocity, tangential entry and swirl generator, can be trialled. By using the validated model to assess whether the proposed improvements result in an increase in the separation efficiency and comparing the data to that obtained from the experimental testing will determine the ability of the proposed modelling approach to be used as a droplet separator design tool since from the literature explored this is not currently available.

Chapter 3 Separator Gas Phase Flow Modelling

3.1 Introduction

The ability of a separator to remove the entrained particles or droplets is highly dependent on the gas flow patterns within the geometry. The gas flow fields within centrifugal type separators are very complex due to the 3-dimensional flow and the degree of swirl leading to high levels of turbulence which is strongly anisotropic. Therefore to allow the performance of a separator to be understood and proposals made for design improvement the turbulent flow within the geometry needs to be captured accurately. The use of computational fluid dynamics (CFD) for the numerical calculations of the gas flow is now the most widely accepted and used method to yield the prediction for the collection performance of a centrifugal separator in comparison to the more traditional method of semi-empirical calculations. The semi-empirical models have been extensively tried and tested in the literature but have been found to have limitations such that they are not able to reflect every geometric detail and result in performance predictions which have limited applicability and accuracy (Gronald & Derksen, 2011).

Since one of the first CFD calculations carried out on an industrial cyclone separator by Boysan et al. the main issue associated with the simulations is the choice of turbulence model. It was quickly discovered that the widely used standard k-ε model was inadequate in the calculation of swirling flows due to the excessive levels of turbulent viscosity and unrealistic tangential velocity distributions. Since this discovery there have been endless studies carried out by researchers to assess the ability of higher order turbulence models to accurately predict the gas flow field within geometries with swirling flow.

Although there is a wealth of information in the literature regarding the continuous phase modelling of cyclone separators, the helical separator being investigated in this study is not a standard cyclone. The unit does however contain some similar features, nevertheless there is a requirement for it to be explored specifically. Due to the perpendicular entry to the main separation space; the helix forcing the flow to descend in a spiral to the bottom of the separator; and the centre tube leading to the outlet causing the flow to reverse; the flow field within the helical separator will exhibit a rotational nature as it travels between the inlet and outlet. It is based on the existence of a rotational flow that the modelling

approaches applied within this investigation will be based, using the published methods for cyclone modelling as a guideline.

To validate the accuracy of the numerical simulation experimental data which captures the mean and fluctuating gas velocities and turbulent parameters is obtained through the use of electronic hot-wire probes being inserted into the flow or the more advanced and non-intrusive optical technique, Laser Doppler Anemometry (LDA). The latter technique has been well validated with the use of CFD in the past for capturing details of the flow in cyclonic separators. In particular the work of Hsieh and Rajamani, who produced successful measurements of the axial and tangential velocity profiles in a hydrocyclone is frequently used for validation of numerical models since the amount of experimental data available is not in abundance (Hsieh & Rajamani, 1991).

In this chapter the LDA experimental measurements of two velocity components within a Perspex replica of the Henry Technologies helical separator will be presented. The velocity profiles obtained will then be compared with those produced from the CFD simulations to allow a validated single phase gas model to be established which can then be used for separation efficiency predictions. Also presented in this chapter are some images obtained using laser sheeting to capture the bulk flow structure within the Perspex separator geometry which helps with the understanding of the complex flow field.

3.2 Laser Doppler Anemometry

Laser Doppler Anemometry (LDA) is a non-intrusive optical measurement apparatus used to determine the gas velocity and turbulence parameters in a flow field by employing the Doppler shift. This concept exists when a siren moves towards and then away from a stationary observer who experiences a downshift in the pitch. A linear relationship exists between the speed of the moving sound source and the shift in frequency that occurs as a result. The same effect can be applied to a light source when it is reflected from a moving object in that the scattered light frequency is shifted to a degree which is proportional to the speed of the object, therefore allowing the speed to be determined by observing the frequency shift. It is the resulting frequency shift that is the governing principle of LDA.

The application of LDA for fluid dynamic investigations in both gases and liquids was first proposed in 1964 before coming into wide spread use in the 1970's and is now a well-established optical technique for the measurement of particle velocities. The basic principle

behind this method is the 'fringe' model. A laser is used as the source for emitting a coherent, monochromatic, intensive and directional light which is directed into a beam splitter called the Bragg cell. The output from this cell are two beams with equal intensity but different frequencies, one shifted and the other unshifted relative to the original light source. The two beams are then expanded through optics, aligned to be parallel and then focused into optical fibres bringing them to a probe. At the exit of the probe the beams pass through a focusing lens so that the beams intersect to produce a measurement volume within the flow. In the region where the beams are focused they have parallel wave fronts of wavelength λ, and at the point of intersection parallel interference fringes are created at the beam waist. As particles pass through this measurement volume they scatter light which is collected by the receiving lens and focused on the photo-detector. The intensity of the scattered light is determined by the Gaussian laser beam intensity profile, known as the pedestal, modulated by the fringe pattern. The photo-detector converts the optical information from the measurement volume to an electrical signal, translated to produce the Doppler frequency, f_D. It is the f_D which is directly proportional to the particle velocity vector V_x normal to the direction of the fringes;

$$f_D = \frac{V_x}{\Delta x}$$ (3.1)

where Δx represents the fringe spacing defined as;

$$\Delta x = \frac{\lambda}{2cos\beta sin\left(\frac{\alpha}{2}\right)}$$ (3.2)

3.2.1.1 The Doppler Effect

The Doppler shift, f_D, is dependent on the particle velocity, V, direction of particle motion, the wavelength of the incident light, λ , and the orientation of the observer. The latter is defined by the angle, α, between the incident light wave and the photodetector. The direction of the particles motion is defined by the angle, β, between the velocity vector and the bisector ABC as shown in Figure 3.1.
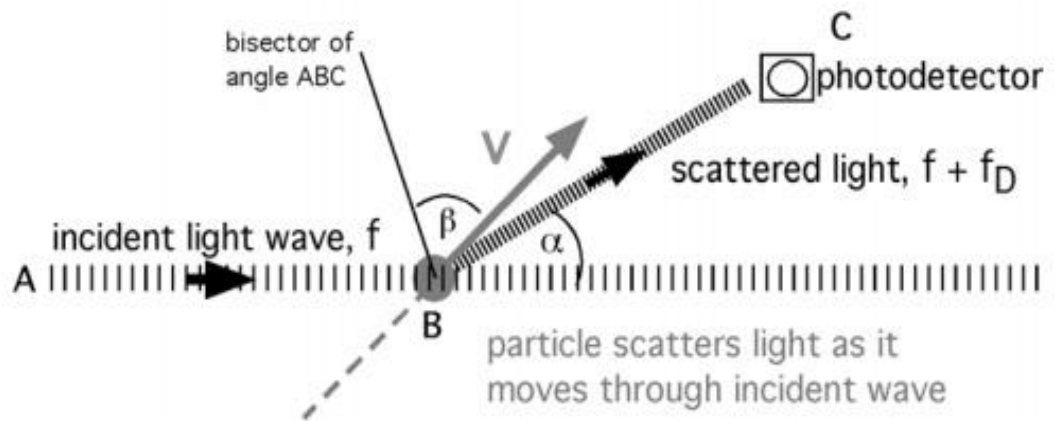
Figure 3.1: Light Scattered by a Particle Passing Through an Incident Light Beam

The direct determination of the Doppler shift can be obtained by measuring the frequency of the incident light, f, and the scattered light frequency, $f+f_D$, and finding the difference. However, the Doppler shift is a very small value compared to the frequency of the incident light beam in practical applications therefore there exists a high degree of uncertainty when estimating a small value from the difference between two large values. To improve the accuracy of the determination a method has been developed using two incident beams, known as heterodyning. This requires the Doppler shifted scattered light to be mixed with the incident light generated from the same light source or that the light from one laser beam interference with scattered light from another beam (Drain, 1980). As a result two LDA systems have been developed, one is known as the dual beam system and the other as the reference beam system both of which have been successfully shown to produce good data (Zhang, 2010). It is the dual beam system that will be used for the measurements in this investigation hence this will be examined in further detail. In the dual beam setup the incident light is split into two beams of equal intensity which are then directed to intersect at a location where the measurement is to be made within the flow. As the particles pass through the volume they scatter light from both beams. The frequency shift of the light scattered from each beam will be different due to the orientation of the two beams relative to the photodector and relative to the particle's velocity. That is the values of α and β shown in Figure 3.1 are different for the two beams. For each of the two beams the Doppler shift is defined as f_{D1} and f_{D2} with the scattered beams having frequencies $f+f_{D1}$ and $f+f_{D2}$. Since f_{D1} and f_{D2} are significantly smaller than f, then the frequencies of the scattered light waves are almost equal. When waves of equal amplitude and nearly equal frequencies

are superimposed, the amplitude of the resulting signal periodically rises and falls; this modulation is defined as a beat. The resulting beat frequency is one half the difference between the two original frequencies. Therefore when the two bursts of scattered light are superimposed within the photodetector the resulting signal has a beat with frequency $|f_{D1} - f_{D2}|/2$ which is the Doppler frequency required to determine the particle velocity.

3.2.1.2 The Fringe Model

As mentioned earlier the LDA system makes use of the Bragg cell as a beam splitter to shift one of the two equal-power beams. When the two coherent beams having plane wave fronts intersect in space a fringe pattern is created in the intersection region (Rudd, 1969). The fringe model is easily visualised and provides a basis for quantitative and qualitative analysis of a number of features of LDA signals. A fringe pattern is shown in Figure 3.2 created by the separation of the original source into two separate beams and then recombining them at different angles of incidence on a viewing surface. The fringe spacing d_f, is the distance between sequential bright (or dark) zones;

$$d_f = \frac{\lambda}{2sin\left(\frac{\theta}{2}\right)}$$

(3.3)

As a particle passes through the fringe pattern, the intensity of the scattered light varies with the intensity of the fringes. Therefore the amplitude of the signal burst varies with the time scale d_f/V, with V representing the velocity component perpendicular to the fringe pattern. The frequency of the amplitude modulation is thus given as;

$$\frac{V}{d_f} = \frac{2V}{\lambda} sin\left(\frac{\theta}{2}\right)$$

(3.4)

which is found to be the same as the Doppler frequency f_D. In the case of the two-beam system, the Doppler frequency is independent of the position of the photodetector since the angles α and β are not included in the formula.
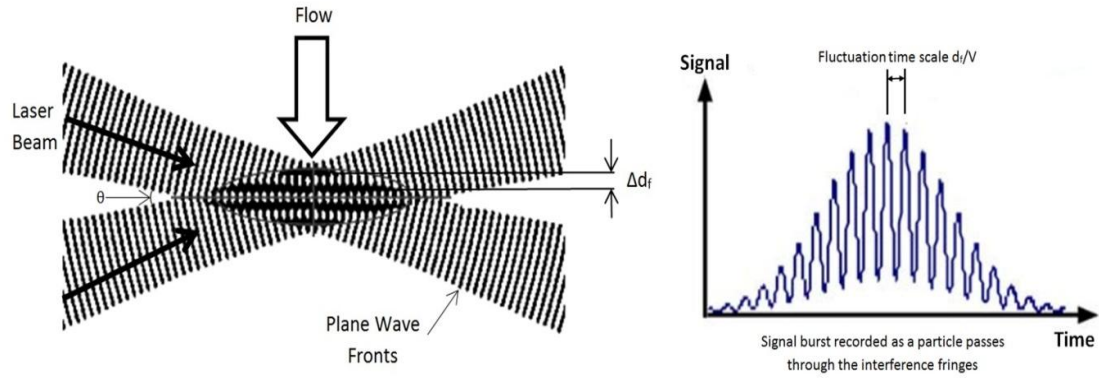
Figure 3.2: Fringe Model

3.2.1.3 Directional Ambiguity

The frequency of the light intensity variation due to a particle passing through the equally spaced fringes measured by an LDA system is an accurate and effective way of obtaining data associated with the fluid flow however it does have two main limitations. Firstly the Doppler frequency depends only on the magnitude of the velocity and not the direction since both a positive and negative value of V will produce an identical Doppler frequency. Secondly, if the particle keeps stable in the measurement volume then no signal will be produced for the photodetector to manipulate. To correct for the directional ambiguity, a frequency shift, f_s, is applied to one of the incoming beams. This in turn causes the fringe pattern to move at a speed $V_s=f_sd_f$ towards the incoming unshifted beam. As a result a particle travelling in the same direction as the fringes will generate a higher Doppler burst signal whilst a particle moving in the opposite direction to the fringes will generate a lower signal. This can be seen in equation 3.5;

$$f_d = \left| f_s + \frac{2V}{\lambda} sin\left(\frac{\theta}{2}\right) \right|$$

(3.5)

with the sign associated with the particle direction in V being reflected in f_d, the detected frequency. This frequency shift allows the directional ambiguity to be removed provided $f_s > \left| \frac{2V}{\lambda} sin\left(\frac{\theta}{2}\right) \right|$ which allows the sign of V to be determined. Therefore to optimise the system a different frequency shift is required for different flow conditions.

In practical applications the generation of the frequency shift is achieved through the Bragg cell which is a transparent medium composed of either liquid or solid through which one of the laser beams is passed. The Bragg cell, usually a piece of glass attached to a piezo-

electric transducer which excites the glass by passing ultrasonic waves through it causing the incoming laser light to be diffracted. A typical frequency shift applied to a laser light in an LDA system is 40 MHz.

3.2.1.4 Measurement Volume

The spatial resolution of the LDA system is governed by the size of the measurement volume and is therefore one of the most important parameters. The region which defines the measurement volume is defined by the region of fringes formed by the intersection of the laser beams which is an ellipsoid due to the Gaussian intensity distribution of the beams in all three directions. The measurement volume is shown in Figure 3.2 with the ellipsoid outlined in grey. The exact dimensions of the measurement volume are dictated by the light intensity distribution of the fringe pattern which is $1/e^2$ of the maximum intensity, which occurs at the centre of the measurement volume. The size of this volume can be calculated from the beam waist diameter d_f, of the focused laser beam and the angle between them (Albrecht, et al., 2003).

$$d_f = \frac{4 f_L \lambda}{\pi E_w d_L} \qquad (3.6)$$

where d_L is the beam waist diameter before expansion, E_w is the beam expansion ratio and f_L is the focal length of the front lens. The detection volume, defined as the volume from which the signals are received is different from the measurement volume, the size of which is dependent on the requirements of the signal processing system.

3.2.1.5 Signal Processing

After the photomultiplier detects a burst, this signal then has to be processed of which there are three possible techniques that can be employed to determine the detected frequency. The first of these techniques is a counter processor which initially isolates the modulation in the burst using a high-pass filter and then counts the number of zero-crossings per unit time. The second technique is a spectrum analyzer which calculates the Fourier transform of the burst signal and then selects the peak frequency as the detected frequency. The final processing method is a correlation processor which employs a correlation algorithm to deduce f_d. The processing technique used to determine the detected frequency in this investigation is the spectrum analyzer.

A single pair of incident light beams of the same wavelength can only extract one velocity component of a particle in a flow field. To allow the remaining components to be obtained additional beam pairs can be added to cross at the same measurement point, with each pair possessing a unique wavelength so that the relevant burst signals can be distinguished during the signal filtering process. Typically, an argon-ion laser, as is the one used as the source in this case, has green (514.5 nm), blue (488.0 nm) and violet (476.5 nm) outputs for multi-component measurements.

The best scattering signals are achieved when the diameter of the particle being measured is several times the wavelength however it is necessary that the particles also be small enough to follow the flow without deviation to achieve accurate data. The light scattered by the particle will propagate in all directions with the intensity values obtained from Mie scattering calculations with the highest intensity light being scattered on the forward side of the particle, i.e. the direction away from the incident light. The setup to capture the scattered light for an LDA system in forward scatter requires the photodetector to be positioned opposite the light source which requires two separate probes to be used for the measurement. It is therefore more convenient to operate in back-scatter mode since all the optics are only on one side of the measurement location therefore requiring only one viewing window and providing an easier traversing arrangement for the system and maintaining alignment among multiple velocity components. To compensate for the reduced scattering intensities when operating in back-scatter the laser power has to be increased accordingly. The basic components of an LDA system operating in back-scatter mode, as used in this investigation, are shown in Figure 3.3.

Prior to analysing the data with an appropriate technique the burst data must be re-sampled onto an equi-spaced time grid. This is due to the lack of consistency in the arrival of particles into the measurement volume making the rate of velocity sampling uneven in time. There is also additionally an increased sampling rate when the velocity is higher such that an ensemble-average of the data does not reflect the true time-average. To eliminate this bias a time-weighted averaging approach is adopted which weights each velocity estimation by the duration of the underlying burst. In doing so this provides proportionally greater weight to lower velocity samples which occur when the samples are less frequent on the assumption that the particle concentration is uniform.
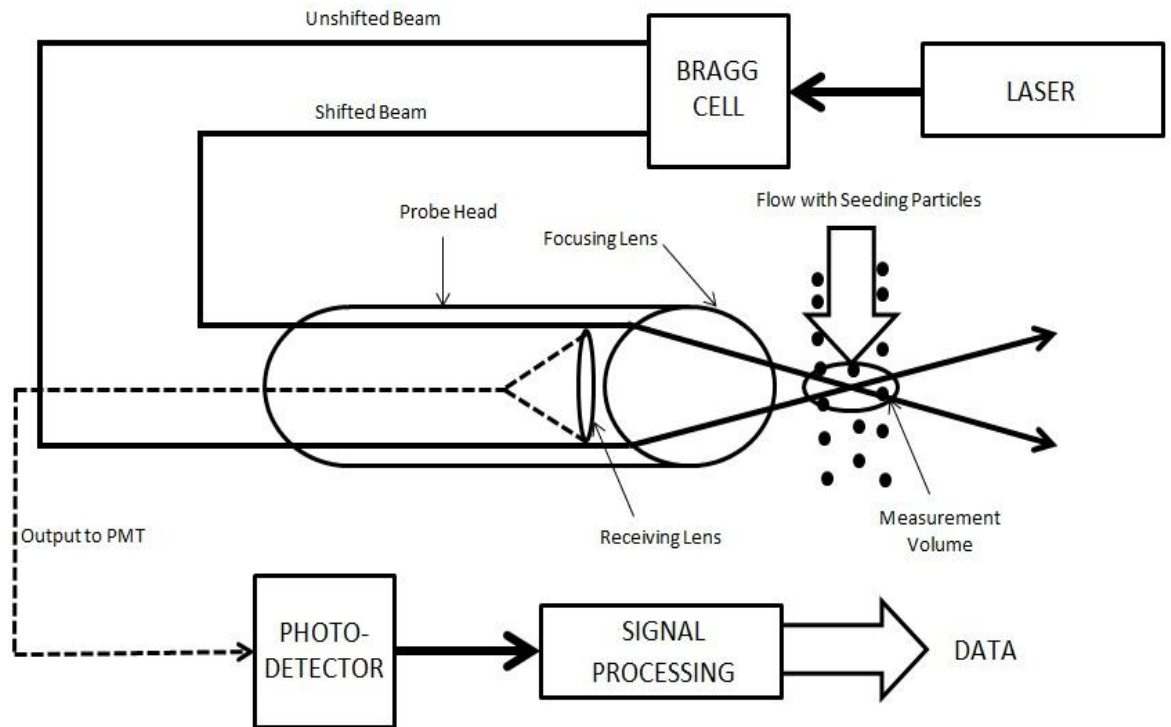
Figure 3.3: Basic Components of an LDA System

3.2.2 LDA System Arrangements

The measurements were made using a 2 component LDA system from TSI operated in back-scatter mode and is shown in Figure 3.4. The system consisted of a 3 phase supply (A) to deliver power to a 5-W Argon-ion laser (B) operated with a water cooled system. A beam splitter and frequency shifter (C) which comprises of a Bragg cell to apply the shift to the mixed-coloured beam. A fibre optic probe (D) where the four beams with almost equal intensity were emitted and crossed at the focal length of the lens to create the measurement volume; the focal length of the lens used for the transmission/receiving optics was 363 mm with a beam spacing of 50 mm. A photomultiplier (E) which collected the scattered light from the measurement volume and passes the signal to the Burst Spectrum Analysers (BSA) (F). The data is then stored on the PC where the analysis software provided by TSI is installed (G). A three-axis traverse control unit (H) and system (I) are used to position the probe corresponding to the required measurement location which is programmed through the same PC as is used to store the measurement data. The schematic of the LDA system is shown in Figure 3.4.
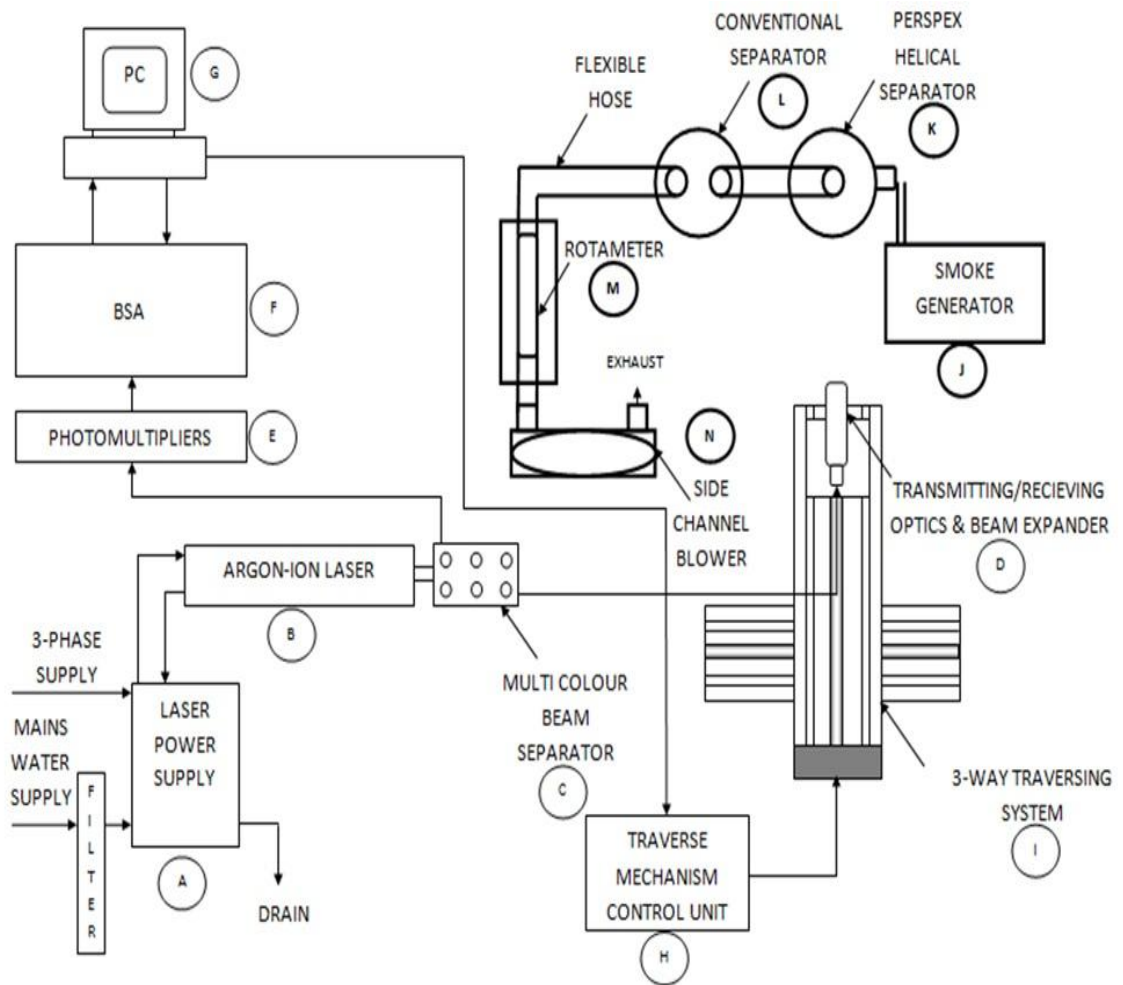
Figure 3.4: Schematic of LDA System (Rig Shown in Bold)

The horizontal (U) and vertical (V) velocity components were obtained through the 2-D LDA system. The complete fluid mechanic measurements were carried out using the continuous phase only without the presence of the oil droplets and liquid film. The presence of the dispersed phase would have resulted in a thin film of oil covering the internal walls of the geometry almost instantaneously hence restricting optical access and adding to the effects of laser beam steering. Tracer particles, which would follow the streamlines of the gas flow without any significant deviation, were generated using an Ondina oil filled smoke machine (J). The characteristics of the tracer particles are important to obtaining accurate data measurements from the LDA system since it is the scattering signal from the particles suspended in the flow which is detected by the photodetector rather than signals from the fluid itself. In a device where the primary function is to remove the dispersed phase it is difficult to keep particles in the flow for the entire gas flow path. A typical particle size for

obtaining accurate LDA measurements is in the region of 10 microns; the particle size range of the Ondina oil was in the 1-5 microns range since this prevents any significant separation occurring. This ensures that the measurements being made in the lower region of the separator still contain the required amount of seeding to produce high quality scattering.

The smoke produced was drawn into the Perspex helical separator (K) along with ambient air through the secondary conventional separator (L) and rotameter (M) by the side channel blower (N). Due to the thickness of the separator wall of 3.0 mm and the radius of curvature of the main body; measurements were started 6.0 mm in from the inner surface of the wall. The refractive index of Perspex is 1.49 which causes the incident light beam to be refracted when passing through this surface to reach the measurement volume. The extent of this change can be estimated using Snell's law;

$$\eta_f \sin\theta_1 = \eta_w \sin\theta_2 \qquad (3.7)$$

where η_f is the refractive index of the fluid (air=1.0); η_w is the refractive index of the window which the beams are transmitted through; θ_1 is the beam angle measured from the vertical; θ_2 is the refracted beam angle measured from the vertical.

The double beam refraction is due to two effects; the angle of the beam intersection θ changes and the true position of the measuring volume differ from the actual location of the traversing mechanism. When dealing with the curvature associated with the cylindrical body of the separator an additional problem arises due to the laser beams of different spatial orientations not hitting the curved surface at the same angle resulting in the location of intersection being offset from the optical axis.

Axial velocity measurements in a cylindrical body need to be orientated such that the incident beams are in a plane which passes through the axis of the cylinder and the bisector between the beams perpendicular to the axis. This means that there is only refraction in the axial direction and the refraction surface will be at right angles to the beam bisector therefore equation 3.7 can be used along with equation 3.8 to calculate the corrected measurement volume location.

$$x_c = x_a + \frac{\tan\theta_1}{t_w(\tan\theta_1 - \tan\theta_2)} \qquad (3.8)$$

where x_c is the corrected position of the measurement volume; x_a is the location of the measurement volume in the absence of a window and t_w is the thickness of the window which the beam is penetrating. In this investigation the difference between the corrected location and the traverse movement was found to be less than 1 mm hence can be neglected.

Obtaining the horizontal component of velocity requires the incident beams to be orientated such that the bisector between the beams is at right angles to and passes through the axis of the cylinder with a plane containing both beams perpendicular to the axis. The radius of curvature of the cylindrical body of the separator will behave like a convex lens which results in the real measurement location moving closer to the optical system. An equation was proposed for the refraction factor, G, assuming that for small angles the sine and tangent are equal;

$$G = \eta_f \big[1 + (r_a/r_o)\{(1 - \eta_w)/\eta_w + (r_o/r_i)(1 - \eta_f)/(\eta_w \eta_f\} \big] \qquad (3.9)$$

where G is the refraction correction factor; r_a is the position of the measurement volume without any window in place; r_o is the outer radius of the cylindrical chamber; r_i is the inner radius of the cylindrical chamber. Therefore the true measurement radius r_c can be calculated as;

$$r_c = r_a/G \qquad (3.10)$$

For the present study the true measurement location error varied from $\pm$ 0.66 mm to $\pm$ 1.00 mm from the centreline to the cylindrical wall. Since the size of the probe measurement volume is typically of the order of a couple of millimetres the error associated with the beam diffraction is deemed to be negligible therefore this is not corrected for. The combination of these marginal discrepancies with respect to the geometrical location being measured within the separator is only really significant when measuring the velocity profiles below the centretube of the separator in the core region where there are steep velocity gradients.

3.2.3 Data Collection Setup

The geometrical configuration of the Perspex unit used in this investigation is based on the Henry Technologies S-5190 helical separator with a maximum discharge volume flowrate of 18.7m^3/hr. As the Perspex unit was to be custom made for the purpose of flow visualisation

the oil collection chamber was simplified to an isolated volume which contained a drain valve on the base to allow any collected fluid to be removed. The main cylindrical body, inlet and outlet connections and centre tube were manufactured from standard pipe dimensions therefore some of the values varied slightly from the standard Henry separator. The exact dimensions of the Perspex geometry are given in Figure 3.6.

3.2.3.1 LDA Acquisition Hardware

The electronic hardware components for the LDA system used in this investigation are the PDM1000 photo detector module and FSA3500 signal processor. The former receives optical signals from the fibreoptic probe and relays them as electrical signals to the latter. The signal processor then extracts frequency, burst transit time and burst arrival time information from the relayed signals and sends them to the supporting computer. The computer contains the Flowsizer software which analyses the data and displays the details of the measurement volume.

The system used was able to be configured as a Phase Doppler Particle Analyser (PDPA) to determine particle size as well as velocity. However due to the geometrical configuration of the separator possessing a high degree of curvature and the rate at which the lubricating oil, used for the performance measurements of the separator, deposited on the cylindrical wall of the unit particle size measurements within the separation space could not be obtained. As a result only two of the velocity channels, and hence two photomultiplier tubes (PMT) were active on the photo detector module to obtain the horizontal and vertical velocity components for this investigation.

The light scattered by the tracer particles in the measurement volume that is collected by the fibreoptic probe goes into the photo detector module which then transmits the signal to the PMT. The signal from each PMT is then amplified and split with one signal passing through a high-pass filter and the other sent to a high voltage clamping circuit. The signal passes through the high-pass filter, which can be 5 or 20 MHz, has the pedestal removed and is then transmitted to the FSA unit. The pedestal is still present in the signal sent to the clamping circuit. When a signal with high light levels are sent to the PMT the clamping circuit holds the high voltage and the saturated led on the front panel is illuminated.

Analogue burst signals are received and processed by the FSA with the results being sent to the computer for analysis. The FSA unit can process between one and five Doppler signals

dependent on the signal processor configuration with the velocity channels being labelled 1, 2 and 3. An overview of the signal processing that takes place within the FSA is shown in Figure 3.5.
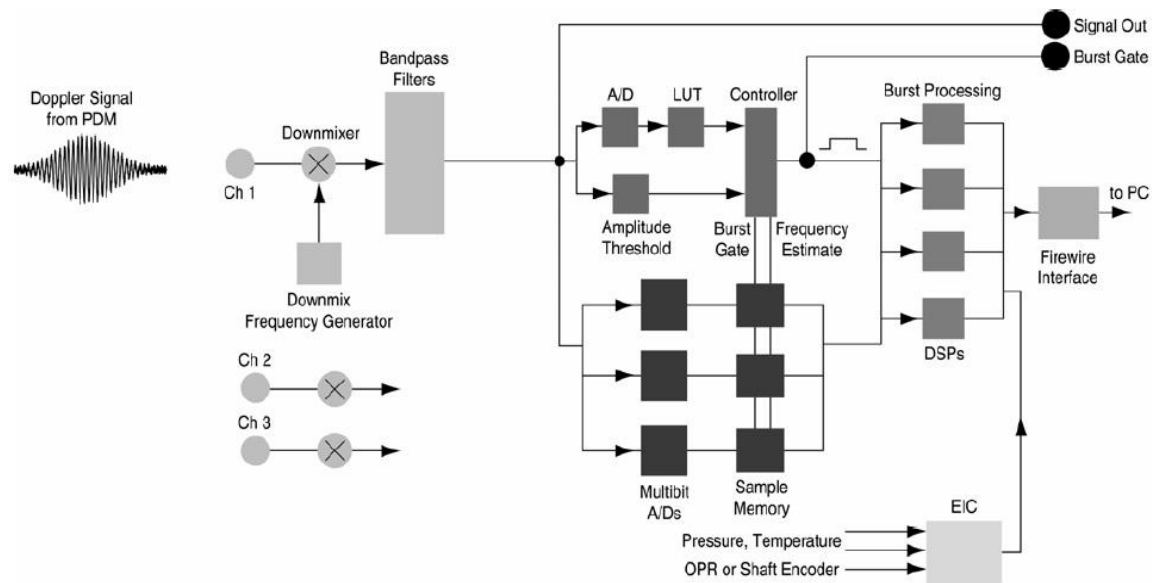
Figure 3.5: Components of FSA Signal Processor

The Doppler signal with the pedestal removed passes through a downmixer on entering the FSA from the PDM. The frequency shift initially introduced by the bragg cell is changed by the downmixer which can have any value between 0 and 40 MHz. This means that some or the entire 40 MHz frequency shift applied by the bragg cell can be left on the signal. In effect the process of the downmixer is equivalent to multiplying the input signal with the downmix frequency selected in the software. The signal out of the downmixer contains two frequency components: the sum and the difference of the input and downmix frequencies. The former frequency is not needed and is removed by the bandpass filters with the latter being the desired signal. Noise and the high frequency sum term component of the signal passing through the downmixer are removed by one of twenty bandpass filters, this signal can be observed through the 'signal out' connector on the front panel of the FSA.

The signal leaving the bandpass filters is split into two parts: one is sent to the burst detector and the other to the burst sampler. The burst detector plays a critical role in processing the measurement signal since the burst occur randomly it is important to identify their occurrence so that they can be processed accurately. The burst detector identifies and flags the beginning and end of a possible Doppler burst from the continuous

background noise. The quality of the signal is continuously monitored by the burst detector which discriminates between a Doppler burst and noise when the signal exceeds a preset value. This task is performed by firstly digitizing the burst then carrying out a real-time Discrete Fourier Transform by using a set of look-up tables.

A signal which exceeds a signal to noise ratio level signifies the start of a burst gate and a burst timer monitors the period of the signal burst. When the signal to noise ratio falls below the required level again the burst gate is closed and the elapsed time is used to determine the centre of the burst. The maximum range of the frequency signal going through the bandpass filters is always within a range of 1-10, the burst detector samples the signal with three sampling frequencies allowing the Discrete Fourier Transform look-up tables to be optimised over a small range. An option is also available for selecting the larger amplitude signals with good signal to noise ratio. All these factors combined are utilised by the burst detector's control logic to determine when to turn on and off the burst gate. The time stamp counter and current value of any external input data requested at the end of the burst gate is stored by the FSA. This stored data is then matched with the other data processed from that burst along with the time period that the burst gate was on which becomes the transit time for each burst.

In parallel with the burst detector, the incoming signals are also sampled using high-speed multi-bit A/D converters which sample the signal simultaneously at multiple rates. The optimum multi-bit sampler for the burst frequency is determined by the burst detector. The signal processor automatically detects the sampling rates based on the bandpass filter range such that there are between 10 and 25 samples per cycle. Similar to the burst detector the 1-10 frequency range is split into three sub-ranges such that there are three possible sample rates for each burst allowing the optimum number of samples per cycle to be used for each burst. The burst detector determines which of the three sub-ranges each burst's frequency is in. During the period where the burst gate opens and closes again 8-bit samples are stored in the memory which can hold data for up to 15 separate bursts. In doing so ensures that multiple bursts which arrive in close succession of each other are not missed even though the processor may be busy. The burst gate also determines the most suitable region of the burst to collect samples from. The optimum sample rate and output from the burst gate are then sent to the burst processor.

3.2.3.2 LDA Acquisition Software

The data acquisition software used for this investigation with the TSI apparatus is Flowsizer which performs two functions; data collection and data analysis. The raw velocity data collected from the measurement volume which is fed to the photomultipliers is collected by the software. Once the hardware is set up and connected the software can be setup to collect data from the system shown in Figure 3.4. The primary inputs to the software are as follows:

1. LDA optics parameters which include; wavelength, beam focal length, beam separation, laser beam diameter, beam expander, Bragg cell frequency for each transmitter channel. (The majority of these values are default but should be checked with the hardware before proceeding).

2. The locations of the measurement points with respect to the (0,0,0) location of the traverse. This was located on the central hole of the baffle plate which represented the centreline of the geometry as shown in Figure 3.7. The (0,0,0) point was found by inserting a sharp pencil point through the hole at the bottom of the separator and traversing the probe until the beams were found to cross on the sharp point.

3. LDA processor controls for each channel which include; photomultiplier voltage, burst threshold voltage, band pass filter frequency, signal to noise ratio and downmix frequency. Further details on setting these parameters can be found in the TSI Laser Doppler Velocimeter Operation Manual Revision E 2006.

One of the key settings to ascertain the velocity data being obtained is valid is to ensure the number of particle measurement attempts is high enough to eliminate any errors. For this investigation the attempts were set to 100,000 and the time out value set to 10 seconds so that if the prescribed sample count was not reached in the period the probe would traverse to the next measurement location, it was found that in the majority of cases 100,000 samples were obtained before the 10 second time period was elapsed. When making measurements in the lower region of the separator below the centre tube some of the data rates were low due to some of the seeding particles becoming separated from the flow. Another issue discovered was the requirement for a high photomultiplier voltage of around 1300 Volts indicating poor signal-to-noise ratio. A summary of the settings used for all the data collected are presented in Table 3.1.

Once all the data was collected for a specific measurement plane the mean velocity values were displayed graphically. The calculations carried by the software to obtain the average values are;

$$V_x = f_D \frac{\lambda}{2sin\frac{\theta}{2}}$$

(3.11)

which gives the velocity component perpendicular to a set of fringes and

$$\bar{V} = \frac{\sum_{i=1}^{N} V_i}{N}$$

(3.12)

gives the mean velocity where V_i is the velocity component of the ith. particle along the x-direction and N is the total number of samples.

Parameter	Channel 1	Channel 2
Wavelength (nm)	514.5	488.0
Focal Length (mm)	363.0	363.0
Beam Separation (mm)	50.0	50.0
Laser Beam Diameter (mm)	2.65	2.65
Fringe Spacing (µm)	3.7441	3.5513
Beam Waist (µm)	89.73	85.11
Bragg Cell Frequency (MHz)	40	40
Velocity Limit Min. (m/s)	-2.62	-2.49
Velocity Limit Max. (m/s)	7.49	7.10
Band Pass Filter (Hz)	0.3-3M	0.3-3M
SNR	Medium	Medium
Downmix Frequency (MHz)	39	39
Gate Scale (%)	250	250

Table 3.1: LDA Measurement Parameters

3.2.4 Error Analysis

In order to assess the validity of the experimental data an estimation of the error associated with the exact location of the measurements and the accuracy of the velocity components obtained has to be examined as well as the repeatability of each data point;

this has been discussed in some detail in the associated literature (Abernethy, et al., 1985), (Kline, 1985). The errors associated with LDA data acquisition include;

1. The error of the frequency output from the FSA unit is quoted as being within 1% for a good signal to noise ratio for the validated data measurements.

2. The uncertainty associated with the measurement of the beam angles which are used to translate the Doppler frequencies into particle velocities.

3. There is a bias towards detection and validation of the velocities associated with a high burst probability independent of the velocity of the fluid itself. This leads to an arithmetic mean value of the sample which is not exactly equal to the true mean of the velocity component normal to the fringes (McLaughlin & Tiederman, 1973).

The exact error associated with the location measurements within the separator was governed by the accuracy of the 3D traverse system which could be controlled accurately to $\pm$ 1 mm and the size of the probe measurement volume being of the order of a couple of millimetres. Throughout obtaining the velocity profile data within the separator the rotameter measuring the flowrate was found to fluctuate by $\pm 3\%$ due to the characteristics of the side channel blower used to create the flow within the system. The repeatability of each point sample measurement was found to be within 9.95% based on the maximum velocity deviation from the mean value at each measurement location taken from the average of the measurements obtained at that location. This is shown with error bars at each experimental data point in all the forthcoming graphs.

3.2.5 Operating Conditions

A centrifugal type separator is generally characterised by the dimensionless Reynolds number (Re); ratio of inertial to viscous forces; and the Swirl number (S); ratio of angular to axial momentum (Gupta, et al., 1984). These dimensionless parameters are defined by equation 3.13 and equation 3.14 respectively.

$$Re = \frac{\rho_l U_{in} D_{in}}{\mu_g} \tag{3.13}$$

$$S = \frac{\pi D_{out} D}{4 A_{in}} \tag{3.14}$$

Given the geometry presented in Figure 3.6; Re is 1.73×10^4 and S is 5.48 corresponding to an inlet velocity of 8.5 m/s. Typical industrial cyclone separators operate with a Reynolds

number of the order 10^5 range and have swirl numbers varying from 1.5-4.0 (Hoekstra, et al., 1999). The inlet velocity of 8.5 m/s is higher than the maximum operating velocity for the S-5190 unit but the flow rate was required to ensure the rotameter could maintain a constant value. It was found that on reducing the flow rate further caused an instability in the flow due to the performance characteristics of the side channel blower which resulted in the rotameter float behaving erratically therefore preventing a reading to be obtained.

The working fluid in the separator was laboratory air, which was measured to be between 12 and 15°C by a type K thermocouple over the duration of the testing. The air was drawn through the test unit using an Elektror side channel blower and allowed to exhaust into the laboratory. The flow rate was maintained at a constant value of 21.7 m^3/hr $\pm$ 3% (0.00737 kg/s) , using a gate valve to throttle the flow on the suction line. The rotameter used to measure the flow rate was a VA Master 10A4500 series with a 1 inch tube with a maximum volume flow rate of 57 m^3/hr, this was calibrated using a hotwire probe.

Measurements were made within the Perspex separator geometry at a location of 90° clockwise from the inlet pipe as shown Figure 3.6. To build up a complete picture of the flow field within the separator measurements were made from wall to wall in increments of 2 mm at y-axis locations of 20 mm and 35 mm, under the entrance to the centre tube. Profiles were also obtained in the areas of the helical flighting from the wall to the centre tube with 2 mm increments in the x-direction at axial locations ranging from 87-108 mm, in 3 mm increments, in the y-direction, this covered the lower section of the helix. A second scan was carried out to map out the upper section, ranging from 147-168 mm, again in 3 mm increments in the y-direction with the same criteria in the x-direction. The measurement planes are denoted 1 and 2 respectively in the upper left drawing of Figure 3.6. The choice of location for the velocity component measurements was dictated by ease of optical access coupled with the predicted degree of separation which occurs in local areas within the separator; with the aim to obtain data in areas where the greatest amount of the separation takes place whilst ensuring the downstream regions are also captured which govern the degree of carryover of the dispersed phase. For all the data points obtained the values were averaged over a 10 second interval, or until 100,000 data samples had been obtained. This allowed a time averaged velocity to be obtained which could then be used to provide a direct comparison to the time averaged data from the CFD models.
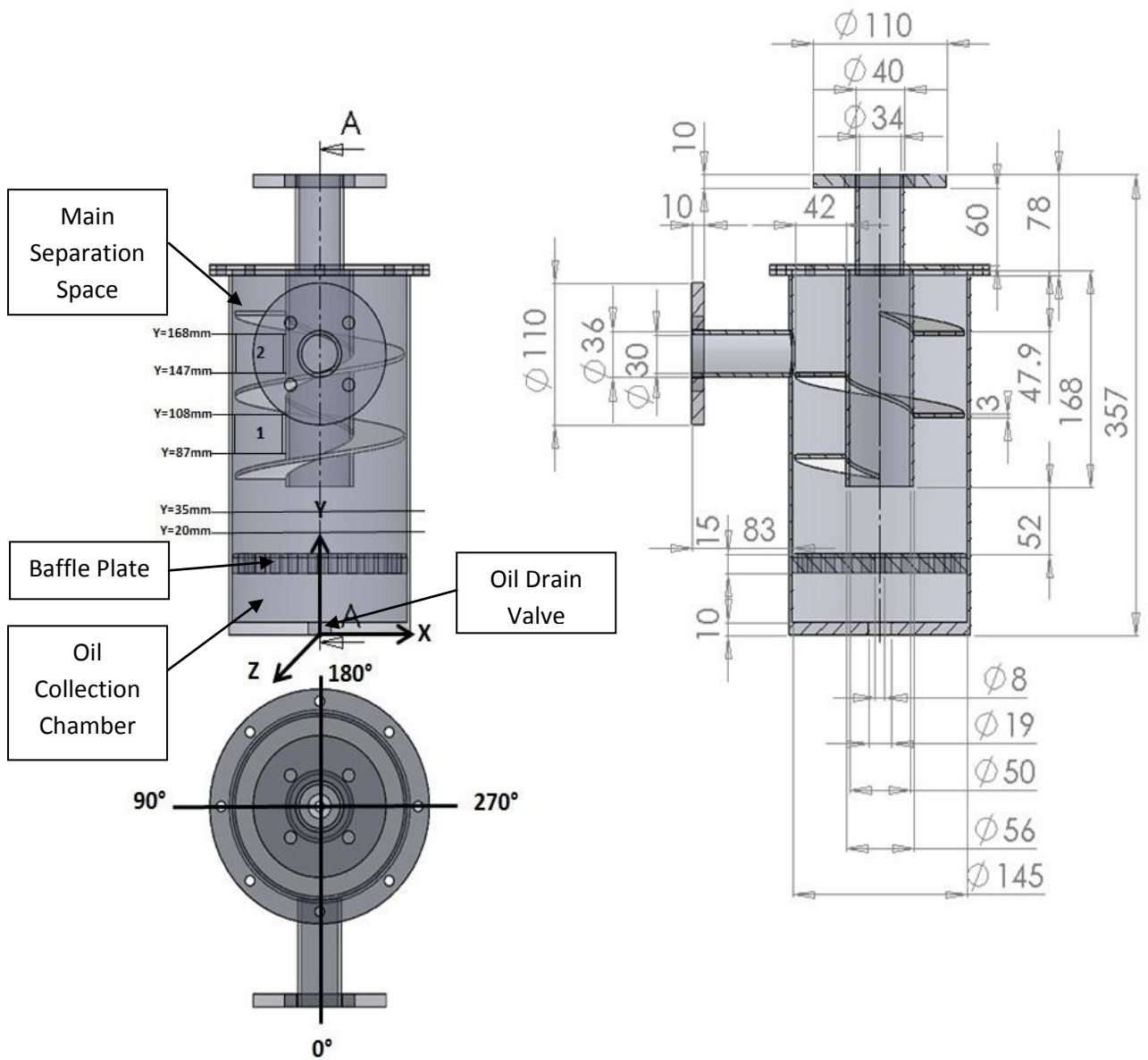
Figure 3.6: Dimensioned Drawing of Perspex Separator used in the Investigation where the Y-axis represents the Axial Component (Dimensions in mm)

3.3 Computational Modelling

3.3.1 Introduction

The numerical simulation of the helical oil separator has been carried out using commercially available CFD software Fluent 6.3.26. The software solves the Navier-Stokes equations which govern fluid flow; the continuity and momentum equations. These

equations are presented below in a Cartesian coordinate system assuming incompressible flow and no mass source terms.

$$\frac{\partial \rho}{\partial t} + \frac{\partial U_i}{\partial x_i} = 0 \qquad (3.15)$$

where U_i is the velocity component in the i-coordinate and x_i is the distance in the i-direction where i=1,2,3 in the case of a three dimensional problem. The momentum equation in RANS form is;

$$\frac{\partial (\rho U_i)}{\partial t} + \frac{\partial (\rho U_i U_j)}{\partial x_j} = -\frac{\partial p}{\partial x_i} + \frac{\partial}{\partial x_i}\left\{\mu \left(\frac{\partial U_i}{\partial x_j} + \frac{\partial U_j}{\partial x_i}\right)\right\} \qquad (3.16)$$

where p is the pressure, ρ the density, U_i the velocity in the i-th direction, x_i and x_j are the spatial coordinates in the i-th and j-th direction respectively, t is the time and μ the molecular viscosity.

Since equation 3.15 and equation 3.16 have no analytical solution a numerical solution is required. However due to the complexity involved in solving the exact equations numerically a time averaging approach is applied. This is achieved through Reynolds averaging by decomposing the governing equations into mean and fluctuating components resulting in the Reynolds Averaged Navier Stokes (RANS) equations. An additional term is introduced in the momentum equation called the Reynolds stress which accounts for the effects of turbulence on the mean flow. The inclusion of this term requires the solution of an additional equation or sets of equations, known as the turbulence model, to account for the Reynolds stress. The RANS momentum transport equation is given as;

$$\frac{\partial (\rho U_i)}{\partial t} + \frac{\partial (\rho U_i U_j)}{\partial x_j} = -\frac{\partial p}{\partial x_i} + \frac{\partial}{\partial x_i}\left\{\mu \left(\frac{\partial U_i}{\partial x_j} + \frac{\partial U_j}{\partial x_i}\right) - \rho \overline{u_i u_j}\right\} \qquad (3.17)$$

where the $-\rho \overline{u_i u_j}$ term represents the Reynolds stress.

The solution of the RANS equations in CFD are carried out with the Finite Volume Method (FVM) which requires the flow domain to be divided into a number of small finite control volumes. Each variable is assumed to be at the centroid of the individual control volumes. The governing equations are then integrated for each volume and interpolation profiles are used to describe the variation of the each variable between the volume centroids.

3.3.2 Choice of Turbulence Model and its implementation

For this investigation a detailed study was carried out to determine which of the available turbulence models could be used to accurately predict the complex flow paths within the helical oil separator geometry.

3.3.2.1 Standard k-ε Model

As a benchmark the well-established standard k-ε model, (Launder & Spalding, 1974), is selected since it is the simplest and widely validated of the two-equation turbulence models based on the eddy-viscosity hypothesis. The fundamental principle behind the k-ε model is that the turbulent effects can be sufficiently characterised by two quantities; the turbulent kinetic energy, k, and its rate of dissipation, ε. The additional transport equations which Fluent solves for k and ε are defined from equating the Reynolds stresses to the mean rate of deformation given as;

$$-\rho\overline{u_i u_j} = \mu_t \left(\frac{\partial U_i}{\partial x_j} + \frac{\partial U_j}{\partial x_i} \right) - \frac{2}{3}\rho k \delta_{ij} \tag{3.18}$$

and when equation 3.18 is substituted into equation 3.17 and is divided throughout by the density term, ρ , gives;

$$\frac{\partial U_i}{\partial t} + \frac{\partial (U_i U_j)}{\partial x_j} = -\frac{1}{\rho}\frac{\partial p}{\partial x_i} + \frac{\partial}{\partial x_i}\left\{ v_{eff} \left(\frac{\partial U_i}{\partial x_j} + \frac{\partial U_j}{\partial x_i} \right) \right\} \tag{3.19}$$

where $v_{eff} = v_l + v_t$ and is classed as effective viscosity. The turbulent kinematic viscosity, v_t, is not a fluid property but is only dependent on the state of the turbulence at any one point unlike v_l. As a result the effects of the turbulent fluctuations are modelled through v_{eff}. The turbulent viscosity is calculated from the Prandtl-Kolmogorov equation;

$$v_t = C_\mu k^{\frac{1}{2}} l_m \tag{3.20}$$

where $C_\mu = 0.5478$ and the mixing length is calculated from

$$l_m = C_d \frac{k^{\frac{3}{2}}}{\varepsilon} \tag{3.21}$$

where $C_d = 0.1643$. Substitution of equation 3.21 into equation 3.20 produces the turbulent diffusivity as;

$$v_t = C_D \frac{k^2}{\varepsilon} \tag{3.22}$$

where $C_D = C_\mu C_d$. The resulting transport equations for k and ε are;

$$\frac{\partial k}{\partial t} + \frac{\partial (U_j k)}{\partial x_j} = \frac{\partial}{\partial x_j}\left(\left(\frac{v_l}{\sigma_l} + \frac{v_t}{\sigma_k}\right)\frac{\partial k}{\partial x_j}\right) + P_k - \varepsilon \tag{3.23}$$

$$\frac{\partial \varepsilon}{\partial t} + \frac{\partial (U_j \varepsilon)}{\partial x_j} = \frac{\partial}{\partial x_j}\left(\left(\frac{v_l}{\sigma_l} + \frac{v_t}{\sigma_k}\right)\frac{\partial \varepsilon}{\partial x_j}\right) + \frac{\varepsilon}{k}(c_{\varepsilon 1} P_k - c_{\varepsilon 2} \varepsilon) \tag{3.24}$$

with the production rate of turbulent kinetic energy defined as;

$$P_k = v_t \frac{\partial U_i}{\partial x_j}\left(\frac{\partial U_i}{\partial x_j} + \frac{\partial U_j}{\partial x_i}\right) \tag{3.25}$$

The modelling coefficients used for the two-equation k-ε model are σ_k=1.0, σ_ε=1.3, C_μ=0.09, C_1=1.44 and C_2=1.92 and have been calibrated (Launder & Spalding, 1974). Although this model has been used to produce many successful results for engineering flows, the assumption that the turbulence is isotropic results in inaccurate predictions in geometries where the flow is swirling due to excessive levels of turbulent viscosity and unrealistic tangential velocity distributions (Boysan, et al., 1982).

3.3.2.2 The RNG k-ε Model

The RNG variant of the k-ε model, based on ReNormalization Group theory, has additional terms for the dissipation rate development (ε) which include the effect of rotation in the calculation of the turbulent viscosity and different numerical constants. By including the effect of swirl on the turbulent parameters the RNG model is able to provide an enhanced result for strongly swirling flows in comparison to the standard k-ε model and in reasonable agreement with experimental data (Griffiths & Boysan, 1996), (Yang, et al., 2004). The modified versions of the transport equations are given in equation 3.26 and equation 3.27;

$$\frac{\partial k}{\partial t} + \frac{\partial (U_j k)}{\partial x_j} = \frac{\partial}{\partial x_j}\left(\alpha_k v_{eff}\frac{\partial k}{\partial x_j}\right) + P_k - \varepsilon \tag{3.26}$$

$$\frac{\partial \varepsilon}{\partial t} + \frac{\partial (U_j \varepsilon)}{\partial x_j} = \frac{\partial}{\partial x_j}\left(\alpha_\varepsilon v_{eff}\frac{\partial \varepsilon}{\partial x_j}\right) + \frac{\varepsilon}{k}(c_{\varepsilon 1} P_k - c_{\varepsilon 2} \varepsilon) - \frac{C_\mu\left(\frac{Sk}{\varepsilon}\right)^3\left(1-\frac{\frac{Sk}{\varepsilon}}{4.38}\right)}{1+0.012\left(\frac{Sk}{\varepsilon}\right)^3}\frac{\varepsilon^2}{k} \tag{3.27}$$

where C_μ=0.0845 through a renormalization group method derivation. The effective viscosity v_{eff} for high Reynolds number flows takes the same form as equation 3.21 and

noting that this value of C_μ is very close to the empirically-determined value of 0.09 used in the standard k-ε model. The constants α_k and α_ε are defined as the inverse effective Prandtl number for k and ε which take on a value of 1.393. The term on the far right of equation 3.27 is the largest contributing factor in comparison to equation 3.24 when dealing with swirling flows. When the rate of strain is large such that $\frac{Sk}{\varepsilon}$>4.38 a negative contribution is made to the rate of dissipation equation. There is less destruction of the dissipation which leads to a reduction in the effective viscosity in comparison to the standard k-ε model. This allows a flow which exhibits rapid strain to produce a lower turbulent viscosity through the RNG k-ε model. As a result the RNG variant responds more effectively to any rapid strain and the effects of streamlined curvature hence the improvement in performance noted over the standard k-ε in complex swirling flow geometries.

3.3.2.3 Reynolds Stress Model

The more advanced and computationally expensive turbulence model is the Reynolds Stress Model (RSM) which involves the solution of each of the individual stress components through their own transport equation which results in six additional equations to be solved, one for each of the components of the Reynolds-stress tensor;

$$\frac{\partial}{\partial t}\left(\rho\overline{u_i u_j}\right) + \frac{\partial}{\partial x_k}\left(\rho u_k \overline{u_i u_j}\right) = P_{ij} + F_{ij} + D_{Tij} + \phi_{ij} - \epsilon_{ij} \qquad (3.28)$$

where P_{ij} is the stress production term, F_{ij} is the production by system rotation term, D_{Tij} is the turbulent diffusion term, ϕ_{ij} is the pressure strain term and ϵ_{ij} is the dissipation term. In the derivation of the Reynolds-stress equation there are twenty-two new unknown quantities introduced to close the equations used to model the latter three terms on the right of equation 3.28. The assumptions required to close the aforementioned equations are described below.

The turbulent diffusion term can be modelled by the generalised gradient-diffusion model and simplified to use a scalar turbulent diffusivity;

$$D_{Tij} = \frac{\partial}{\partial x_k}\left(\frac{\mu_t}{\sigma_k}\frac{\partial\overline{u_i u_j}}{\partial x_k}\right) \qquad (3.29)$$

where σ_k=0.82 as derived by Lien and Leschziner (ANSYS, 2009) which is different from the standard k-ε model and the turbulent viscosity can be calculated using equation 3.22.

The classical modelling approach for the pressure-strain term, ϕ_{ij}, as proposed by Gibson and Launder, Fu et al. and Launder (ANSYS, 2009) uses the following decomposition:

$$\phi_{ij} = \phi_{ij,1} + \phi_{ij,2} + \phi_{ij,w} \tag{3.30}$$

where the first term on the right of equation 3.30 is the slow pressure-strain term, also known as the return-to-isotropy term defined as;

$$\phi_{ij,1} = -1.8\rho\frac{\varepsilon}{k}\left[\overline{u_i u_j} - \frac{2}{3}\delta_{ij}k\right] \tag{3.31}$$

The second term in equation 3.30 is the rapid pressure-strain term modelled as;

$$\phi_{ij,2} = -1.6\left[\left(\frac{P_{ij}+F_{ij}+5}{6G_{ij}-C_{ij}}\right) - \frac{2}{3}\delta_{ij}\left(\frac{0.5P_{kk}+5}{3G_{kk}-0.5C_{kk}}\right)\right] \tag{3.32}$$

where P_{ij} and F_{ij} are previously defined, G_{ij} and C_{ij} represent the buoyancy production term, and convection term, second term on the left of equation 3.28, respectively.

The final term in equation 3.30 is the wall reflection term which is responsible for the redistributing the normal stresses near the wall; stresses parallel to the wall are enhanced whilst those that are perpendicular are dampened;

$$\phi_{ij,w} = \begin{aligned}0.5\frac{\varepsilon}{k}\left(\overline{u_k u_m}n_k n_m\delta_{ij} - \frac{3}{2}\overline{u_i u_j}n_j n_k - \frac{3}{2}\overline{u_j u_k}n_i n_k\right)\frac{C_l k^{\frac{3}{2}}}{\varepsilon d}\\ +0.3\left(\phi_{km,2}n_k n_m\delta_{ij} - \frac{3}{2}\phi_{ik,2}n_j n_k - \frac{3}{2}\phi_{jk,2}n_i n_k\right)\frac{C_l k^{\frac{3}{2}}}{\varepsilon d}\end{aligned} \tag{3.33}$$

where n_k is the x_k component of the unit normal to the wall, d is the normal distance to the wall and $C_l = \frac{C_\mu^{\frac{3}{4}}}{\kappa}$, where C_μ=0.09 and κ is the von Karman constant, which in this case is prescribed a value of 0.4187. The dissipation tensor, ϵ_{ij}, is modelled as;

$$\epsilon_{ij} = \frac{2}{3}\delta_{ij}(\rho\varepsilon + Y_M) \tag{3.34}$$

with

$$Y_M = 2\rho\varepsilon\frac{k}{a^2} \tag{3.35}$$

where a denotes the speed of sound. The scalar dissipation rate, ε, is computed with equation 3.24.

3.3.2.4 Large Eddy Simulation

The intermediate stage between using a computational model to represent the turbulent flow and modelling using Direct Numerical Simulation (DNS); which is currently not possible due to the excessive computational memory required; is to separate the small eddies from the large ones. The large eddies are computed directly whereas the small eddies are modelled with a sub grid model; Large Eddy Simulation (LES). By resolving only the large eddies allows the use of a coarser mesh and larger time steps in comparison to DNS.

In comparison to the RANS approaches described in the previous sections LES simulations still require much finer mesh resolutions as well as sufficiently long flow run-times to obtain stable statistics of the flow being modelled. The main difference between LES and the other turbulence models discussed is the averaging approach used to obtain the equations of motion. To divide the eddies in to their respective categories requires a filter function to be employed. The governing equations used in LES modelling are obtained by filtering the time-dependent Navier-Stokes in either Fourier space or physical space. The filters effectively categorise those eddies with scales which are smaller than the grid spacing used in the computations. The equations given in this section are all one dimensional to avoid complexity;

$$\overline{u_i} = \int G(x,x)\, u_i(x)dx \qquad (3.36)$$

where $\overline{u_i}$ and G(x,x') represent the filtered velocity and the applied top-hat filter function respectively. A large filter function exists only when G(x,x') is less than the filter width Δ_i, a length scale, over which the averaging process is performed. This is applied to the Navier-Stokes equations such that flow eddies larger than the filter width are resolved directly whereas those smaller than the prescribed length scale are modelled.

$$G(x_i) = \begin{cases} \frac{1}{\Delta_i} & |x_i| \leq \frac{\Delta_i}{2} \\ 0 & |x_i| > \frac{\Delta_i}{2} \end{cases} \qquad (3.37)$$

The filtered form of the Navier-Stokes equations can then be written as;

$$\frac{\partial \overline{\overline{u_i}}}{\partial t} + \frac{\partial (\overline{u_i u_j})}{\partial x_j} = -\frac{\partial \bar{P}}{\partial x_i} + \frac{1}{Re}\frac{\partial^2 \overline{u_i}}{\partial x_j \partial x_j} - \frac{\partial \tau_{ij}}{\partial x_{ij}} \qquad (3.38)$$

which accounts for the large scale evolution, while the small scales are represented by the sub grid scale stresses which require computational modelling;

$$\tau_{ij} = \overline{u_i u_j} - \overline{u}_i \overline{u}_j \qquad (3.39)$$

Smagorinsky introduced the first sub grid scale (SGS) model in 1963 and is based on the Boussinesq eddy-viscosity approximation (Smagorinsky, 1963). Assuming turbulent equilibrium and isotropic flow the sub grid stresses are set equal to the turbulent viscosity multiplied by the mean strain rate, where the sub grid viscosity is given as;

$$\nu_t = 2(C_S \Delta)^2 \sqrt{2 S_{ij} S_{ij}} \qquad (3.40)$$

where C_S=0.1 representing the Smagorinsky constant. This model is dependent on large scales only and as a result is generally too dissipative. An additional damping function needs to be included in the near wall region to allow the turbulent phenomenon to be captured;

$$f_\mu = 1 - exp\left[-\left(\frac{y^+}{A^+}\right)^3\right] \qquad (3.41)$$

as presented by Launder et al (Launder & Spalding, 1974), with A^+=25 representing the van Driest factor and y+ is the dimensionless wall coordinate;

$$y^+ = \frac{u_\tau y}{\nu} \qquad (3.42)$$

where u_τ is the friction velocity.

3.3.3 3D Flow Simulations

CFD simulations have been carried out to evaluate the ability of the models to predict the single phase gas flow field in a Perspex replica of the helical oil separator. For the purpose of validating the experimental measurements obtained from the LDA apparatus a model was created similar to that shown in Figure 3.6, with the exception of the flanges at the inlet and outlet to the separator; the omission of the oil collection chamber at the base of the unit; and the baffle plate which would normally divide the separated oil from the separation volume was modelled as a circular flat plate defining the base of the unit as shown in Figure 3.7. Due to the non axi-symmetric nature of the geometry the model had to be created in three dimensions. The initial stage in the analysis of the computational code was to treat the flow field as being steady state since this was the most computationally effective in terms of both time and memory. The steady state model

analysis allows for the standard k-ε, RNG k- ε and RSM models to be compared, a suitably refined mesh to be achieved and the choice of discretization scheme to be selected.
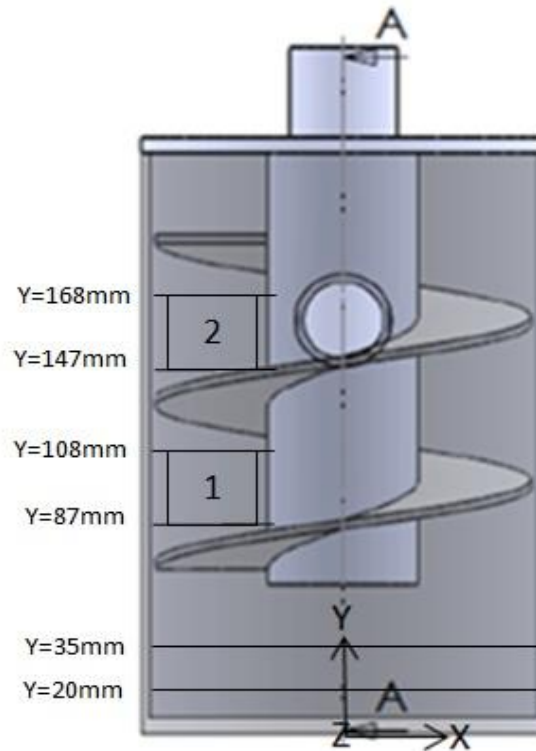
Figure 3.7: CFD Model for LDA Validation

3.3.3.1 Computational Mesh

A sensitivity study on the model of the Perspex separator geometry was carried out with six different mesh sizes to allow a suitably refined mesh to be achieved which is a generally accepted practice for CFD simulations. The geometry was initially created using the Computer Aided Design (CAD) package Solidworks which was then imported into Gambit 2.4.6 where the geometry could be simplified to one complete volume with an inlet and outlet face defining the entry and exit regions for the continuous phase fluid. The generation of each computational grid consisted of quadrilateral cells in the main separation space and tetrahedral cells at the walls. To compare the effects of the mesh sensitivity study the RSM turbulence model will be used and the vertical velocity (X-Y plane) component at Y=20 mm will be used as a point of comparison since if this is captured correctly then all the flow upstream must be accurate also. The QUICK-scheme, of Leonard and Mokhtari (ANSYS, 2009), for approximation of the momentum, turbulent kinetic energy, dissipation rate and Reynolds stress along with PRESTO!, of Pantakar (ANSYS, 2009), for solution of the pressure have been chosen; the justification for which will be covered in

92

the next section. The finite difference equations are solved using the SIMPLE algorithm. All simulations in this work have been performed on a quad core Intel i7-2600K CPU 3.4GHz workstation.

Initial grids constructed contained 242178 mesh elements and the computation was carried out until the degree of convergence was 10^{-3} for all solution variables. The inlet boundary condition was defined as a constant mass flow rate and prescribed the value of 0.00737 kg/s corresponding to an inlet velocity of 8.5 m/s with the outlet defined as a pressure outlet at 0 Pa gauge. For the RSM model the turbulence specification method was chosen to be defined by the turbulence intensity and hydraulic diameter which for the inlet was 4.7% and 0.03 m respectively; for the outlet the prescribed values were 4.8% and 0.034 m respectively. The turbulence intensity is defined as $0.16(Re_{IN/OUT})^{-1/8}$ where $Re_{IN/OUT}$ is the Reynolds number at the appropriate boundary surface. The mesh was increasingly refined to 375840, 479734, 557519 and finally 1278174 cells; Figure 3.8 shows the results of the mesh sensitivity study. The mesh containing 557519 cells was found to produce a solution which was to a sufficient level of accuracy whilst being able to be solved within a CPU time of 160 hours which was acceptable. Therefore it is this mesh which will be used for the remainder of this section. Further mesh refinement to 1278174 cells showed no real benefit for the extra CPU time which took the total CPU time up to 350 hours. A cross-sectional view of the 557519 cell mesh directly through the centreline of the geometry is shown in Figure 3.9.
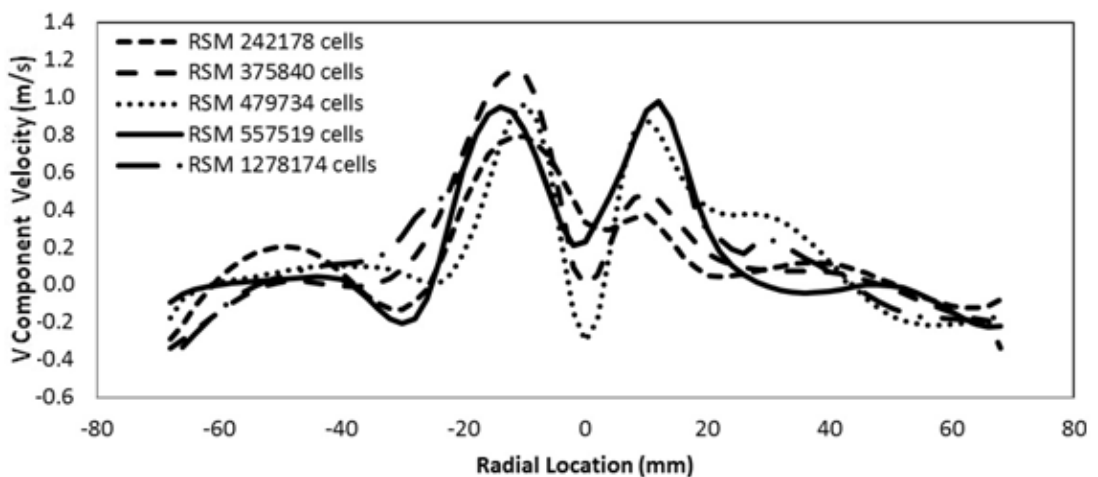
Figure 3.8: Mesh Sensitivity Study
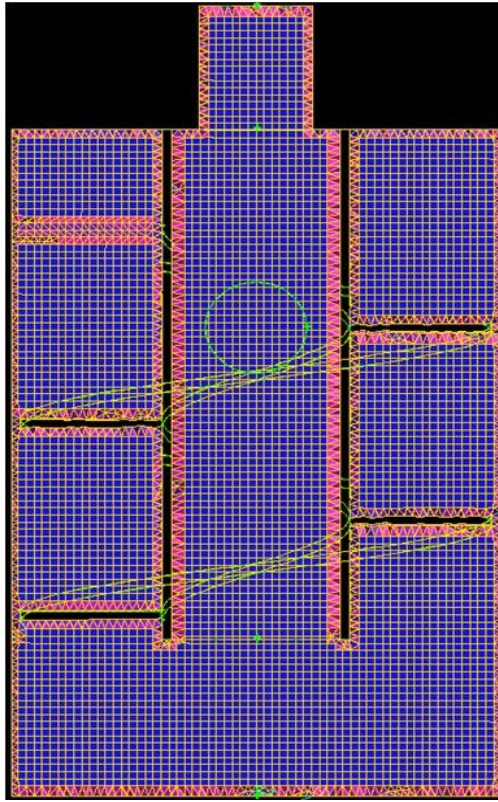
Figure 3.9: Cross-sectional View of Mesh Through Centreline of Separator-557519 Cell Mesh

3.3.3.2 Convection and Diffusion Discretization Methods

The governing equations of continuity, momentum and the appropriate equations defining the turbulence model are solved by focusing on the field values at specific locations in the geometry known as grid points. The finite-volume method employed requires the entire domain be divided into a number of small regions known as control volumes or cells. By adopting the finite-volume method the general transport equations can be converted to algebraic equations. By integrating the algebraic equations over each of the individual cells in the domain results in a discrete equation describing the conservation laws on a control-volume basis. For the general transport equation;

$$\frac{\partial \rho \phi}{\partial t} + \frac{\partial \rho U_j \phi}{\partial X_j} = \frac{\partial}{\partial X_j}\left(\Gamma \frac{\partial \phi}{\partial X_j}\right) + S \qquad (3.43)$$

where ϕ is a scalar quantity, Γ is a diffusion coefficient and S a source. The discretized form of equation 3.43 contains the unknown variable ϕ at the centre of the cell as well as unknown values at the neighbouring cells. This equation is non-linear in most cases with respect to these variables. The linearised form is given as;

$$a_p \phi = \sum_{nb} a_{nb} \phi_{nb} + b \qquad (3.44)$$

where a_p is the centre coefficient, a_{nb} are the influence coefficients of the neighbouring cells, and b is the contribution of the constant part of the source term. The number of neighbours for each cell depends on the topology of the mesh, but is typically equal to the number of faces enclosing the cell with boundary cells being the exception. This results in a set of algebraic equations with a sparse coefficient matrix. The scalar equations are solved for this linear system using a point implicit, Gauss-Seidel, linear equation solver in conjunction with an algebraic multigrid method. Discrete values of the scalar quantity φ are stored at the cell however the face values are required to solve the convection term in equation 3.43 therefore require an interpolation to be carried out using the value at the cell centre. This is achieved using an upwind scheme which derives the cell face values based on quantities of the upstream cell relative to the direction of the normal velocity v_n.

There are a number of upwind schemes available; the simplest being the first-order upwind scheme where the face value is set equal to the cell centre value of the upstream cell. This scheme assumes that the cell-centre value for any flow variable represents a cell-average value and holds true throughout the entire cell. When a higher level of accuracy is required the second-order upwind scheme can be applied which computes the cell faces quantities using a multidimensional linear reconstruction approach. In doing so a Taylor series expansion of the cell-centred solution about the cell-centroid is carried out. The calculation of the cell face variable is determined through;

$$\phi_{f,SOU} = \phi + \nabla\phi \cdot \vec{r} \qquad (3.45)$$

where φ and $\nabla\phi$ are the cell-centred value and its gradient in the upstream cell and $\vec{r}$ is the displacement vector from the upstream cell centroid to the face centroid. This formulation requires the calculation of the gradient $\nabla\phi$ in each cell. The determination of the gradient of the scalar φ at the cell centre is computed using the Green-Gauss theorem which in the discrete form is;

$$(\nabla\phi)_{centre} = \frac{1}{v} \sum \overline{\phi_f} \vec{A_f} \qquad (3.46)$$

where $\overline{\phi_f}$ is the value of φ at the cell face centroid and the summation is over all the faces enclosing the cell and v is the number of faces surrounding the cell. A node-based gradient

evaluation is used to determine $\overline{\phi_f}$, which is the arithmetic average of the nodal values of φ on the face given by;

$$\overline{\phi_f} = \frac{1}{N_f} \sum_n^{N_f} \overline{\phi_n}$$

(3.47)

where N_f is the number of nodes on the face. The nodal values $\overline{\phi_n}$ are constructed from the weighted average of the cell values surrounding the nodes. The scheme rebuilds the exact values of the linear function at a node surrounding cell-centered values on arbitrary unstructured meshes by solving a constrained minimization problem and preserves a second-order spatial accuracy (ANSYS, 2009).

The QUICK discretization scheme is available to use with quadrilateral and hexahedral meshes where unique upstream and downstream faces and cells are present. This scheme is based on a weighted average of second-order upwind and central interpolations of the flow variable. For the one dimensional control volume shown Figure 3.10 in the face e can be written as;

$$\phi_e = \theta \left[\frac{S_d}{S_c+S_d} \phi_P + \frac{S_c}{S_c+S_d} \phi_E \right] + (1-\theta) \left[\frac{S_u+2S_c}{S_u+S_c} \phi_P - \frac{S_c}{S_u+S_c} \phi_W \right]$$

(3.48)
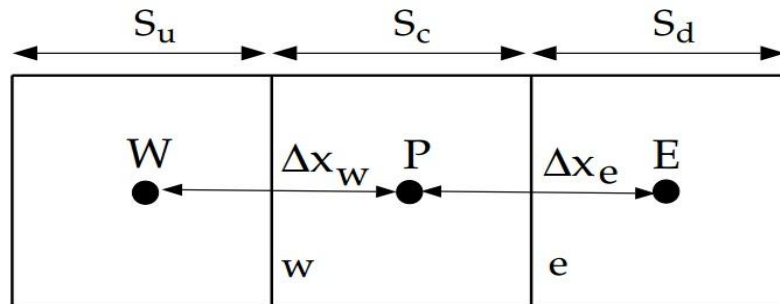
Figure 3.10: One-Dimensional Control Volume (ANSYS, 2009)

when θ=1 in equation 3.48 the result is a central second-order interpolation while θ=0 the result is a second-order upwind value. The traditional QUICK scheme is obtained by letting $\theta=\frac{1}{8}$. When this scheme is implemented a solution-dependent value of θ is chosen to avoid new solutions to be computed. This scheme is more accurate on structured meshes where the mesh is in line with the flow direction. When the mesh is unstructured the second-order upwind scheme is implemented.

3.3.3.3 Pressure Discretization Methods

The determination of the pressure field and face mass fluxes are also required as part of the computation. Therefore an interpolation scheme is required to compute the face values of pressure from the cell values. The Standard method in Fluent interpolates the pressure values at the faces using momentum equation coefficients;

$$P_f = \frac{\dfrac{P_{c0}}{a_{p,c0}} + \dfrac{P_{c1}}{a_{p,c1}}}{\dfrac{1}{a_{p,c0}} + \dfrac{1}{a_{p,c1}}} \tag{3.49}$$

where c0 and c1 are two cells with a common face, a_p is the cell centre coefficient and P is the pressure. This scheme is effective provided the pressure variation between cell centres is smooth; however when there are steep source term gradients between cells, particularly associated with strongly swirling flows, this scheme fails unless the mesh is sufficiently refined in such regions (ANSYS, 2009). The PRESTO! scheme uses the discrete continuity balance for a staggered control volume about the face to determine the face pressure. This approach is similar to a staggered-grid scheme used with structured meshes.

Using the grid with 557519 mesh cells and the RSM model the first-order upwind with Standard pressure interpolation; second-order upwind and QUICK discretization with PRESTO! pressure interpolation schemes; are compared with the LDA data at y=20 mm above the base of the separator as shown in Figure 3.11.
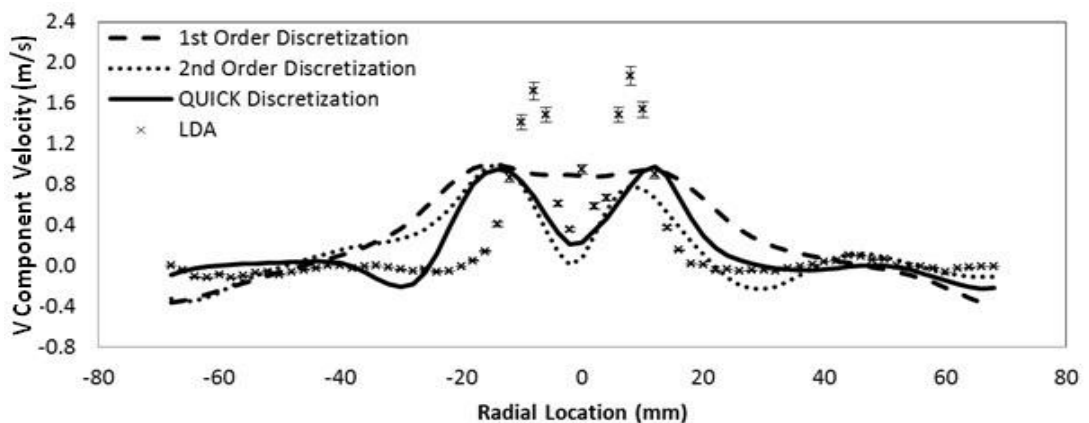
Figure 3.11: Discretization Scheme Study

From the discretization study it is apparent that the choice of numerical scheme is significant to allow the model to capture the complex flow field obtained from the

experimental measurements. Without having the experimental data to allow a comparison to be made the first order scheme looks plausible; which is one of the dangers associated with CFD (Hoffmann & Stein, 2008). The reason for the discrepancy between the first order scheme and those of higher order is that the former are susceptible to numerical diffusion, which is similar to the effect of viscosity in the solution of the Navier-Stokes equations, but in this case it is generated purely due to numerical inaccuracy. The effect of different discretization schemes in predicting the flow in a cyclone separator was carried out and the results were found to be similar to the investigation carried out by Phyfe (Phyfe, 1999). The effect of numerical diffusion is particularly significant in flows with a strong cross-grid component such as the helical separator.

3.3.4 Steady State Turbulence Model Comparison

The velocity vectors within the Perspex helical separator geometry were used to assess the performance of the turbulence models available in Fluent 6.3.26 as described in section 3.3.2 for a steady state analysis. This involved an assessment of the standard k-ε model, the RNG k-ε, with the swirl dominated flow option activated, and the RSM model. The predictions of these three turbulence models depicting two components of the velocity below the entrance to the centre tube, 20 mm and 35 mm, as shown in Figure 3.7, from the base of the unit; are shown in Figure 3.12 to Figure 3.15 and are compared with the results obtained from the experimental measurements. The CPU time to achieve a converged steady state solution was approximately 48 hours.
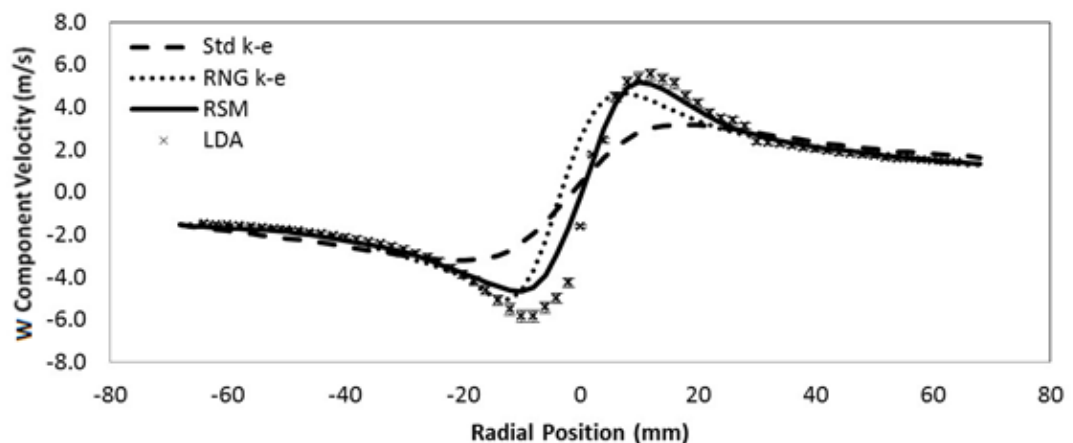
Figure 3.12: Steady State Turbulence Model Comparison at Y=20 mm from the Base of the Perspex Separator-W Component (X-Z plane)
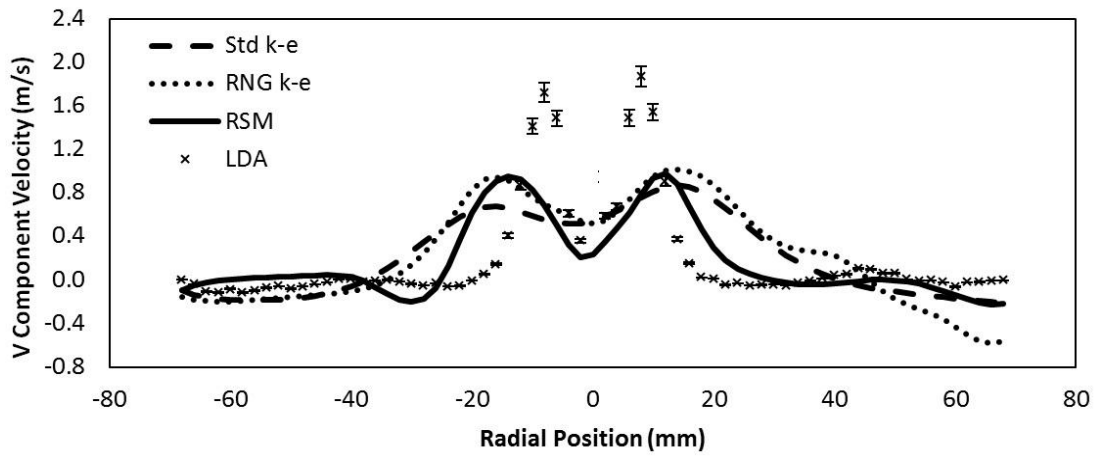
Figure 3.13: Steady State Turbulence Model Comparison at Y=20 mm from the Base of the Perspex Separator-V Component (X-Y plane)
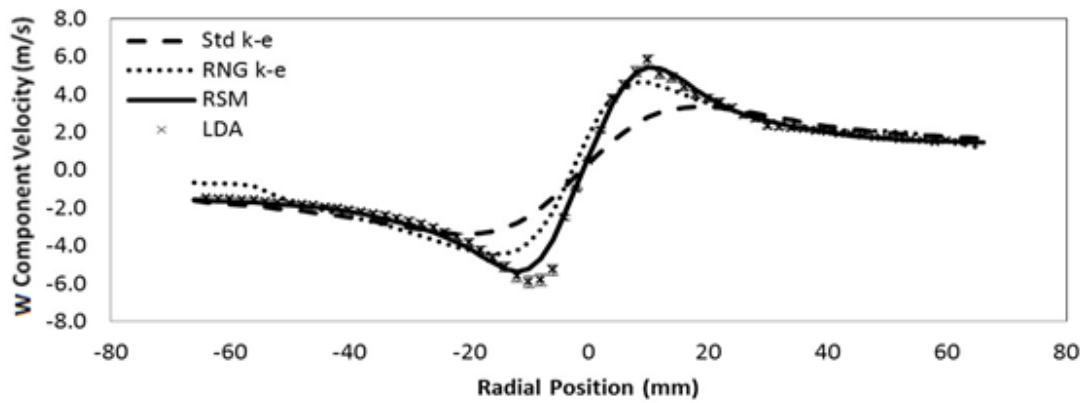
Figure 3.14: Steady State Turbulence Model Comparison at Y=35 mm from the Base of the Perspex Separator-W Component (X-Z plane)
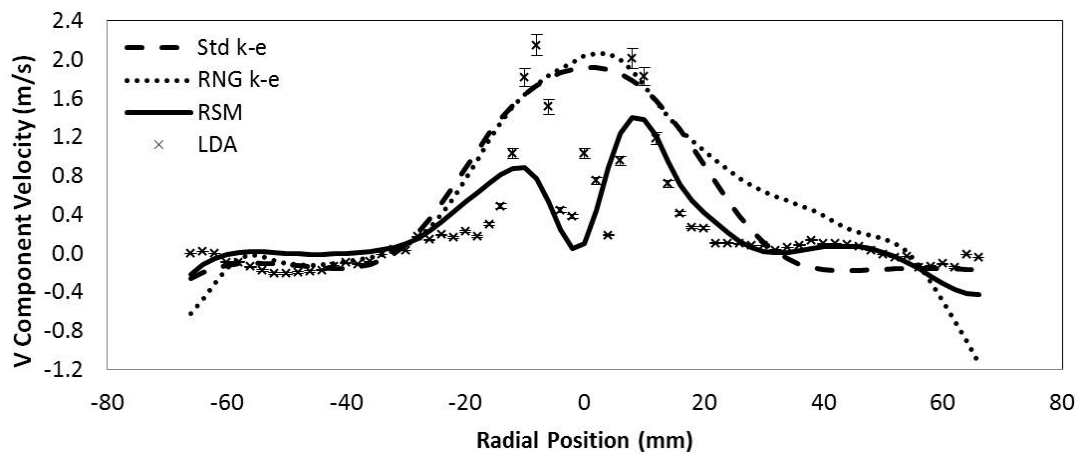
Figure 3.15: Steady State Turbulence Model Comparison at Y=35 mm from the Base of the Perspex Separator-V Component (X-Y plane)

The standard k-ε model performs poorly in predicting both components of the velocity measured; this is due to its inability to capture the high shear within the flow and instead predicts a solid-body rotation (Hogg & Leschziner, 1989). This is due to the k-ε model over predicting the extent of the diffusion in the radial direction which accounts for the inability to pick up the dip in vertical velocity at the centreline of the separator. The LDA data in Figure 3.12 to Figure 3.15 supports the phenomenon of a forced inner vortex and a free outer vortex which is typically found in cylindrical type cyclonic separators (Hoffmann & Stein, 2008).

A noticeable improvement was observed when the RNG-k-ε with the swirl dominated flow option activated as this allowed for the effects of rotation in the flow field to be included in the calculation of the turbulent viscosity (Griffiths & Boysan, 1996). This was most noticeable in the prediction of the horizontal velocity component, but still failed to accurately produce a profile which closely resembled the results from the experimental data for the vertical velocity component. The extent of this is most significant in Figure 3.15 which is directly under the entrance to the centre tube.

The prediction of the vertical velocity profile by the RSM model can be seen to produce results closer to that obtained from the LDA measurements in comparison to the other two turbulence models which are based on the eddy-viscosity concept. The RSM model predicts the velocity in the outer region of the separator, the free vortex region, with a much higher degree of accuracy than the standard k-ε and the RNG-k-ε models with the results being in line with the LDA data. Within the centre tube region the LDA captures the inverted W-shaped velocity profile, which is associated with classic cyclone separator geometries; the RSM model is able to predict this profile. The radial locations of the velocity maxima and the magnitudes of these values are seen to have discrepancies with the LDA data peaking much closer to the centreline with a velocity magnitude almost double that of the RSM which displays less abrupt peaks in the axial velocity. However it should also be noted that lack of asymmetry given by the LDA data in Figure 3.15 can be accounted for by the extent of the time averaging of the individual location measurements which is as a result of the precessing vortex core.

3.3.5 Unsteady Solver

Slack et al. reported that the flow field within a centrifugal type separator cannot be accurately modelled using a steady state solver (Slack, et al., 2000). This may be seen in the

cycling of the residuals which indicates that the flow is transient in nature. Consequently the flow was simulated using the unsteady solver and applying adaptive time stepping as the solution progressed until a total simulation time of 20 seconds was obtained. This allowed for a meaningful prediction of the flow to be derived since the average residence time within the separation space was smaller than an order of magnitude of the total simulated time. Using the total simulation time of 20 seconds allowed for any regions where flow recirculation may occur to be accounted for. By adopting the transient solver a significant improvement in the definition of the velocity and pressure field profiles were obtained.

As with the steady state solution the same boundary conditions were applied with the PRESTO! and QUICK numerical discretization schemes. The SIMPLE algorithm, which handles the pressure-velocity coupling, does not satisfy the momentum balance for new velocities and corresponding fluxes when the pressure-correction equation is solved, which results in the calculation having to be repeated until the balance is satisfied. Instead the PISO algorithm is used which performs two additional corrections, neighbour and skewness correction, to improve the efficiency of the calculation. Although the PISO algorithm takes slightly more CPU time per solver iteration the number of iterations required for convergence can be drastically reduced, particularly for transient solutions. The steady state results were used as the initial conditions for the transient solution which required a further 120 hours of computational time to achieve the 20 seconds of real flow time.

The temporal discretization used for the unsteady solutions was a second order implicit scheme which integrates every term in the transport equations over a time step Δt. The evolution of a variable, ϕ, over a period of time is;

$$\frac{\partial \phi}{\partial t} = F(\phi) \tag{3.50}$$

where the right hand side is any spatial discretization. The second-order temporal discretization is then given by;

$$F(\phi) = \frac{3\phi^{n+1} - 4\phi^n + \phi^{n-1}}{2\Delta t} \tag{3.51}$$

where n+1 is the value of ϕ at the next time level $t+\Delta t$, n is the value at the current time and n-1 is the value at the previous time level $t-\Delta t$.

3.3.6 Comparison between Steady State and Transient Models

From the results of the turbulence model for the steady state simulations the RSM model was then run transiently since it produced the best predictions of the flow velocities when compared with the LDA data. Again the data was compared with the LDA and the steady state simulations with the RSM model at axial locations of 20 mm and 35 mm from the base of the separator. All unsteady CFD data presented has been time averaged over the duration of the simulation to allow an accurate comparison with the time averaged LDA values.
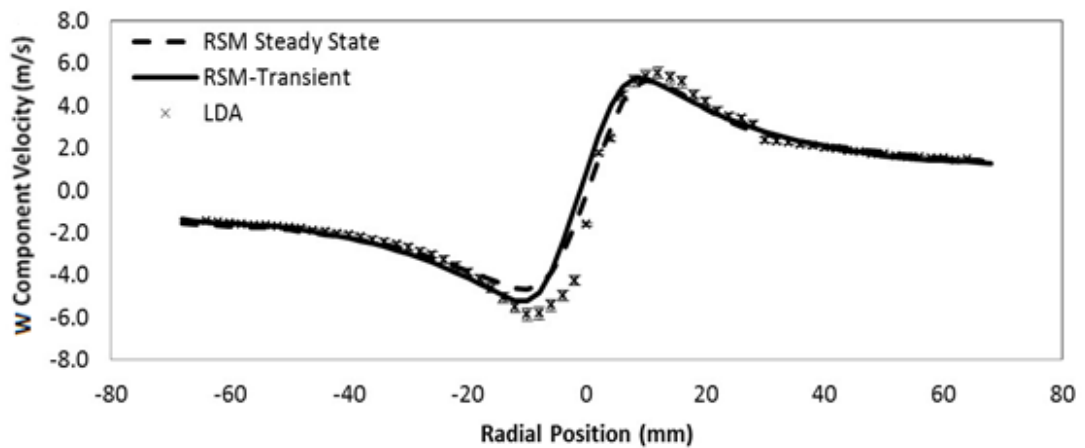
Figure 3.16: Steady State and Transient Simulation Comparison at Y=20 mm from the Base of the Separator-W Component (X-Z plane)
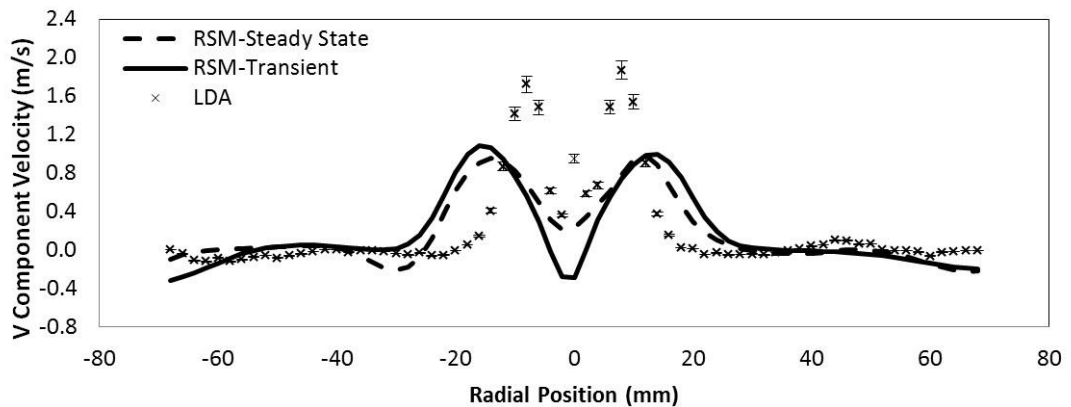
Figure 3.17: Steady State and Transient Simulation Comparison at Y=20 mm from the Base of the Separator-V Component (X-Y plane)
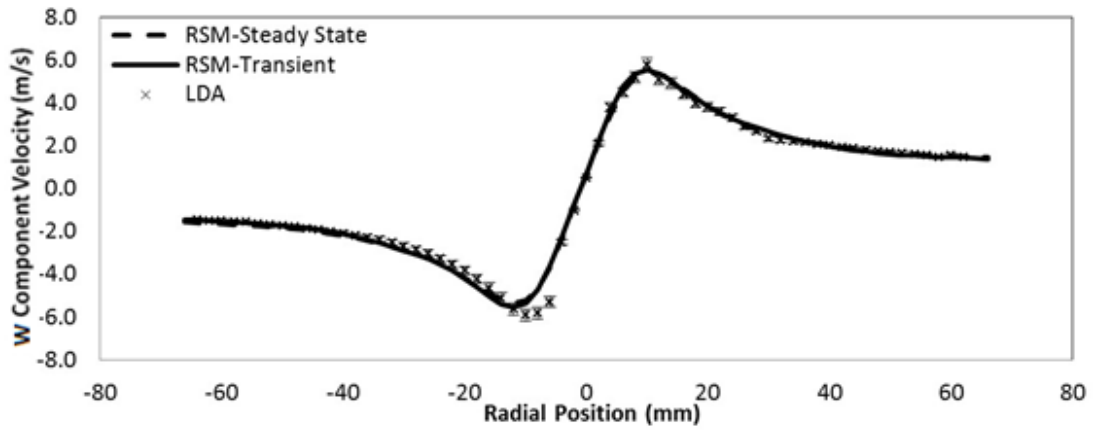
Figure 3.18: Steady State and Transient Simulation Comparison at Y=35 mm from the Base of the Separator-W Component (X-Z plane)
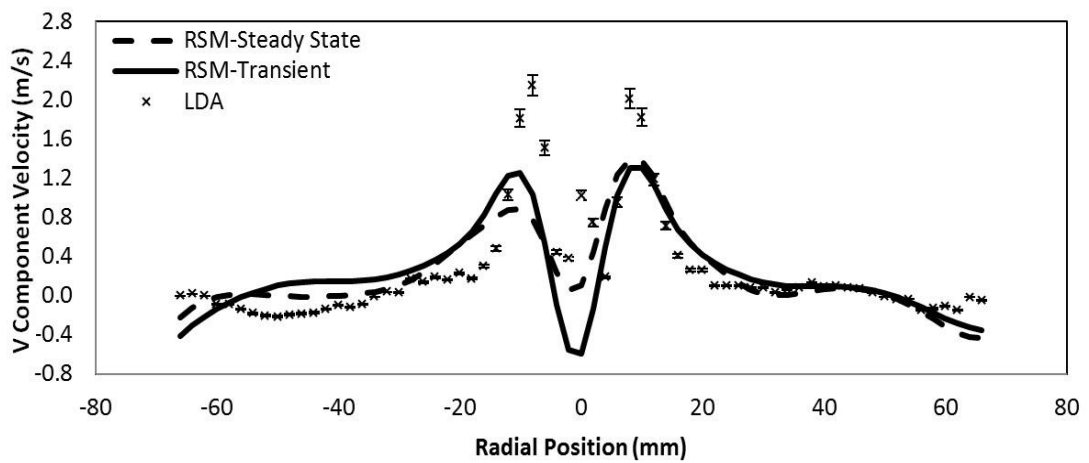
Figure 3.19: Steady State and Transient Simulation Comparison at Y=35 mm from the Base of the Separator-V Component (X-Y plane)

The effect of the precessing vortex core (PVC) which oscillates about the centreline causing the velocity profile under the centre tube to change with time can be seen from Figure 3.17 and Figure 3.19 where the steady state profile displays a larger velocity in the positive radial direction in comparison to the same location in the negative radial direction whereas the results from the transient analysis average out the effects of the PVC oscillations and result in a velocity profile which corresponds qualitatively with the LDA data. The horizontal velocity component shown in Figure 3.16 and Figure 3.18 exhibits no change in its profile as a result of the use of a transient solver.

3.3.7 Advanced Turbulence Model Comparison

The LES model is a transient solver so was compared only with the results of the transient simulations of the turbulence models. The discretization schemes used for the solution of

103

the LES equations were PRESTO! for pressure, bounded central differencing for momentum and SIMPLE pressure-velocity coupling. The momentum discretization scheme used in this case is second-order-accurate and is only available for LES simulations but provides improved accuracy. The scheme calculates the face value for a variable ϕ_f as;

$$\phi_{f,CD} = \frac{1}{2}(\phi_0 + \phi_1) + \frac{1}{2}(\nabla\phi_0 \cdot \overrightarrow{r_0} + \nabla\phi_1 \cdot \overrightarrow{r_1}) \qquad (3.52)$$

where the indices 0 and 1 refer to the cells that share face f, $\nabla\phi_{r,0}$ and $\nabla\phi_{r,1}$ are the reconstructed gradients at cells 0 and 1 respectively and $\vec{r}$ is the vector directed from the cell centroid toward the face centroid. This numerical scheme is the ideal choice for LES simulations because it has low numerical diffusion but is notorious for displaying unphysical oscillations in the solutions which is exaggerated by the low sub-grid scale turbulent diffusivity. The bounded scheme is a composite of the normalized variable diagram (NVD) approach and the convection boundedness criterion (CBC) that consists of pure central differencing (ANSYS, 2009).

The LES model was solved with a constant time step of 1x10^{-4} seconds, with the results being averaged over a real time period of 7 seconds as this was found to provide the most accurate comparison with experimental data given that a time step of 1x10^{-3} seconds did not produce such accurate data. To model transient phenomenon accurately a time step of at least one order of magnitude smaller than the smallest time constant in the system is suggested (ANSYS, 2009). For a cyclone separator, the average residence time (separator volume/gas volume flowrate) is widely used to estimate the time step (Elsayed & Lacor, 2013). For the Perspex separator used in this investigation the average residence time is 0.69 seconds therefore the time step used is just a small fraction of the average residence time. This was confirmed by the simulation reaching a time independent solution after approximately 160 hours of computation time. Since the transient RSM data has so far predicted the profiles within the separator closest to that obtained from the experimental data it will be used to compare with the LES results. A mesh refinement study was also carried out for the LES model where a computational domain containing 1.3 million cells was solved using a time step of 1x10^{-4} seconds and required three weeks to simulate the 7 second real time period. The results obtained show very little differences in the velocity profile plots in comparison to the 557519 cell grid indicating that the increased

computational effort was not justified therefore the data for the 557519 cell model will be presented for comparison with the RSM model and LDA data.
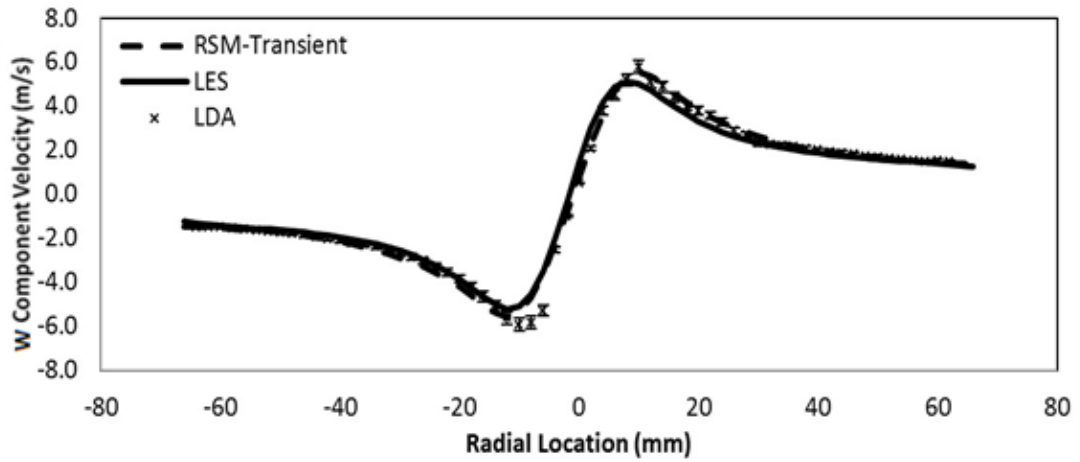
Figure 3.20: LES Turbulence Model Comparison at Y=20 mm from the Base of the Separator-W Component (X-Z plane)
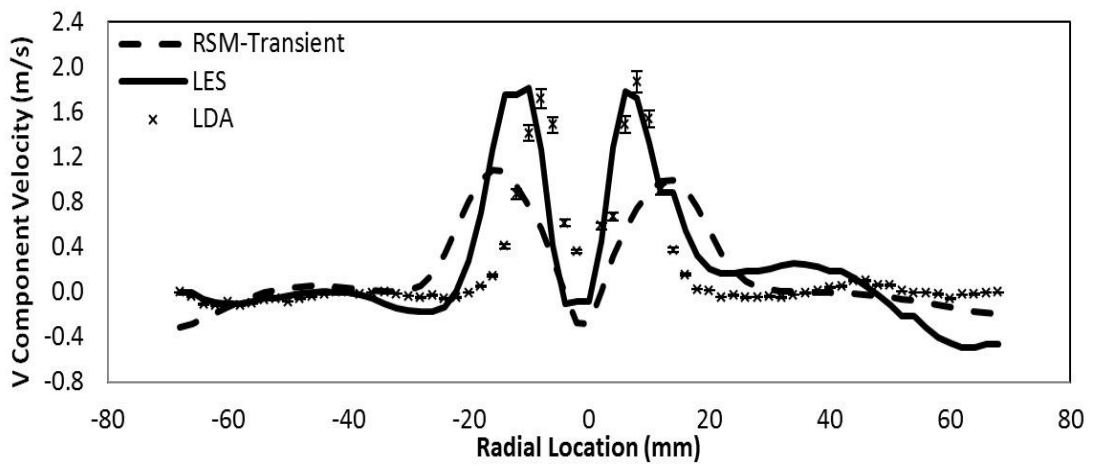
Figure 3.21: LES Turbulence Model Comparison at Y=20 mm from the Base of the Separator-V Component (X-Y plane)
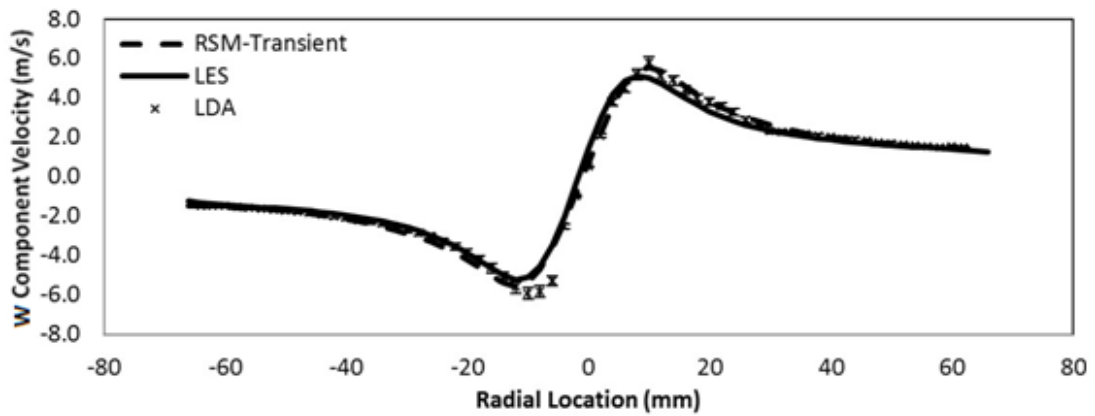
Figure 3.22: LES Turbulence Model Comparison at Y=35 mm from the Base of the Separator-W Component (X-Z plane)
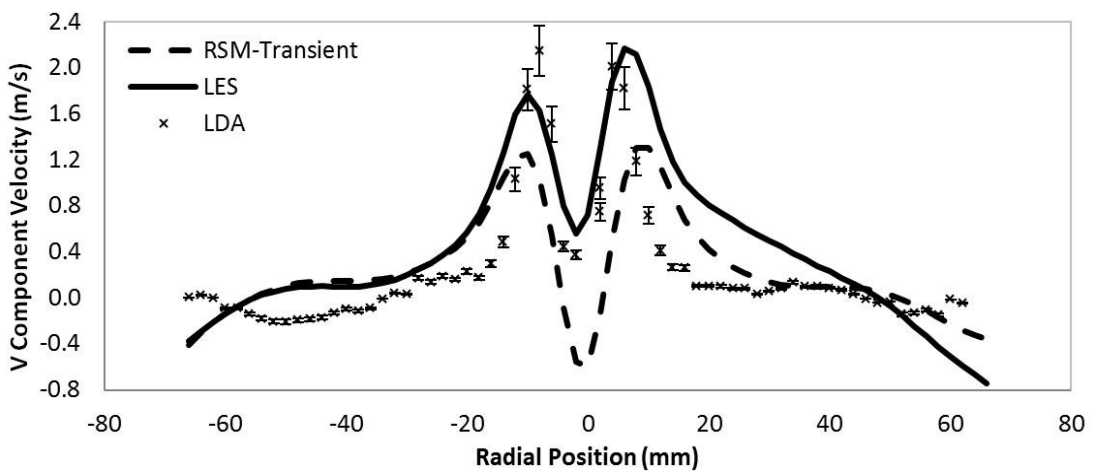
Figure 3.23: LES Turbulence Model Comparison at Y=35 mm from the Base of the Separator-V Component (X-Y plane)

Figure 3.20 to Figure 3.23 show that the advanced LES model compares more favourably with the LDA data particularly in picking up the magnitude of the two velocity peaks in the X-Y plane which the other models failed to achieve. These results would suggest that the LES model should be used to computationally simulate the flow field in the helical separator. However the bulk of the separation happens within the helical path itself therefore, in order to examine the model in more detail, further data was compared in radial traverses at 4 axial locations within the main separation space at Y=87, 108, 147 and 168 mm.
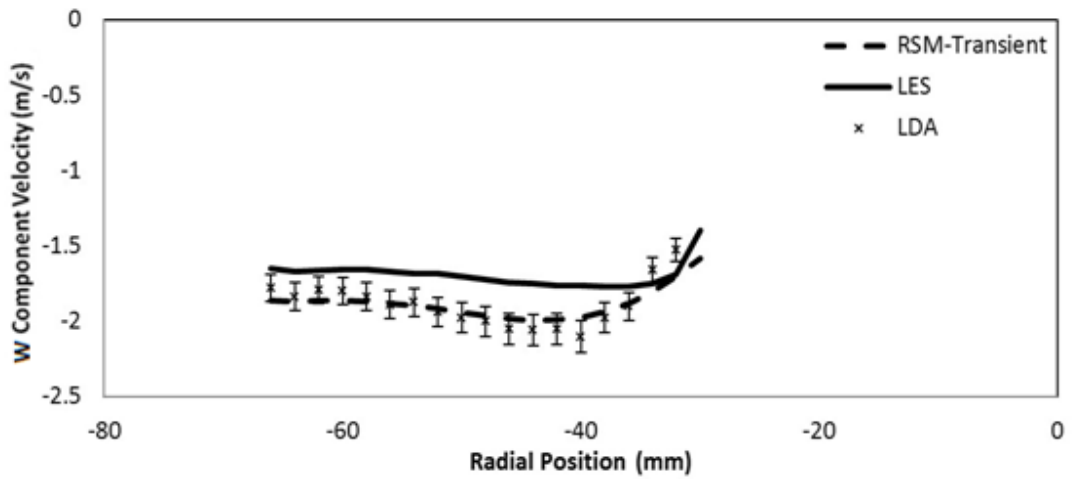
Figure 3.24: Comparison at Y=87 mm from the Base of the Separator-W Component (X-Z plane)
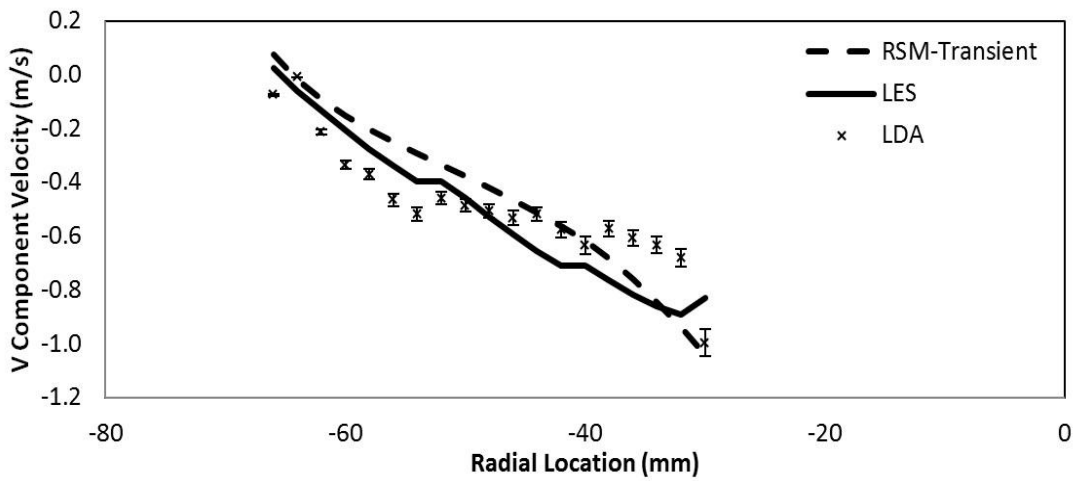
Figure 3.25: Comparison at Y=87 mm from the Base of the Separator-V Component (X-Y plane)
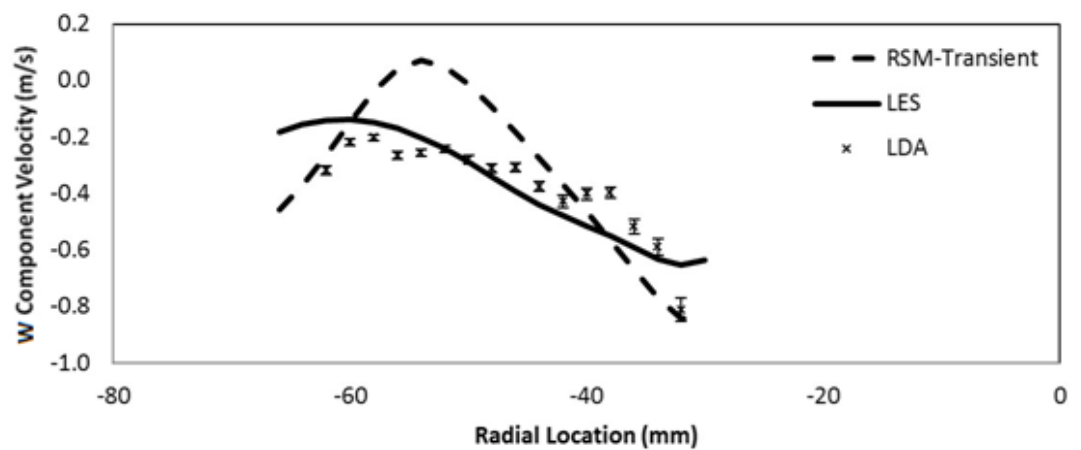
Figure 3.26: Comparison at Y=108 mm from the Base of the Separator-W Component (X-Z plane)
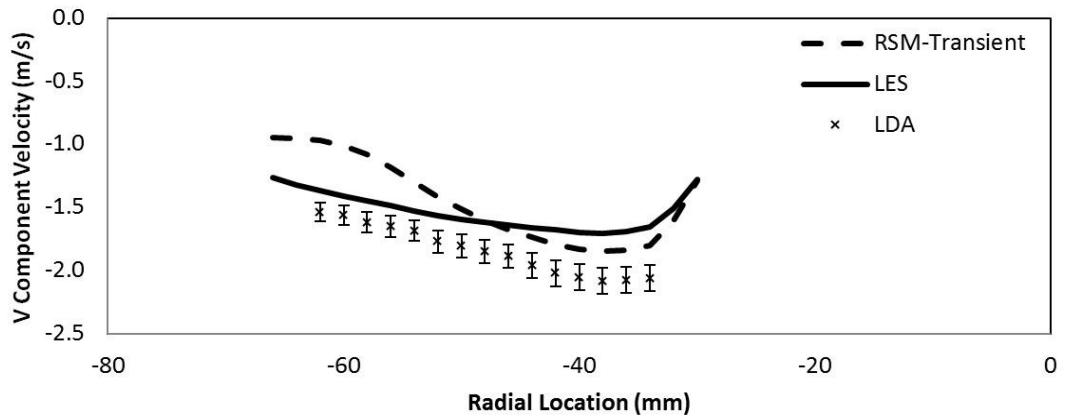
Figure 3.27: Comparison at Y=108 mm from the Base of the Separator-V Component (X-Y plane)
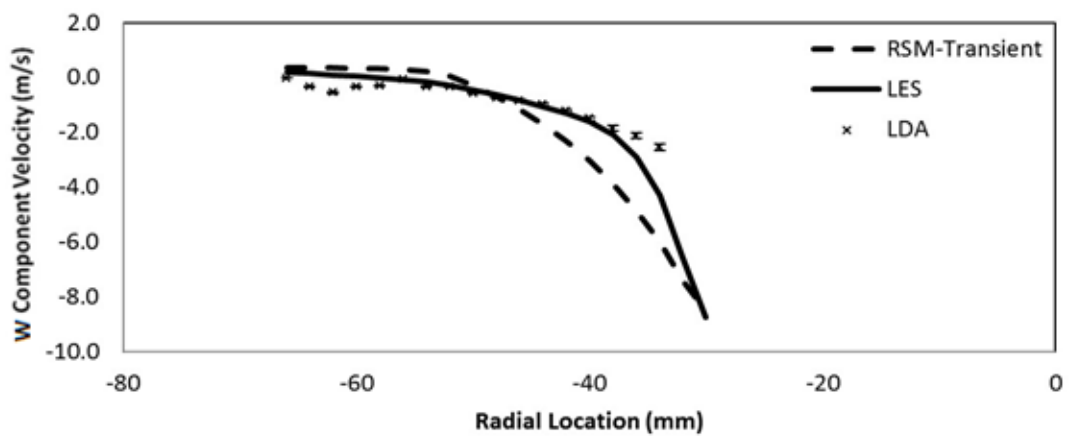
Figure 3.28: Comparison at Y=147 mm from the Base of the Separator-W Component (X-Z plane)
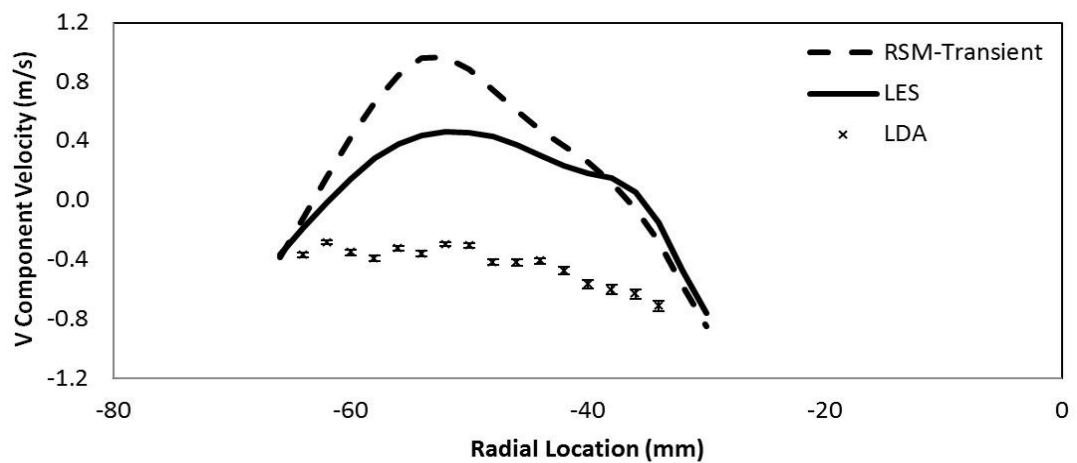
Figure 3.29: Comparison at Y=147 mm from the Base of the Separator-V Component (X-Y plane)
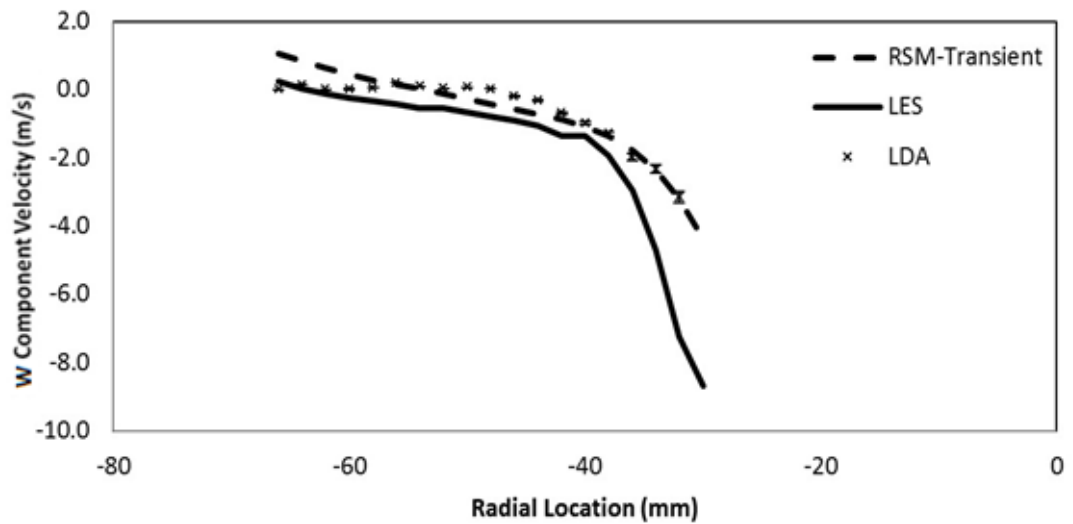
Figure 3.30: Comparison at Y=168 mm from the Base of the Separator-W Component (X-Z plane)
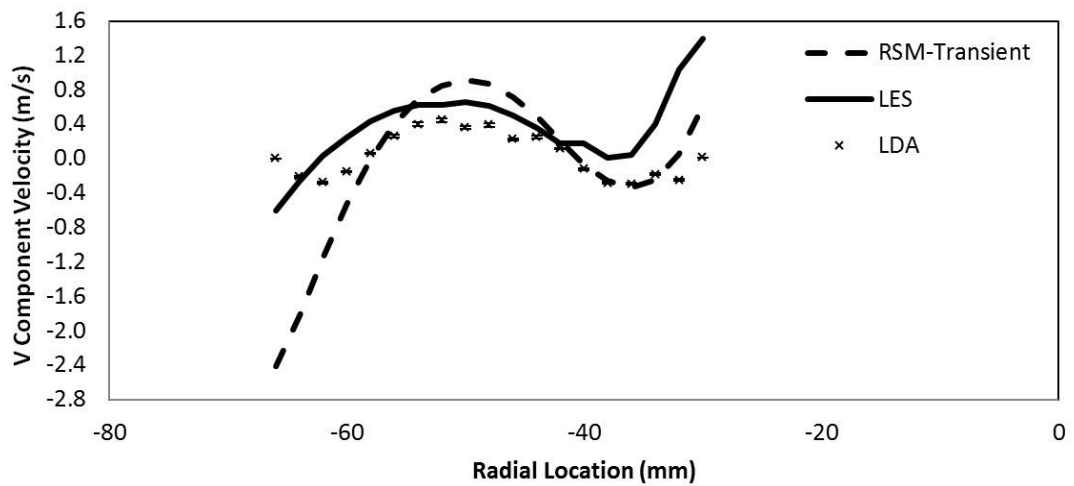
Figure 3.31: Comparison at Y=168 mm from the Base of the Separator-V Component (X-Y plane)

It can be seen for the data displayed in Figure 3.24 to Figure 3.31 that there are some instances where the transient RSM model replicates the experimental data better than the LES, but overall the results from the LES simulations are more consistent with the LDA data throughout the entire geometry. Using the LES model velocity contour plots are displayed in Figure 3.32 and Figure 3.33 showing a comparison between the two components of velocity measured versus those predicted through the simulation.
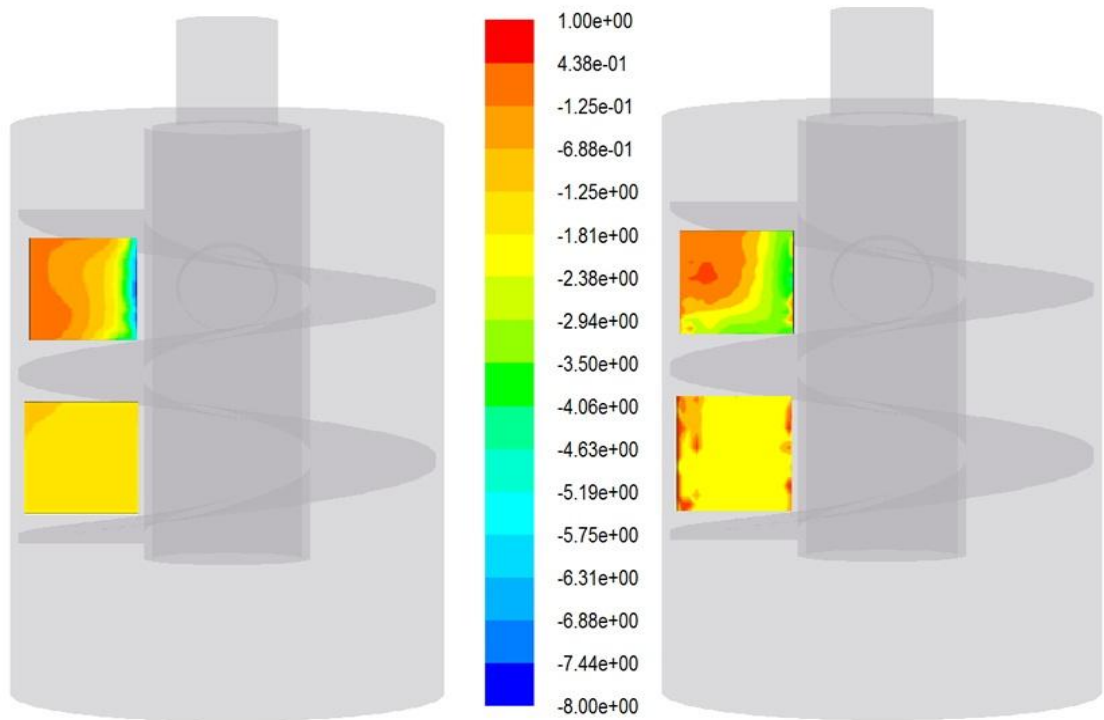
Figure 3.32: Comparison of W Component Velocity (X-Z plane) Left Image: CFD-LES; Right Image: LDA
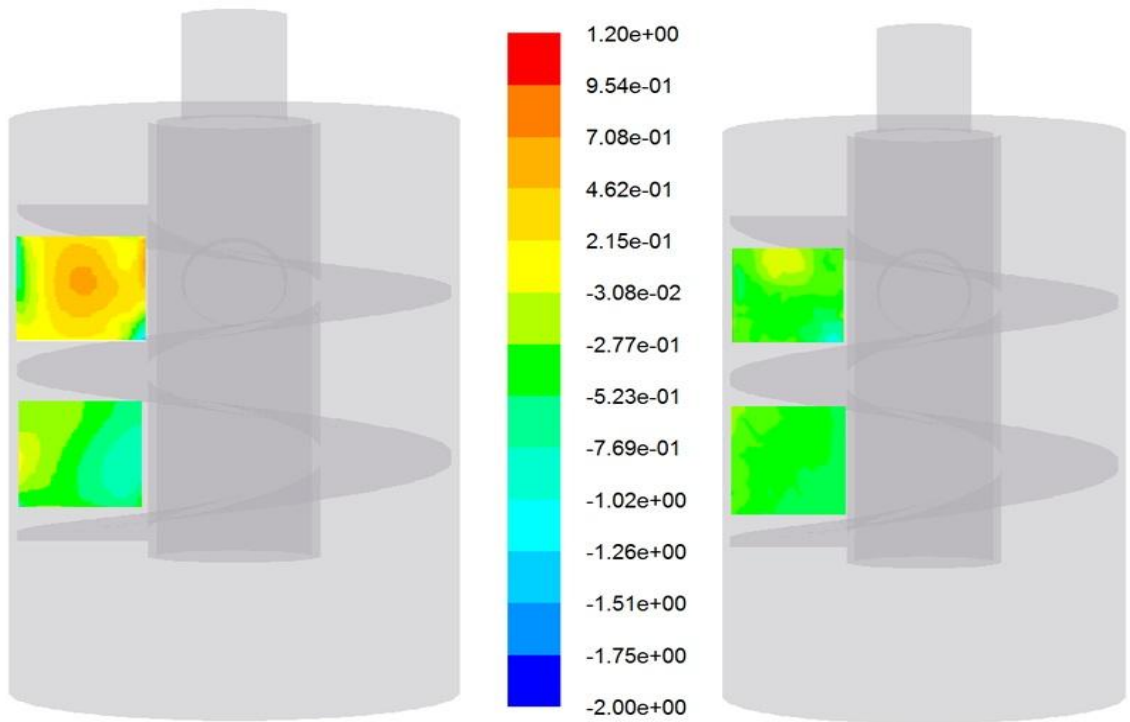
Figure 3.33: Comparison of V Component Velocity (X-Y plane) Left Image: CFD-LES; Right Image: LDA

It can be seen from Figure 3.32 that the horizontal velocity component measured experimentally using the LDA system versus that obtained from the simulation are qualitatively and quantitatively in agreement. This supports the data shown graphically for the W component velocity within the helix region in Figure 3.24-3.31. However in Figure 3.33 it is clear to see that there is a degree of discrepancy between the LDA and CFD contour plots particularly in the upper region of the helix immediately to the left of the inlet. The plots indicate a variation in the direction of the flow at this location with the LDA showing a positive flow region at the upper section of the contour plot whereas the CFD shows this to be in the centre of the flow region being captured. This flow structure indicates the presence of a recirculation zone which is further highlighted in Figure 3.36. The size of this flow structure can be seen to be of the order of a few millimetres therefore the discrepancies which are seen in the V component contour plots can be explained due to the marginal discrepancies associated with the curvature of the geometry and the size of the measurement volume being of the same order as the flow structure itself. The implications of this discrepancy will lead to the droplets travelling in the positive y direction, V component, as oppose to the negative y direction. However since the dominant velocity component is in the z direction, W component, then the overall contribution of this error to the separation efficiency will not be significant since the prediction in the lower region of the helix is found to be more in line with the experimental data.

3.3.8 Velocity Vector Planes

Further information on the flow field within the separator can be obtained by examining the velocity vectors in the horizontal and vertical planes in the geometry. By examining the velocity vector plots at key regions within the main separation volume of the unit can produce insight into the physical processes which result in the dispersed phase droplets becoming separated. Figure 3.34 shows the velocity vectors in a horizontal plane at Y=155 mm from the base of the separator which corresponds to the location defining the midpoint of the inlet.
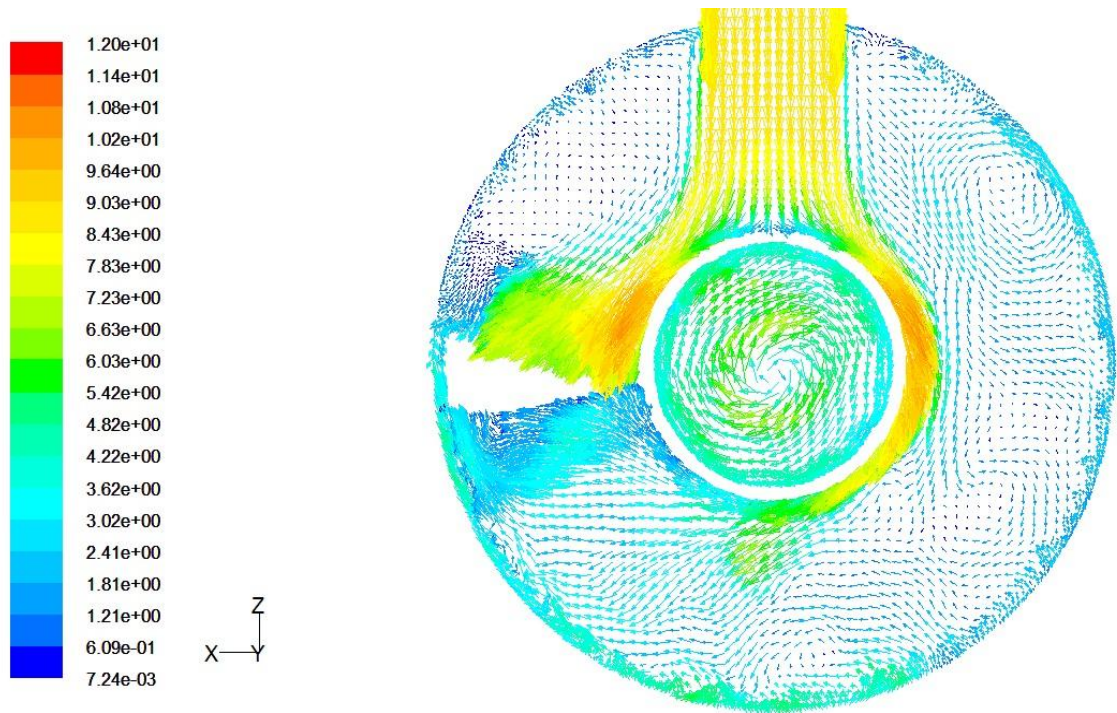
Figure 3.34: Velocity Vector Plot at Y=155 mm-LES (Vectors Coloured by Velocity Magnitude in (m/s))

From Figure 3.34 it is clear to see that on entry to the separator through the radial inlet nozzle the flow has a high inertia, denoted by the amber coloured arrows. The flow then impacts on the centre tube reducing the inertia which would result in a droplet impingement process. After impact the gas is either directed clockwise round the centre tube to the bottom of the separator or anti-clockwise round the centre tube to the upper region of the unit where there is a recirculation zone above the inlet jet, which will be discussed later. Apart from the region of flow which follows the streamlines of the centre tube there is no significant indication of the formation of a centrifugal flow field at this level. Immediately to the left and right of the inlet jet, close to the cylindrical wall of the separator, two recirculation zones can be seen to exist which could result in possible deposition and re-entrainment of droplets on the wall. At the rear side of the centre tube from the inlet the flow can be seen to become separated from the surface and either directed radially to the cylindrical wall or directed towards the lower region of the separator. The flow in the centre tube directed towards the outlet of the separator is strongly swirling with the core of the PVC clearly visible with the bulk fluid motion rotating about this point. At this y-axis location the core of the PVC is effectively centred, but as will be seen in the next image this is not the case hence demonstrating the unsteady nature of

112

this flow phenomenon. Figure3.35 shows the velocity vectors in a horizontal plane at Y=100 mm from the base of the separator, this denotes the region below one complete revolution of the helical path.
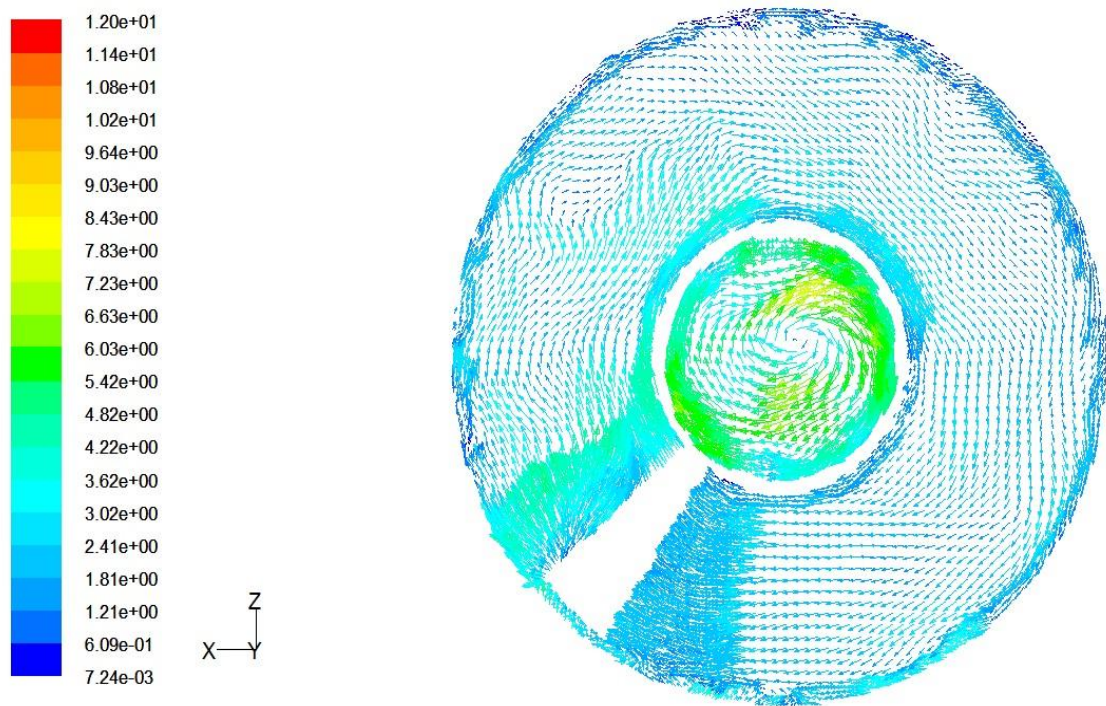
Figure 3.35: Velocity Vector Plot at Y=100 mm-LES (Vectors Coloured by Velocity Magnitude in (m/s))

The velocity vectors shown in Figure 3.35 demonstrate the gas flow is now ordered and follows the curvature of the cylindrical body of the separator. This flow structure is more representative of what would exist in a conventional geometry which exhibits a combined free vortex/forced vortex therefore a centrifugal force will be generated resulting in the radial transport of the dispersed droplets to the peripheral walls. Within the centre tube region, as with Figure 3.34, it is clear that the flow is strongly swirling, however the core of the PVC at the y-axis location shown in Figure 3.35 is visibly off centre. The movement of the PVC core from Figure 3.34 to Figure 3.35 demonstrates the transient nature of the flow within the separator therefore confirms the requirement to use an unsteady simulation approach to determine the time-averaged velocity components which have been measured experimentally. The variation in the flow structure throughout the separator geometry can be seen by examining the velocity vectors in a vertical plane through the centreline of the unit, Z=0 mm, as shown in Figure 3.36.
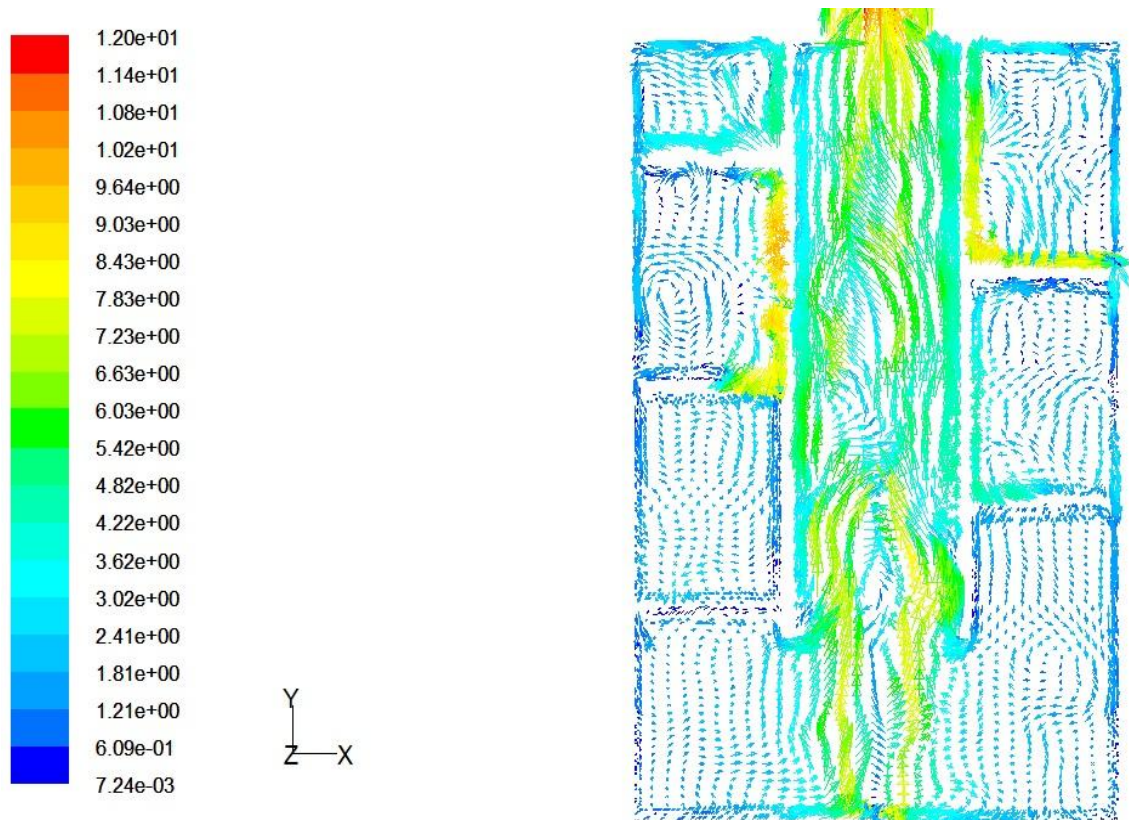
Figure 3.36: Velocity Vector Plot at Z=0 mm-LES (Vectors Coloured by Velocity Magnitude in (m/s))

Within each of the regions in the bulk separation volume of the separator, which are partitioned in Figure 3.36 by the blade of the helix, there are recirculation zones. Within each of these recirculating fluid regions, the dispersed droplets will agglomerate and eventually become separated from the gas flow. In the upper most region of the separator, top left of Figure 3.36, the flow is predominantly directed radially towards the cylindrical wall hence any droplets that have entered the separator and been carried into this upper region will be directed towards the wall where they will become separated. As with the previous two horizontal plane vector plots, the presence of PVC is clearly seen to traverse the diameter of the centre tube from its entry point at the lower region of the unit to where the flow exits at the upper most part.

3.6 Laser Sheeting

The experimental data obtained from the LDA system allows point velocity measurements to be made and then used as a direct comparison with the CFD data to allow model validation and refinement. However the bulk flow field within the separator is also of great interest since this allows the flow structure to be captured and examined, but can also act

114

as a secondary validation. This can be achieved by creating a high intensity light sheet in a plane within the separator volume, seeding the flow with tracer particles and capturing still images using a digital camera. This setup is shown in Figure 3.37.
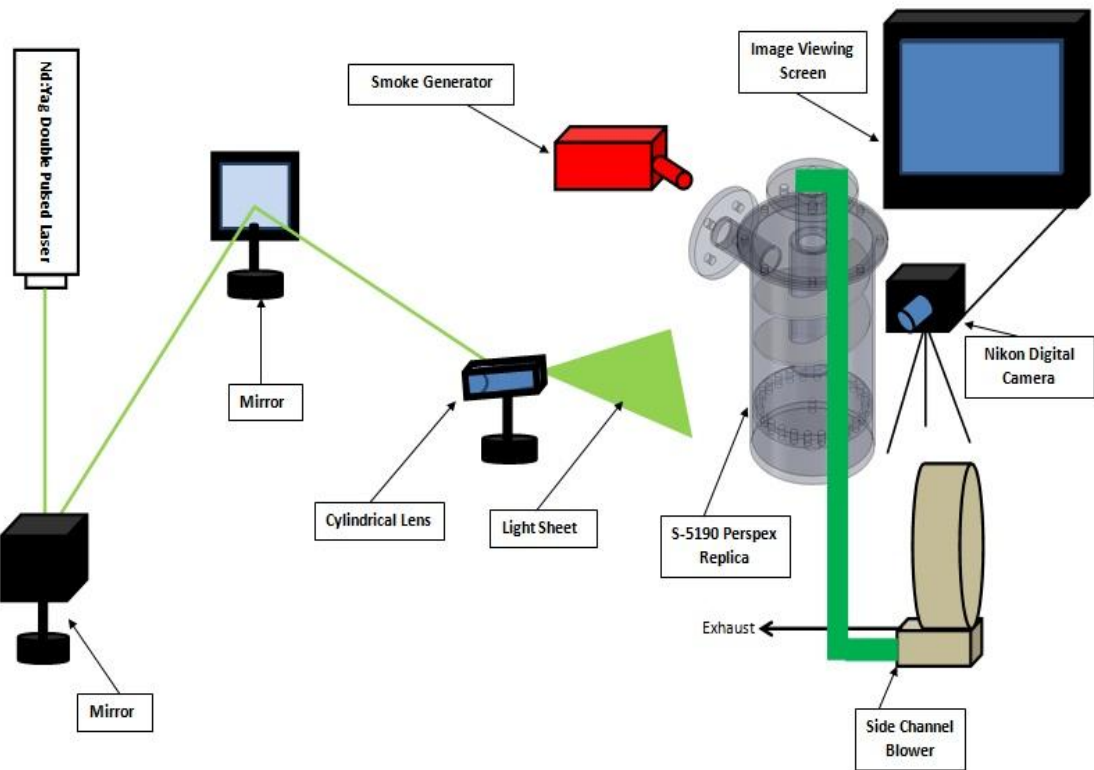
Figure 3.37: Laser Sheeting Experimental Setup

An Nd:Yag (Neodymium-doped Yttrium Aluminium Garnet) double pulsed laser with a wavelength of 532 nm was used to provide the high intensity, monochromatic light. The laser light path was directed, using a series of optical mirrors, into a cylindrical lens where the beam was expanded creating a sheet of light within the Perspex separator volume. The side channel blower and rotameter setup used in the LDA investigation was used to draw ambient air through the separator and monitor the flowrate. The air flow was seeded with fine smoke particles which were generated using a theatrical smoke generator positioned at the inlet to the separator. As with the LDA it is assumed that the smoke particles follow the gas flow path without any significant deviation due to the small Stokes number. The density of the smoke generated was initially so great that the separator volume was completely obscured, however as it began to dissipate the flow structure slowly became visible. A high speed Nikon D90 camera connected through an AV cable to a television

monitor was used to capture and display the images from the illuminated plane. From the LDA and CFD data presented earlier in this chapter it is clear that a precessing vortex core exists in the region at the bottom of the separator below the centre tube. Apart from being the most suitable region to capture images from in terms of optical access the PVC flow phenomenon has been successfully imaged before in cylindrical cyclone type geometries, (Kumar & Conover, 1993), therefore acts an indication of what may be expected from the Perspex separator.

The image in Figure 3.38 is taken with the laser sheet created in the X-Y plane of the Perspex separator at approximately Z=0 mm and shows the presence of the unsteady PVC, enclosed within the black rectangle, around the centreline of the geometry. The low pressure core of the PVC contains a very low volume of the smoke seeding particles since it is much less turbulent than the outer flow region therefore shows as a dark region when imaged, this has also been found when carrying out visual observations of water in a vortex tube (Escudier, et al., 1980).
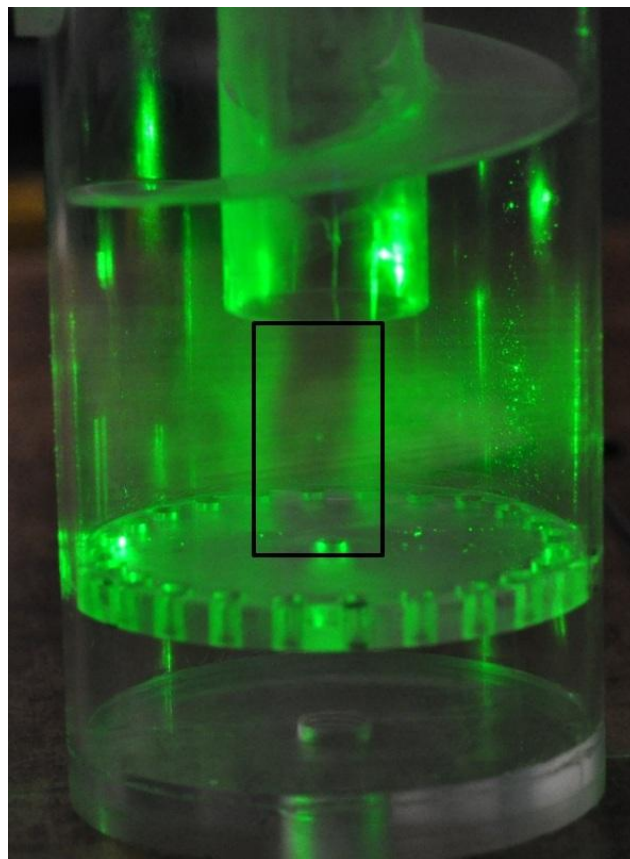
Figure 3.38: X-Y Plane Laser Sheeting Image Showing PVC

The vector plot showing the magnitude of the velocity obtained from the LES computational simulation in the X-Y plane through the centreline of the Perspex separator is shown in Figure 3.39. By comparing the vector plot to the image obtained from the laser sheeting Figure 3.38, which are in the same plane, it can be seen that the CFD captures the existence of the PVC denoted by the low velocity central core, surrounded by a high velocity outer region as highlighted by the rectangle in Figure 3.39.
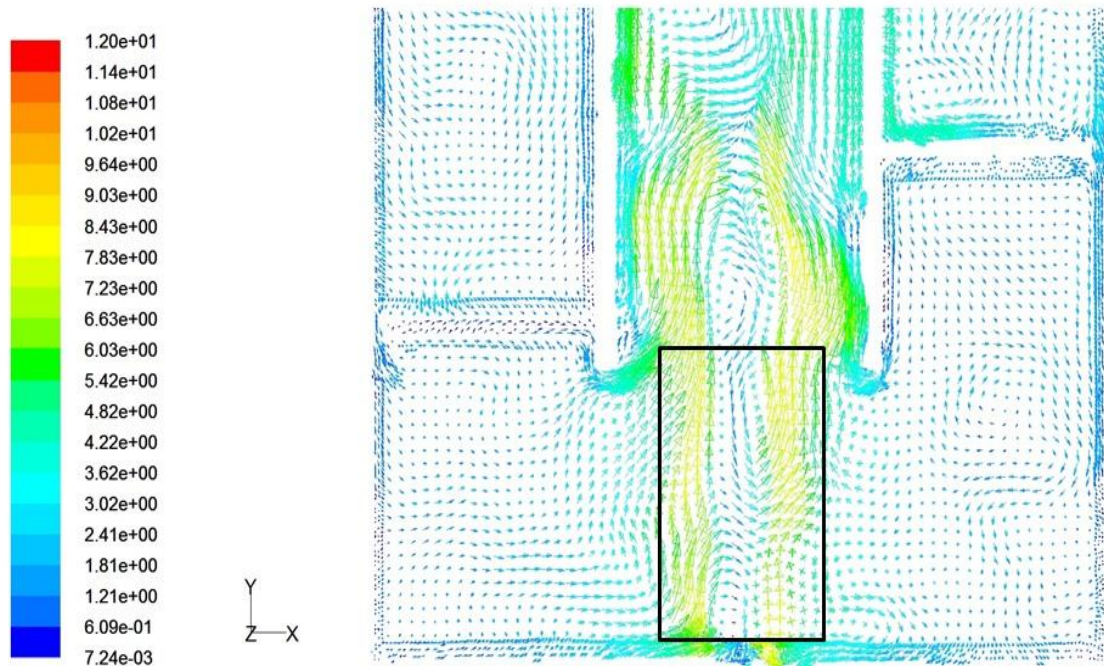
Figure 3.39: X-Y Plane Velocity Vector Plot Showing PVC-LES

The cylindrical lens was rotated through 90° to create a light sheet in the horizontal X-Z plane at approximately Y=20 mm from the base of the unit and again the presence of the PVC was observed by the dark central core, located within the black rectangle, in Figure 3.40. The core of the vortex, identified by the dark spot in the illuminated plane in Figure 3.40, is not exactly located on the centreline of the geometry indicating that it is unsteady hence reiterating the requirement for a transient numerical solver.
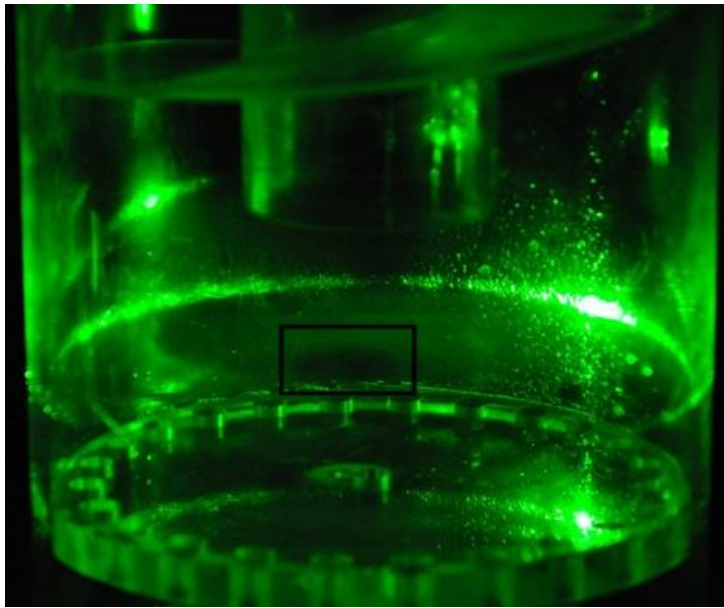
Figure 3.40: X-Z Plane Laser Sheeting Image Showing PVC

The vector plot of velocity magnitude from the CFD simulation in the X-Z plane at the same axial location as Figure 3.40 is shown in Figure 3.41.
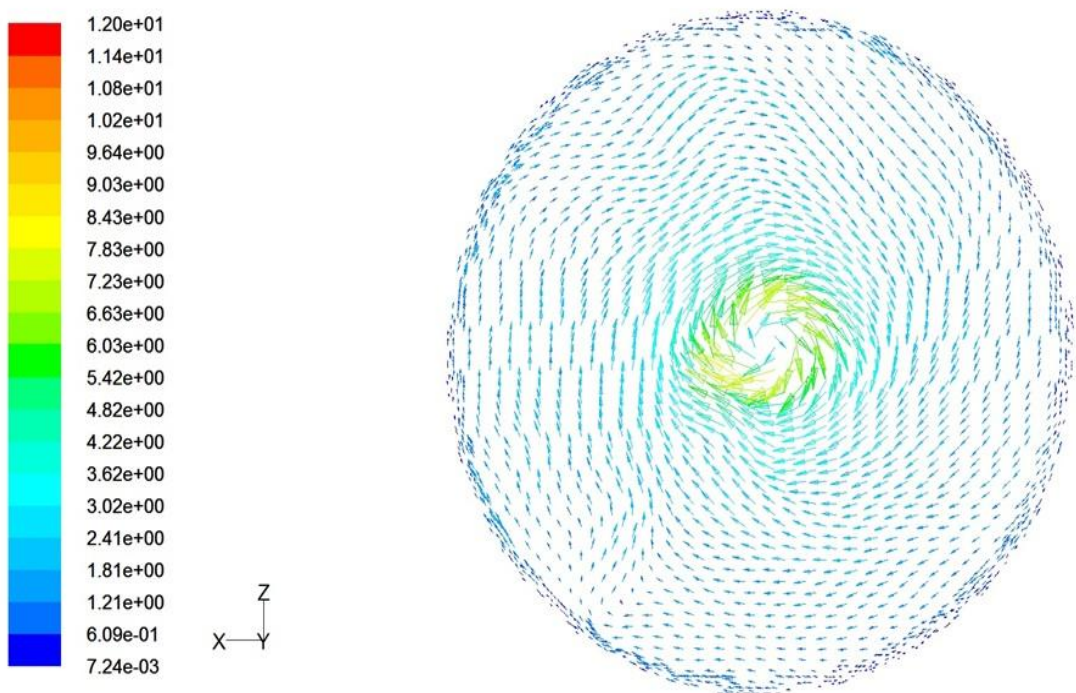
Figure 3.41: X-Z Plane Velocity Vector Plot Showing PVC-LES

The laser sheeting images obtained contribute to the analysis of the flow field in the helical separator and provide additional validation to the results from the CFD simulations. The

physical phenomenon associated with a swirling flow such as that which exists within the helical separator geometry is captured; in particular the presence of the unsteady precessing vortex core, the existence of which is clearly visible in Figure 3.38 to Figure 3.41, as highlighted in the black rectangles. The outer core of the PVC is dominated by a large tangential velocity component combined with a low velocity in the core region. The velocity out with this region is clearly significantly lower than that of the PVC therefore the degree of centrifugal separation will also be very low therefore the geometry must rely on other mechanisms to promote droplet separation. This velocity distribution is clearly shown in the velocity profile plots obtained from the experimental LDA measurements and has been shown to be the case in the majority of geometries which have swirling flows.

3.5 Major Outcomes

This chapter has covered the process involved to model the flow field within the helical separator geometry. This has been achieved through experimental measurements of the velocity within a Perspex replica of the separator using LDA. The velocity profiles obtained through the LDA measurements were then used to validate a CFD model which could replicate the flow field which exists in practice. In doing so a mesh refinement study was carried out to allow an optimum grid to be achieved in terms of accuracy versus computational time and memory. A detailed comparison of the various turbulence models and discretization methods available in Fluent was performed and the need for a transient solution method was determined due to the unsteady nature of the flow field mainly associated with the presence of the PVC.

The use of the advanced LES turbulence model with a high order discretization was found to produce the most accurate results in terms of predicting the velocity components obtained from the LDA measurements. Without the availability of the LDA data one of the lower order discretization methods, less advanced turbulence models and coarser computational grids could have been incorrectly selected as acceptable to describe the flow within the separator geometry and resulted in significant levels of inaccuracy when used to predict the separation performance of the unit.

Laser sheeting was also used to analyse the bulk flow within the separator in further detail. The most notable feature observed during this investigation was the presence of the PVC which could be identified in both the horizontal and vertical plane illuminations as a dark region which could be further compared with the vector plots obtained from the CFD

simulations. This confirmed the unsteady and precessing nature of the precessing vortex core in the region below the centre tube of the separator.

With a validated computational model available to describe the single phase flow field within the helical separator geometry, attention can now turn to the performance capabilities of the separator which can be obtained through the use of the Discrete Phase Model (DPM) which applies the Euler-Lagrange method for particle tracking.

Chapter 4 Oil Separator Experimental Testing

4.1 Introduction

Having investigated the complex single phase gas flow structure within the helical separator geometry the attention of this investigation now turns to capturing the performance of the unit by carrying out two phase flow investigations to obtain separation efficiency and pressure drop data. Since this is the first time the helical oil separator has been investigated a test facility had to be designed, constructed and commissioned to allow the relevant performance data to be measured. In carrying out the experimental testing of the separator compressed air was used to replicate the refrigerant gas that exists in real plant conditions, and synthetic refrigerant lubricating oil was used as the dispersed phase.

This chapter examines firstly the rationale behind the experimental testing including background information, what needs to be tested and the parameters to be measured. The design of the experimental test rig, the operational procedure and capabilities will then be presented. Following on from this the measurement methods used to gather the experimental data will be given along with the variables which will be altered to simulate different compressor discharge conditions. The results from the experimental measurements will then be given and the findings analysed and discussed. Finally the major outcomes from the experimental investigation will be presented.

4.2 Rationale to Testing

4.2.1 Background

The purpose of the experimental work is to obtain both separation efficiency and pressure drop data at different discharge volume flowrates for the helical oil separator subject to a range of liquid loading conditions at atmospheric pressure and 3 BarG. In an industrial refrigeration system the compressor flowrate and speed determine the oil loading. In this investigation the operating pressure dictates the gas mass flowrate which in turn determines the injected oil volume flowrate since the choice of separator is based on a volumetric flowrate requirement which relates to an oil volume flowrate. Since there has been no previous investigations relating to the helical oil separator, except a basic in house study carried out by Henry Technologies in the US in the early 1990's, an experimental test facility was designed, constructed and commissioned within the Department of Mechanical and Aerospace Engineering at the University of Strathclyde. The experimental facility had to

be designed in such a way as to replicate the conditions which exist at the discharge of the compressor in an industrial refrigeration system using a compressed air supply as the continuous phase working fluid. The air supply then had to be fed with a dispersed phase oil mist to represent the two phase flows that exists at the inlet to refrigerant oil separators. The overall objective of this investigation is to gain insight into the performance of the helical separator over a range of controlled conditions.

The initial aim for the experimental test program was to obtain performance measurements for a number of different sized separators available in the Henry Technologies range; however this had to be reduced to one separator due to the wide range of operating conditions that each unit may be subject to. The separator selected as the test unit for this investigation was the S-5190 which has a maximum discharge volume flowrate of 18.7 m^3/hr. This particular separator was selected as it lies in the middle of the range of separators offered in terms of the discharge volume and was also found to be in the top five best-selling units as discovered through a sales review (Brown, 2010).

The helical separator is designed to operate over a pressure range of 0 to 31 BarG and temperature range -10 to 130°C with a variety of industrial refrigerants including HFC-R404A, HCFC-R22 and Ammonia-R717. The density range of the various refrigerants used is 12 kg/m^3 up to 198 kg/m^3 and the separator has a recommended operating range of 25-100% of the discharge volume flowrate of 18.7 m^3/hr. The resulting mass flowrate range for the S-5190 separator is 0.0156 to 0.988 kg/s. Since the working fluid for the experimental testing was compressed air, the operating flowrate range was governed by the maximum working pressure of the compressor which was 17 BarG. The operating range of the gas flow for the experimental test facility therefore ranged from 0.00159 kg/s up to 0.112 kg/s. The presence of the oil entrained in the discharge line of the compressor is attributed to the fact that lubrication is required for the machinery responsible for the compression of the gas. The refrigerant gas within the discharge line typically contains between 1 and 8% oil mass fraction, (Cremaschi, et al., 2004), however for the purpose of this investigation this will be extended to include up to 10% mass fraction. For the air mass flowrate range over which the S-5190 separator is to be tested in this investigation the resulting oil volume flowrate ranges from 1 mL/min to a maximum of 750 mL/min.

There are a range of lubricants available dependent on the system, refrigerant and type of application. The choice of lubricant is dictated by the refrigerant which the system is to be

operated with rather than the type of compressor. Amongst the categories of oils available there are mineral oils which are particularly suited for use with CFC's, HCFC's and ammonia and have an excellent fluidity at low temperatures; Poly Alpha Olefin (PAO) are synthetic oils and are used for systems working in extreme conditions with R-22 or ammonia due to their low pour points and excellent thermal stability; Polyol Ester (POE) are a second generation of synthetic oils developed to be used with HFC's which are less hygroscopic than their predecessors and intended for all refrigeration and air conditioning applications. Based on this the lubricant oil chosen for this investigation was Emkarate RL22H which is a POE. This specific lubricant was chosen as it was representative of the physical properties, i.e. density, viscosity and surface tension, at atmospheric temperature as the lubricant typically used in an industrial refrigeration compressor at normal operating conditions which are between 40 and 60°C. A range of the lubricants available and their properties are given in Figure 4.1. The graph shown in Figure 4.2 shows the variation in kinematic viscosity with temperature. The density and surface tension for RL22H are 995 kg/m^3 and 0.03 N/m respectively at atmospheric pressure.

PROPERTY & PROCEDURE	RL22H	RL32-3MAF	RL32H*	RL68H	RL68HP*	RL100E	RL170H	RL220H+	RL220HC+
Viscosity @ 40°C (cSt), ASTM D-445	18.9	31.2	33.7	72.3	72.3	100	170	230	220
Viscosity @ 100°C (cSt), ASTM D-445	4.2	5.8	5.9	9.8	9.8	12.0	17.0	19.5	19.0
Typical SUS Viscosity @ 100°F	100	150	150	300	300	500	850	1100	1100
Viscosity Index, ASTM D-2270	120	125	110	120	120	120	108	100	97
Pour Point (°C), ASTM D-97	-52	-40	-46	-39	-39	-20	-25	-15	-30
Density @ 20°C (g/ml), ASTM D-1298	0.995	0.981	0.977	0.977	0.976	0.970	0.968	0.976	0.980
Flash Point (COC) (°C), ASTM D-92	240	230	270	270	260	230	290	280	300
Acid Value (mgKOH/g), ASTM D-974 modified	0.01	<0.05	0.02	<0.02	<0.02	<0.05	<0.02	<0.02	<0.05
Water Content (ppm), ASTM E 1064-85	<50	<50	<50	<50	<50	<50	<50	<50	<50
Refractive Index @ 28°C	1.4519	1.4540	1.4530	1.4557	1.4566	1.4574	1.4590	1.4580	1.4580

Figure 4.1: Refrigerant Lubricant Oils and Properties
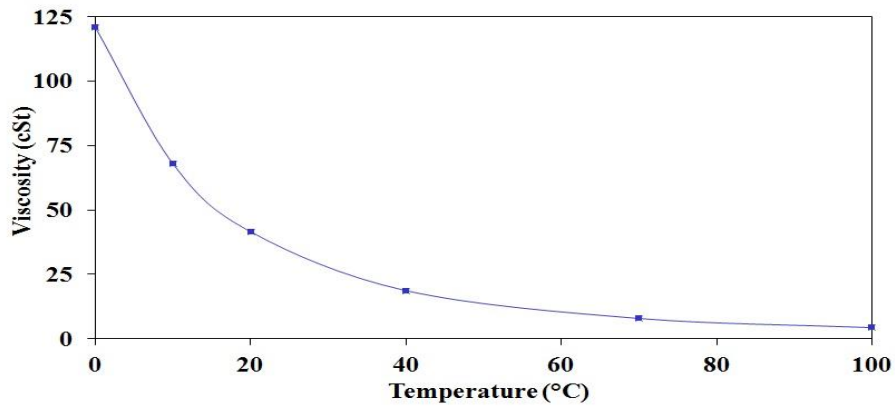
Figure 4.2: Variation of Kinematic Viscosity with Temperature for Emkarate RL22H

4.2.2 Flow Regimes

In order to assess the consequences of testing the separator at flow conditions which are out with the normal plant operational conditions a Baker map, as shown in Chapter 2, is used to highlight the difference in inlet flow conditions which exist between what can be captured with the custom built test facility and those which exist in practice. Due to issues associated with pumping the oil into the system, as will be explained later in this chapter, the performance testing of the separator could only take place between atmospheric pressure and 3 BarG. The flow regimes which can be expected at the inlet to the separator at these working pressures are shown in Figure 4.3 as well as those which exist in practice.
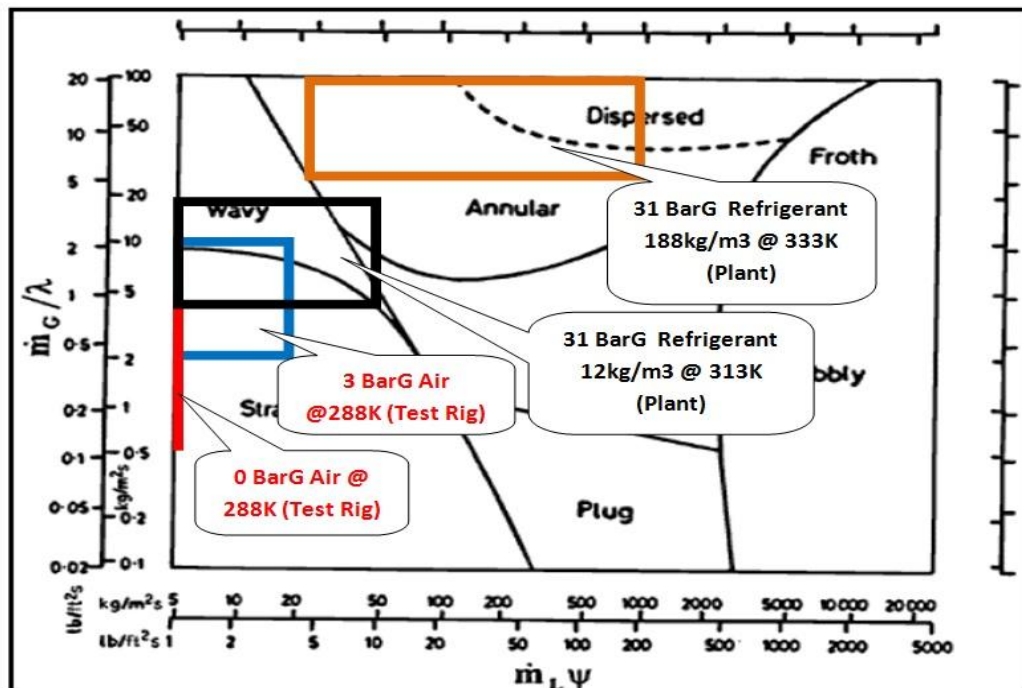
Figure 4.3: Baker Flow Regime Map

From Figure 4.3 it is clear to see that the flow regimes which can be simulated by the test facility are predominantly stratified flows with the exception of high gas and liquid flowrates at the 3 BarG operating condition producing a marginally wavy flow regime. The vast density range of refrigerants which the oil separator is used with potentially generates flow regimes which span the stratified, wavy, annular and dispersed regions therefore the test facility is only able to capture a fraction of the conditions which exist in normal plant operating conditions. The flow regime boundaries which are given in the Baker map are based on the assumption of a fully developed two phase flow regime. However in practice, the predominant use of short pipe lengths, the existence of bends and the interchange between horizontal and vertical pipe configurations results in flow regimes which are combinations of stratified/dispersed regimes. From a preliminary investigation it was discovered that the flow at the inlet to the separator comprised of a stratified liquid film and a droplet mist in the core of the flow.

4.2.3 Methodological Approach to Experimental Testing

As already mentioned the main objective of this investigation is to obtain separation efficiency and pressure drop data which describes the performance of the helical oil separator. In doing so it was necessary to obtain a range of data to allow a detailed assessment of the separation efficiency of the geometry to be determined. The second objective of the experimental performance assessment of the separator was to obtain the necessary information required to validate the two phase CFD model and in doing so exploring the capabilities of the current models to be used as a tool for future separator design. The internals of the geometry for which the validated single phase flow model was obtained does not contain any internal mesh screens whereas the standard unit which is used in industrial refrigeration systems does. The justification for creating the CFD model without any internal mesh screens was due to the complexity involved in producing computational performance data for internal meshes and this is supported by the lack of available data within the literature. Therefore to allow the two phase model to be validated and the performance results obtained to be compared with the experimental data a no mesh variant of the S-5190 separator was manufactured for the experimental performance testing. Further details of the mesh screen properties and locations will be given in a subsequent section. For the remainder of this thesis the standard S-5190 helical oil separator with the internal meshes will be referred to as the "Standard Unit" and the

custom design with the internal mesh screens removed will be referred to as the "No Mesh Unit."

The determination of the separation efficiency required a variety of measurement approaches to be taken. Firstly the global separation efficiency of the standard unit separator subject to the inlet conditions generated by the custom built test facility were obtained which simply consisted of measuring the flowrate of oil entering the system and the flowrate of separated oil returned by the separator. As previously mentioned the predicted flow regime at the inlet to the separator was stratified. However as the flow was not fully developed at the point of entry into the separator a simple visualisation study was carried out to examine this flow field. This was carried out by inserting a Perspex pipe, back-lighting the flow and visually observing the flow regimes which exist at 0 BarG. It was immediately apparent that the inlet flow comprised of a combined stratified liquid film along the bottom surface of the pipe and a dispersed droplet mist in the core region, as shown in Figure 4.4. The presence of the dispersed droplet mist allows for the test facility to capture the performance of the separator at the real plant conditions since the predicted flow regimes given in Figure 4.4 indicate that an annular-dispersed mist exists in practice. To allow separation efficiency measurements to be obtained for a dispersed droplet inlet condition alone required the stratified liquid film to be extracted upstream of the separator inlet and quantified. The droplet only separation efficiency of the unit could then be obtained by subtracting the flowrate of liquid film from the total inlet flowrate.
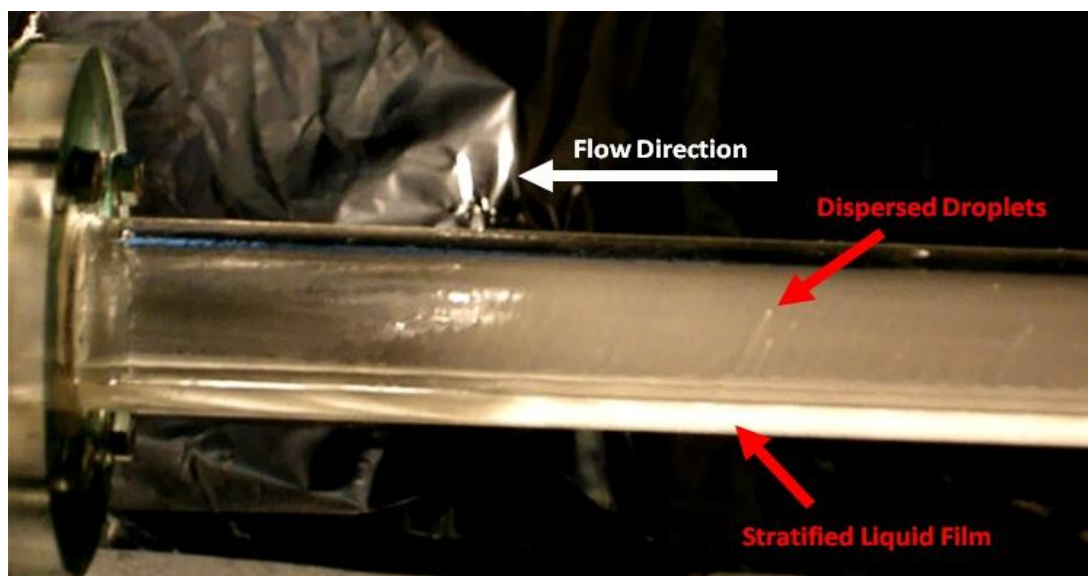
Figure 4.4: Separator Inlet Pipe Flow Regime

Further insight into the droplet only separation performance of the separator can be obtained by measuring the droplet size and distribution at the inlet and outlet of the unit. This information combined with the droplet separation efficiency allows an experimental grade efficiency curve (GEC) to be produced which summarises the ability of the separator to remove droplets of a certain diameter. The resulting droplet data at the inlet to the separator combined with the experimental GEC can then be used to validate the discrete phase model (DPM) which will be used to computationally model the two phase droplet flow. This will be covered in a subsequent chapter.

The other factor which governs the overall performance of separators is the pressure drop, therefore this also needs to be accurately measured. To capture the pressure loss across the helical separator unit requires static pressure tapings to be located upstream of the separator inlet and downstream of the outlet. The static pressure at the two locations are measured by a differential pressure transducer allowing the pressure drop to be directly obtained.

4.3 Experimental Test Rig Design

4.3.1 Droplet Generation

Generating the type of flow conditions which exist in the discharge line of the compressor was the key to successfully testing the performance of the helical oil separator. In doing so meant creating a flow condition where oil droplets are entrained within the continuous phase compressed air flow. The main difficulty associated with creating this type of flow was due to the lack of available data on the droplet sizes which physically exist at the outlet of an industrial refrigeration compressor. The only reference found by the author giving an indication of what droplet sizes may be expected from refrigerant oils in aerosol form ranges from less than 0.1 to 40 microns typically with the majority of aerosols in the discharge gas being in the 0.4 to 10 micron range (Temprite, 1999). To mechanically generate droplets which are representative of this range required the use of an atomising nozzle. There are a range of nozzles available capable of producing a droplet mist which include air assist, air blast, rotary and pressure atomiser designs (Lefebvre, 1989). In analysing the capabilities of the range of atomising nozzle types the air assisted internal mix was selected to be the most suitable to produce the droplet size range required to be representative of a compressor discharge line.

A schematic of a typical air assisted internal mixing nozzle is shown in Figure 4.5 which requires the parallel supply of a liquid and gas into a small chamber where the two phases are mixed. The high velocity gas shears the liquid film into small droplets which are then discharged through the nozzle orifice with a droplet diameter distribution governed by the flowrates of both phases. Internal mixing atomisation is particularly suitable for high viscosity fluids and slurries over a wide turn down ratio (Sakai, et al., 1978).
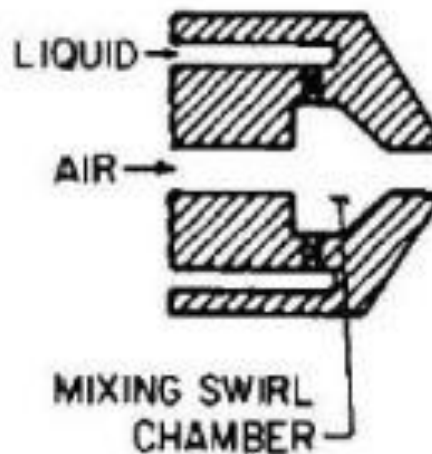
Figure 4.5: Internal Mixing Air Assisted Nozzle (Lefebvre, 1989)

The nozzle used in this investigation was manufactured by Delavan Spray Technologies and consisted of three main parts; the air cap, the liquid tip and the main nozzle body. To produce a condition which would replicate the discharge of the compressor the AL-45 series was selected with the metering set 45-03 to provide for the flowrates at the range of operating pressures; the resulting spray pattern from the exit orifice is a narrow spray with an included angle between 15° and 20°. Figure 4.6 shows the AL-45 nozzle and component assembly. Oil is delivered into the central bore of the nozzle body (5) where it is directed through the ventral micro bore of the liquid tip (3) and forced through the air cap (2) where it is mixed with the compressed air supply prior to exiting through the discharge orifice. The compressed air is supplied through an outer annulus in the nozzle body (5) where it is forced through 4 small holes in the outer diameter of the liquid tip (3) by passing the outside of the micro bore and into the air cap (2).
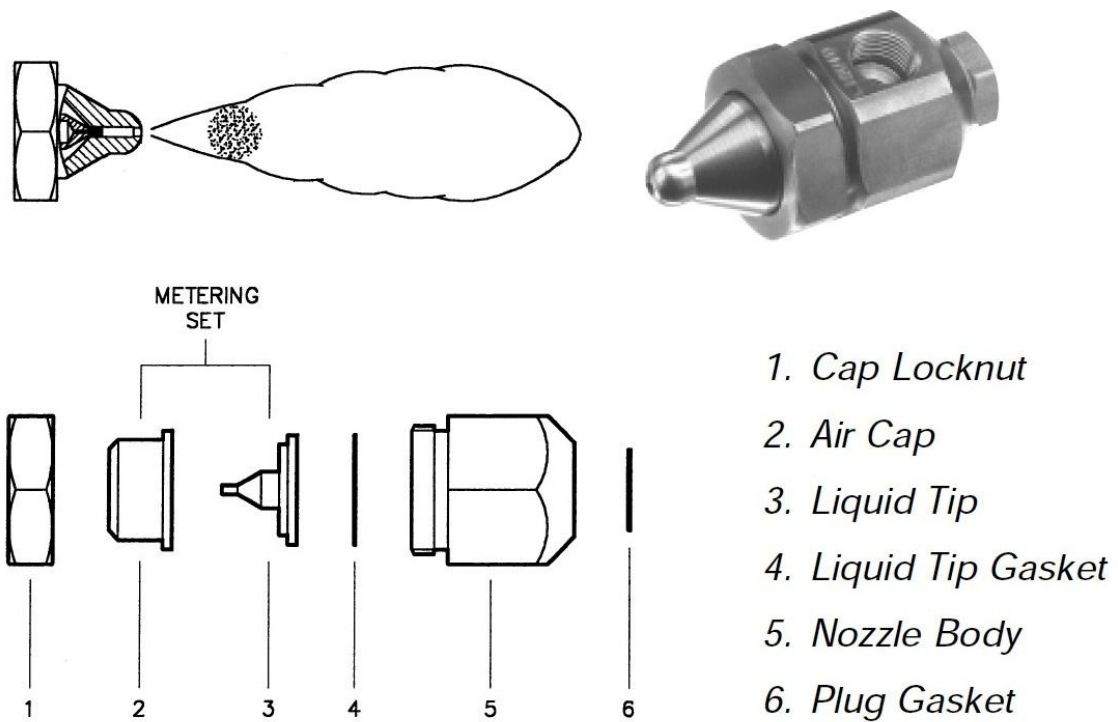
Figure 4.6: Delavan AL-45 Section Drawing

The AL-45 nozzle does not have an obvious mixing chamber like that shown in Figure 4.5; however the liquid tip micro bore extends into a channel where the length of the bore is significantly longer than the bore diameter. It is likely that this feature reduces the drag coefficient of the nozzle exit orifice conserving more energy to be used in the atomisation of the liquid itself (Lefebvre, 1989).

4.3.1.1 Droplet Data for Delavan Nozzle

The droplet sizes produced by the air atomising nozzle are governed by the flowrate of liquid and the pressure differential across the nozzle. In general as the liquid flowrate increases; the mean droplet size increases and the distribution range of droplet sizes becomes wider for a constant pressure differential. Likewise for a constant liquid flowrate and increasing pressure differential the resulting mean droplets size decreases and the distribution range of droplet sizes reduces. The change in mean droplet diameter with variation in pressure differential and oil flowrate is shown in Figure 4.7. The data has been obtained 150 mm downstream of the nozzle exit using a Malvern Spraytec laser diffraction measurement instrument, the details for operation will be discussed in a subsequent section.
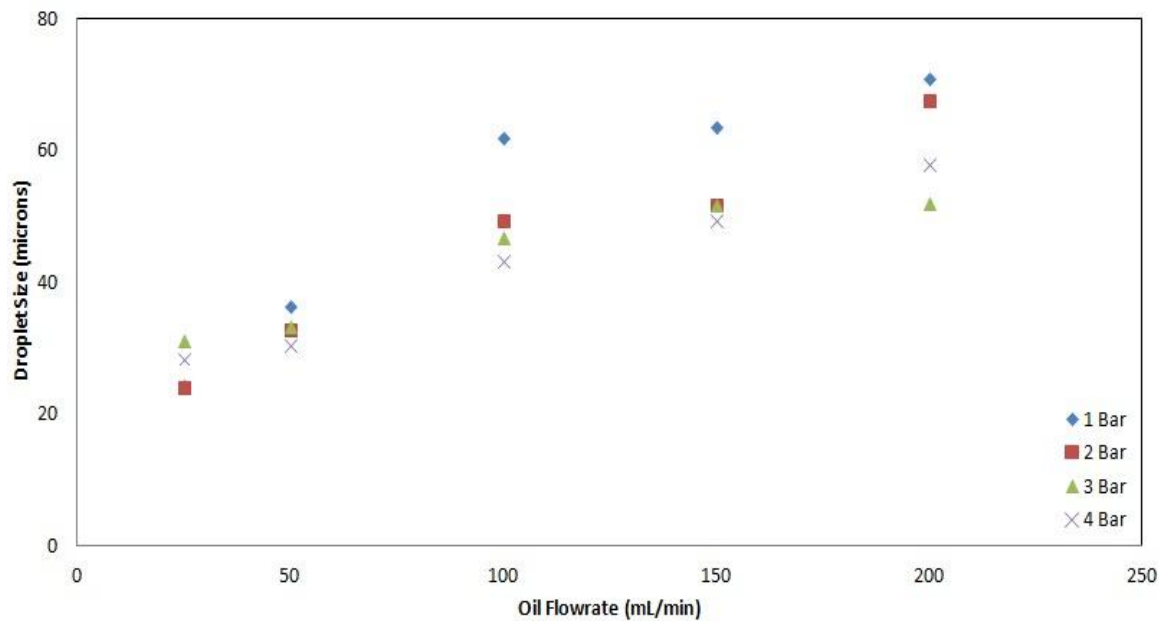
Figure 4.7: Variation in Mean Droplet Diameter with Liquid Flowrate and Differential Pressure

4.3.2 Oil Supply

Two pumps have been used to deliver the oil supply to the atomising nozzle, the first being from HNP Microsystems high performance micro-annular gear pump series, which was able to deliver a continuous flowrate accurately between 0.048 and 288 mL/min with an operating pressure up to 40 Bar. The model used for the experimental testing was the MZR-7205 which was able to deliver the viscous refrigerant oil at the desired flowrate continuously for the duration of the testing; the pump was accompanied with controller software where the required flowrate was input. The second pump used to supply the oil was a Hydra Cell P200 metering diaphragm pump from Wanner Engineering Inc. which was capable of delivering 64 to 640 mL/min at 35 Bar with the use of a 25:1 ratio gearbox. The pump model number was P200MSTSS025S which can be used to identify the exact makeup of the pump in terms of configuration, valve and spring materials, O-ring material etc. To set the required flowrate for the diaphragm pump an Allen-Bradley adjustable frequency AC drive was used to control the frequency of the motor between 0 and 87 Hz.

Oil is supplied to the appropriate pump from a storage vessel which can hold around 40 Litres of the lubricant. Mounted on top of the storage vessel is a degassing vessel, which can hold around 30 Litres of oil. The degassing vessel can be completely isolated and an Edwards two stage high vacuum pump connected to allow a batch degassing process of the oil. This takes place at the end of each experimental test to remove any air which has gone

into solution during the run; the requirement for this procedure will be explained in a subsequent section. The storage vessel and degassing vessel both have 2 flanged connections, top and bottom, and a series of ports on the cylindrical body which cater for sight glasses to allow the internal liquid levels to be monitored. The 40 Litre supply vessel has a 1/4" connection which allows 8 mm OD flexible hose to be connected to supply the suction line of the micro-annular gear pump and a 1/2" connection to supply the diaphragm pump suction line. Dependent on the flowrate required to the rig the appropriate valve is opened to allow the flow of oil to the appropriate pump. The degassing vessel is fitted with 1/4" connections to allow the separated oil to be returned to the vessel when a measurement is not taking place. During the degassing process the lubricant requires to be heated to around 80°C, to allow optimum air removal, therefore the oil is pumped by a Mirrlees IMO positive displacement pump through a Eltron Chromalox 1000 W continuous circulation heat exchanger. As a result the degassing vessel has two 1/4" connections to cater for this process. To enhance the degassing process further the oil is mechanically mixed during the heating and air removal process. This requires a vacuum feed through assembly which consists of a propeller connected through a shaft to a solid shaft Rigaku Superseal rotary vacuum feedthrough. This assembly is then driven by a motor with a gearing ratio of 5:1 capable of rotating at 3090 rpm with a supply of 12 V. The motor is powered by a DC regulated power supply which can deliver between 3 and 15 V. The motor, vacuum feedthrough and couplings are enclosed within a housing assembly which permits it to be connected through the port on the vessel providing a tight seal. The entire oil supply loop is shown in Figure 4.16.

4.3.3 Oil Test Separators

The separator used in the performance investigations was the Henry S-5190 helical separator which is currently in production and operating in industrial refrigeration plants worldwide. The exact geometry is given in Figure 4.8 with the fully dimensioned unit shown in Figure 4.9. The separator has two main connections; one radial connection which is the inlet to the vessel where the continuous phase with entrained oil enter and one on the top cap which allows the continuous phase to exit with any small droplets of oil which have escaped separation still suspended within. To allow the separator to be connected to the adjoining pipework flanged connections were manufactured and welded onto these connections; pressure tapings were also created on the inlet and outlet flanges to allow the pressure drop across the separator to be determined. Directly below the inlet connection to

the separator is a 3/8" flare connection which allows the oil to be returned from the collection chamber at the lower part of the geometry. In an industrial application this allows the oil to be returned to the compressor sump, but in the context of this study provides the point of measurement for the separated oil volume.

The main separation space contains a centre tube which leads to the outlet connection. At the entrance to the centre tube there is a wire mesh bag mounted onto a drip ring. The mesh is a single layer screen which comprises of 60, 0.16 mm diameter, strands per inch which leaves an open area percentage of 39%. The purpose of the drip ring is to prevent any liquid film running down the centre tube from being easily carried over to the outlet by causing it to be projected towards the cylindrical wall of the separator. Also mounted on the centre tubes peripheral is a helical flighting which runs from 33.7 mm below the top cap to the bottom of the centre tube where the drip ring is located. Wrapped round the cylindrical wall from the 12.3 mm below the inlet connection to the bottom of the separation space there is a wire mesh screen which has the same properties as the mesh at the entrance to the centre tube. Dividing the separation space from the lower section of the separator where the oil is collected is a baffle plate which contains a series of holes to allow the separated oil to drain through. Within the oil collection chamber is a mechanical ball float and needle valve assembly and permanent magnet which allows the oil level to be maintained and any metallic debris to be captured.

In addition to the standard S-5190 geometry the unit used for testing was fitted with a sight-glass 73.9 mm from the base of the oil collection chamber to allow the collected volume of oil to be visually monitored during experimental runs. The only other modification prescribed to the test unit geometry was the inclusion of a Rotalock boss and valve on the end cap to allow the oil collection chamber to be pre-charged with oil prior to commencing any testing and then completely drained of oil before being removed from the test rig. These minor modifications are highlighted on the geometry given in Figure 4.9.

Figure 4.8: S-5190 Helical Oil Separator

Figure 4.9: S-5190 Helical Separator Dimensioned Drawing (Dimensions in mm)

As previously discussed two separator configurations will be experimentally tested in this investigation the standard unit and no mesh unit. The no mesh unit contains all of the parts shown in Figure 4.8 except for the wire mesh screen on the cylindrical wall and on the entrance to the centre tube as indicated on the image. The performance results from both separator configurations will be presented and discussed in the results section of this chapter.

A secondary separator was also needed to remove any oil which the helical unit failed to separate; as a result the S-5690 Henry conventional oil separator was chosen which has the same discharge volume as the S-5190 of 18.7 m^3/hr. The conventional separator used is shown in Figure 4.10 with the dimensioned drawing in Figure 4.11. This separator has both the inlet and outlet connections mounted on the top cap which like the helical unit required flanged connections to be manufactured to allow it to be installed into the rig, this time without pressure tapping ports as the pressure drop across this unit was not the focus of the investigation. The oil return, also a 3/8" flare connection, for the conventional separator is normally located between the inlet and outlet connections on the top cap however this was modified so that it was located on the cylindrical wall at the same location as the helical separator. The flow enters the conventional separator through the left hand connection and passes through a wire mesh screen. The droplet laden flow is then forced to change direction to exit through the right hand connection which is also fitted with a wire mesh screen. Both wire mesh screens in the conventional separator have the same properties as the helical separator mesh screens. To prevent the flow from being directly transported from the inlet to outlet a deflector plate is fitted next to the outlet mesh. Unlike the helical separator there are no other internals within the cylindrical volume to promote separation other than the wire mesh fitted to the internal walls which begins 27.4 mm from the top cap and covers the separation space to the sight glass. The internals of the oil collection region including the sight glass positioning have the same configuration as the helical unit with the exception of a baffle plate.
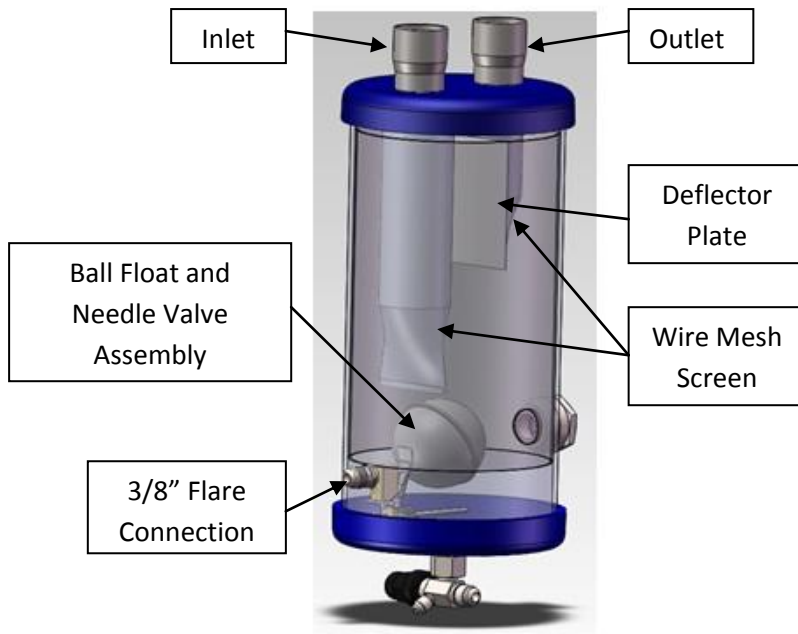
Figure 4.10: S-5690 Conventional Oil Separator
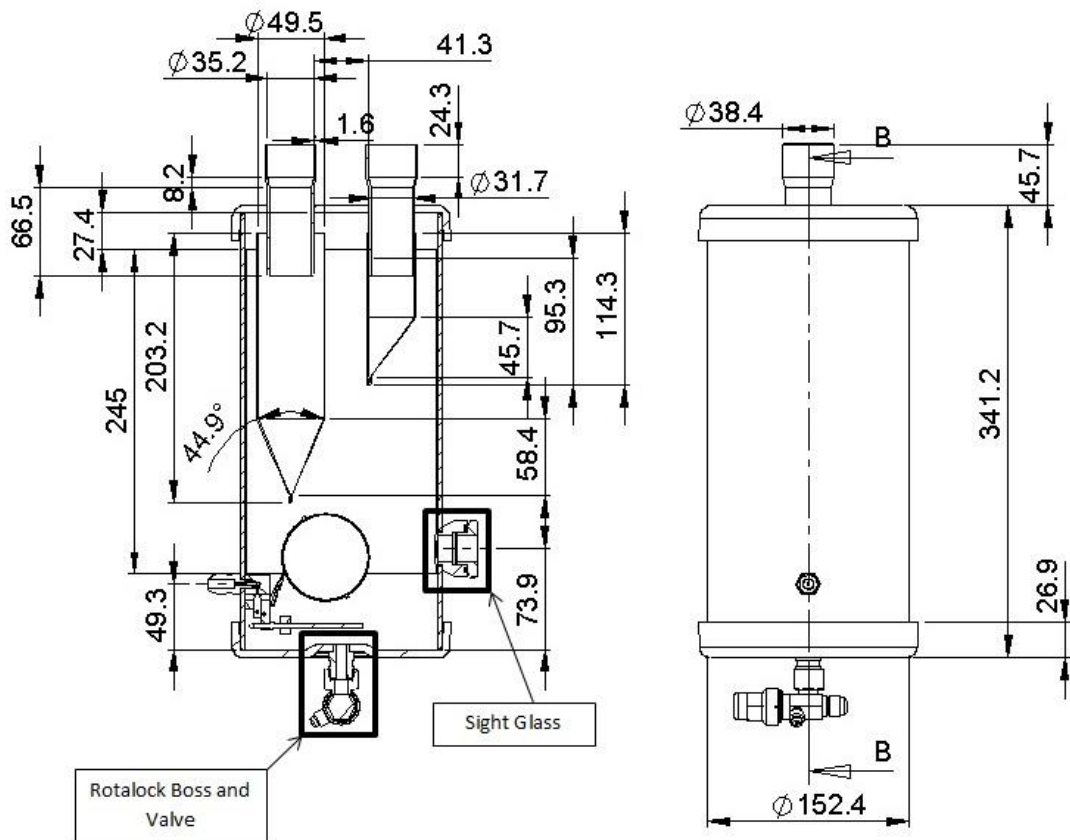
Figure 4.11: S-5690 Conventional Separator Dimensioned Drawing (Dimensions in mm)

A tertiary separator was also included in the experimental test facility as it was discovered during the initial commissioning of the system that small droplets of oil were still present in the air flow at the outlet of the secondary separator. A high efficiency coalescing filter capable of intercepting oil droplets up to 0.01 micron in diameter was selected from the ABAC range of compressed air threaded filters. The AHF1000 model was chosen with a volumetric capacity of 1000 m^3/hr and 2" BSP threaded connections at the inlet and outlet connections. An automatic float valve was provided with the unit to allow the separated oil to be drained as the level increased, but this was replaced with a plug to allow all the separated oil over a run to be drained at once and measured. To indicate when the filter cartridge was clogged and needing replaced a pressure gauge was installed onto the filter to measure the static pressure drop across the filter; when the reading was greater than 0.6 Bar it is recommended that the filter be replaced. The filter housing is manufactured from cast aluminium and the filter element itself is made of a layer of borosilicate fibre-layer supported by two inner and outer stainless steel structures.

4.3.4 Liquid Film Quantification Device

The stratified liquid film which exists in the inlet pipe will enter the separator and run down the cylindrical wall under the influence of gravity, thereby creating a liquid film on the internal surfaces, and accumulate in the oil collection chamber. The volume fraction of injected oil which is present as a stratified liquid film on entry to the separator will have a prominent effect on the overall separation efficiency of the unit if it accounts for a significantly large volume fraction. Therefore to quantify the volume fraction of inlet flow which exists as liquid film a device was required which would extract this oil volume just upstream of the separator inlet. From the initial flow visualisation investigation of the inlet flow regime, as discussed in section 4.2.2, it was evident that the liquid film was only present on the bottom surface of the inlet pipe therefore it could be gravitationally drained from the system just upstream of the separator inlet. A 35 mm thick flange block was manufactured with the same internal diameter as the inlet pipe, 31.5 mm, and a 25.4 mm drain hole created on the bottom surface from which the stratified liquid film could be removed and quantified. The drain hole was threaded to allow a ball valve to be fitted and a connection to the vessel where the extracted liquid film volume was collected. The dimensioned drawing and an image of the liquid film removal device is shown in Figure 4.12.
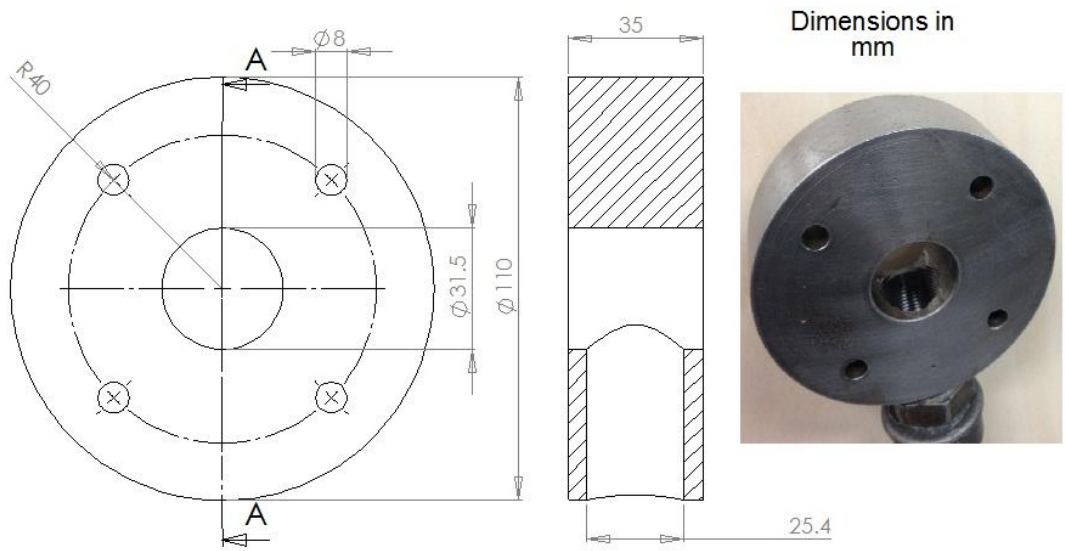
Figure 4.12: Stratified Liquid Film Removal Device

To allow the test facility to run continuously whilst quantifying the liquid film a liquid hold up vessel was designed with a Henry optical liquid level sensor, S-9424, and solenoid valve assembly to control the discharge of collected liquid from the vessel as shown in Figure 4.13.

Figure 4.13: Liquid Holdup Vessel for Film Quantification

4.3.5 Test Rig Structure

A four leg support structure with a platform and two support rails, from which the inlet injection system and three separators are suspended from above the platform, was used to house the equipment needed for the performance measurements for the separator as shown in Figure 4.14. On the platform the micro-gear pump, oil flowmeters, oil heater and measuring cylinders needed for obtaining the separated volume of oil were positioned. The pump for circulating the oil for degassing was supported from underneath the platform, the oil storage vessel and degassing vessel were located directly behind the support structure, the diaphragm pump and vacuum pump were both positioned directly underneath the platform so they did not pose a trip hazard when operating the rig. A line diagram detailing each of the individual test rig components for the performance measurements and the oil supply/recirculation loop along with the air and oil lines is shown in Figure 4.15 and Figure 4.16 respectively.
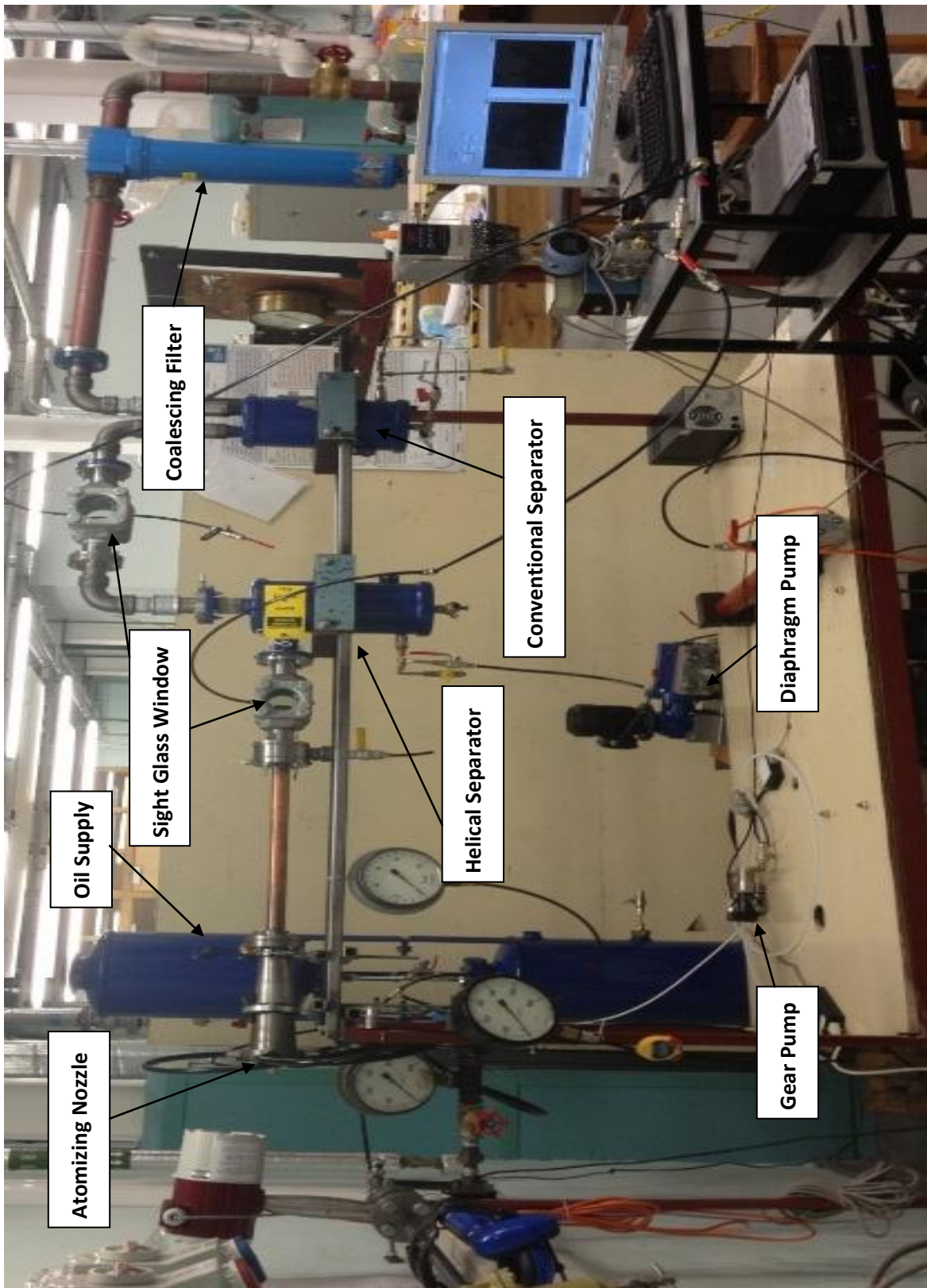
Figure 4.14: Experimental Test Facility

Figure 4.15: Line Diagram of Separator Measurement Setup

1:- Norgren 1" 20AG-X86/PH100 Pressure Regulator   2:- ½" Sierra Innova-Mass Series 240 Vortex Air Flowmeter   3:- Omega FMA-A2323 Air Flowmeter

4:- Delavan AL 45-03 Air Atomising Nozzle   5:- Omega PX 760 Differential Pressure Transmitter   6:- Silencer   7:- Henry 119-3/8" Check Valve

⬛ :- Ball Valve   ⬛ :- Throttle Valve   ⬛ :- Needle Valve   🔵 :- Pressure Gauge   ⬜ :- Flow Sight Glass

—— :- Compressed Air Line   —— :- Air/Oil Mixture Line   —— :- Oil Line   —— :- Pressure Measurement Line   ········· :- 4-20 mA Output Line

Figure 4.16: Line Diagram of Oil Supply/Recirculation Loop

A:- Oval Keromate-RN LSN39 Flowmeter   B:- Oval M-III LSF-40 Flowmeter   C:- Hydra Cell P200 Metering Pump   D:- HNP Microsystems MZR Micro Gear Pump
E:- Allen-Bradley Adjustable Frequency AC Drive   F:- National Instruments 16-Bit, 250kS/s M series Multifunction DAQ   G:- Henry S-4005 Oil Filter/Drier
H:- Mirlees IMO Positive Displacement Pump   I:- Chromalox 1000 W Oil Heater   J:- 24 V Power Supply   K:- 12 V Motor   L:- Rigaku Vacuum Feedthrough and Mixer
M:- 10 micron Filter   N:- Edwards High Vacuum Pump   (T) :- Thermocouple   (↻) :- Vacuum Pressure Gauge   ⋈ :- Ball Valve

──── :- Oil Line   ──── :- Degassing Line   ─·─·─· :- Electrical Connection   ─·─·─ :- Pressure Measurement Line·····   :- 4-20 mA Output Line

4.3.6 Setup for Malvern Spraytec Apparatus

The Malvern Spraytec apparatus employed for measuring the droplet size and distribution data at the inlet and outlet of the helical separator requires the laser beam to pass directly through a plane perpendicular to the direction of the gas-droplet flow on the centreline. To provide the necessary optical access, sight glass viewing windows were required directly upstream of the inlet and downstream of the outlet of the helical separator as can be seen in Figure 4.14. During the commissioning phase of the Spraytec apparatus contamination of the glass windows by incoming droplet was found to provide erroneous scattering data, therefore to prevent this from happening the glass was removed from the viewing window bosses ensuring no beam steering due to the formation of a liquid film on the glass. This was possible since the test facility was only operating at atmospheric pressure. However to allow droplet data to be acquired at an elevated system operating pressure an air purge system could be implemented creating a curtain of air over the glass window thus preventing droplets from fouling the surface (Marchetti & Svendsen, 2011).

To site the Spraytec apparatus at the measurement locations two adjustable height support platforms were manufactured to stand at either side of the main test rig support structure. This allowed the 1400 mm optical bench for the instruments optics to straddle the rig without interfering with the rest of the apparatus. To ensure accurate beam alignment and stability of the instrument a spirit level was used to ensure both support platforms were at the same height and the adjustable feet on the optical bench were at the same level each time the apparatus location was changed. Figure 4.17 shows the Spraytec in situ at the separator inlet (left image) and separator outlet (right image).
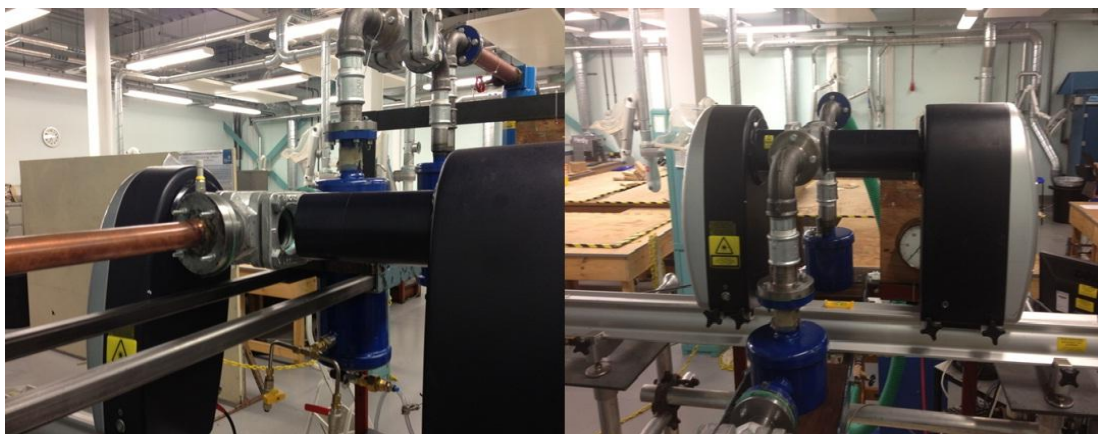
Figure 4.17: Malvern Spraytec Instrument at Helical Separator Inlet (Left) and Outlet (Right)

Although the liquid film removal device was in place upstream of the inlet flow sight glass boss, a volume of liquid accumulated on the lower surface of the boss over the duration of the droplet measurement test, as a result a drain was created in the boss allowing the carried over liquid to be extracted and quantified.

4.4 Test Rig Measurements

4.4.1 Test Rig Instrumentation

The parameters measured to determine the separation efficiency and pressure drop of the helical oil separator include; the mass flowrate of air entering the system; the flowrate of oil entering the system and the volume of oil separated by each separator; the flowrate of air supplied to the atomising nozzle; the temperature of air and oil entering the system; the pressure differential across the helical separator; and the droplet size and distribution at the inlet and outlet of the helical separator. The instrumentation was selected to ensure accurate measurements could be made over the range of operating conditions the separator was to be subject to whilst allowing the test facility to be operated in a safe and controlled manner. The parameters measured, the instrument employed and the accuracy of the measurement are given in Table 4.1.

4.4.2 Data Acquisition from Labview

The high range flowrate air flow meter, both oil flow meters and the differential pressure transducer were hardwired to a National Instruments NI-6210 unit which was connected through a USB to a PC where the data was displayed through a custom built Labview programme as shown in Appendix 1. From this the air flowrate was visually monitored continuously, the number of pulses generated by the oil flow meter was continually counted for each sample measurement (the numerical constant in Labview is altered dependent on the flow meter being used). From the total oil inlet flow count the inlet flowrate could be determined. The pressure drop data was sampled every 5 seconds and averaged over the duration of the test. The necessary data for the separation efficiency and pressure drop could then be extracted and input into a compiled spreadsheet.

Measurement Parameters	Measurement Method	Measurement Instrument	Variables to be Measured	Range	Accuracy
Air Flowrate (High)	Vortex Shedding	Sierra-Innova-Mass Series 240	Air Mass Flowrate; Temperature; Density	0.001-0.1444 kg/s	$\pm$0.7% for gases over 30:1 turndown
Air Flowrate (Low)	Capillary Thermal Technology	Omega FMA-A2323	Air Volumetric Flowrate	0-100 SLPM	$\pm$1% full range
Inlet Oil Flowrate (High)	Positive Displacement Gearing	Oval M-III LSF-40	Oil Volume (0.5 mL/pulse)	8.3-833.33 mL/min	$\pm$1% full range
Inlet Oil Flowrate (Low)	Positive Displacement Gearing	Oval Keromate-RN LSN39	Oil Volume (0.158 mL/pulse)	1.67-166.67 mL/min	$\pm$1% of reading or better
Inlet Oil Temperature	Differential Voltage	Type K Thermocouple	Oil Temperature	0-100°C	$\pm$1°C
Differential Pressure	Micro-processor	Omega PX760	Static Pressure Differential	0-18 mBar	$\pm$0.17% of nominal range
Separated Oil Volume	Measuring Cylinder	Kartell Kartell Kartell Pyrex Gradplex	Oil Volume	0-10 mL 0-25 mL 0-50 mL 0-100 mL 0-250 mL	$\pm$0.2 mL $\pm$0.5 mL $\pm$1.0 mL $\pm$1.0 mL $\pm$2.0 mL
Oil Droplet Size and Distribution	Laser Diffraction	Malvern Spraytec	Droplet Size and Distribution	0.1-900 µm (300 mm Lens)	Apparatus Better than 1%

Table 4.1: Parameters Measured and Equipment Used

4.4.3 Measurement of Separated Oil and Associated Issues

4.4.3.1 Separated Oil Volume

Due to the issues which will be discussed in section 4.4.3.2 in relation to gases entrained within the oil, the flowrate of oil separated by the primary, secondary and tertiary separation units discussed in the previous section had to be measured manually. This was achieved using graded measuring cylinders rather than by flowmeters in the oil return lines which would have allowed the test rig to be completely closed loop. The separated volume of oil from the helical and conventional separators is released from the oil collection chambers via the ball float assembly through a 3/8" flare connection on the cylindrical wall of the separator. This is drained from the unit into a measuring cylinder via a funnel. Dependent on the separated oil volume to be measured, which is dictated by the inlet oil

flowrate, the appropriate sized measuring cylinder, from the range shown in Table 4.1, is selected to reduce the measured volume error.

During the commissioning phase of the experimental test facility it was discovered that the output from the separator was inconsistent for each sample measurement due to the response of the internal mechanical ball float mechanism which controls the outflow of oil from the collection chamber. As a result multiple samples had to be obtained for each test operating condition and averaged to allow a true separation efficiency of the unit to be obtained, however this meant that each performance test required multiple hour's worth of data acquisition. A typical test run output oil volume variation over the duration of the test is shown in Figure 4.18. Each point plotted in Figure 4.18 is representative of the average flowrate returned by the separator for that particular sample measurement i.e. volume of oil measured divided by the time taken to collect. The volume and time dictated by the inlet oil flowrate being assessed. It can be seen from the graph that the response of the ball float mechanism displays the characteristics of a sinusoid. When a complete wave cycle is obtained it can be deduced that on averaging the data over one complete cycle the efficiency value obtained will accurately represent the separation efficiency of the unit at that condition. This is calculated by summing all the individual sample point flowrates and dividing by the number of samples obtained. For this particular flow condition the volume of oil collected for each measurement sample was around 200 mL with a time period of around 300 seconds. The number of samples obtained was 19 for flowrate condition shown in Figure 4.18 which required just over 2 hours.
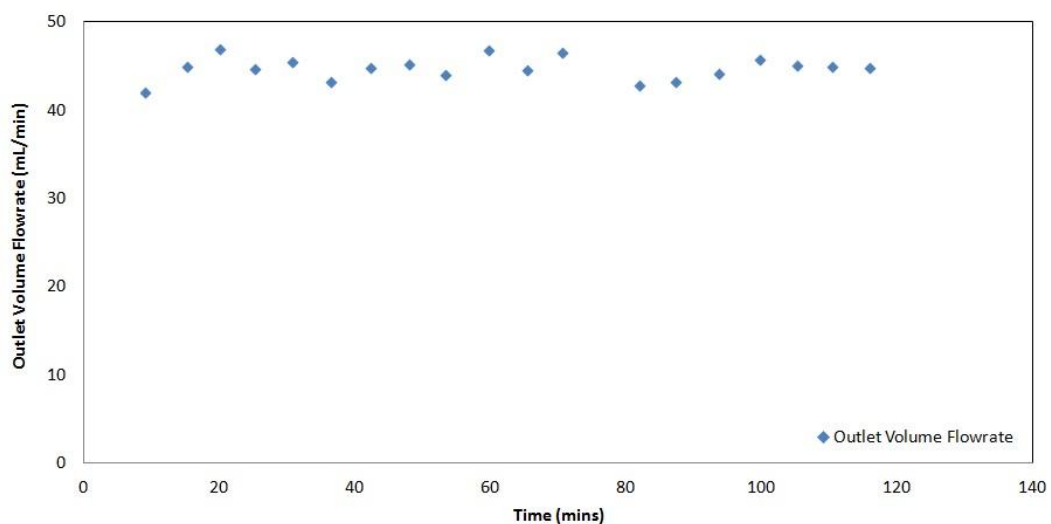
Figure 4.18: Separator Oil Output Volume Variation During Test Run

4.4.3.2 Issues Associated with the Lubricant Oil

The Emkarate RL 22H POE oil used in this investigation is prone to absorbing gases from the air and is also hygroscopic due to the molecular structure of the oil attracting water molecules. The process by which the oil droplets are mechanically generated uses air to atomise the incoming liquid by applying a high shear force to the fluid in the mixing chamber. The production of the oil droplets and the fact that the continuous phase fluid is also air leads to the gases in the air being absorbed by the oil thereby producing an air-oil mixture which enters the separator. When the separated volume of oil is returned by the separator and collected in the measuring cylinder it is seen to contain a significant volume of air micro bubbles. To ensure these micro bubbles were not produced as a result of the liquid jet entraining the surrounding air when it impacts on the volume of oil in the measuring cylinder the separated oil was delivered into the vessel below the liquid level and the micro bubbles were still seen to exist. It is due to this phenomenon that prevented the returned oil volume from being measured with a flowmeter since a false reading would have been produced hence the requirement for a manual measurement process. Each manual measurement of the separated oil volume required the micro bubbles to gravitationally separate before the reading could be obtained or else a false volume would be recorded. For a 250 mL measuring cylinder almost completely filled with separated fluid it was found that approximately 2 mL of the initial volume reading was micro bubbles. The sample points shown in Figure 4.18 represent the absolute volume of oil returned by the separator after the micro bubbles have had time to settle out.

The separated oil is then transferred back into the oil storage vessel and recirculated into the rig. As a result of the absorption of the gases into the oil, when pumping the recycled oil the pump begins to cavitate. This is due to the absorbed gases being compressible resulting in the pump underperforming and the required liquid flowrate not being delivered. When the test rig is operated at an elevated pressure the effects of this problem are magnified, as a result the ability to carry out performance testing at a system pressure greater than 3 BarG proved not to be possible with either oil pumps; hence it was this issue which defined the upper limitations of the test conditions.

To mitigate against these cavitation problems a vacuum degassing process was developed where the oil was batch degassed after each separator performance test was complete. To enhance the degassing process the oil is heated to around 80°C and when the vacuum

pump is running the oil volume is mechanically mixed. By carrying out this degassing process after each test ensures the degree of gases in the oil is kept to a minimal hence preventing unnecessary cavitation of the pump and unstable oil flowrates to the atomising nozzle.

4.4.4 Measurement of Liquid Film Volume

A schematic of the setup used for evaluation of the upstream flow conditions to the helical separator is shown in Figure 4.19 from which the percentage volume of liquid film and droplet mist can be determined. The oil is injected into the system through the atomising nozzle (V_{in}) and is transported through the inlet pipe to the liquid film removal device where the stratified liquid film is gravitationally drained into the liquid holdup vessel. Immediately downstream of the liquid film removal device is a sight glass window which is used to observe the flow and to allow the droplet size and distribution entering the separator to be measured, as will be discussed in the next section. A liquid pool was discovered to gather in the sight glass boss therefore a drain connection was added to it allowing the liquid pool to drain into the liquid holdup vessel. This results in a droplet only flow to enter the separator ($V_{droplets}=V_{in}-V_{liquid\ film}$). At the outlet of the separator a second sight glass window is installed to allow the droplet data leaving the separator to be assessed at which point there is only a fraction of the initial inlet volume of oil still present which was not separated by the system ($V_{out}=V_{in}-V_{liquid\ film}-V_{separator}$).
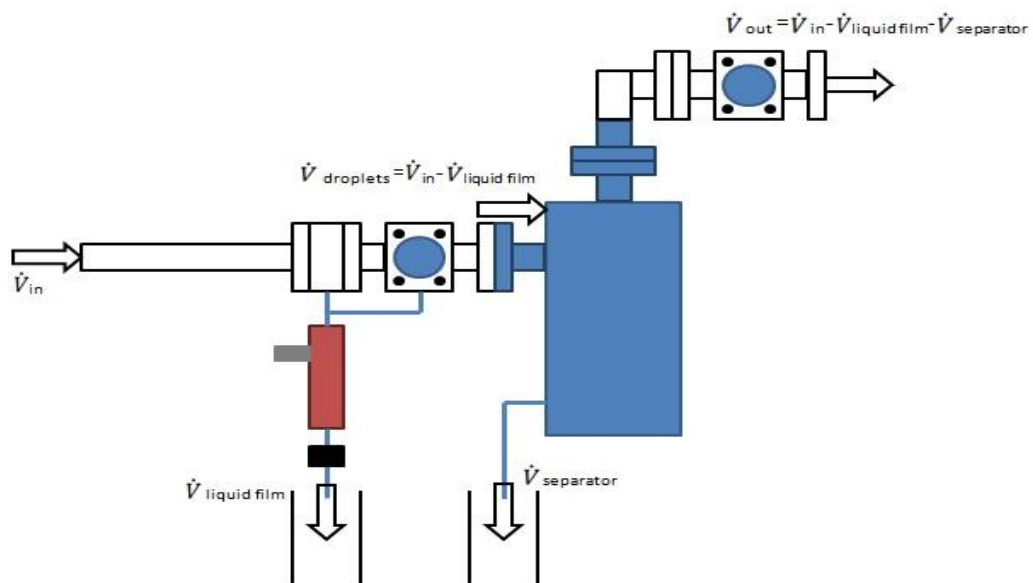
Figure 4.19: Schematic of Setup for Evaluation of Upstream Flow Conditions

4.4.5 Droplet Size Measurements

To gain further information on the conditions which exist at the inlet to the separator and how these compare to those which are believed to exist in practice in the compressor discharge line requires the measurement of the droplet size and distribution just upstream of the inlet to the separator. Furthermore in order to characterise the droplet performance of the helical oil separator and produce the corresponding grade efficiency curve requires the droplet size and distribution data at the outlet of the separator to be measured also. To acquire this data for the separator operating at atmospheric pressure a Malvern Spraytec 10K STP5291 model, which employs laser-diffraction theory, was obtained on loan from the EPSRC equipment pool. This method of droplet size determination has been employed to investigate the performance of horizontal separators in oil-injected compressor units which are found in refrigeration systems with the resulting droplet sizes ranging from 1.9-188 microns (Feng, et al., 2008). Since the flow regime in the inlet pipe to the separator at atmospheric pressure consists of a stratified liquid film and droplet mist, the liquid film was extracted as previously described, allowing only the gas-droplet core to pass through the Spraytec measurement volume. Simmons and Hanratty also applied this method for measuring the droplet size in a horizontal annular flow with a liquid film (Simmons & Hanratty, 2001).

4.4.5.1 Laser Diffraction Theory

The Spraytec apparatus employs laser diffraction theory as its measurement principle to determine the size and distribution of the droplets in a spray which can range in size from 0.1-2000 microns. The system uses Mie scattering theory and Fraunhofer approximation to accurately measure the droplet data and output the droplet size history from which the necessary size and distribution parameters can be obtained. A 4 mW Helium-Neon collimated laser beam of 632.8 nm is emitted from the optic and passes through the measurement volume where it is diffracted by a certain amount dependent on the droplet size in the flow. The receiver can be fitted with two different lenses; a 300 mm or 750 mm lens option with the former used to measure droplets in the 0.1-900 microns range and the latter used for the 2-2000 micron range. Based on the droplet sizes generated by the atomising nozzle the 300 mm lens was selected for this investigation. It has been highlighted that the selection of the correct lens for the detector is highly important to minimise any errors in the measurement (Combellack & Matthews, 1981), (Azzopardi, 1985). Due to the range of techniques used for different flow systems by various workers it

makes it difficult to determine whether the differences in drop size distributions are due to the artefacts of the system or the technique (Simmons & Hanratty, 2001).

The lens focuses the scattered light from the measurement volume onto a series of detector rings as shown in Figure 4.20. 36 detector rings are present in the Spraytec apparatus which are able to capture beam diffraction over a wide range of angles ranging from 0.015-17°. The light energy which is incident on the detector rings is converted to a droplet diameter using a series of algorithms in the operating software where the data is displayed as a size history plot indicating any changes in droplet sizes over time. Any rapid changes in the droplet characteristics are captured due to the apparatus sampling 10,000 samples per second.
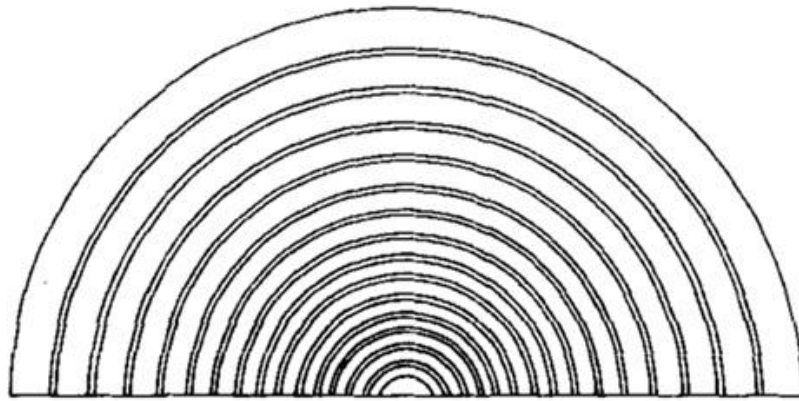
Figure 4.20: Receiver which Consists of a Number of Concentric Rings Separated by Insulating Layers

4.4.5.2 Size Distribution

The spread of droplet sizes in a suspension can be generally described as being mono-dispersed or poly-dispersed; the latter defines a distribution in which the standard deviation is greater than 10% of the mean droplet diameter. The simplest way of displaying the distribution of droplet sizes is to choose intervals, Δd_d, and display the value in each interval as a percentage of the total number of droplets in the sample in the form of a histogram. In the separation literature this distribution is referred to as the probability density function or PDF, of which the normalised form is given in equation 4.1 with $\widetilde{f_n}(d_{di})$ representing the number frequency;

$$\sum_{i=1}^{N} \widetilde{f_n}(d_{di}) = 1 \qquad (4.1)$$

If the size of the intervals is continually reduced to the point where Δd_d approaches zero this produces a continuous frequency distribution curve. Normailising the continuous distribution results in the integral;

$$\int_0^{d_{dmax}} f_n(d_d)dd_d = 1 \qquad (4.2)$$

where d_{dmax} is the maximum droplet diameter. The continuous cumulative distribution is given through the integral of the continuous frequency distribution given by equation 4.3 and when plotted graphically produces the S-shaped curve which is frequently used to describe the separator cut size, d_{50}.

$$F_n(d_d) = \int_0^{d_d} f_n(\zeta)d\zeta \qquad (4.3)$$

Droplet sizes are commonly described in terms of the Sauter Mean Diameter (SMD) since it is more appropriate than a number mean since it represents the drop size that contains the largest volume; i.e. it is the ratio of particle volume to surface area in a distribution as defined in equation 4.4;

$$D_{Sa} = \frac{\int_0^{d_{dmax}}[d_d{}^3 f_n(d_d)dd_d]}{\int_0^{d_{dmax}}[d_d{}^2 f_n(d_d)dd_d]} \qquad (4.4)$$

The most frequently used distribution for representing droplet size distributions within sprays is the function of Rosin Rammler (Mugele & Evans, 1951), and is given in equation 4.5 in terms of the cumulative volume distribution;

$$F_v(d_p) = 1 - exp\left[-\left(\frac{d_d}{\delta}\right)^n\right] \qquad (4.5)$$

where δ and n are empirical constants and for $F_v(0)=0$ and $F_v(\infty)=1$. The two constants can be obtained by plotting the volume distribution with log-log coordinates; by taking the logarithm of equation 4.5 results in;

$$\ln[-\ln(1-F_v(d_d))] = n\ln d_d - n\ln\delta \qquad (4.6)$$

The gradient of the plot $-\ln[1-F_v(d_d)]$ versus droplet diameter plotted on log-log paper allows the value of n to be determined. The second constant δ is given by using the value of n obtained and the mass median diameter;

$$\delta = \frac{d_{dmM}}{0.693^{\frac{1}{n}}} \qquad (4.7)$$

where d_{dmM} is the mass median droplet diameter.

A typical droplet size sample measurement captured using the Spraytec apparatus is shown in Figure 4.21.
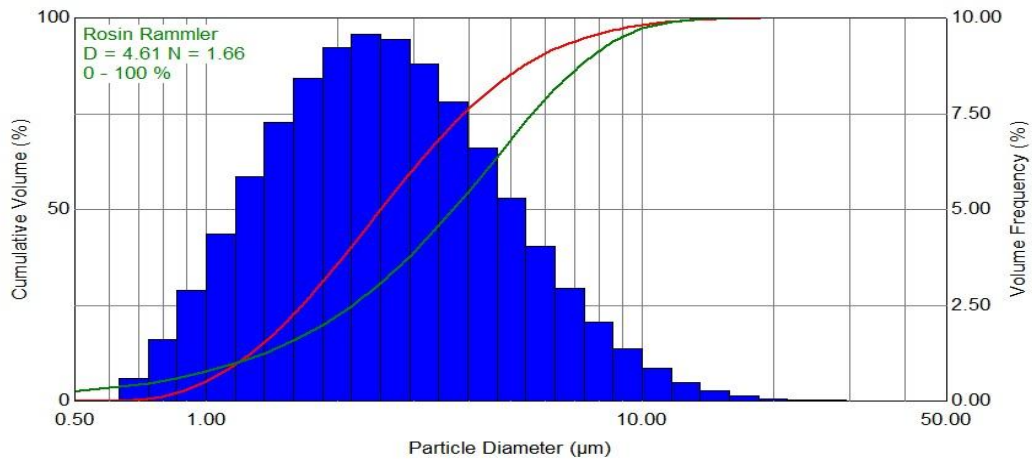
Figure 4.21: Droplet Size Distribution Sample Measurement

4.5 Test Rig Operation

4.5.1 Liquid Film and Droplet Separation Efficiency and Pressure Drop Measurements

The operating procedure for the test facility is presented in detail in Appendix 2 and when followed allows separation efficiency and pressure drop measurements to be made safely and accurately.

The error associated with the separation efficiency determination is dependent upon the accuracy of the inlet oil flowmeter combined with the measuring cylinder accuracy used to collect the separated oil. The latter is dependent upon the volume flowrate of oil being separated, however based on the accuracy of the measuring cylinder which can lead to the largest error the overall experimental measurement error was ±3%. The accuracy of the oil flowmeters were checked on a regular basis using a 250 mL measuring cylinder, which has an accuracy of ±0.8%, and found to always be within ±1% of the measured value. The repeatability of the average separation efficiency measurement for a particular flow condition test was found to be within 2%. The overall mass balance of oil for each separation efficiency test was also always within 2%.

4.5.2 Liquid Film Volume Fraction and Droplet Only Separation Efficiency Measurements

The liquid film removal device and liquid film holdup vessel shown in Figure 4.12 and Figure 4.13 should be installed into the test rig between the downstream flange of the inlet pipe and the inlet flange of the helical oil separator. The operation of the test facility for the quantification of the liquid film fraction is the same as that outlined in Appendix 2. The additional procedures required for this measurement process are given in Appendix 3.

The error and repeatability associated with this separation efficiency determination is the same as for the combined liquid film and droplet separation efficiency measurements as discussed in section 4.5.1.

4.5.3 Droplet Size and Distribution Measurements

In carrying out the droplets size and distribution measurements at the inlet and outlet of the helical oil separator the coalescing filter downstream of the conventional separator is removed and the side channel blower, used in chapter 3 of this thesis, is attached to the outlet of the conventional separator to assist in drawing the air flow through the system. Without the side channel blower in place the droplet mist was found to diffuse into the laboratory from the measurement locations since the glass had to be removed from the flow sight glass bosses. The coalescing filter had to be removed since it generated a significant pressure drop across the system when in place therefore making the side channel blower ineffective. The procedure for obtaining the droplet data is outlined in Appendix 4.

Although the accuracy of the Spraytec apparatus itself is better than 1%, the overall error of the droplet size measurements is found to be greater. Fouling of the optics due to stray droplets impacting on the lenses was found to generate a peak in the droplet distribution graph. This peak would record that a large droplet diameter, which was significantly out with the rest of the droplet diameters being measured in the sample, was present in the flow and hence skew the droplet distribution data towards the large diameter. Based on a discussion with an expert from Malvern Instruments, it was decided that these outlier large droplet diameters were not representative of the flow being measured and were removed from the data set. The repeatability of each droplet size and distribution measurement was found to have a maximum value of ±10%. As a result for each flow condition the

measurement was repeated 3 times from which an average value was obtained and used to produce the graphs for distribution at the inlet and outlet and the GEC's.

Due to the measurement and system requirements for obtaining the data required to produce the GEC's for the separator the separated liquid volume data, section 4.5.2, had to be acquired independently of the droplet size and distribution measurements, section 4.5.3.

4.6 Experimental Test Conditions

As discussed at the start of this chapter the Henry Technologies helical oil separator operates with a range of fluids of different densities over a range of discharge flowrates. To allow the effects of these factors to be captured using the custom built test facility the following properties were varied; system operating pressure, compressed air flowrate, injected oil flowrate and separator geometry. Due to the aforementioned issues associated with the absorption of gases into the oil and the impact this had on the ability to pump a range of liquid flowrates to the system at pressure, all the data obtained for this investigation for the separation efficiency and pressure drop of the helical oil separator was at either 0 or 3 BarG. Given the discharge gas volume flowrate for the separator is recommended to be between 25% and 100% of the maximum value 18.7 m^3/hr for the S-5190 unit used in this study, and the entrained oil mass fraction is between 1% and 10% mass fraction, the respective air and oil flowrates for a particular system operating pressure can be determined using equation 4.8 to equation 4.11;

$$\dot{m}_{air} = \frac{18.7\left(\frac{\% \, of \, discharge \, volume}{100}\right)}{3600} \rho_{air} \qquad (4.8)$$

where ρ$_{air}$ is computed from;

$$\rho_{air} = \frac{(P_{Gague} + P_{atmos})}{RT_{air \, compressor}} \qquad (4.9)$$

and the oil mass fraction is;

$$\chi = \frac{\dot{m}_{oil}}{\dot{m}_{air} + \dot{m}_{oil}} \qquad (4.10)$$

therefore the oil volume flowrate can be calculated from;

$$\dot{V}_{oil} = \frac{\frac{\chi \dot{m}_{air}}{1 - \chi}}{\rho_{oil}} \qquad (4.11)$$

The test matrix given in Table 4.2 summaries the conditions for which the experimental data has been obtained;

Operating Pressure (BarG)	Discharge Volume (%)	Oil Mass Fraction (%)	Separator Type (Inlet Flow Condition)
0	100	1,2,3,4,5,6,7,8,9,10	Standard Unit (Liquid Film + Droplets Separation Efficiency)
	50	1,2,3,4,5,6,7,8,9,10	
	25	1,2,3,4,5,6,7,8,9,10	
3	100	1,2,3,4,5,6,7,8,9,10	Standard Unit (Liquid Film + Droplets Separation Efficiency)
	50	1,2,3,4,5,6,7,8,9,10	
	25	1,2,3,4,5,6,7,8,9,10	
0	100	2.5,5,10	Standard and No Mesh Unit (Droplet Only Separation Efficiency + Liquid Film Volume Fraction)
	50	2.5,5,10	
0	100	2.5,5,10	Standard and No Mesh Unit (Droplet Size and Distribution)
	50	2.5,5,10	

Table 4.2: Experimental Test Matrix

4.7 Experimental Results

4.7.1 Liquid Film and Droplets Separation Efficiency Results

The separation efficiency results for the standard unit tested at 0 BarG (atmospheric pressure) and 3 BarG are shown graphically for the three discharge volume flowrates with oil mass fractions ranging from 1% to 10%. The absolute separation efficiency for the unit which is plotted in Figure 4.22 to Figure 4.24 is determined using equation 4.12;

$$\eta_{absolute} = \frac{\left(\frac{\sum helical\ unit\ volume\ flowrate\ separated}{number\ of\ sample\ measurements}\right)}{\left(\frac{\sum inlet\ oil\ volume\ flowrate}{number\ of\ sample\ measurements}\right)} x100 \qquad (4.12)$$
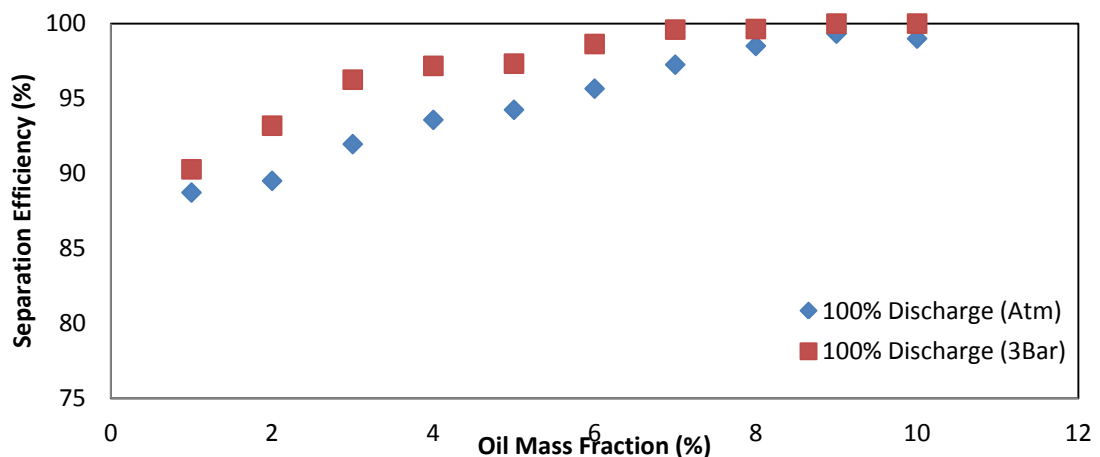
Figure 4.22: Standard Unit Separation Efficiency at 100% Discharge Volume
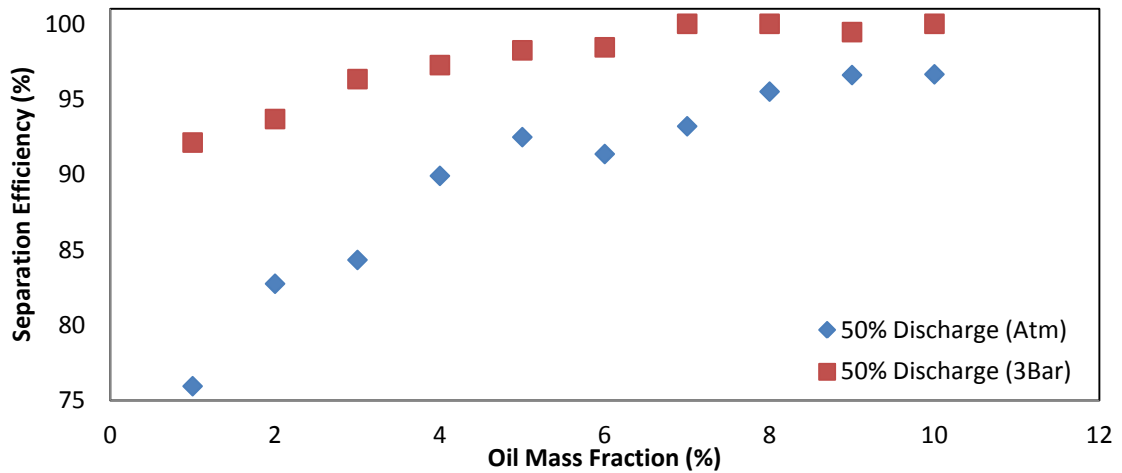
Figure 4.23: Standard Unit Separation Efficiency at 50% Discharge Volume
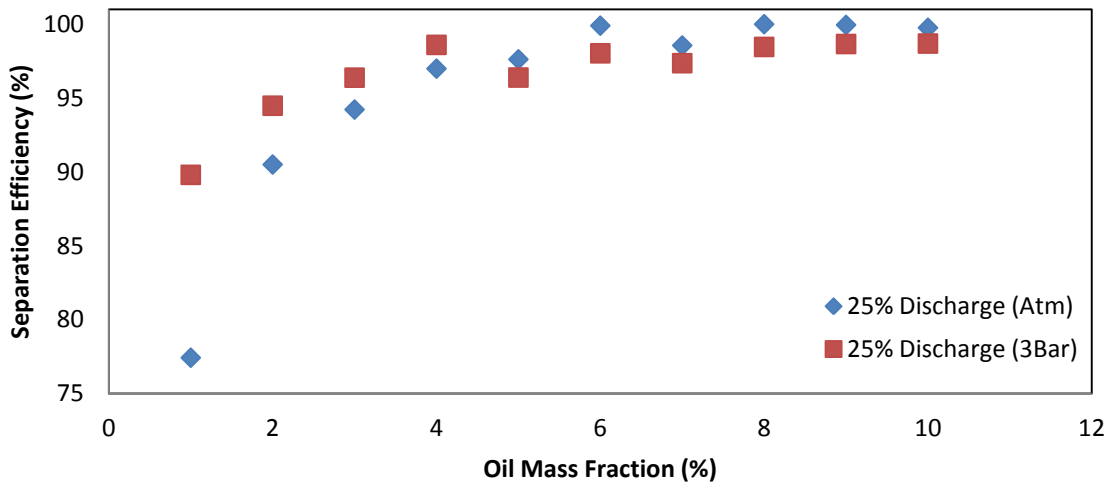
Figure 4.24: Standard Unit Separation Efficiency at 25% Discharge Volume

4.7.2 Liquid Film Volume Fraction and Droplet Only Separation Efficiency Results

Extracting the liquid film directly upstream of the separator inlet allows the efficiency of the separator to be determined subject to a droplet only inlet flow, which is typical of the flow conditions which the unit experiences in practice. Since the results of this test are required to validate the two phase flow modelling of the separator this piece of work was carried out for both the standard and no mesh separator units at atmospheric pressure. The liquid film volume fraction is determined from equation 4.13 given in Figure 4.25 and Figure 4.26;

$$\%Vol\ Liquid\ Film = \frac{\left(\frac{\sum liquid\ volume\ flowrate\ extracted}{number\ of\ sample\ measurements}\right)}{\left(\frac{\sum inlet\ oil\ volume\ flowrate}{number\ of\ sample\ measurements}\right)} x100 \qquad (4.13)$$

155
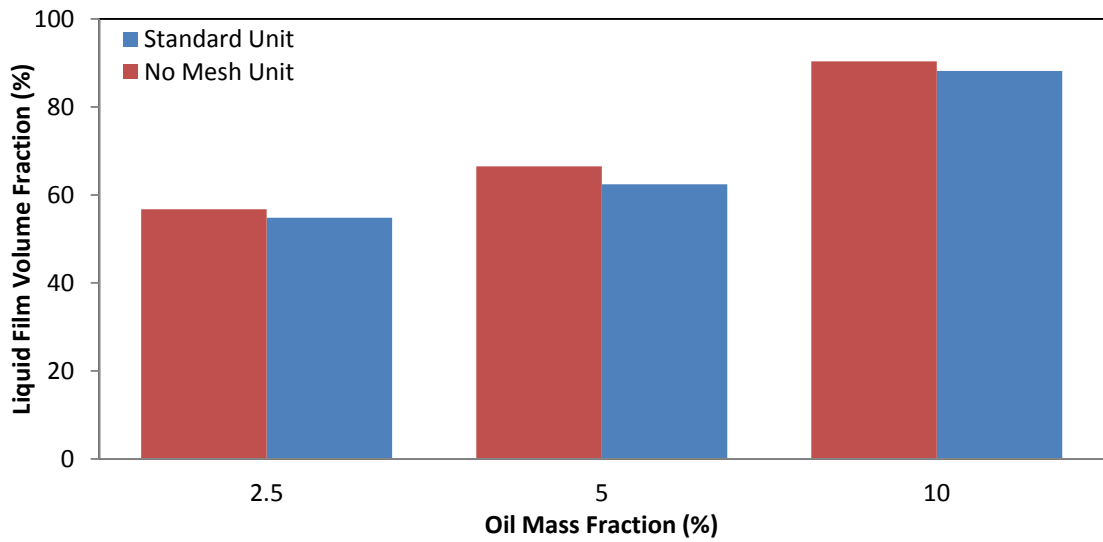
Figure 4.25: 100% Discharge Film Extraction Volume Fractions
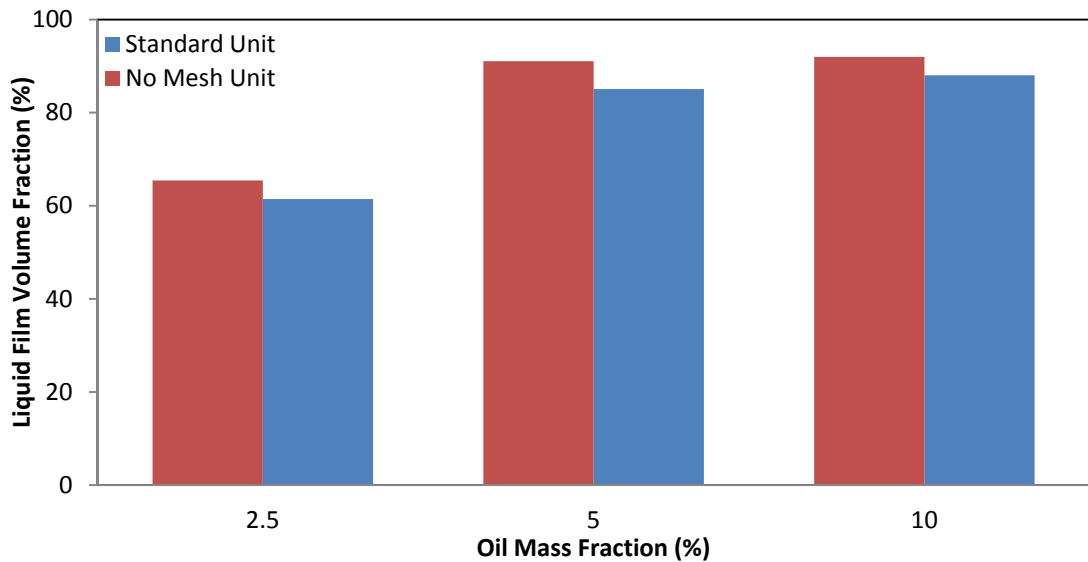
Figure 4.26: 50% Discharge Film Extraction Volume Fractions

With the liquid film removed and quantified the droplet only separation efficiency of the units can be calculated using equation 4.14. Since significant volumes of the injected inlet volume of liquid are removed prior to entering the separator the oil mass fraction values presented for the droplet only separation efficiency are given as the actual mass fraction of droplets the separator is subject to. Due to the slight variation in the volume fraction of the liquid film between the standard and no mesh units the actual mass fractions for the droplet only conditions vary slightly. The discrepancies are only marginal and are associated with the experimental volume measurement accuracy. The results from the droplet only separation efficiency measurements are given in Figure 4.27 and Figure 4.28;

156

$$\eta_{droplet} = \frac{\left(\frac{\sum helical\ volume\ flowrate\ separated}{number\ of\ sample\ measurements}\right)}{\left(\frac{\sum inlet\ oil\ volume\ flowrate}{number\ of\ sample\ measurements} \quad \frac{\sum liquid\ film\ volume\ flowrate\ extracted}{number\ of\ sample\ measurements}\right)} x100 \quad (4.14)$$
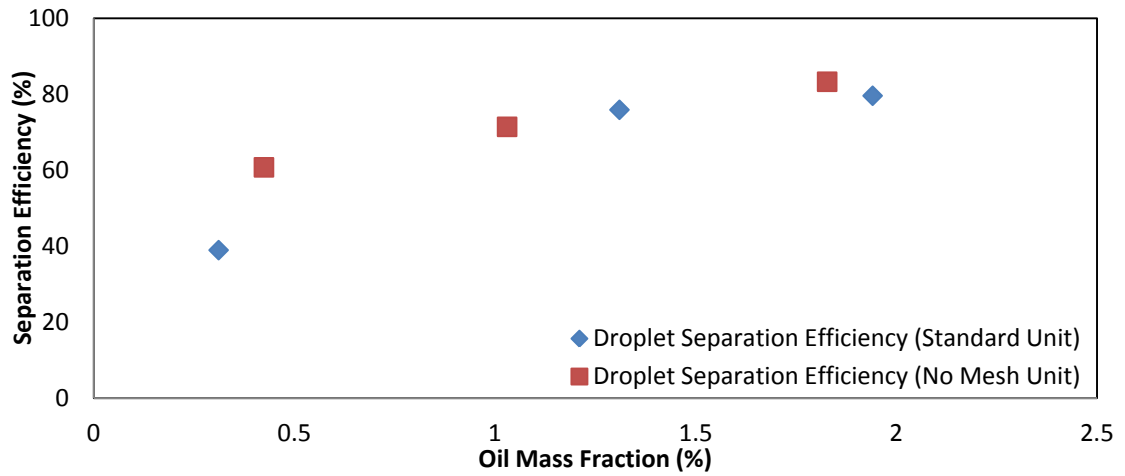
Figure 4.27: 100% Discharge Separator Droplet Separation Efficiency
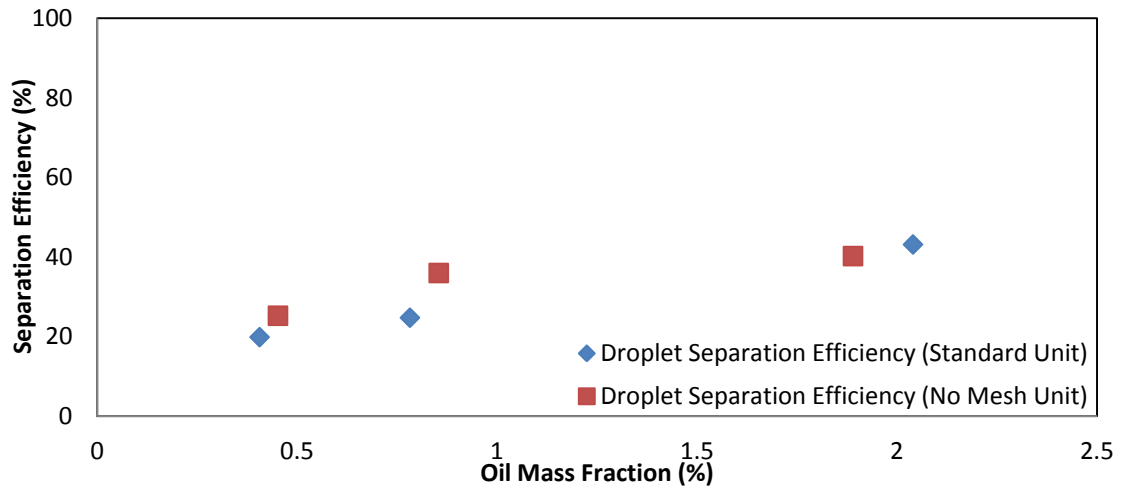
Figure 4.28: 50% Discharge Separator Droplet Separation Efficiency

The overall system separation efficiency for the standard and no mesh units; liquid film volume flowrate plus helical unit droplet flowrate separated, given by equation 4.15, are presented in Figure 4.29 and Figure 4.30;

$$\eta_{droplet} = \frac{\left(\frac{\sum helical\ unit\ volume\ flowrate\ separated}{number\ of\ sample\ measurements} + \frac{\sum liquid\ film\ volume\ flowrate\ extracted}{number\ of\ sample\ measurements}\right)}{\frac{\sum inlet\ oil\ volume\ flowrate}{number\ of\ sample\ measurements}} x100 \quad (4.15)$$
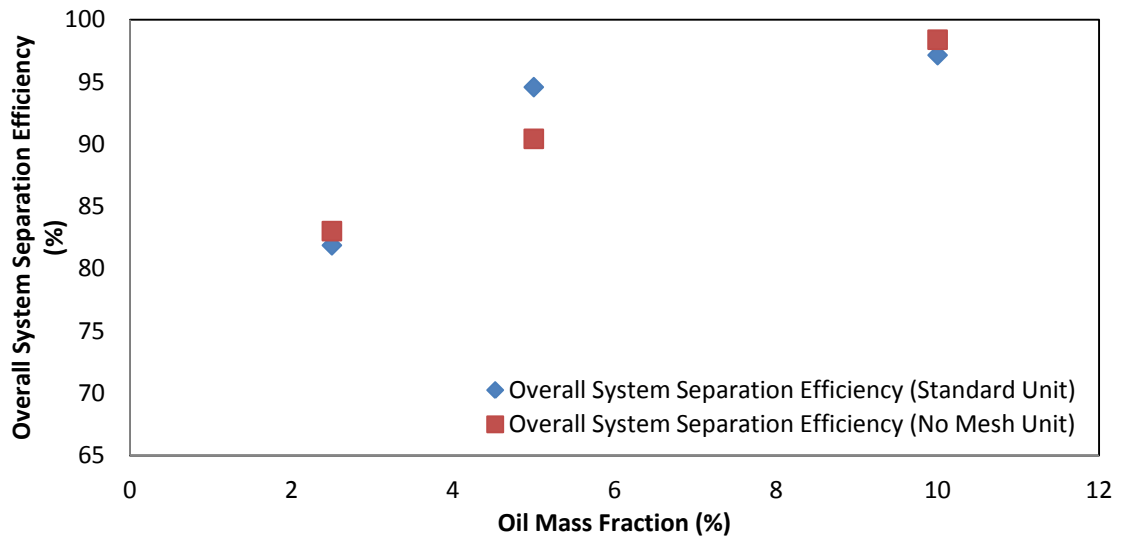
Figure 4.29: 100% Discharge Overall System Separation Efficiency
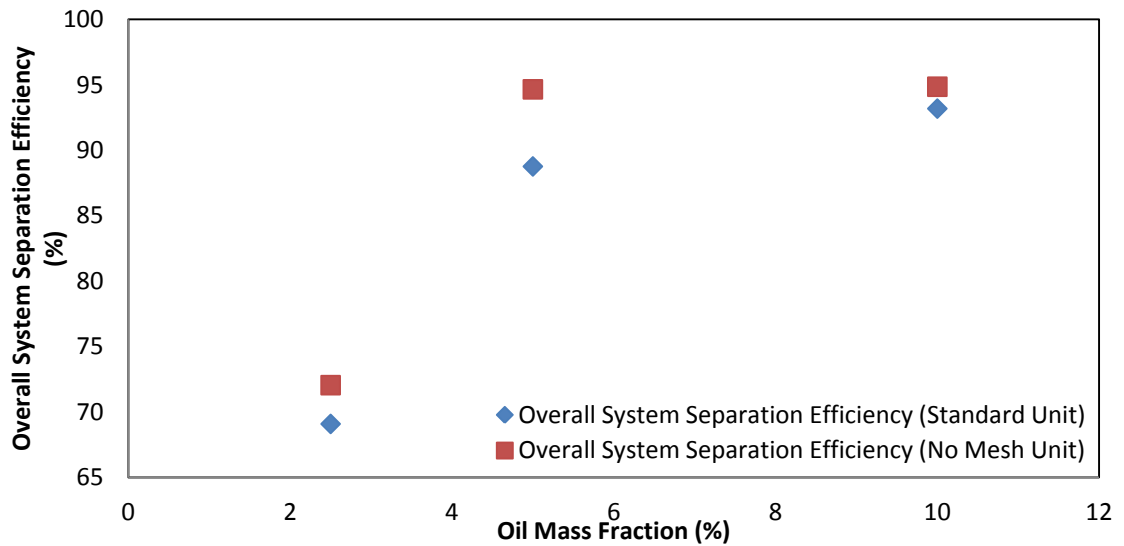
Figure 4.30: 50% Discharge Overall System Separation Efficiency

4.7.3 Droplet Size and Distribution Results

The droplet size and distribution at the inlet to the separator is plotted with the data at the outlet for both the standard and no mesh units as this allows a direct comparison of the separation efficiency of both units since the inlet condition is independent of the unit being tested. The droplet size versus volume frequency, defined as the percentage volume of a particular droplet size in the spray, for 100% discharge flowrate are given in Figure 4.31 to Figure 4.33 and for 50% discharge flowrate in Figure 4.34 to Figure 4.36.

158
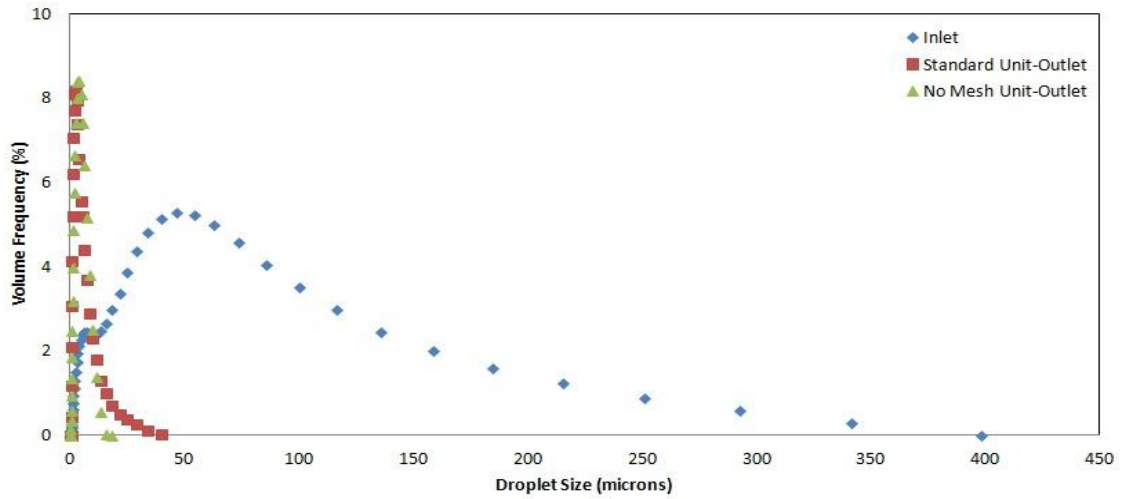
Figure 4.31: 100% Discharge with 10% Oil Mass Fraction Droplet Size Distribution at Inlet and Outlet
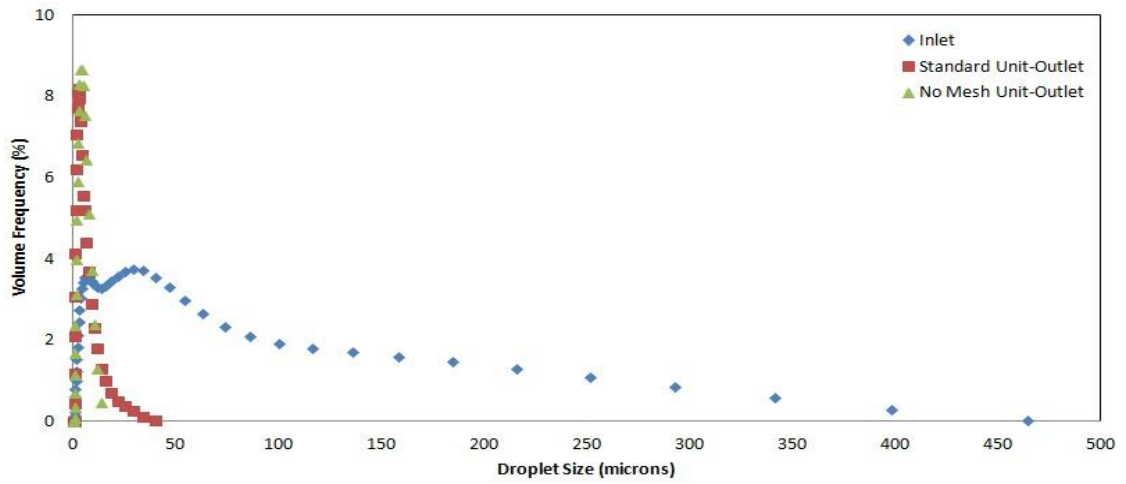
Figure 4.32: 100% Discharge with 5% Oil Mass Fraction Droplet Size Distribution at Inlet and Outlet
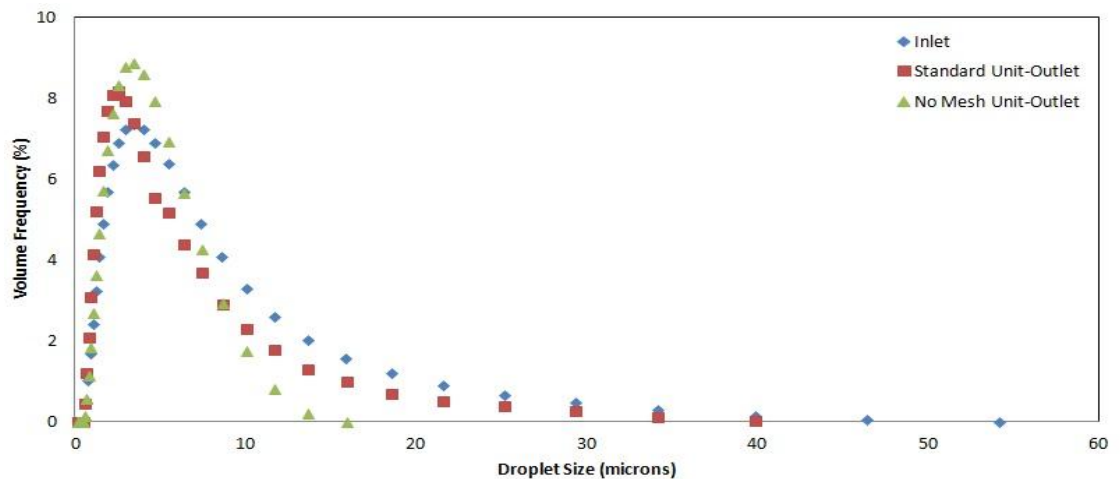
Figure 4.33: 100% Discharge with 2.5% Oil Mass Fraction Droplet Size Distribution at Inlet and Outlet

159
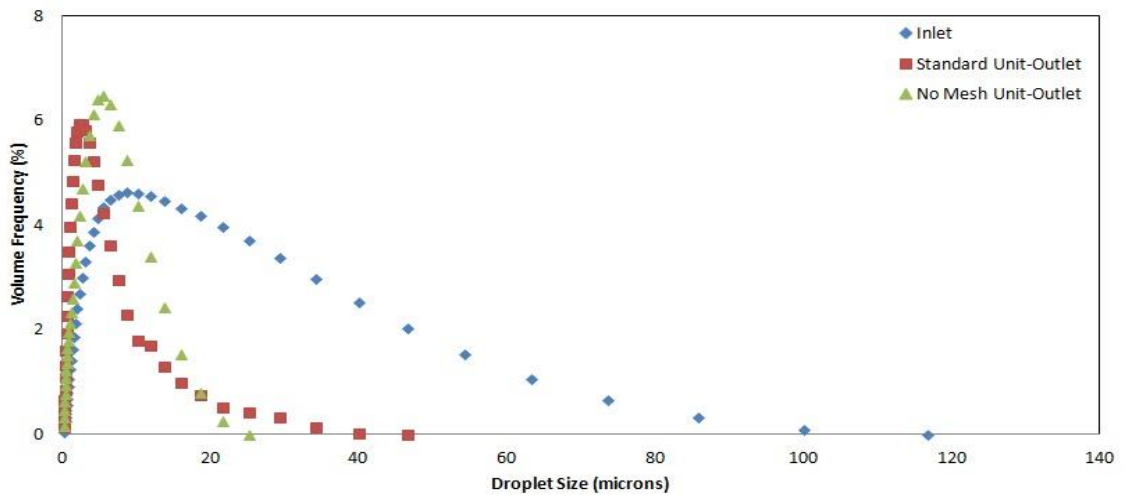
Figure 4.34: 50% Discharge with 10% Oil Mass Fraction Droplet Size Distribution at Inlet and Outlet
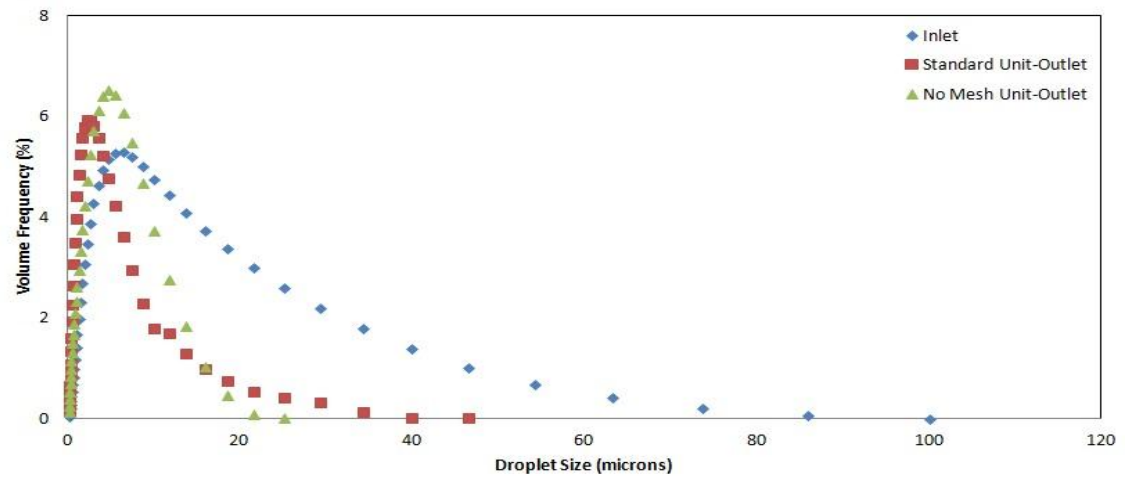
Figure 4.35: 50% Discharge with 5% Oil Mass Fraction Droplet Size Distribution at Inlet and Outlet
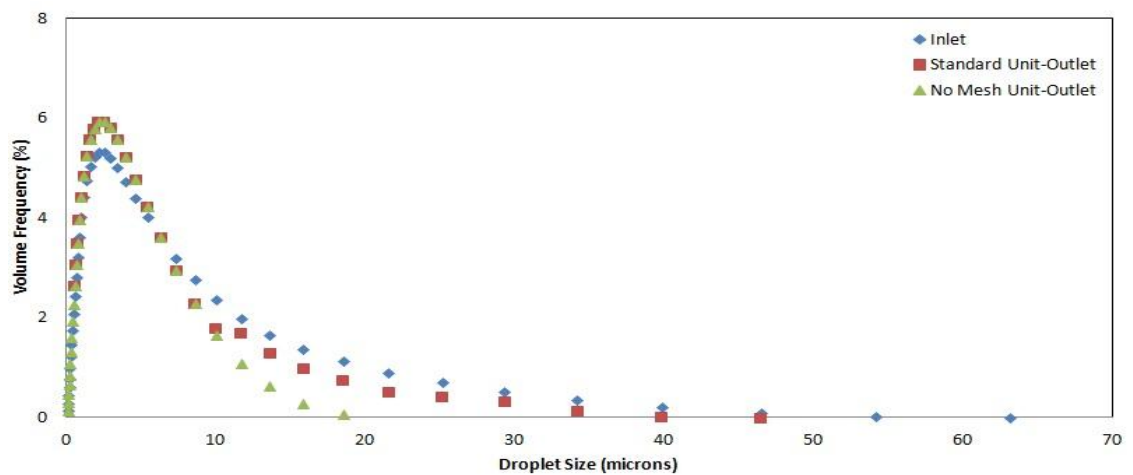
Figure 4.36: 50% Discharge with 2.5% Oil Mass Fraction Droplet Size Distribution at Inlet and Outlet

160

Combining the droplet size measurements at the inlet and outlet of the separators with the liquid film extraction data and the droplet separation efficiency of both the standard and no mesh units GEC's can be produced to characterise the droplet separation performance of the separators. The calculation procedure used to produce the GEC is given by equation 4.16 with the resulting GEC's shown in Figure 4.37 to Figure 4.40.

$$\eta_{GEC} = \left(1 - \left(\frac{(\%Volume\ frequency x Volume\ flowrate)_{Outlet\ droplet\ mist}}{(\%Volume\ frequency x Volume\ flowrate)_{Inlet\ droplet\ mist}} \right) x100 \right) \qquad (4.16)$$
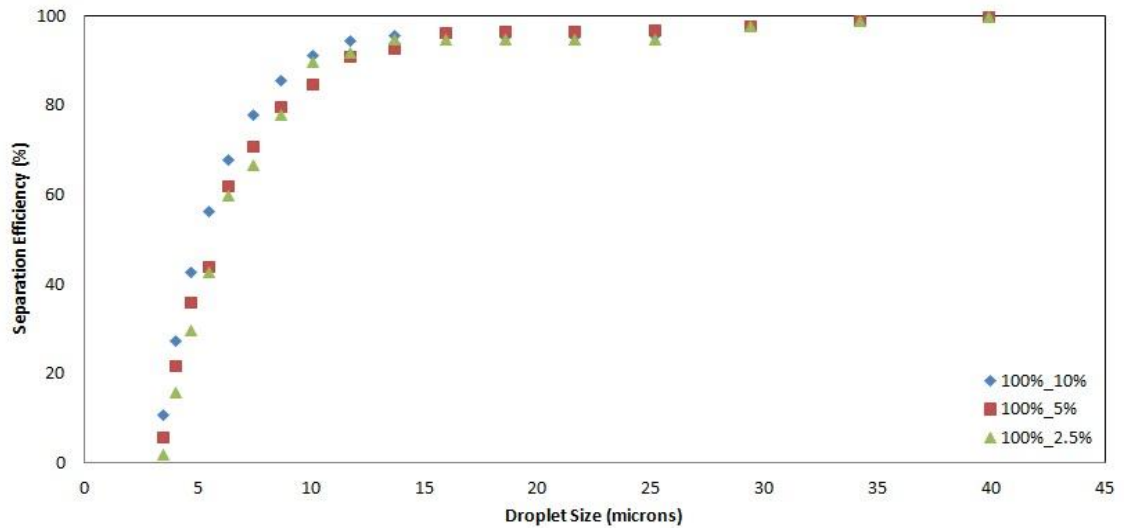
Figure 4.37: Standard Unit 100% Discharge Grade Efficiency Curve
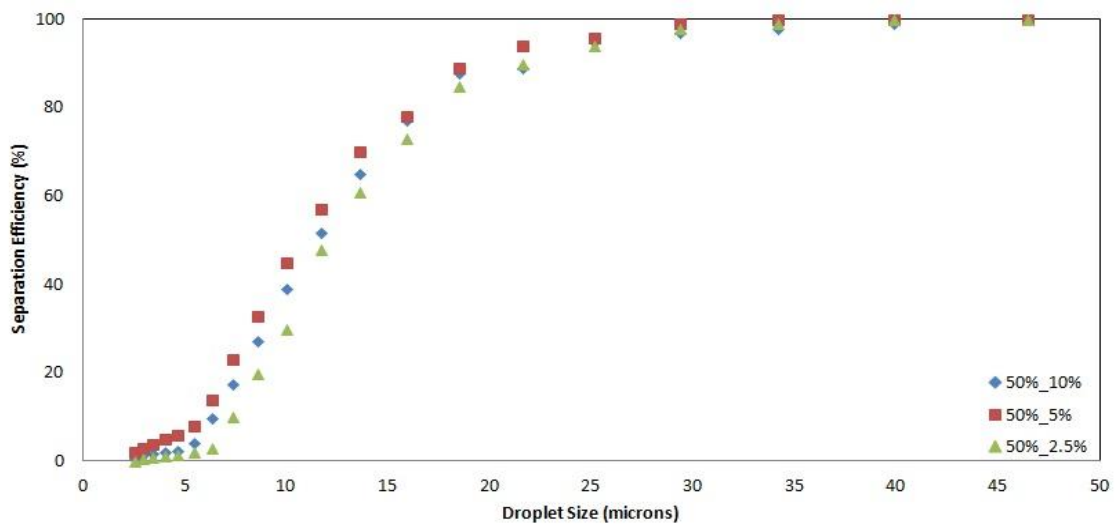
Figure 4.38: Standard Unit 50% Discharge Grade Efficiency Curve
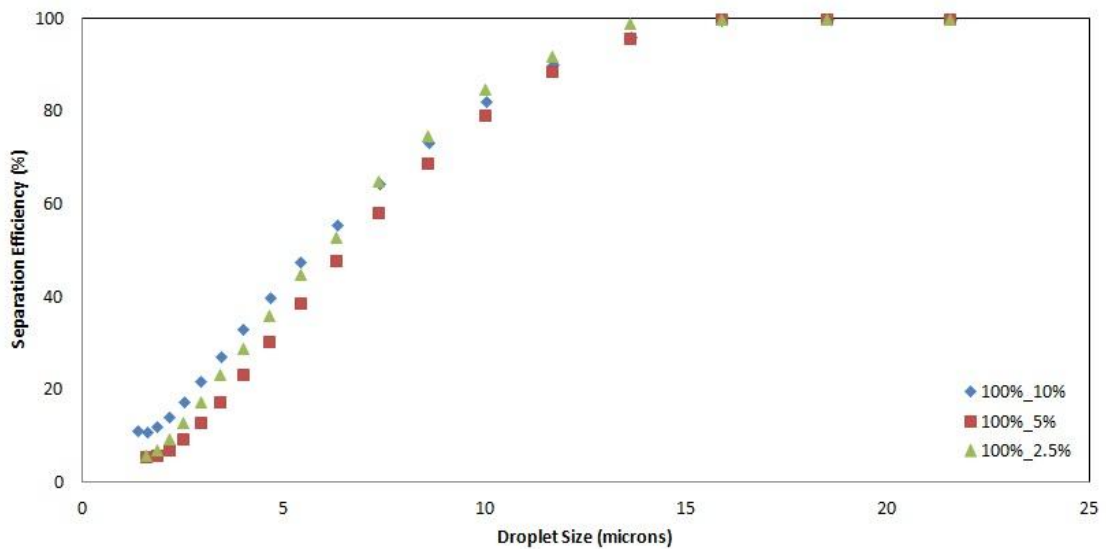
Figure 4.39: No Mesh Unit 100% Discharge Grade Efficiency Curve
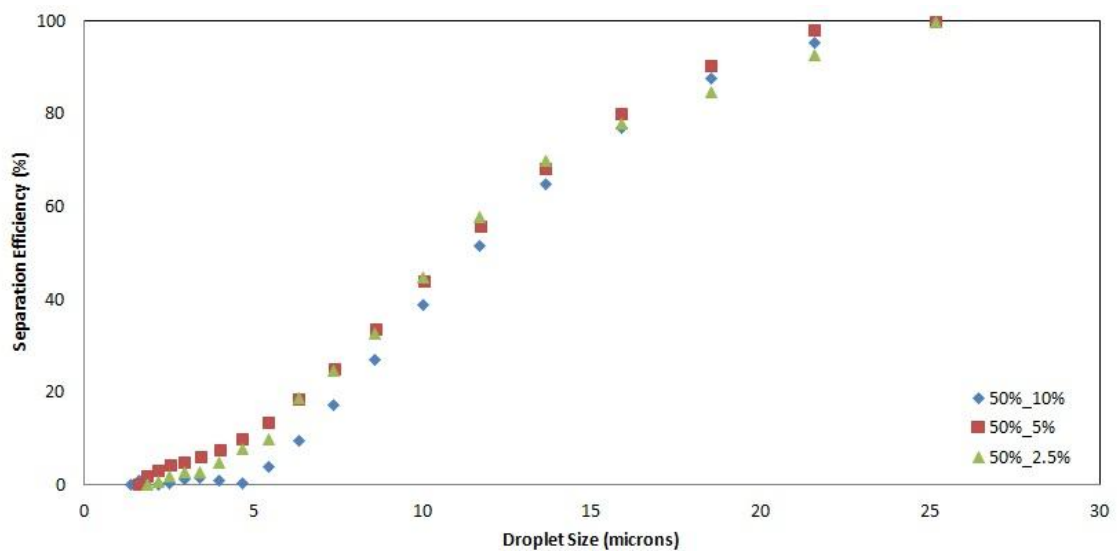
Figure 4.40: No Mesh Unit 50% Discharge Grade Efficiency Curve

4.7.4 Pressure Drop Results

The pressure drop across both standard and no mesh separator units has been determined with the liquid film extracted upstream of the inlet static measurement point. Initially the static pressure measurement points were located in the inlet and outlet flanges of the helical separator units, however during the commissioning phase of this investigation the pressure drop reading were found to be erratic with a liquid load present; the readings were however more stable with no liquid load. The erratic nature was believed to be due to the transient nature of the build up and removal of liquid film at the static pressure tapping point. As a result the static pressure taps were created on the upper surfaces of the inlet

and outlet flow sight glass bosses, which are non-standard measurement locations however the measured pressure drops were in line with those predicted from the CFD simulations therefore the tapping locations were deemed acceptable.

The diameter of the actual tapping holes were kept to 1 mm to prevent the readings from being subject to any distortions in the flow such as vortex development, fluid turbulence and fluid stagnation which would occur if the diameter of the hole was made larger. The pressure drop across the standard and no mesh units at atmospheric pressure are shown in Figure 4.41 and Figure 4.42 respectively with the liquid load fractions denoting the actual % liquid load of droplets entering the separator. The 0% liquid load point represents the pressure loss across the separators with no oil being injected, the system cleared through of any residual oil and the separator left overnight to allow any oil on the internal surfaces to drain into the collection chamber therefore is representative of the gas only pressure drop.

As with the separation efficiency measurements the pressure drop data had to be acquired over approximately a 90 minute time period. This was to allow for any fluctuations due to the turbulence intensity to be averaged out and, when assessing the effects of liquid loading, to allow the liquid films on the internal surfaces to establish. This was most notable for the standard unit when the system was started from dry the pressure drop across the unit was seen to steadily increase until the internal mesh reached saturation after which the pressure drop reached a steady state.
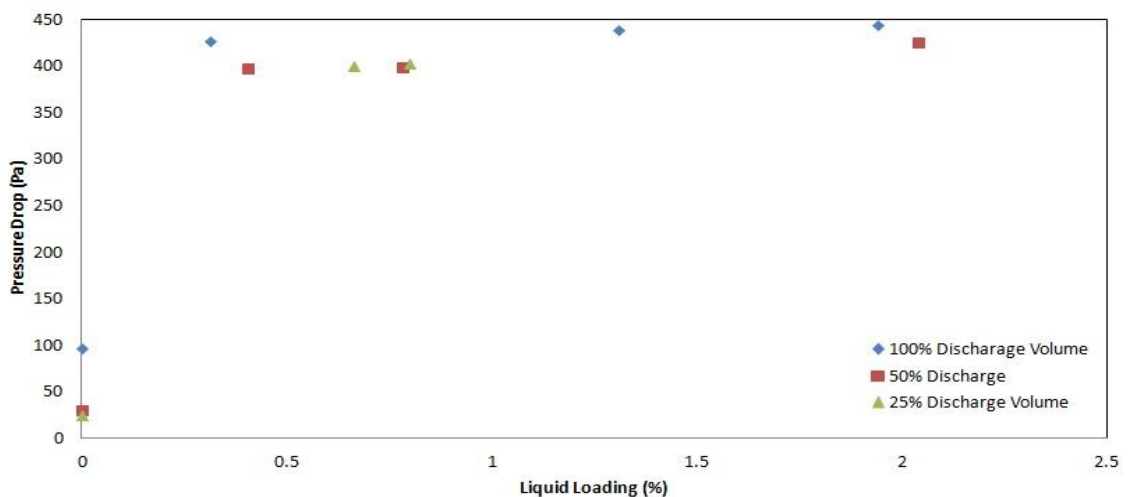
Figure 4.41: Standard Unit Pressure Drop at 0 BarG Working Pressure
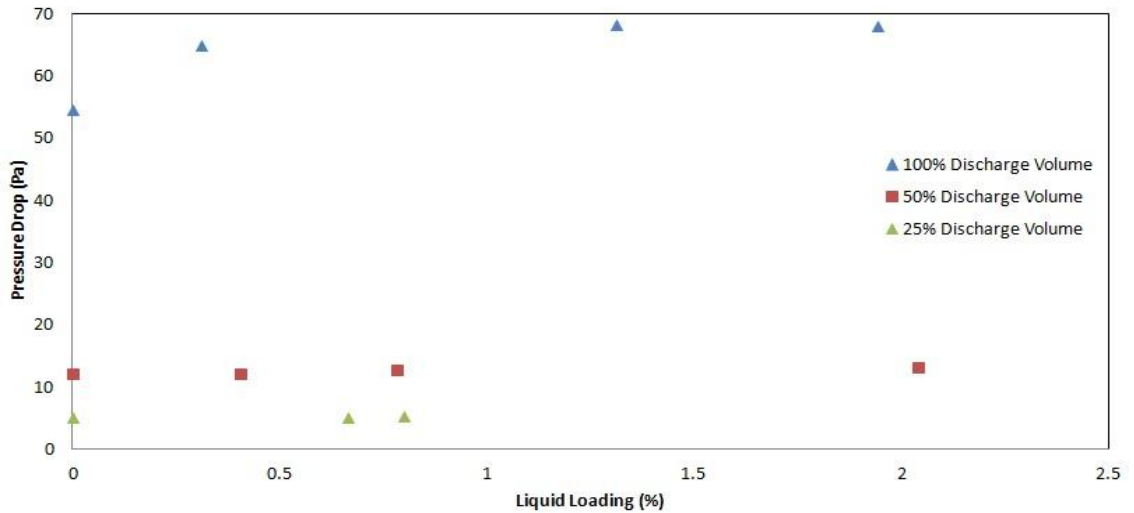
Figure 4.42: No Mesh Unit Pressure Drop at 0 BarG Working Pressure

To provide an assessment of the effects of fluid density on the pressure drop across the separator data was acquired from the no mesh unit at 3 BarG with no liquid loading for the 25%, 50% and 100% discharge flowrates. The 0% liquid load data at atmospheric pressure and 3 BarG is given in Figure 4.43 along with the predicted pressure drop data from the single phase flow CFD simulations of the no mesh unit at atmospheric pressure to assess the ability of the models to predict the pressure loss over the separator unit. The inlet and outlet pressures for the computational model were obtained from a plane directly upstream of the point where the inlet pipe meets the main cylindrical body of the separator and directly downstream of the point where the outlet pipe emerges from the top cap of the separator respectively.
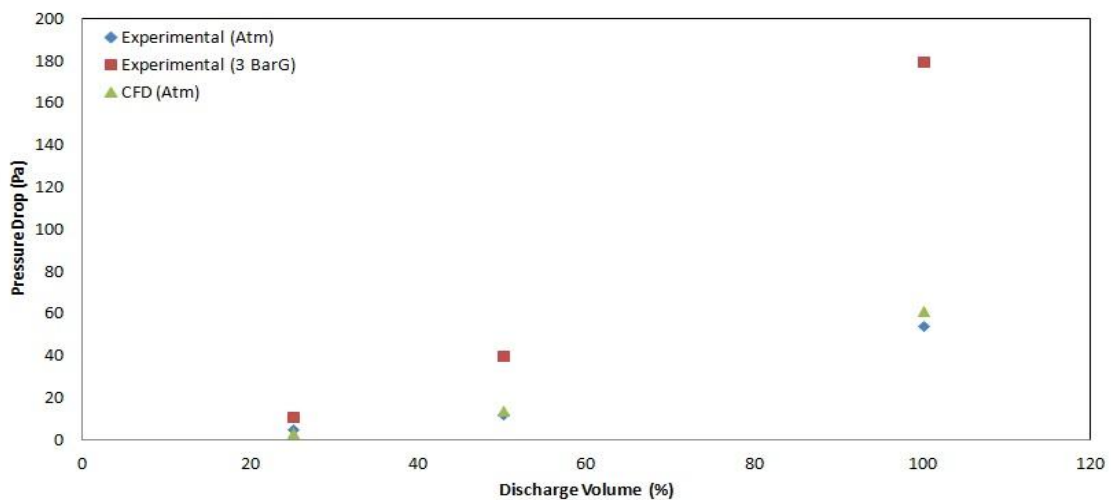
Figure 4.43: Effects of Density on Pressure Drop and CFD Prediction

164

4.8 Discussion of Results

The results from the separation efficiency, liquid film extraction and quantification, droplets size and distribution measurements and the pressure drop have been presented in the previous section. Therefore the purpose of this section is to provide a detailed discussion of the findings from the two phase flow experimental investigation and draw conclusions from the findings.

4.8.1 Liquid Film and Droplet Separation Efficiency Discussion

The data from the combined droplet and liquid film inlet flow to the standard separator unit at atmospheric pressure and 3 BarG given in Figure 4.22 to Figure 4.24 generally demonstrate that at the higher system operating pressure the separation efficiency is increased. It is also apparent for all the gas discharge flowrates which have been investigated there is a decrease in the overall separation efficiency of the unit as the mass fraction is reduced. The absolute measurements for all the data obtained for this testing are within the 75% to 100% range however it is apparent that for the 50% and 25% discharge flowrates, at atmospheric pressure, for low oil mass fractions there is a significant drop off in efficiency. The volume flowrate of oil injected into the system is dependent upon the operating pressure and discharge volume being assessed as presented in section 4.7.1 with Figure 4.22 to Figure 4.24. As previously discussed, the degree of atomisation of the nozzle generating the droplet mist is dictated by the volume flowrate of oil passing through the orifice; therefore with an increase in oil flow to the nozzle there is a resulting increase in the diameter of the droplets generated. For larger droplet diameters the probability of becoming separated is high due to them having a higher inertia. The generation of large droplets at the atomising nozzle exit increases the probability that they will drop out of the inlet flow to the separator in the upstream pipework forming a stratified liquid film. Upon entry to the separator the liquid film will gravitationally drain down the cylindrical walls to the oil collection chamber. The size and distribution of the droplet mist entering the separator is therefore the governing factor which dictates the overall performance of the unit. This is applicable not just for the conditions being tested in this investigation but also applies to the separator operating in an industrial refrigeration system.

4.8.2 Liquid Film Volume Fraction and Droplet Only Separation Efficiency Discussion

By extracting the stratified liquid film immediately upstream of the separator inlet allowed the liquid film volume to be quantified and the separation efficiency to be obtained for a droplet only inlet condition. The data obtained from extracting the liquid film upstream of both the standard and no mesh separator units for 100% and 50% discharge flowrates given in Figure 4.25 and Figure 4.26 show that the liquid film volume fraction accounts for between 56% and 92% of the overall volume of oil injected into the system. For both separator configurations at the aforementioned discharge flowrates there is a decrease in the volume of oil present in the liquid film as the mass fraction decreases. This again can be attributed to the fact that the degree of atomisation is greater, hence the size of droplets produced by the liquid supply nozzle are smaller, for lower mass fractions of oil. The presence of smaller droplets for the low mass fractions increases the probability of the droplets being carried by the gas flow into the separator rather than impacting on the internal surfaces of the inlet pipe and becoming part of the liquid film. The liquid film data also generally shows that there is a greater volume fraction of oil contained in the liquid film for the 50% discharge flowrate conditions in comparison to the 100% flowrate. The reduced momentum of the gas/droplet flow for the lower discharge flowrate condition will in turn increase the probability that the droplets will drop out of the inlet pipe flow and become part of the stratified liquid film on the lower surface of the inlet pipe and hence extracted from the system by the liquid film removal device. This is shown in Figure 4.25 and Figure 4.26 but does not lead to improvements in overall efficiency as shown in Figure 4.29 and Figure 4.30.

The droplet only separation efficiencies and the overall system separation efficiencies shown in Figure 4.27 to Figure 4.28 and Figure 4.29 to Figure 4.30 respectively show that the absolute droplet separation efficiency of the units for 100% and 50% discharge flowrates to be in the range 19% to 83%. The extensive efficiency range provides further evidence that the performance of the separators are highly dependent upon the conditions which exist in the upstream pipework. In comparing the droplet only separation efficiency data with the overall system data for the individual discharge flowrates it is clear to see that although the former is extremely low at the low mass fractions the latter is in general above 70%. The difference in performance of the standard unit to no mesh unit is marginal but in general the no mesh unit has higher separation efficiency for both the droplet only flow

and the overall system efficiency. The reduced performance of the standard unit could be associated with the increased wall roughness due to the internal cylindrical wall mesh reducing the intensity of the swirling flow and hence preventing the droplets entrained in the flow from reaching the cylindrical wall where they become part of the liquid film and hence separated. The wire mesh bag at the entrance to the centre tube will become saturated with oil during the initial setup of the system. During the course of the performance measurements there is the possibility of the mesh being a droplet generator through the gas flow shearing the coalesced liquid from the strands of the wires and carrying this liquid upwards and out of the separator hence reducing the separation efficiency of the unit.

4.8.3 Droplet Size and Distribution Discussion

From all the data presented in Figure 4.31 to Figure 4.36 it can be seen that there is a significant variation in the maximum droplet size and distribution at the inlet of the separator dependent on the gas discharge flowrate and the oil mass fraction. Based on the inlet data alone it is increasingly apparent why the performance of the separator at higher oil mass fractions is greater than at lower mass fractions. This can be explained due to the droplet sizes and the corresponding volume frequencies being greater for the high oil mass fractions than the low fractions; i.e. for 100% discharge flowrate and 10% oil mass fraction the cumulative volume of oil droplets with a diameter less than 20 microns is approximately 35% whereas for the same gas flowrate at 1% oil mass fraction the cumulative volume of droplets less than 20 microns is approximately 98%. By comparing Figure 4.32 and Figure 4.35 it can be seen that the maximum droplet size present at the inlet for 100% discharge flowrates is larger than maximum for the 50% discharge conditions. The inertia of the droplets will be greater for the 100% discharge condition than the 50% discharge condition, therefore at the lower gas flow condition the larger droplets will drop out of the gas flow and become part of the liquid film whereas for the larger gas flowrate these large droplets will remain suspended in the annular flow and enter the separator. This explanation is supported by the data for the liquid film quantification which showed that the volume fraction of inlet flow contained as liquid film was marginally greater for the 50% discharge flow condition than the 100% flowrate.

The droplet size distribution data also illustrates the maximum droplet size which is not removed by the separator units. In the case of the standard unit this was between 40 and

46 microns and for the no mesh unit between 16 and 23 microns irrespective of the flow condition since this is the maximum droplet size range measured at the separator outlet. Not only does this data define the separation efficiency limitations of the units but it also provides information which can be used for potential design improvement for the separator. The fact that the droplet size measured at the outlet of the standard unit is larger than the no mesh unit is supported by the fact that the no mesh unit in general has higher droplet separation efficiency than the standard unit. This supports the conclusion drawn previously regarding the mesh reducing the internal gas velocities hence preventing droplets migrating to the cylindrical wall and acting as a droplet generator at the entrance to the centre tube. As a comparison, in the study of an oil-gas cyclone separator in a compressor system by Gao, et al., they measured droplet diameters up to 25 microns at the outlet of their separator and also reported that sub 5 micron droplets were difficult to separate (Gao, et al., 2012). In comparing this with the data from the no mesh unit, since this is the closest geometrical representation to the cyclone separator of Gao et al., the droplet diameter range with the largest volume frequency at the outlet for this unit was between 3 and 5.5 microns supporting the claim that sub 5 micron droplets prove difficult to separate.

The experimentally determined grade efficiency curves from the 100% discharge flowrate tests show the cut size of the separator, d_{50}, to be between 5 and 6 microns for the standard unit and between 6 and 7 microns for the no mesh unit. However for the 50% discharge flowrate tests the cut size was found to be between 11 and 12 microns for both separator configurations tested. The increase in cut size for the lower discharge flowrate can be attributed to the lower velocities which will exist within the main separation space. The reduced tangential velocity component will produce a lower centrifugal force hence the probability of smaller droplets reaching the cylindrical wall during their residence time in the separator is less than for the 100% discharge flowrate where the tangential velocity and resulting centrifugal forces are greater. Although the standard unit has a marginally smaller cut size diameter at the higher flowrate condition it is the small volume fraction of droplets in the 25-46 microns range which are not separated by this unit which prevent the overall separation efficiency from being better than the no mesh unit.

4.8.4 Pressure Drop Discussion

The data shown in Figure 4.41 to Figure 4.42 from the separator units tested show unsurprisingly that the pressure drop is greater for the standard unit in comparison to the no mesh unit. It is clear to see that the effects of liquid loading on the standard unit pressure drop are significant which can be accounted for by the reduction in flow area on the mesh attached to the centre tube due to the formation of a liquid film on the wire strands. This effect was supported by monitoring the pressure drop as the oil was injected into the system, after having been operated with no liquid loading, which resulted in a steady increase in the reading until the mesh reached a saturated state. Contrary to this the no mesh unit exhibited only minimal increase in the pressure drop across the unit due to the presence of the oil droplets in the flow.

Figure 4.43 combines the pressure drop predictions from the single phase CFD analysis of the separator at atmospheric pressure with the no mesh unit gas only pressure loss data at atmospheric pressure and 3 BarG. It is immediately apparent that the predictions from the CFD match the experimental data extremely well which provides further evidence that the gas flow within the computational geometry has been accurately captured. Comparing the experimental data at the two working pressures illustrates that the pressure drop increases by approximately a factor of 3 from atmospheric to 3 BarG. This is to be expected since the fluid density is increased 3 times by increasing the system pressure. The increase in pressure drop also increases exponentially as the discharge flowrate, and hence gas velocity, increases. Again this is no surprise since pressure drop increases with the square of the velocity hence doubling the gas flowrate results in a fourfold increase in pressure drop. Based on this evidence the Euler number can be determined, which was found to be between 1.8 and 2.9 from the experimental data, and used to predict the pressure drop which would be expected at real plant operating conditions.

4.9 Major Outcomes

This chapter has covered the rig design, data acquisition procedure and results from the experimental separation efficiency and pressure drop testing of the helical oil separator. The configuration of the separator units which have been tested include the standard Henry Technologies helical oil separator and a no mesh variant to allow validation of the two phase flow computational modelling. In determining the separation efficiency of the helical separator a variety of experimental testing procedures have been employed to allow

the performance of the unit to be fully characterised. These included assessing the performance of the standard unit subject to a combined liquid film and droplet inlet flow at two working pressures to assess the effects of pressure. Extracting and quantifying the stratified liquid film which is present in the inlet pipe and obtaining separation efficiency data of the two separator configurations subject to a droplet only inlet flow. Measuring the size and distribution of the droplet flow at the inlet and outlet of both separator units; thereby allowing the formation of grade efficiency curves capturing the droplet separation efficiency. Obtaining the pressure drop across both separator units over a range of conditions and comparing these to the single phase pressure drop data predicted by the computational models.

The major outcomes resulting from the experimental testing of the helical oil separator are as follows;

• The separation efficiency of the unit increases as the working pressure increases. It was also evident that the efficiency increases with increased discharge flowrate which can be associated with the increase in gas velocity within the main separation space leading to the entrained droplets reaching the walls.

• The stratified liquid film on entry to the separator accounts for between 56% and 92% of the overall volume of oil injected into the system at atmospheric pressure for 50% and 100% discharge flowrate.

• To allow an accurate assessment of the separation efficiency of the unit requires the liquid film to be extracted upstream of the inlet allowing only a droplet mist to enter the separator. The droplet only separation efficiency combined with the droplet size and distribution at inlet and outlet allow quantified data to be used to produce GEC's.

• The GEC's for the separator indicate the independence of the separation efficiency to liquid loading for a fixed discharge volume flowrate.

• The cut sizes, d_{50}, for the standard unit and no mesh units are between 5 and 6 microns and 6 and 7 microns respectively for 100% discharge and between 11 and 12 microns for both units at 50% discharge. However the overall separation efficiency of the standard unit is marginally lower than the no mesh unit since larger droplet sizes remain at the outlet of

the standard unit which can be accounted for due to the internal mesh acting as a droplet generator.

• The pressure drop across the no mesh unit is significantly lower for all conditions tested in comparison to the standard unit and the no mesh unit does not experience a significant increase in pressure drop with liquid loading whereas the standard unit does. It has also been shown that the results from the single phase CFD assessment can predict the pressure drop measured experimentally and the Euler number can be used to determine the pressure drop for real plant working conditions.

The data acquired from the experimental two phase flow investigation can be used to provide the necessary boundary condition and validation data to allow an assessment of the discrete phase model to predict the separation efficiency of the helical separator.

Chapter 5 Two Phase Flow Modelling

5.1 Introduction

Having obtained a validated single phase flow model for the separator and experimental data characterising the separation efficiency of the unit combined with detailed information of the inlet two phase flow conditions and droplet size measurements, the focus of this investigation now turns to the computational modelling of the droplet flow. As indicated by the literature there are a range of approaches which can be used for two-phase flow modelling, however the two that are found to be the most commonly employed are the Euler-Euler and the Euler-Lagrange methods. The former method treats each phase as a continuum which have their own set of transport equations in addition to the interfacial equations. The latter method only treats the continuous phase as a continuum with the dispersed phase being solved independently through their equations of motion; this method is suitable when the dispersed phase volume fraction is less than 10-12% (ANSYS, 2009). Due to the low volume fraction occupied by the dispersed droplet phase in this investigation, less than 1%, the Lagrangian discrete phase model (DPM) approach will be used to track the droplets through the resolved gas flow continuum. This Euler-Lagrange approach for modelling dispersed phase separation has been investigated within the literature and has been shown to produce separation performance predictions which are in line with experimental data.

The majority of the literature which currently exists however focuses on solid particle separation modelling (Kegg, 2008), (Jia, et al., 2007), (Gimbun, et al., 2005). Droplet separation modelling has been carried out in a cyclonic geometry but discrepancies were found between the model predictions and the experimental data (Gao, et al., 2012). Based on the lack of published work it is clear that there is a knowledge gap in the modelling of droplet separation. To assess the feasibility of the models to determine the experimentally measured performance of the helical oil separator geometry the droplet separation efficiency for the no mesh unit will be used to allow a direct comparison to be made. The droplet size and distribution data measured at the separator inlet will be used to define the dispersed phase inlet boundary condition. The available models in the literature for simulating the droplet dynamics will be assessed along with the wall boundary conditions and the solution methodologies. The overall aim of this chapter is to assess the ability of the DPM model to predict the separation efficiency obtained experimentally. In carrying

out the assessment the approach has been divided into subsections which include; background information on the droplet equations of motion and how they are affected by turbulence, the physical models available for droplet coalescence and breakup, the wall models and prediction of the droplet-wall interaction and the solution approaches which can be used to deliver the overall separation efficiency for the helical separator.

5.2 Single Phase Flow Model

The separator geometry used for validation in Chapter 3 of this thesis was based on the dimensions of the Perspex replica used to obtain the LDA measurements which vary slightly from the actual geometry of the S-5190 unit used for the experimental performance measurements. As a result a new model was created which has the same internal separation space dimensions as the no mesh helical separator used for the performance testing in Chapter 4. A dimensioned drawing of this model is shown in Figure 5.1 below.
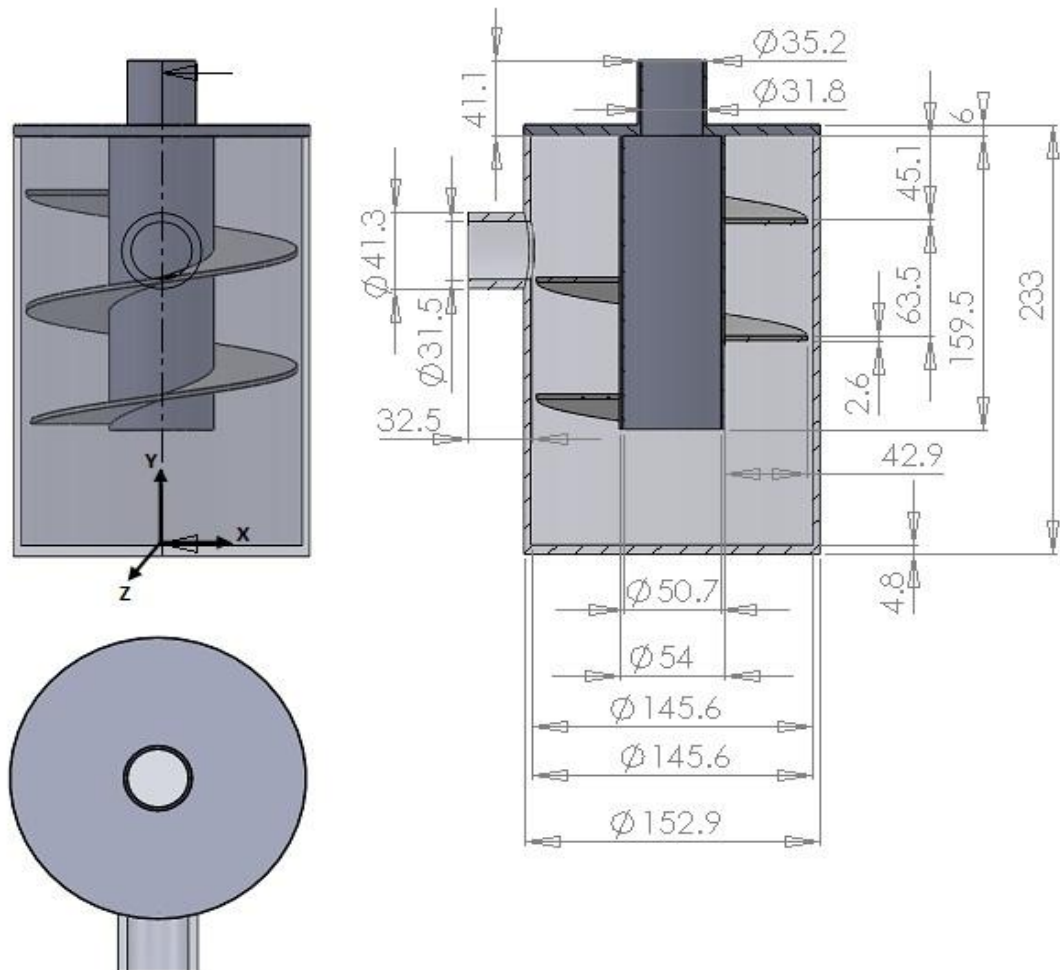
Figure.5.1: Dimensioned Drawing of S-5190 No Mesh Separator Model

The validated single phase flow model obtained in Chapter 3 consisted of 557519 mesh cells. To determine the cell count for the no mesh unit which would produce an equally refined grid required taking the mesh size for the Perspex replica unit and multiplying it by the flow volume ratio of the two units. The volume ratio of the no mesh unit to the Perspex replica was found to be 1.045 which resulted in a mesh size for a grid independent solution for the no mesh unit to be at least 582500 cells. Applying a computational mesh to the geometry shown in Figure 5.1 resulted in a total cell count of 584325, which consisted of a structured grid throughout the domain except near the walls where the grid was unstructured.

This mesh was solved using the LES turbulence model with a time step of 1×10^{-4} seconds using the PRESTO! and Bounded Central Differencing discretization schemes for pressure and momentum respectively. The pressure-velocity coupling used was the SIMPLE method and the simulation was solved for 7 seconds of real flow time which required 160 hours of CPU time to obtain the converged solution which captured multiple cycles of the transient flow events which exist within the separator. The inlet boundary condition was defined as a mass flow inlet and prescribed a flowrate dependent on the discharge volume condition being assessed. This ranged from 0.00318 kg/s (3.33 m/s) at 50% discharge volume, up to 0.00636 kg/s (6.67 m/s) at 100% discharge volume since all simulations were run to replicate the atmospheric pressure condition with the fluid phase treated as air with a density of 1.225 kg/m^3 and dynamic viscosity of 1.789×10^{-5} kg/ms. The outlet was assigned as a pressure outlet at 0 Pa.

5.3 Discrete Phase Modelling (DPM) Background

5.3.1 Droplet Equations of Motion

The Euler-Lagrange method has been developed to allow the effect of the dispersed phase on the continuous phase through heat, mass and momentum transfer between the phases. This modelling approach determines the trajectories of the discrete phase droplets by performing integration on the force balance for the droplet which is defined in a Lagrangian reference frame. The equation which describes this phenomenon equates the forces acting on the droplet being tracked with the inertia of the droplet itself, which is given in a Cartesian coordinate system in the x direction as;

$$\frac{du_d}{dt} = F_D(u - u_d) + \frac{g_x(\rho_d - \rho)}{\rho_d} + F_x \qquad (5.1)$$

where F_x is an added acceleration term and the first term on the right hand side of equation 5.1 is the drag force per unit droplet mass, with F_D defined as;

$$F_D = \frac{18\mu}{\rho_d d_d^2} \frac{C_D Re}{24} \qquad (5.2)$$

with u and u_d representing the gas and droplet phase velocities respectively, ρ and ρ_d denoting the gas and droplet densities respectively, μ is the gas dynamic viscosity and d_d is the droplet diameter. The Reynolds number, Re, is defined here in terms of the absolute relative velocity;

$$Re \equiv \frac{\rho d_d |u_d - u|}{\mu} \qquad (5.3)$$

The drag coefficient C_D can be defined in terms of the spherical drag law since it can be assumed for this investigation that all the droplets being modelled are spherical and smooth therefore C_D is;

$$C_D = K_1 + \frac{K_2}{Re} + \frac{K_3}{Re^2} \qquad (5.4)$$

where the coefficients K_x are dependent on the Reynolds number. However for sub micron droplets where Stokes Law governs the droplet motion, F_D is given as;

$$F_D = \frac{18\mu}{d_d^2 \rho_d C_c} \qquad (5.5)$$

where C_c is the Cunningham correction factor to account for drag on small droplets for Stokes drag law which is computed from;

$$C_c = 1 + \frac{2\lambda}{d_d}(1.257 + 0.4e^{-\left(\frac{1.1 d_d}{2\lambda}\right)}) \qquad (5.6)$$

with λ denoting the molecular mean free path.

Inclusion of additional forces experienced by the droplets due to the dynamics of the flow field are included in the added force term in equation 5.1 such as the virtual mass which accounts for drag due to the droplet causing the surrounding fluid to accelerate; the Bassett force which accounts for the viscous effects due to the delayed development of the boundary layer caused by the droplet accelerating through the flow; the Saffmann lift force

due to shear and the effects of Brownian motion for sub micron droplets. Due to the density ratio of the liquid droplets to gas having a large value, close to 1000, then the virtual mass and Basset force terms can be neglected (Hoffmann & Stein, 2008). The droplet sizes present at the inlet to the separator are relatively small, 0-400 microns, therefore the velocity difference between the lower and upper surface, due to the shear flow, of an individual droplet will not be significantly different. As a result the Saffman force can be also be ignored since the drag force experienced by the droplet will be far more significant. The effects of Brownian motion on the sub micron droplets will however be considered since part of the inlet volume for all the conditions assessed consists of droplets in this category. Due to the low volume fraction occupied by the dispersed droplet phase the assumption that collisions amongst the droplets is negligible and a one-way coupling approach can be adopted, since $\alpha_d < 1 \times 10^{-6}$, such that the droplets do not affect the continuous phase but the continuous phase can impart momentum to the droplets.

5.3.2 Turbulent Dispersion of Droplets

The Stokes number used to define the droplets in this investigation is given as;

$$Stk = \frac{\rho d_d^2 U}{18 \mu D}$$
(5.7)

where U is the droplet velocity in the cylindrical body of the separator and D is the diameter of the cylindrical body of the separator. For the range of gas velocities at atmospheric pressure the Stokes number ranges from 5.18×10^{-10} to 0.00132. Based on these values the effects of the sub-grid scale fluctuations are worthy of being accounted for. The motion of the dispersed phase droplets is highly dependent on the turbulence effects in the continuous Eulerian fluid phase. There are two parameters; the relative turbulence intensity and the turbulence length scale-droplet diameter ratio, which are used to quantify the effects of the continuous phase turbulence on the droplet drag. The former is defined by;

$$I_r = \frac{\sqrt{\overline{u'^2}}}{|u-v|}$$
(5.8)

where $\sqrt{\overline{u'^2}}$ is the root mean square value of the continuous phase fluid turbulent fluctuations. Equation 5.8 becomes negligible when the relative velocity between the phases reduces. The length scales associated with turbulent flows are extensive with the smallest being the Kolmogorov length scale, $(v^3/\varepsilon)^{1/4}$ where v is the fluid kinematic viscosity

and ε is the average rate of dissipation of the turbulent kinetic energy per unit mass. At the Kolmogorov length scale viscous forces become dominant and the turbulent kinetic energy is dissipated into heat. The effects of this turbulent dispersion can be predicted using a stochastic droplet tracking, discrete random walk (DRW) model, where the effects of instantaneous turbulent velocity fluctuations on the droplets trajectories can be included. The fluctuating velocity component of the continuous phase fluid for each interaction between the dispersed droplet and the turbulent eddies is sampled by assuming the fluctuations obey a Gaussian probability density function such that;

$$u' = \zeta \sqrt{\overline{u'^2}} \qquad (5.9)$$

with ζ representing a normally distributed random number and the multiplier is the local root-mean-square (RMS) value of the fluctuations. When the LES turbulence model is applied, as is the case for this investigation, the effect of the sub-grid scale (SGS) fluctuations on the droplet within the fluid phase may be considered. However it is reported that the SGS fluctuations are far less coherent than the large scale eddies present in the continuous phase and hence the small scale fluctuations only have an impact on the instantaneous droplet behaviour (Elsayed & Lacor, 2013). As a result the statistical properties of the droplet motion including concentration, mean velocity and RMS velocity are insignificantly affected by the sub-grid scale fluctuations. The droplets do however experience the sub-grid scales through the sub-grid model used to resolve the velocity field even if the individual effects of the sub-grid scale fluctuations on the droplet dispersion is neglected. Investigations have been carried out to assess the importance of including SGS fluctuations and it has been found that when the filter width is small and the particle relaxation time is significantly large, which is the case for the helical separator, there is very little deviation found between the filtered velocity field and one which has been resolved using DNS. With an appropriately refined grid the motion of the dispersed phase can be computed to have dispersion statistics within 8% of the DNS computation with the errors being associated with operation of the SGS filter rather than modelling errors (Armenio, et al., 1999).

A uniform, isotropic process is used to replicate the effects of the SGS fluctuations with an average velocity of zero and the RMS value of $u_{SGS} = \sqrt{2/3 k_{SGS}}$. The SGS kinetic energy, k_{SGS}, is based on the assumption of an isotropic, local equilibrium mixing-length model

estimated by $k_{SGS} = C_k c_s^2 \Delta^2 |S|^2$ where $|S|$ represents the resolved deformation rate, Δ is the grid spacing and C_k and c_s are constants prescribed values of 5 and 0.1 respectively where the latter is from the Smagorinsky SGS model. As with the RANS approach to modelling eddy interactions an eddy life-time concept is used where $t_{SGS} = C_L k_{SGS}/\varepsilon$ where the constant C_L is equal to 0.15 as which was implemented by Derksen, (Derksen, 2003).

In applying the aforementioned DRW model to a LES simulation of the gas flow field the velocity fluctuations are assumed to be isotropic and the LES time scales are used when the eddy-droplet time is compared to the integral time scales. Therefore through the use of the LES solution the effects of the sub-grid scale fluctuations are directly accounted for. Based on this approach; droplets within the flow domain predominantly only see the computed LES flow field rather than the instantaneous sub-grid scale fluctuations. The strength of this approximation is highly dependent on the geometry having a suitably refined grid and on the Stokes number of the droplets being simulated, since a coarse grid will contain a higher degree of SGS energy and small droplets are more likely to experience the effects of the fluctuations.

5.3.3 Droplet Models

The physical models available for droplet modelling include droplet collisions and droplet breakup. The droplet collision model requires two droplets to co-exist in the same computational cell and as previously mentioned, due to the low volume fraction of dispersed phase it can be argued that the probability of a collision is low therefore this model is not used in any part of the separator analysis. The breakup model of O'Rourke and Amsden which causes droplets to breakup due to pneumatic pressure, shear stress and disturbances due to turbulence, (O'Rourke & Amsden, 1987), has been shown to produce successful results when predicting the separation efficiency of oil-gas cyclone separators (Gao, et al., 2012). The model makes use of the Taylor Analogy Breakup (TAB) approach and is the most widely used model to describe the breakup of a single oil droplet. When this model is activated in the software the user can define the resultant number of breakup parcels produced. The effects of implementing the TAB model in simulating the performance of the helical oil separator will be presented later.

5.3.4 Wall Models

When a droplet reaches a wall within the computational domain, an appropriate wall interaction model needs to be implemented to determine the outcome of the collision. The outcomes of the droplet-wall interactions applicable to this investigation are;

1) The droplet impacts the wall and is reflected as either an elastic or inelastic collision, should the collision be inelastic then a coefficient of restitution must be defined.

2) The droplet impacts the wall and sticks to the surface and is therefore defined as removed from the flow field. In this case the droplet tracking equation for that particular trajectory is terminated.

3) The droplet can impact on the wall and produce a wall-film from which a number of resulting splashed droplets can be defined.

Applying the correct wall model to the internal surfaces of the helical separator is critical to allow the separation efficiency of the unit to be accurately determined. In the investigation of Gao et al., the reflect boundary condition is applied to all internal surfaces and the assessment of the separation efficiency is dictated by the number of droplet trajectories which do not pass through the outlet plane and are therefore assumed separated (Gao, et al., 2012). However in the bulk of the literature there is at least one internal surface of the computational geometry defined as a particle/droplet removal boundary. In the case of a standard cylinder-on-cone cyclone separator the trajectory calculations are terminated when the dust outlet, at the base of the unit, is reached and the mass of the dispersed phase which is collected is used to determine the efficiency (Elsayed & Lacor, 2013).

In the case of the Henry Technologies helical separator droplets of oil enter the separation volume and can be subject to a number of physical processes including impacting onto the wall and either becoming part of the liquid film and draining to the base of the separator or rebounding back into the flow domain and generating secondary droplets due to the impact with the wall film. To determine the appropriate boundary condition for the internal surfaces of the separator the model of Bai et al. will be used in which there are four potential outcomes for droplet impingement namely stick, rebound, spread and splash with both stick and spread resulting in droplet deposition on the surface (Bai, et al., 2002). The various droplet wall-film interaction outcomes are shown in Figure 5.2.
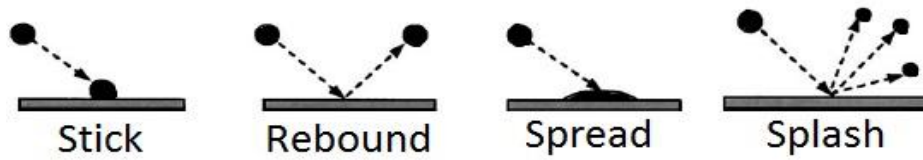
Figure 5.2: Droplet-Wall Film Interaction Fates

The interaction fate is dependent on the impingement energy of the droplet, which is calculated from the droplet Weber number, as given in equation 5.10;

$$We_d = \frac{\rho_d D_d v_n^2}{\sigma}$$
(5.10)

where v_n is the normal component of the droplet velocity. If the value of We_d is less than or equal to 5 then the droplet will impact with the wall and stick hence becoming separated from the flow field. If $5 < We_d \leq 10$ then the droplet will rebound from the surface with the resulting velocity components dictated by the angle of the incoming droplet with respect to the wall and the coefficient of restitution. For $We_d > 10$ the incoming droplet will impact on the wall boundary and spread onto the surface forming a layer of liquid on the surface. All of the aforementioned droplet wall interaction outcomes do not result in the droplet breaking up. However the final fate shown in Figure 5.2 illustrates the generation of secondary droplets when the incoming drop impacts on the surface and splashes. To define the criterion at which this happens involves determining the splashing parameter, defined as $K = We_d^{0.5} Re_d^{0.25}$. When the value of K is greater than 57.7 then the impact energy of the droplet is sufficient enough to splash and consequentially generate secondary droplets. For $K \leq 57.7$ the impact energy is lower than the critical energy threshold therefore no break-up occurs and the fate is determined based on the droplet Weber number as previously discussed.

To allow suitable boundary conditions to be applied to the internal walls of the no mesh separator model the droplet Weber number and impact energy approach of Bai et al. was determined based on the droplet size range measured at the inlet to the separator and the gas velocity range obtained from the single phase flow simulation of the separator (Bai, et al., 2002). For the range of droplet diameters and velocities expected in the helical separator the resulting droplet-wall interaction outcomes are shown in Figure 5.3.

The results from the droplet-wall interaction analytical analysis will be used to prescribe the boundary conditions applied to the separator model walls. Ensuring the correct wall models

are applied to the boundary surfaces of the separator is critical to ensure the separation efficiency of the unit is captured accurately since it is the result of the wall interaction which determines if the droplet remains in the flow field or whether it is removed. Choosing the wrong wall model will result in the separation efficiency of the computational model to be either over-predicted or under-predicted thus delivering false performance data which is not representative of the physical processes which are occurring in practice.
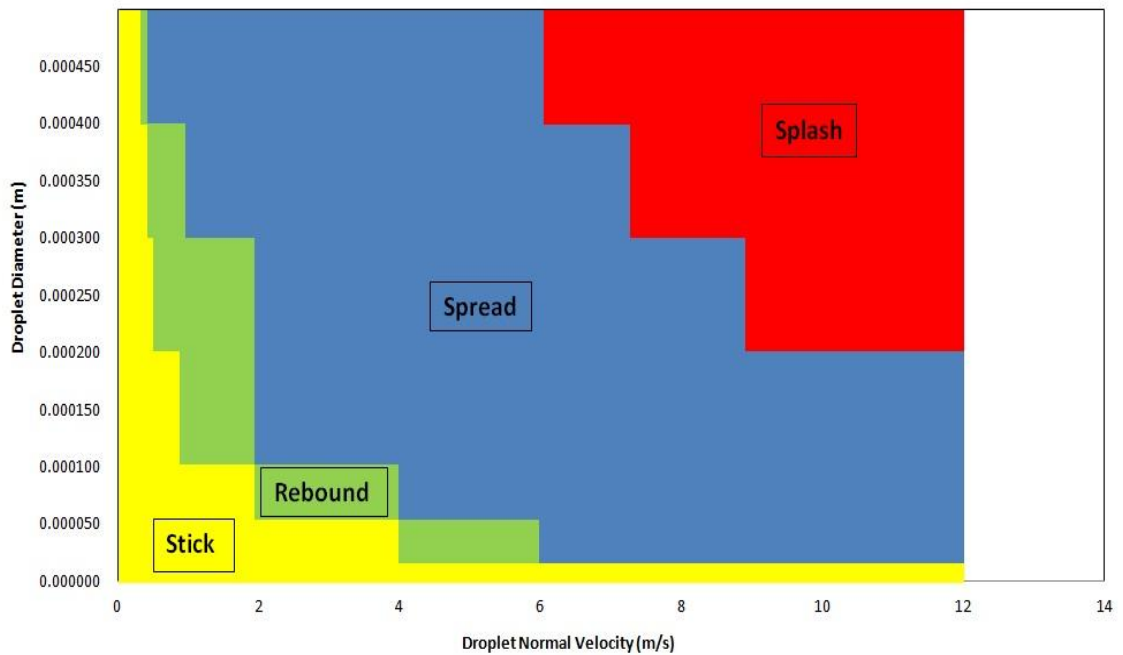
Figure 5.3: No Mesh Separator Droplet-Wall Fates

5.3.5 DPM Solution Procedure

Derksen explored the various approaches presented within the literature for handling the discrete phase motion in separators (Derksen, 2003). One of these is the concurrent simulation method where droplets are continuously injected into the computational domain for a defined time period. At each time step the location of the droplets is updated using the droplet time step equal to the flow time step. The simulation is run until there is no considerable increase in the number of droplets leaving the domain at which time the separation efficiency can be determined. Derksen uses an integral time scale, defined as the ratio of the separator diameter to the gas inlet velocity, to characterise the duration of simulation periods and shows that after 228 integral time scales there was a significant amount of the injected volume of dispersed phase circulating within the domain. It was also found even long after the discrete phase injection had ended there was still small numbers

of particles escaping through the outlet of the cyclone (Derksen, 2003). As a result the computational time required for simulating the separation is extensive which is undesirable when a range of conditions are to be modelled.

The long time-span of the concurrent simulation approach prompted Derksen to investigate an alternative method for modelling the transport of the discrete phase. This method involved the discrete phase being released into statistically independent flow field realizations-the gas flow field is frozen at an instant in time and the trajectories are computed through the stationary flow domain. It was suggested that 16 different static flow fields were used to obtain the average separation efficiency with 2 integral time steps between each one. Although the gas flow does not change during the particle tracking procedure the discrete phase is still subject to random fluctuation due to the subgrid-scale velocity. Carrying out the analysis in this manner saves 99% of the run time required for the concurrent simulation method (Derksen, 2003). Comparing the results from both simulation approaches the shape of the grade efficiency curves are similar, however the cut-off diameter obtained using the frozen flow field approach was found to be marginally smaller by 0.5 microns, than the concurrent simulation (Derksen, 2003). This will be investigated for this study.

5.3.6 Integration of the Droplets Equations of Motion

The solution of the droplet trajectory equations are solved by stepwise integration of the equations of motion over discrete time steps. The integration of equation 5.1 with respect to time results in the droplet velocity at each location along its trajectory where the trajectory itself is determined by;

$$\frac{dx_d}{dt} = u_d \tag{5.11}$$

Since equation 5.1 to equation 5.9 and equation 5.11 are coupled ordinary differential equations then the former can be reconfigured into the general form of the equation of motion of a droplet where the last term on the right hand side includes accelerations from all forces with the exception of the drag forces;

$$\frac{du_d}{dt} = \frac{1}{\tau_d}(u - u_d) + a \tag{5.12}$$

where

$$\tau_d = \frac{\rho_d d_d^2}{18\mu} \qquad (5.13)$$

Equation 5.13 is the droplet response time which determines the time period required for it to experience changes in motion. In solving the droplet trajectories the solution begins at a time step, n=1, and is continued until the maximum number of steps has been reached, which is assigned a value of 500000 for this investigation. If the droplet has not reached a prescribed boundary after this time step limit has been reached then the fate of the droplet will be reported as incomplete. For all the DPM simulations carried out in this study the maximum number of incomplete droplet trajectory fates was never greater than 2. The time taken for the result of the droplet tracking is dependent upon the diameter being tracked; small droplet diameters required a longer time period where as the larger droplet diameters were resolved quickly. This is due to a larger number of the small diameter droplets not reach a boundary in which they were separated from the simulation whereas the larger diameter droplets were removed from the solution and therefore required far less computational time for this to be achieved.

5.3.7 Droplet Injection Properties and Modelling Assumptions

Taking the converged single phase solution for the LES simulation after 7 seconds of real flowtime, as described in section 5.2, droplets were injected into the computational domain, with the flow field in a fully developed state, and tracked using the equation of motions previously discussed. For the purpose of determining the separation efficiency of the no mesh separator it is assumed that all the oil mass at the inlet to the separator is present as droplets and no liquid film exists. In doing so the DPM model can be implemented and the results from the simulation can be compared directly to those obtained experimentally for the no mesh unit with the stratified liquid film extracted upstream of the separator. The volume flowrate of oil injected into the experimental system minus that extracted by the liquid film removal device results in the volume flowrate of droplets entering the separator. The droplet mass flowrate at the inlet to the separator is therefore known and can be input directly into the injection properties window for the DPM model setup procedure. Since the droplet flow downstream of the liquid film extraction point accounts for the entire volume of dispersed phase upstream of the separator inlet the surface injection boundary condition is applied which releases droplets into the computational domain from each computational cell defining the inlet face of the model. The scale flowrate by face area option was also activated which allows the droplet

mass flowrate for each trajectory to be scaled according to the area of the cell face from the origination of the trajectory; $\dot{m}_{droplet\,(face)} = \frac{A_{cell}}{A_{face}} \dot{m}_{droplet}$. The droplets were injected into the domain with the same velocity as the corresponding continuous phase discharge volume velocity. The physical properties of the material used to represent the oil droplets were modified to the appropriate values for the Emkarate RL 22H POE oil used in the experimental testing; these were 995 kg/m^3 for the density, 0.048 kg/ms for the dynamic viscosity and 0.03 N/m for the droplet surface tension. The dynamic viscosity and surface tension were only required when the droplet breakup model was activated as will be discussed later.

To assess the performance of the separator for a specific droplet size and hence produce a computational grade efficiency curve which could be compared with those obtained from the experimental data presented in Chapter 4 uniform droplet diameters between 0.5 and 35 microns were injected into the domain and the separation efficiency obtained. To allow an overall performance comparison between the CFD and experimental data the diameter distribution was set to Rosin-Rammler to allow the actual droplet size distribution measured by the Malvern Spraytec apparatus at the separator inlet to be input directly. This required information on the minimum, maximum and mean droplet diameters to be defined and the spread of the droplet diameters at the inlet.

Depending on the solution approach for the DPM model the calculations were either carried out as a post-processing stage or in a transient manner. For the latter approach the droplets are continuously injected into the domain for a defined time period and their position within the domain updated either with the same time step as the continuous phase or with an independent time step and the simulation continued until there is no considerable change in the number of particles within the domain at which point the efficiency can be obtained. The various solution approaches will be discussed later in this chapter.

5.4 Separation Efficiency Determination Procedure

To determine the effects of the aforementioned parameters on the overall separation efficiency prediction for the no mesh separator a range of simulations have been carried out. To allow a means for validation of the proposed models the experimental data for the droplet only performance of the no mesh helical separator operating at atmospheric

pressure with 100% discharge flowrate and the average from the 10%, 5% and 2.5% mass fraction GEC data points will be used since the variation associated with the individual mass fractions is due to experimental errors. Since the DPM model only simulates the dispersed phase droplets the mass flow of the droplet mist was used as the inlet boundary condition for the simulation which was 6.63×10^{-5}kg/s of oil. This flowrate is representative of mass flow of droplets entering the separator for the 10% mass fraction case (2% droplet mass fraction), varying this value does not have any consequence on the separation efficiency value obtained since the droplet diameter at the inlet is uniform. As previously mentioned the velocity of the droplets at the inlet to the separator was assumed to be the same as the inlet gas velocity, which in this case was 6.67 m/s. These two values remain fixed for the purpose of establishing a validated discrete phase modelling approach for the helical separator.

5.4.1 Concurrent versus Frozen Flow Field Solution Approach

The concurrent simulation approach injects the droplets into the domain at 7.0000 seconds for 1 time step of 1×10^{-4} seconds. This results in 33,000 droplets with a uniform diameter being tracked in an unsteady manner and being advanced with a time step equal to that of the gas flow, 1×10^{-4} seconds. The solution is run until the number of droplets within the computational domain became steady, i.e. running the simulation for a longer time period would not result in any further change of the droplet mass in the domain. This was found to require up to an extra 2 seconds of real time simulation (20000 time steps), for the smallest droplet diameter simulated but for larger droplet diameters the time taken for the steady state condition to be reached required fewer time steps. As a result the CPU time for each droplet diameter was in the region of 48 hours. Once the steady state condition was achieved the droplet separation efficiency was determined by reporting the number of droplets which had passed through the outlet of the separator using equation 5.14. The first droplet diameter simulated was 0.5 microns; subsequent simulations were carried out for droplet diameters increasing by 2 microns each time until the droplet diameter separated with 100% efficiency was achieved.

$$\eta = \left(1 - \left(\frac{Number\ of\ Droplets\ Escaped\ at\ Outlet}{Number\ of\ Droplets\ Injected\ at\ Inlet}\right)\right) x 100 \qquad (5.14)$$

The frozen field realization approach proposed by Derksen to determine the separation efficiency involves carrying out unsteady particle tracking on 16 statistically frozen flow

fields which are 2 integral time steps, $T_{int}=D/U_{in}$, apart. In this investigation $2T_{int}$ equated to 0.0436 seconds for an inlet velocity of 6.67 m/s. The first realization was carried out at 7.0000 seconds where 33,000 droplets with a uniform diameter of 0.5 micron were tracked through a steady state gas flow field. As with the concurrent simulation approach subsequent droplet tracking was carried out with the droplet diameter increasing by 2 microns in each case. The CPU time required for each droplet diameter was between 1 and 5 minutes dependent upon the droplet diameter being simulated; smaller droplet diameter required a longer simulation time. Once the droplet diameter which is separated with 100% efficiency was obtained the single phase solution could be advanced by $2T_{int}$, which for the 100% discharge condition resulted in the second frozen flow field realization being carried out at 7.0436 seconds. This process was repeated until data had been acquired for 16 frozen flow fields. The overall separation efficiency from the frozen field approach which was used for comparison between the experimental data and the concurrent simulation approach was taken from the average of the 16 realizations as given in equation 5.17. For each individual realization there is a maximum of 2% variation about the mean of overall separation efficiency values of the 16 realizations due to the stochastic tracking of the droplets within the domain which are subject to the turbulent fluctuations. For the purpose of assessing the effects of the solution approach all the walls within the domain were assigned the escape boundary condition such that when a droplet reaches a solid wall surface it is removed from the simulation. No other additional models are activated in this instance. To determine the overall separation efficiency equation 5.15 was used;

$$\eta = \left(1 - \left(\frac{(\sum_{i=1}^{i=16} Number\ of\ Droplets\ (i)\ Escaped\ at\ Outlet)/16}{(\sum_{i=1}^{i=16} Number\ of\ Droplets\ (i)\ Injected\ at\ Inlet)/16}\right)\right) x100 \qquad (5.15)$$
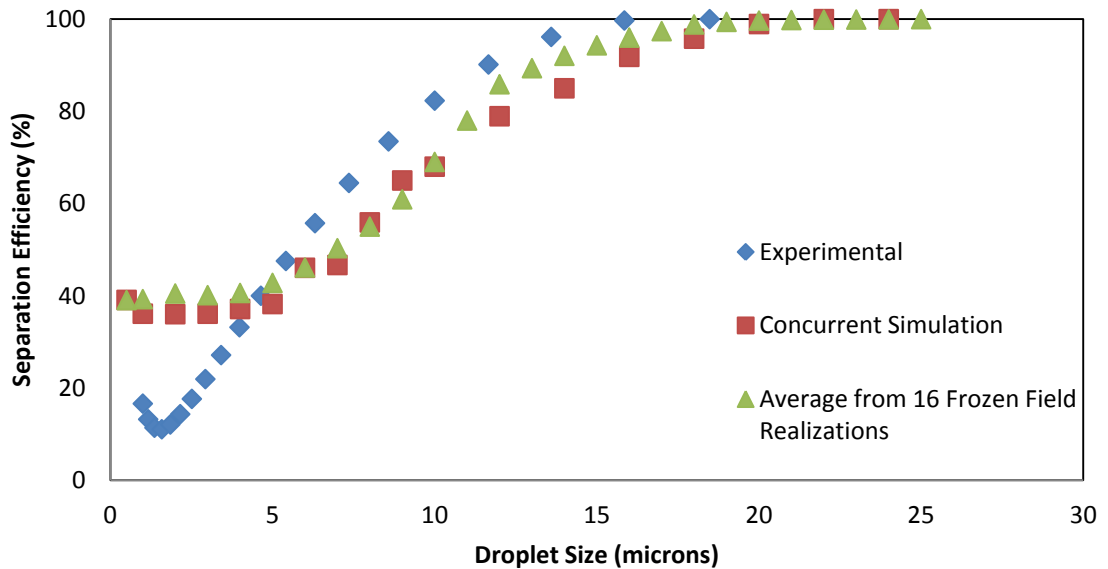
Figure 5.4: Solver Method Comparison

From the data presented in Figure 5.4 it is clear to see that in the 0.5-4 micron range the discrete phase model over predicts the separation efficiency for both the concurrent simulation approach and the average from the frozen field realizations. Down at the 0.5-4 micron size range the droplets will begin to experience effects of the fast moving molecules within the gas which will alter the path of the droplet trajectory. In order to account for this phenomenon the effects of Brownian motion were included in the trajectory calculations, however the overall separation efficiency results for the 0.5-4 micron range did not change as a result. At 5 microns and above the DPM data slightly under predicts the separation efficiency measured experimentally, however the maximum error between the experimental and computational separation efficiencies is 17%. In comparing the two different solution approaches it is clear to see that there is little deviation between the concurrent approach and the average from 16 Realizations, the maximum difference between the different methods is 9%. The variation of separation efficiencies for all droplet diameter simulated over the 16 realizations was found to be no greater than $\pm 5\%$ from the mean. The difference between the solution approaches is deemed acceptable due to the vast reduction in computational solution time required for the realization approach in comparison to the concurrent simulation with the former requiring approximately 11 hours to obtain all the required data versus approximately 168 hours for the latter. The time saving using the average realization method rather than the time intensive concurrent simulation approach is 93.5% which is slightly less than the 99% stated by Derksen. After

further analysis of the data from the realizations for the global separation efficiency values it became apparent that the resulting average from the 16 realizations was achieved after the 9th realization, which further reduced the computation time required to produce the grade efficiency curves for the separator performance. This resulted in a time saving of 96.5% in comparison to the concurrent simulation approach. Based on these findings it is therefore immediately apparent that the significant time saved using the average realization method combined with the ability to closely replicate the results obtained from the experimental data demonstrates that it is the average realization method which should be used when modelling the droplet trajectories within the helical oil separator geometry.

In carrying out unsteady droplet tracking further insight into the physical separation process can be obtained by examining the plots showing the droplet locations at various time steps throughout the transient simulation process. To illustrate this 33,000 droplets with a diameter range of 0.5 to 50 microns, with a spread parameter of 0.9; determined from the experimental measurements, were injected with a velocity of 6.67 m/s from the inlet face and tracked through the computational domain until every droplet trajectory fate was reported to have escaped. The plots shown in Figure 5.5 to Figure 5.10 display the droplet locations at different instances in time with respect to the time at which they were released into the domain. The particles are coloured by droplet diameter, in meters, in all of the subsequent droplet location plots.
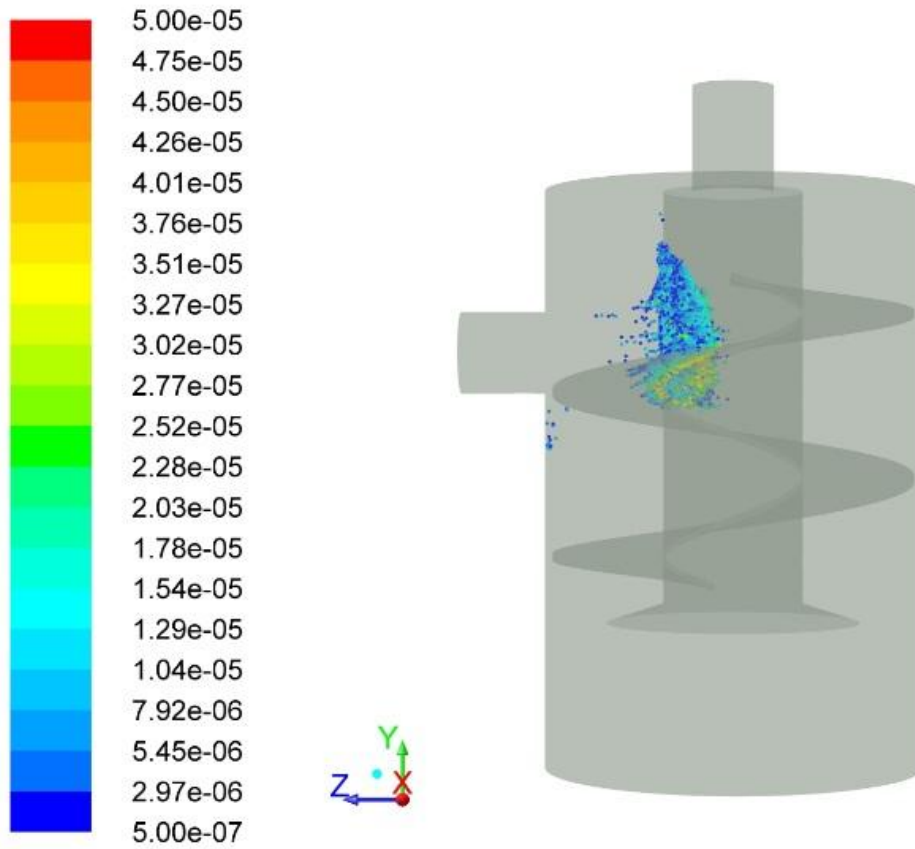
Figure 5.5: Droplet Injection at 0.0150 secs
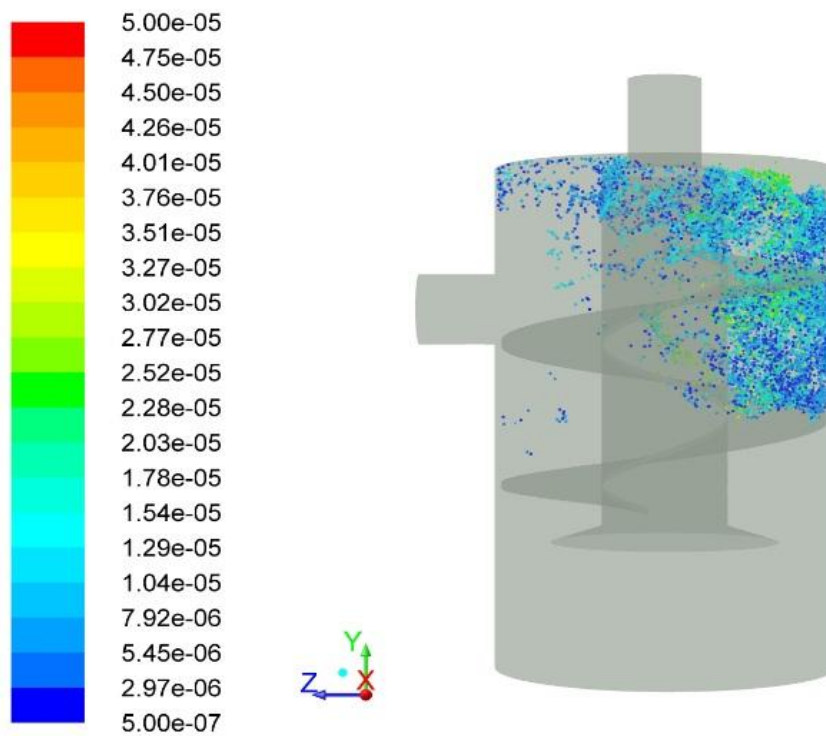
Figure 5.6: Droplet Injection at 0.0450 secs
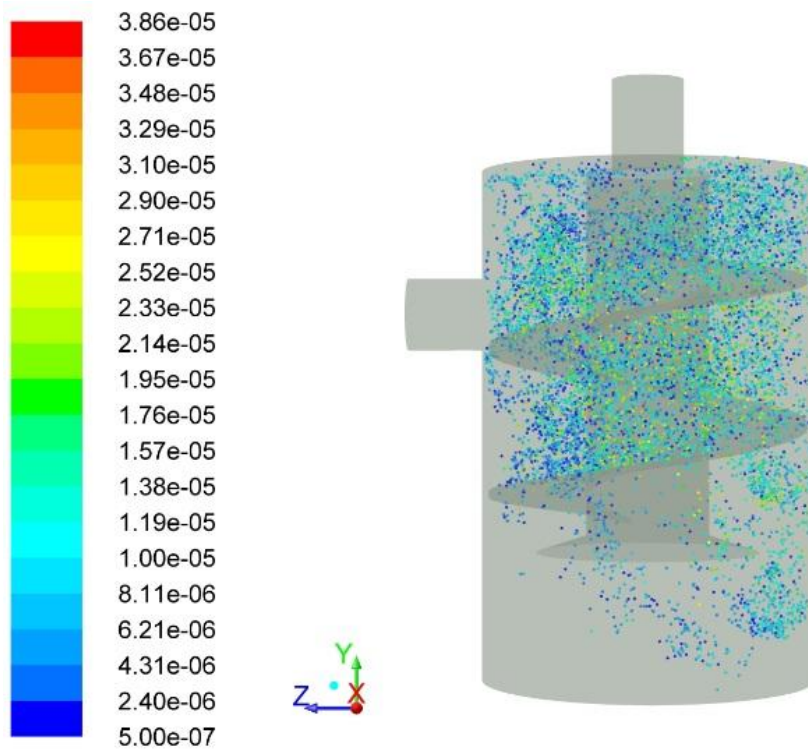
Figure 5.7: Droplet Injection at 0.1050 secs
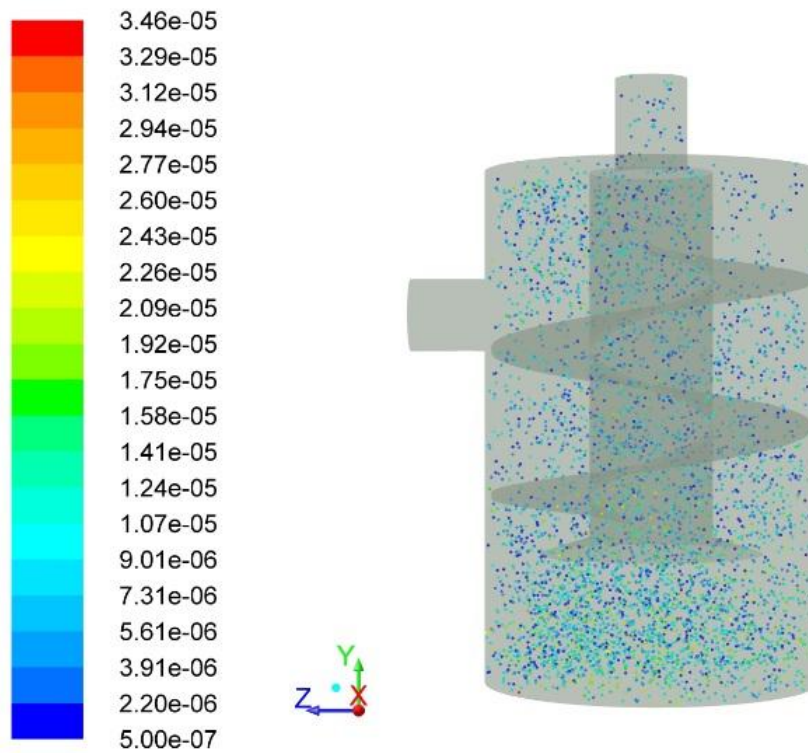
Figure 5.8: Droplet Injection at 0.500 secs

190
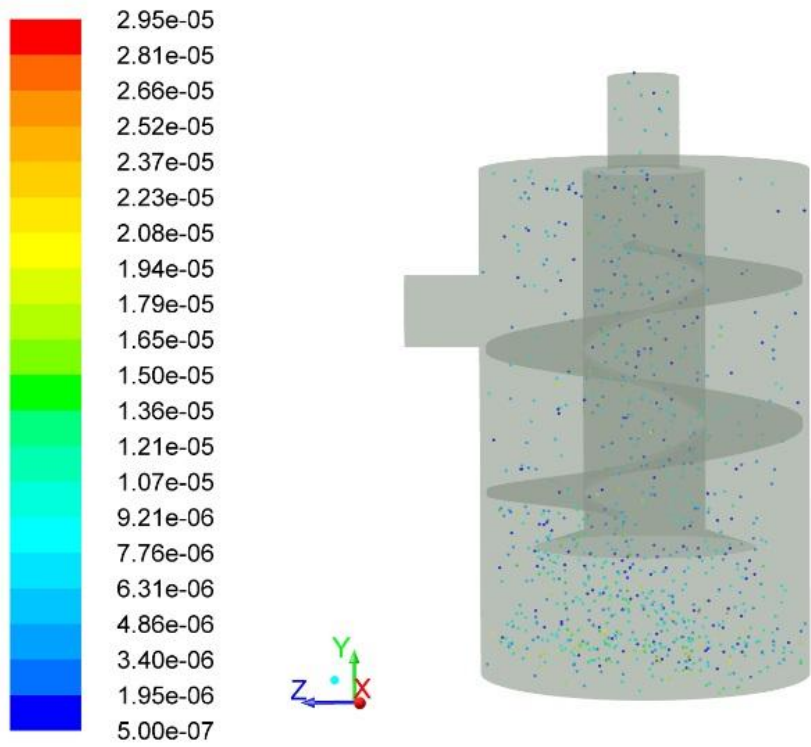
Figure 5.9: Droplet Injection at 1.0000 secs
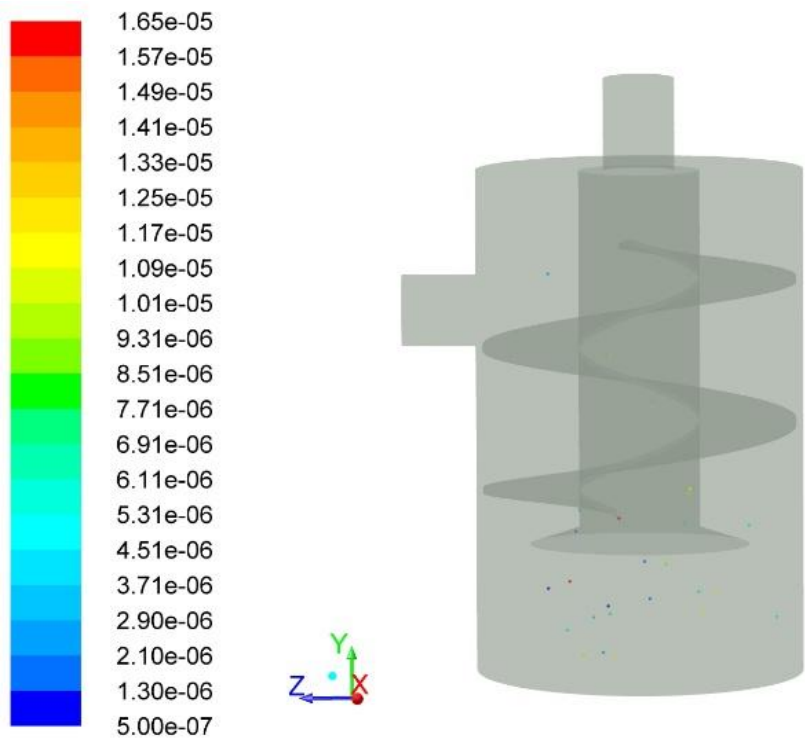
Figure 5.10: Droplet Injection at 2.0000 secs

Combining the information from the GEC with the droplet trajectory plots it is apparent that droplets with a diameter between 38.6 and 50 microns are captured by the separator within the first 0.1050 seconds at which point the droplets are almost completely dispersed within the main separation space. These droplets diameters are predominantly removed from the simulation due to the impact with the centre tube and helix and to a lesser extent by the cylindrical wall. 0.5 seconds after the time of injection the maximum droplet diameter which still exists within the domain has not changed significantly but sub 10 microns droplets can be seen to be leaving the separator through the outlet face and hence not separated. After 1.0 second within the domain the maximum droplet diameter which still exists is now below 30 microns with the vast majority of remaining droplets being in the 0.5-15 microns range. These are the droplet diameters which the GEC shows are not always completely separated. Two full seconds after the injection, the mass of remaining droplets is small with the diameter ranging from 0.5-16.5 microns. The probability of these droplet diameters being separated will always be less than 100% as per the GEC.

5.4.2 Droplet Breakup Model Assessment

The TAB model which has been tested for sprays and used for simulating the flow in an oil-gas cyclone separator has been shown to produce data which closely predicts that obtained from experimental measurements. In the investigation of Gao et al they found that without the use of the TAB model the discrete phase simulation over predicted the separation efficiency by up to 30% in some cases (Gao, et al., 2012). However when the effects of droplet breakup were considered the results from the model matched the experimental data very well with the maximum error being less than 10% and this was found to be at lower inlet gas velocities, 9-11 m/s, where the collision energy of the droplets was lower. The inlet velocity range used in the investigation of Gao et al was 9-14 m/s whereas in the case of the helical oil separator the velocity range is between 1.67 and 6.67 m/s for the recommended 25-100% discharge volume flowrate range specified by Henry Technologies. Should the separator be tested at discharge flowrates higher than 100% the velocity might then be within the range of Gao et al. therefore the effects of droplet breakup may need to be considered. The droplet breakup model can only be activated when the transient solver method is used therefore the approach of Derksen cannot be implemented for this particular study. Figure 5.11 displays the results with and without the droplet breakup model activated in comparison with the experimental values. To allow a direct comparison the data without the breakup model activated is from the concurrent simulation approach.

As with the study assessing the different solution approaches all walls within the domain was assigned the escape boundary condition with the overall separation efficiency calculated using equation 5.16.
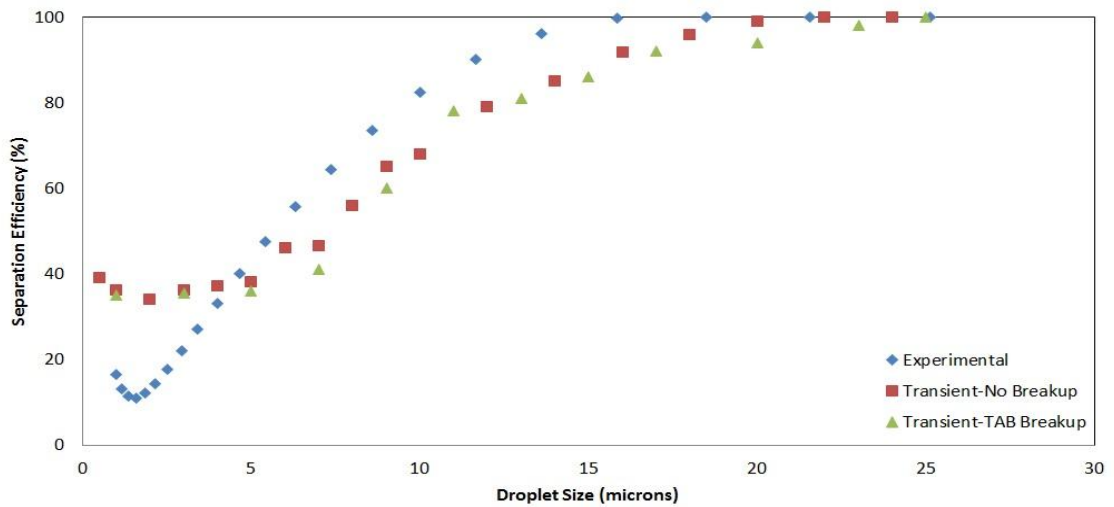
Figure 5.11: Effect of Droplet Breakup

From the data presented in Figure 5.11 it can be seen that the inclusion of the TAB droplet breakup model, with the number of resulting breakup parcels being 2 in each case, does not have any significant effect on the results for the grade efficiency curve which represents the separators overall performance and therefore will not be included in the subsequent performance predictions for discharge flowrates of 100% and below. The insignificant difference in overall separation efficiency obtained from implementing the breakup model in comparison to having no breakup model is supported by the fact that the velocities within the separation space are relatively low which combined with the small diameters of the droplets being simulated result in a small Weber number as is demonstrated in the droplet-wall interaction fate map shown in Figure 5.3.

5.4.3 Wall Boundary Conditions Assessment

To determine the appropriate boundary conditions to apply to the internal faces of the helical separator geometry the results from the droplet fate assessment shown in Figure 5.3 are used. From the droplet-wall interaction fate calculations it is apparent that at low velocities over the range of droplet diameters which enter the separator the outcome of the collision is that the droplet will become attached to the wall and hence removed from the calculation hence the escape boundary condition should be applied to model this process. There is a small range within the low droplet velocities where the outcome of the

interaction results in the droplet rebounding back into the domain in which case the reflect wall boundary condition should be applied to capture this phenomenon. The upper right quadrant of the droplet-wall fate diagram defines the droplet diameters/velocities where the outcome of the interaction is splashing in which case the wall-film boundary condition should be applied to allow a number of splashed droplets to be generated and entered into the domain after the collision have taken place. By exploring the effects of these three different wall boundary condition types allows a full assessment of the effects of varying the condition since the first two options define the droplet fates for the upper and lower bound separation efficiencies. In carrying out this assessment the average realization approach has been used without the inclusion of the droplet breakup model based on the results from the investigations in the previous sections. When implementing the wall reflect boundary condition the coefficient of restitution which defines whether the collision is elastic or inelastic needs to be defined a constant between 0 and 1. In varying this value it was found that there was no overall impact on the separation efficiency of the separator therefore a value of 1.0 has been used in this assessment, since this is the default setting. When implementing the wall-film model the default setting for the number of splashed drops is 4, again this will be used for the purpose of this comparison. The cylindrical wall of the separator and baffle plate at the base of the unit are always assigned the escape boundary condition for the data presented in Figure 5.12. The other internal walls of the separator are either assigned the escape, reflect or wall-film boundary conditions with the data presented for each one in Figure 5.12.
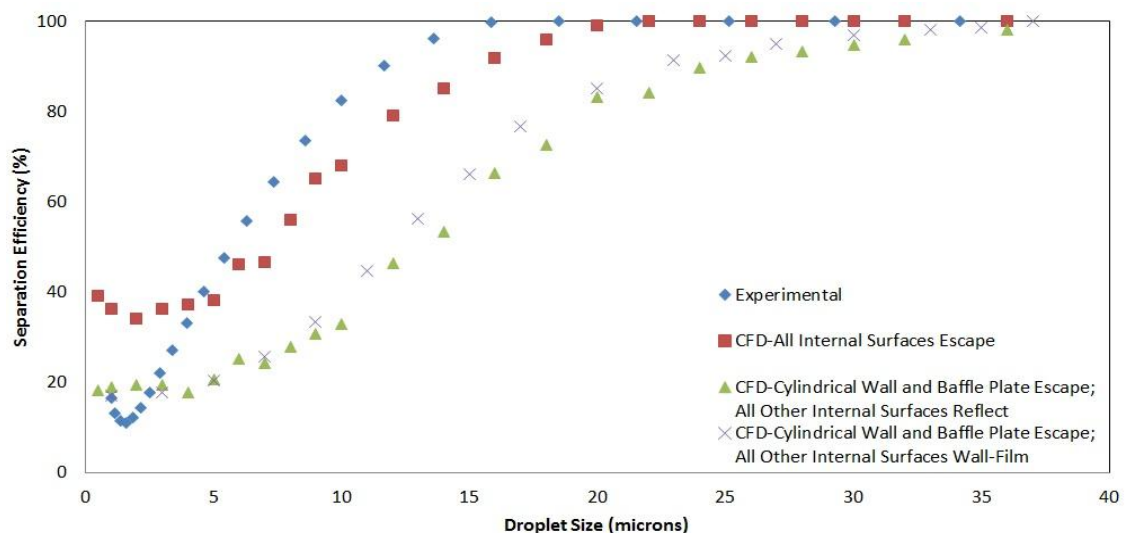
Figure 5.12: Wall Boundary Conditions Comparison

Figure 5.12 shows that the 0.5-4 micron droplet size range is well predicted by having just the cylindrical wall and baffle plate as droplet removal boundary conditions and all other internal walls assigned the reflect or wall-film boundary type. However for droplet sizes greater than 4 microns the reflect and wall-film boundary condition types significantly under-predict the separation efficiency of the separator compared with the data obtained from the experimental investigation whereas the all surface escape wall condition is in line with the experimental data albeit with a maximum discrepancy of 17%. Referring to the droplet-wall interaction fate map produced in Figure 5.3 it demonstrates that for the droplet size range used in the production of the GEC's the outcome of the wall interactions predominantly results in the droplets sticking to the wall and hence becoming separated from the flow field. However in the case where the velocity is significantly large the outcome of the interaction is for the droplet to bounce off the wall and re-enter the domain; in assessing the velocity magnitudes within the domain this fate is only possible at the inlet plane where the flow enter the separator and impacts on the centre tube with velocities in the 7-11 m/s range. The effects of including the wall-film model in predicting the separation efficiency produces results which are in line with those obtained using the reflect boundary condition type assigned to the same internal surfaces. Again referring back to the map produced in Figure 5.3 it is clear that for the result of the droplet-wall interaction to emanate in splashed droplets the size of the droplet needs to be 200 microns combined with a high incident velocity. Droplet sizes above the diameter range used to produce the GEC's can be assumed to be separated 100% therefore limiting the number of droplet diameters which need to be simulated.

5.4.4 Summary of Model Assessment

From the information presented in this assessment of the available wall interaction models it is clear to see that there is not one particular set of modelling conditions which are able to accurately predict the separation efficiencies obtained from the experimental measurements across the entire droplet size range. However it is apparent from the aforementioned data that some conditions provide predictions which are more in line with the experimental results than others. In summary the realization approach of Derksen can be used to produce results which are very similar to a full transient simulation of the droplet flow however in using the realization approach there is a significant reduction in the amount of computational time required therefore it is this approach which will be used in the remainder of simulations carried out in this investigation. It is also apparent for the

discharge flowrates of 100% and below that the effects of droplet breakup has no effect on the overall separation efficiency due to the small Weber number of the droplets of interest, however when the flowrate is increased droplet breakup may have an impact therefore this needs to be reassessed, but will mean reverting back to the transient solution approach. As a result the significance of the outcome on the efficiency will need to be assessed to compensate for the increase in computational time required to deliver a solution. The factor producing the most significant effect on the droplet separation efficiency predictions using the discrete phase model is in assigning the appropriate wall boundary condition. Although assigning the escape boundary to all internal surfaces over predicts the performance between 0.5-4 microns, the results from the overall droplet size range of interest are in favour of the escape wall condition rather than a reflect/wall-film type therefore it is the former which will be applied in all consequent simulations.

5.1 50% Flowrate Grade Efficiency Curve Predictions

To further assess the ability of the DPM model to predict the separation efficiency of the helical oil separator the single phase flow field was solved for 50% discharge flowrate, 0.0032 kg/s and the particle tracking carried out on the converged flow field. The integral time step for the 50% flowrate was 0.0435 seconds therefore the realizations were obtained in increments of 0.0870 seconds starting from 7.0 seconds. The results from each flowrate were averaged over 9 realizations since this was found to produce enough data to produce an independent average. Similar to the 100% discharge flowrate assessment the average from the 10%, 5% and 2.5% GEC data points will be used since the variation associated with the individual mass fractions is due to experimental errors.
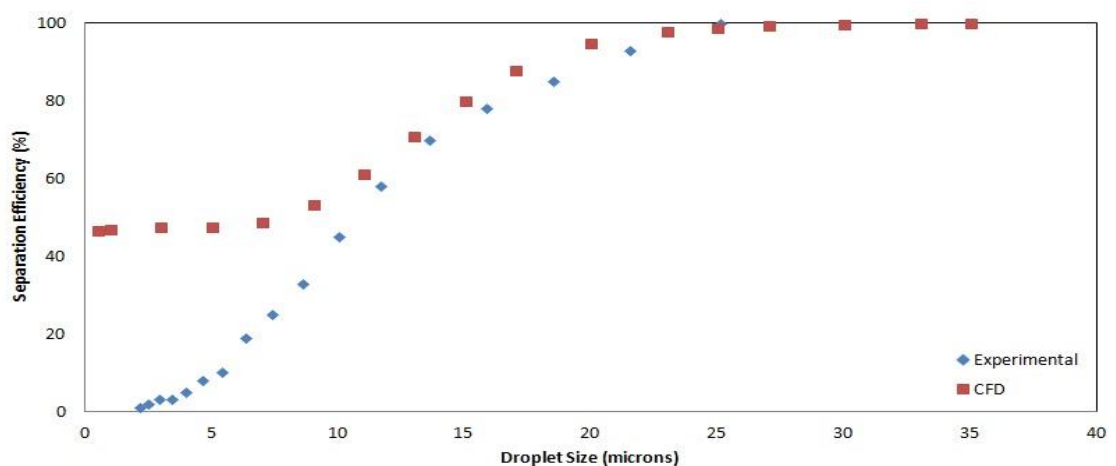
Figure 5.13: 50% Discharge GEC Comparison

The GEC for the separator at 50% discharge flowrate, shown in Figure 5.13, corresponds well with the experimentally determined GEC for droplet diameters greater than 10 microns. However for droplet diameters in the sub 10 microns range the CFD data over predicts the separation efficiency by up to 45% in some cases. The over predicted separation efficiency for the sub 10 micron droplets, similar to the over prediction of sub 4 micron droplets for the 100% discharge condition, indicates that although an optimal modelling approach has been determined using the available models there is still aspects of the physical separation process which are not being accurately captured. Based on the data presented in this chapter it is apparent that further work is required to refine the droplet separation modelling approach for the helical oil separator.

5.6 Major Outcomes

The aim of this chapter was to use the validated single phase gas flow combined with the droplet separation efficiency data to assess the capabilities of the available modelling techniques within the DPM framework in predicting the GEC's for the helical separator. The results from the assessment of the modelling approach used to determine the droplet separation efficiency demonstrated that the realization approach of Derksen can be used by taking the average efficiency from 9 frozen flow field simulation. This approach provides data which can replicate the efficiencies obtained from the time intensive transient tracking approach providing a time saving of approximately 96.5%. Given the flow velocities and droplet sizes which are present within the separator the appropriate wall boundary condition to be applied to all internal surfaces of the separator was found to be the escape condition since the droplet/wall interaction fate was predominantly in the stick region indicating that on impact with a surface the droplets would not re-enter the domain. The effects of applying the TAB droplet breakup model have also been assessed and resulted in no significant change in the overall separation efficiency for the range of droplet diameters simulated.

For both discharge flowrates simulated the models were found to over predict the separation efficiency for small droplet diameters particularly in the 0.5-4 micron range for 100% discharge flowrate and sub 10 micron diameters for the 50% discharge condition. As a result further work needs to be carried out to refine the modelling approach to accurately capture the separation efficiency of these droplet diameters. The major assumption in this work is that when a droplet impacts with any surface it is assumed separated and hence

removed from the simulation. However it is known from the experimental testing that a liquid film forms on all internal surfaces, which is currently not accurately accounted for, therefore further work needs to be carried out to model the presence of this film on the walls.

Nonetheless one of the major objectives of this investigation was to assess the ability of the current models to be used as a tool for separator performance improvement determination. The results presented within this chapter indicate that this is possible however this will be explored further in the subsequent chapter where suggested separator design changes will be modelled and then experimentally tested to determine whether the predictions are in line with the physical testing results.

Chapter 6 Separator Design Improvement Aspects

6.1 Introduction

The aim of this chapter is to explore potential design changes which can be used to achieve at least one of the following factors; increased separation efficiency, reduced pressure drop and an overall reduction in the cost of manufacture of the helical oil separator. The design improvements which have been considered are based on the data obtained from the testing of the current separator configuration presented in this thesis and the information contained within the literature for enhancing particle/droplet separation mechanisms. In accordance with one of the initial aims of this investigation, to assess the ability of the currently available computational models to be used as a tool for separator design improvement, some of the suggested improvements will be assessed utilising the modelling approaches discussed in previous chapters and conclusions drawn on the feasibility as an industrial design tool.

6.2 Increased Gas Flowrate

Given the local velocity components within the main separation space of the helical unit are low relative to the velocities in a typical centrifugal separator, even at the maximum recommended discharge flowrate condition for the separator, the resulting centrifugal force experienced by the droplets is therefore also low. By simply increasing the discharge flowrate through the separator and hence increasing the local velocities within the main body the centrifugal force generated will increase as the tangential velocity component increases. This will increase the probability of the smaller droplets, particularly those in the sub 20 micron range, being transported to the cylindrical wall where they can be removed from the flow field. To provide an initial indication of whether this proposed change in the operational discharge flowrate range would lead to an increase in the overall separation efficiency of the helical separator a CFD simulation was carried out using the validated modelling approach presented in previous chapters of this thesis for a gas discharge flowrate of 200%. A grade efficiency curve was produced from the data acquired from the 200% flowrate simulation and compared with the GEC's from the 100% and 50% discharge experimental measurements to assess whether there was an increase in separation efficiency. The results are given in Figure 6.1.
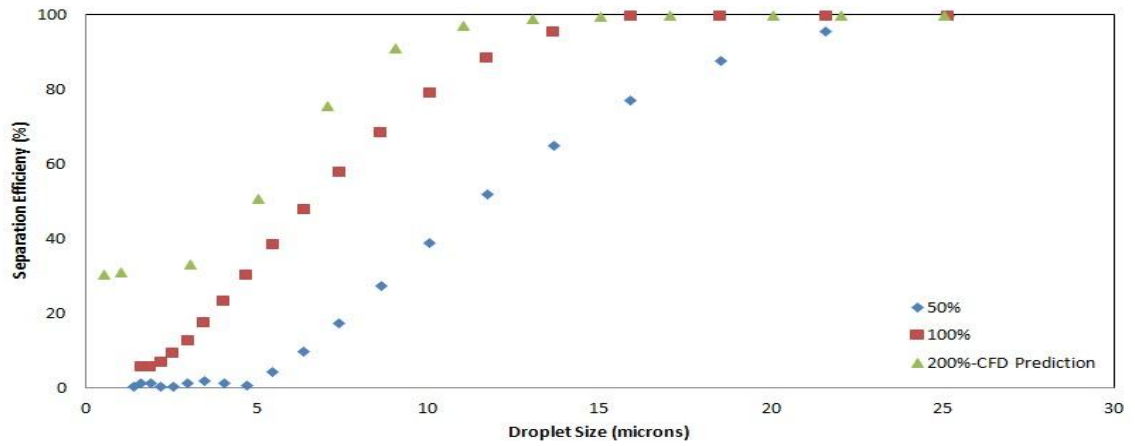
Figure 6.1: 200% Discharge Flowrate Prediction Comparison

As predicted the increase in gas flowrate and hence the centrifugal force experienced by the droplets within the main cylindrical body of the separator results in an overall increase in the separation efficiency by shifting the GEC to the left as can be seen in Figure 6.1. By increasing the gas flowrate to 200% subjects the droplets to an increased centrifugal force and hence increases the probability of them being transported to the cylindrical wall and removed from the airflow.

To assess this concept further an experimental investigation was carried out for five different gas discharge flowrates, with an inlet velocity ranging from 3.33 m/s to 26.68 m/s, which corresponds to a range of 50% to 400% of the standard operating value, with a constant oil flowrate of 15 mL/min being injected into the system. The resulting grade efficiency curves, shown in Figure 6.2, were determined for the no mesh unit subject to a droplet only inlet flow condition.
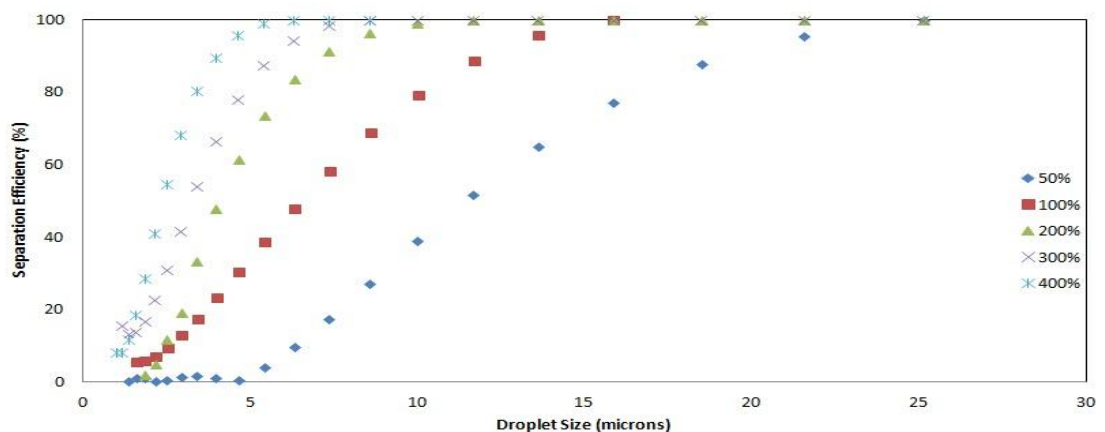
Figure 6.2: Experimental GEC's for Various Gas Discharge Flowrates

From the data presented in Figure 6.2 it is clear to see that by increasing the gas discharge flowrate through the separator results in an increase in the overall separation efficiency of the unit and overall decrease in the maximum droplet size which is not removed from the flow field. In comparing the 50% and 400% discharge flowrate data sets the d_{50} droplet diameter is decreased from 11.5 microns to 2.5 microns and the maximum droplet size which is not removed by the separator has been decreased from 25 microns to 8 microns. Although increasing the gas flowrate through the separator produces an improvement in the overall separation efficiency of the helical separator there is a penalty to pay in terms of the pressure drop. By increasing the inlet gas velocity by a factor of 8 from 50% to 400% gives rise to an increase in pressure drop by a factor of 64 since pressure loss is proportional to the square of the velocity. Therefore the pressure drop is seen to increase from approximately 12 Pa for the 50% flowrate to approximately 780 Pa for the 400% flowrate when operating at atmospheric pressure.

The results from the assessment of increasing the gas flowrate on the separation efficiency have found to produce two positive outcomes. Firstly, the CFD modelling approach which has been validated in this investigation can be used to provide an indication of the expected separation efficiency improvements as a result of changes to the operating conditions of the separator. The results from this simulation provide evidence to support the proposed modelling approach as a potential tool for commercial separator design. Secondly, a definitive conclusion can be drawn from Figure 6.2 in that by increasing the gas flowrate through the helical separator unit to 200% discharge flowrate the d_{50} cut size diameter is now in the sub 5 micron range. It is also shown that droplet diameters greater than 10 microns can be separated almost 100% of the time which is an improvement upon the 100% discharge flowrate condition although it is coupled with an increased pressure drop as a penalty for the higher flow velocities.

6.3 Geometrical Modifications

There is an extensive range of droplet separation mechanisms currently in use (Burkholz, 1989).The cyclone separator/swirl tube configurations exhibits the closest geometrical resemblance to the helical oil separator under investigation. Apart from the lower region of the separation space normally being in the form of a cone for the standard cyclone separator design, the other major geometrical difference from the helical separator is the presence of the tangential inlet to the cyclone in comparison to the radial entry to the

helical unit. Introducing the flow into the main separation space via an inlet which connects to the cylindrical body tangentially immediately imparts a swirling component to the flow which follows the streamlines of the geometry. Replacing the radial inlet connection of the helical oil separator with a tangential entry inlet will allow a swirling flow to form on entry to the separator rather than taking one full revolution of the helix to develop as is the case with the current radial inlet. By generating a swirling flow on entry to the separator will increase the probability of the entrained droplets being radially transported to the cylindrical wall of the separator and hence improving the overall separation efficiency in comparison to the standard radial inlet.

Another factor which will enhance the probability of the droplets reaching the cylindrical wall within the main separation space is to increase the residence time. Since the bulk flow follows the helix from the inlet to the centre tube entrance, by increasing the number of revolutions of the helix and hence the number of revolutions the gas flow makes, will therefore increase the droplet residence time and lead to an increase in overall separation efficiency. The current helix contains 2 full revolutions around the centre tube therefore to potentially double the residence time the number of complete revolutions is increased to 4.

It has already been discussed that increasing the discharge flowrate through the separator results in an increase in efficiency due to the higher velocities which are generated within the separator body, but this also results in an increased pressure loss. However, by reducing the flow cross-sectional area for the same mass flowrate will produce an increase in velocity to satisfy continuity. To achieve this the helix is compressed such that the pitch is reduced from 63.5 mm to 35 mm since this will allow for four complete revolutions of the helix to be attached to the centre tube of the standard S-5190 geometry and also an increase in the droplet residence time. The results from standard and no mesh units presented in chapter 4 indicate that the internal wire mesh screens have no significant effect on the overall separation efficiency and are therefore not included in the redesigned separator unit. The three modifications to the standard unit which have been described are shown in Figure 6.3 with A, B and C denoting the change of inlet location from radial to tangential, the compression and increased number of revolutions of the helix and removal of the internal mesh screens respectively.

As with the increase in gas flowrate proposed design improvement, a model of the tangential inlet with compressed helix was created and a CFD simulation carried out to

determine the potential improvements in separation efficiency that would result by implementing the aforementioned modifications. The predicted GEC of the tangential inlet design for a discharge flowrate of 100% is shown in along with the experimental data of the standard and no mesh units for the same discharge flowrate condition.
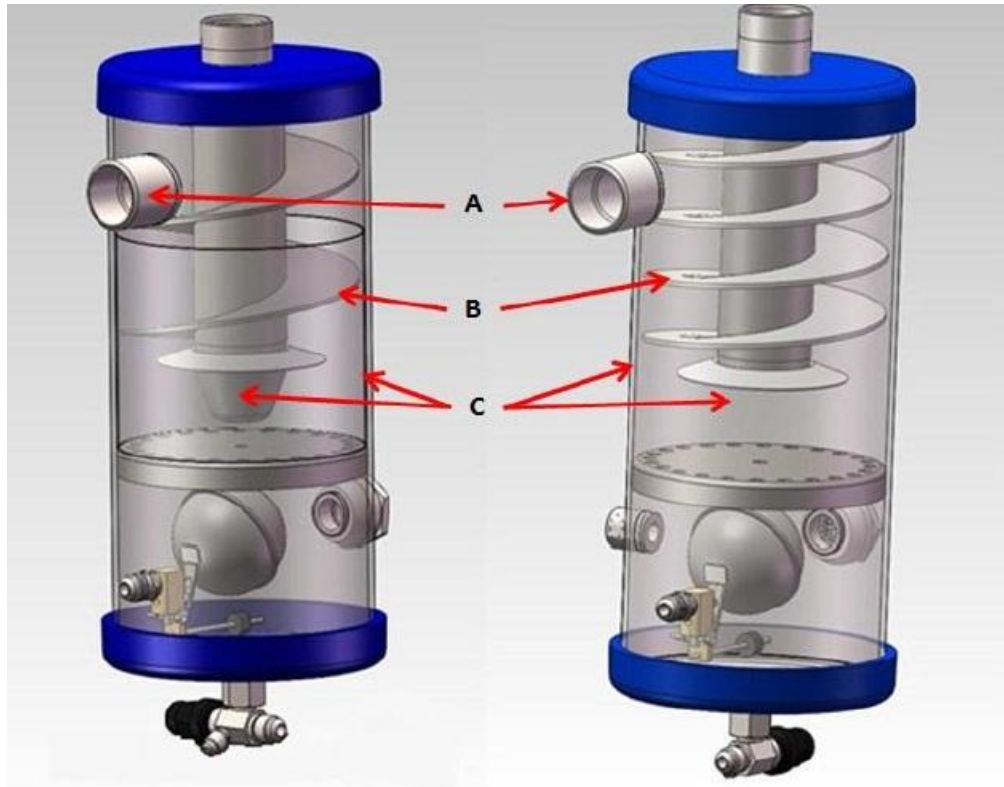
Figure 6.3: Comparison of Standard Unit and Tangential Unit with Compressed Helix
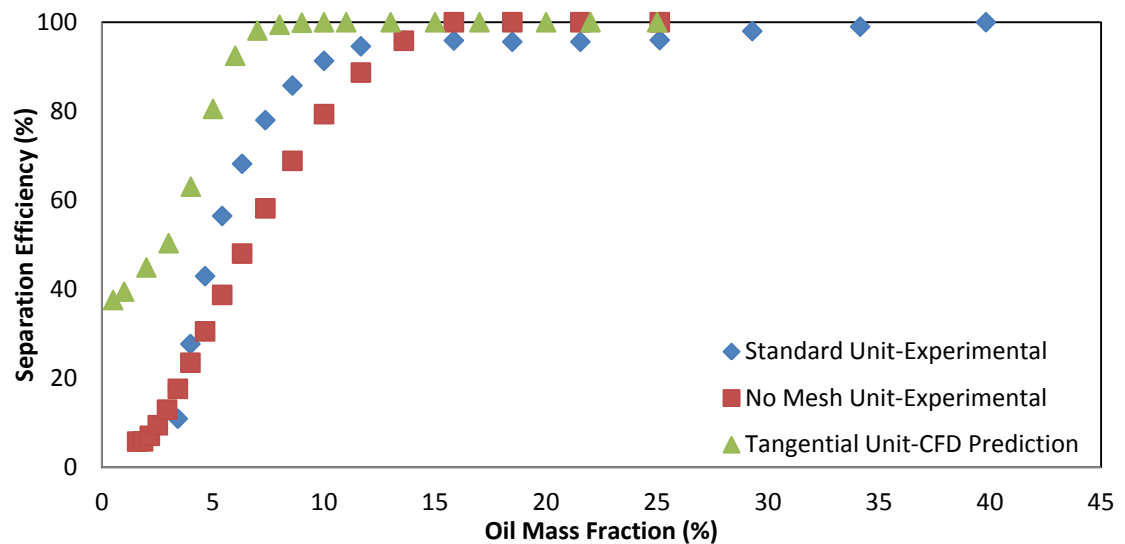
Figure 6.4: Tangential Inlet Prediction Comparison

The results from the CFD simulation of the tangential inlet unit with the compressed helix indicates that there is a significant improvement in performance in comparison to the standard and no mesh units with all droplets of diameters larger than 11 microns being 100% separated. The predicted d_{50} cut size diameter for tangential unit is 3 microns in comparison to the 5 and 6 microns d_{50} diameters which have been experimentally determined for the standard and no mesh units respectively. The predicted pressure drop across the tangential unit for the 100% discharge flowrate condition was 212 Pa which is approximately two times greater than the standard unit and four times greater than the no mesh unit. Since the results from simulating the tangential unit have indicated separation efficiencies which have notable improvements compared to the standard and no mesh units a prototype was manufactured to allow for experimental performance data to be obtained.

The separation efficiency measurements obtained for the tangential inlet unit with the compressed helix have been carried out at 3 BarG with a combined liquid film and droplet inlet flow condition for three gas discharge flowrates, 100%, 50% and 25%. The data is presented in Figure 6.5 to Figure 6.7 and contains the results from the standard unit separation efficiency testing at the same operating conditions thereby allowing a comparison to be made.
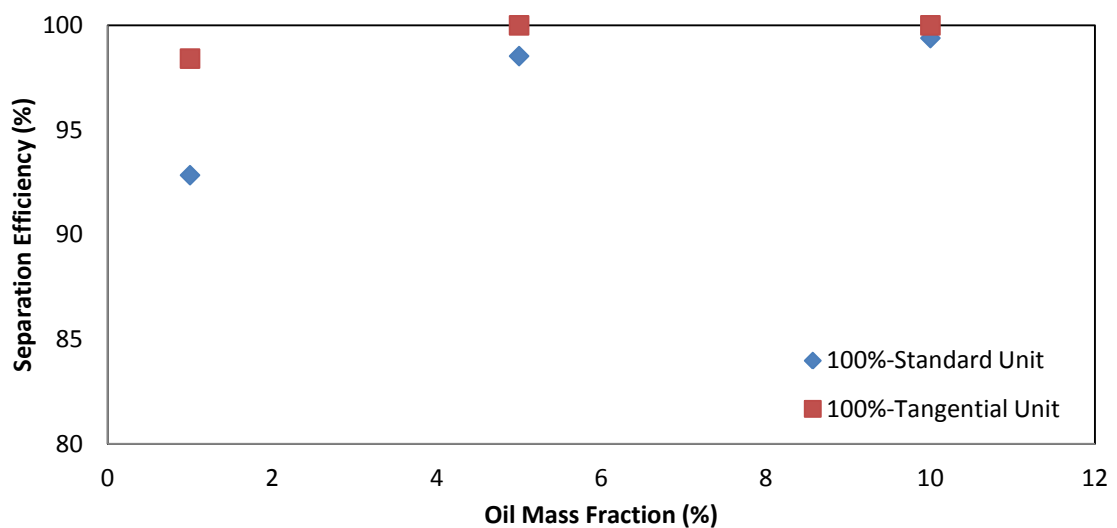
Figure 6.5: Standard and Tangential Unit Separation Efficiency at 100% Discharge Flowrate
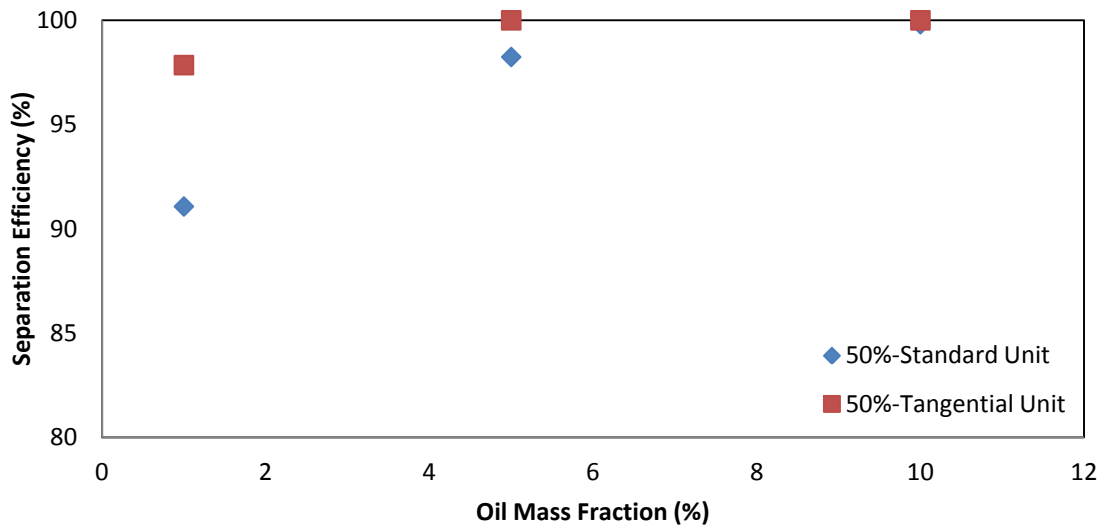
Figure 6.6: Standard and Tangential Unit Separation Efficiency at 50% Discharge Flowrate
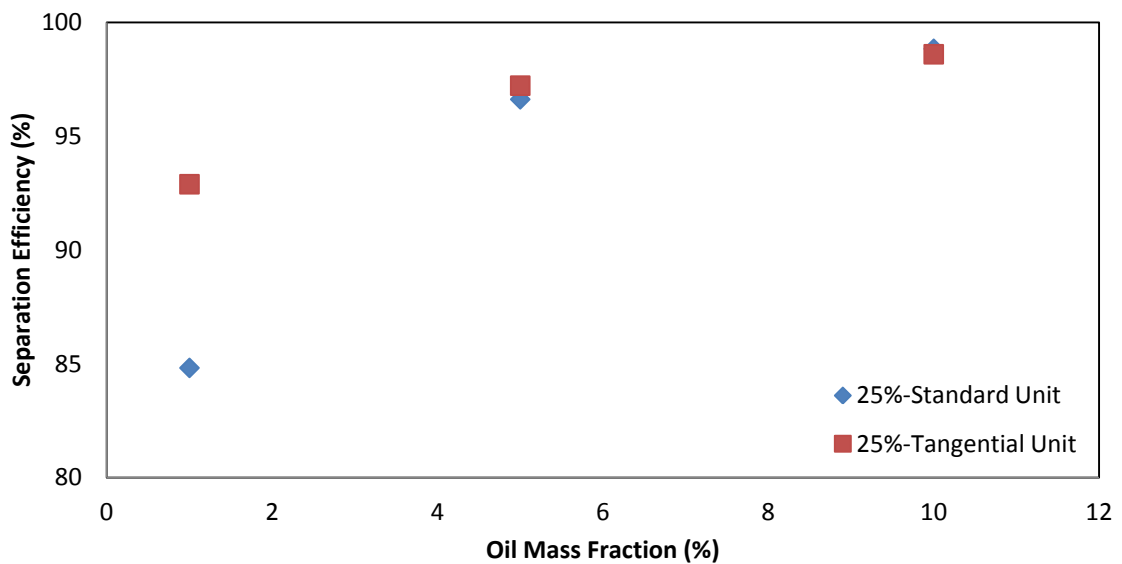
Figure 6.7: Standard and Tangential Unit Separation Efficiency at 25% Discharge Flowrate

The experimental data from the testing of the tangential inlet unit was obtained out with the loan period of the Malvern Spraytec apparatus therefore no experimental GEC could be obtained for the this unit. From the experimental data which was obtained for the tangential inlet unit at 3 BarG the results can be seen to support those presented from the results of the CFD simulation for this modified unit. It was found that across the range of conditions tested the tangential unit has higher separation efficiency than the standard unit. The improvement in performance achieved by the tangential inlet unit is most notable at low oil mass fractions where the overall separation efficiency is increased by up to 8% compared with the standard unit separation efficiency. From the droplet size

measurements carried out previously it was confirmed that at lower oil mass fractions the volume fraction of droplets entering the separator which have diameters in the sub 20 microns range is greater than at higher oil mass fractions. It is as a result of this that the overall separation efficiency of the separator unit decreases for these low oil mass fractions. By initially imparting a swirl component to the flow on entry to the separator via a tangential inlet; increasing the droplet residence time by forcing the flow to have a greater number of revolutions within the separation volume; and increasing the gas velocity through reducing the flow area by compressing the helix the overall separation efficiency for the redesigned tangential inlet unit has a minimum value of 92.89% compared with the standard unit with 84.82% for all the conditions tested. Combining the separation efficiency data with the predicted GEC from the CFD simulation provides good evidence that the high performance of the tangential inlet unit is a result of its ability to separate smaller droplets than both the standard and no mesh units and is therefore worthy of consideration as a replacement for the current standard helical separator unit.

6.4 Performance Enhancement Attachments

In addition to the aforementioned proposals for improving the separation efficiency of the helical oil separator two simple performance enhancement attachments were also designed and tested; an improved mesh screen and a swirl generator. The design requirements for the mesh screen and swirl generator were to provide an increase in separation efficiency without significantly sacrificing the pressure drop and be able to be inserted into the current test facility with minimal modifications. Based on these requirements the mesh screen was chosen to be sandwiched between the downstream face of the inlet pipe and the inlet flange of the separator since this is allows the relatively high velocity at the inlet to be harnessed and is also easily accessible for installation. The swirl generator was chosen to be located within the centre tube of the unit since this is also a region of high velocity within the separator and is also the region where the small droplet diameters which fail to be separated in the main separation space have to pass through to leave the unit. To allow the swirl generator to be installed in the centre tube a modified version of the no mesh separator previously used in this investigation had to be manufactured with hermetically sealed top and end caps, as shown in Figure 6.8, to allow access to the internals of the separator.
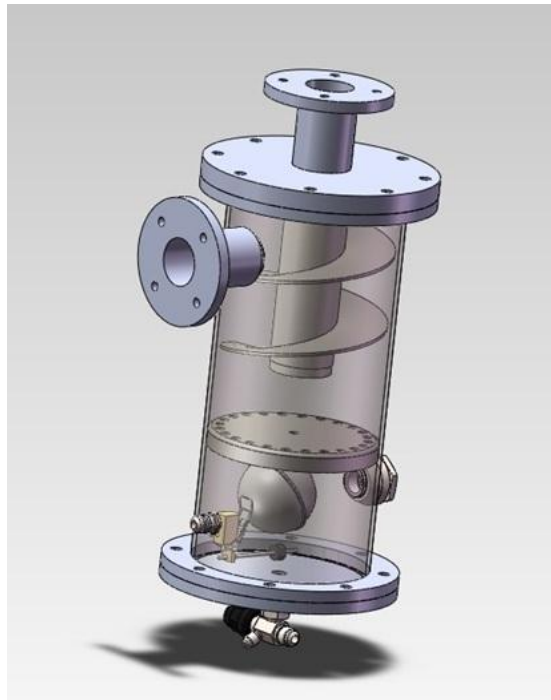
Figure 6.8: Hermetically Sealed No Mesh Separator

The experimental data from the droplet size measurements at the outlet of the separator have shown that droplet diameters less than 20 microns are not completely separated and that sub 10 micron droplets are extremely difficult to separate in the current separator configuration. Based on this evidence the wire mesh screen at the inlet and the swirl generator in the centre tube were designed with the focus of increasing the separation efficiency for droplets in the sub 10 microns region. Using the design criterion of Burkholz for the wire mesh screen and that of Ramachandran et al for the swirl generator, the optimum design configuration based on separation efficiency and pressure drop specifications for each attachment are given in Appendix 5 (Burkholz, 1989), (Ramachandran, et al., 1994).

Given the requirements for the attachments the optimal wire mesh screen configuration to be used at the separator inlet had a 68% closed area and a wire diameter of 1.14×10^{-4} m. The predicted separation efficiency for a 5 micron droplet with a 100% discharge flowrate for the aforementioned configuration was 56% and a pressure loss of 30 Pa; however the pressure drop calculation does not take into account the further reduction in flow area due to the formation of liquid film on the wire strands of the mesh. The mesh screen was held in place using a flange with an internal removable disc assembly, as shown in Figure 6.9,

which would allow the mesh to be held in place across the entire 31.5 mm diameter of the inlet pipe.

Figure 6.9: Wire Mesh Screen Flange Assembly

The swirl generator was designed such that the entire length of the centre tube was utilised and include a mechanism to reduce the energy losses associated with imparting swirl by gradually introducing a rotational motion to the flow. In doing so 25% of the overall centre tube length was used for gradually introducing swirl to the flow and the remaining height, 120 mm, was used to apply three revolutions to the flow via a swirl tube with a 40 mm pitch. The predicted separation efficiency of a 5 micron droplet by the swirl generator was 82.1% with an associated pressure loss of 80 Pa with a 100% discharge flowrate condition. To allow the 43.3 mm diameter, 1.5 mm thick swirl generator to be installed into the centre tube of the hermetically sealed separator it was fitted into a 1.5 mm thick sleeve which with a threaded ring to allow it to screw into an internal thread created at the entrance to the centre tube. A 2 mm drain hole was created on the base of the threaded ring to allow the oil separated by the swirl generator to be returned via flexible tubing to the oil collection chamber. Around the circumference of the sleeve, housing the swirl generator, four layers of holes were created to allow the separated oil to drain down the internal wall of the sleeve to flow through and accumulate on the threaded ring with the drain hole where it is then led to the oil collection chamber. The swirl generator and sleeve housing assembly are shown in Figure 6.10.

Figure 6.10: Swirl Generator Assembly

Each attachment was installed into the separator test facility independently. The overall separation efficiency obtained for a droplet only inlet flow condition for the attachments with a 100% discharge flowrate at atmospheric pressure are shown in Figure 6.11 and are compared with the droplet only performance of the no mesh unit for the same flow conditions.
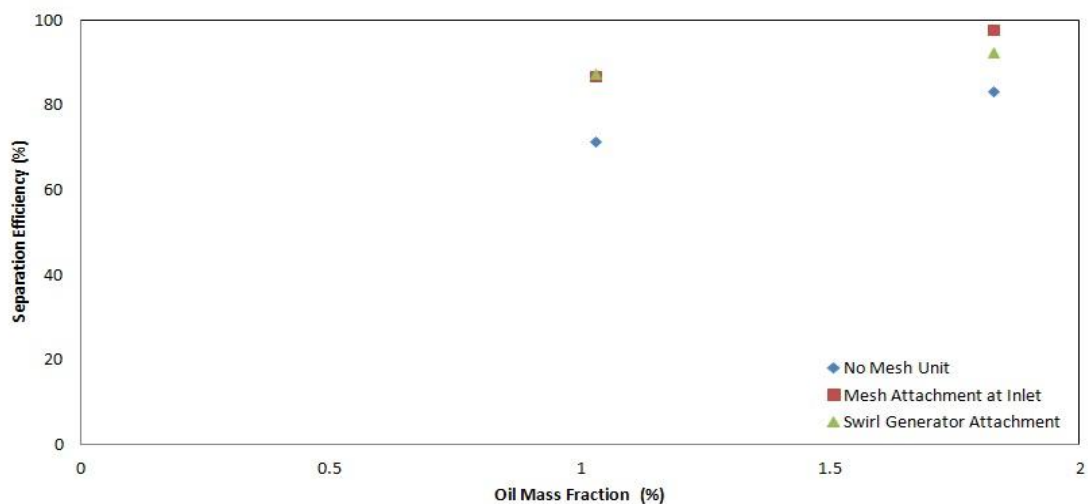
Figure 6.11: 100% Discharge Separator Droplet Separation Efficiency Comparison with Enhancement Attachments

The results from the experimental testing of the inlet mesh screen and exit tube swirl generator in Figure 6.11 show a notable improvement in droplet separation efficiency in comparison to the no mesh unit without any attachments. The addition of the inlet mesh screen increases the droplet separation efficiency of the unit by as much as 20% such that

the efficiency of the unit is increased from 80% up to 96% for the 2% oil droplet mass fraction case. The swirl tube has a similar effect but the increase in efficiency is 15% with an increase in separation efficiency from 80% to 92% for the 2% mass fraction case. The resulting pressure drop across the system with the wire mesh screen attachment in place was 700 Pa. This is significantly greater than the theoretical prediction however, as previously mentioned, a liquid film was found to build up on the wire mesh strands reducing the available flow area and hence increasing the pressure loss. With the swirl generator attachment located in the centre tube the total pressure loss across the system was found to be 136 Pa, which is lower than the theoretical prediction. This can be attributed to the inclusion of the swirl introducer which accounted for 25% of the overall length of the attachment. Therefore given the operational requirements for a droplet separator to have a high separation efficiency coupled with a low pressure drop, the suggestion would be for the swirl generator in the exit tube to be implemented in the current separator to improve the separation efficiency.

6.5 Major Outcomes

The purpose of this chapter was to assess potential design changes to the current helical separator geometry to satisfy one or more of the following; increase the separation efficiency, reduce the pressure drop or lower the cost of manufacture. In doing so the effects of increasing the gas discharge flowrate were explored; changing the location of the inlet pipe from a radial to a tangential location combined with compressing the helix and increasing the number of revolutions; inserting a wire mesh attachment to the inlet of the separator; and fitting a swirl generator to the centre tube. The results from all the suggested design changes resulted in an increase in the overall separation efficiency of the helical separator but were also coupled with an increase in the overall pressure drop across the system, some being only marginal while others were significant. In terms of lowering the cost of manufacture in comparison to the current design the removal of the internal mesh screens and increasing the recommended maximum discharge flowrate for the units would satisfy this requirement as all the other possibilities require further parts and materials to be used.

Given the extensive use and high separation efficiencies achieved with tangential entry cyclones presented within the literature combined with the initial results obtained from the testing of the helical separator with the tangential inlet, the author believes this design

improvement to be the most suitable in terms of the overall requirements for a redesigned separator. However before this design is considered for production further experimental testing and design refinement is required to produce an experimental GEC over the wide range of conditions which the separator operates in.

Chapter 7 Conclusions and Future Recommendations

The work presented in this investigation has been carried out to satisfy the objectives presented in Chapter 1. The results from the computational and experimental studies combined with the discussions of the findings have allowed an assessment of the state of the art models to predict the performance of a droplet separator.

The work presented within this thesis has consisted of three main sections. Firstly, obtaining experimental measurements of the gas flow within the helical oil separator and then using the data to validate the single phase gas flow model. Secondly, capturing separation efficiency and pressure drop measurements to characterise the performance of the separator which could then be used combined with the validated single phase model to assess the DPM model in predicting the droplet separation efficiency. Finally, a separator improvement investigation to assess the ability of the computational models to be used as a design tool and implement some of the droplet separation efficiency enhancement mechanisms recommended within the literature. The major outcomes from these investigations were presented at the end of each chapter, however the findings will again be summarised here and conclusions made on the results with respect to the initial objectives set out in the introduction to this thesis.

7.1 Single Phase Flow Investigation

The single phase flow investigations consisted of two stages; experimentally obtaining velocity component measurements within a Perspex replica of the helical oil separator using LDA and then using this data to validate a CFD model which could replicate the flow field which exists in practice. The results from this investigation allowed the following conclusions to be derived;

1. LDA measurements can be obtained within a geometrical replica of the helical oil separator with a sufficient level of accuracy to allow the data to be used to validate the single phase gas flow modelling approach.

2. The flow field within the separator is unsteady due to the presence of the PVC therefore to accurately capture this phenomenon a transient solution approach has to be adopted. Furthermore, due to the swirling flow in the main separation space the RANS approach for modelling the turbulent flow field does not accurately capture the physics of the flow. As a result the advanced LES turbulence modelling approach with high order discretization

schemes needs to be implemented to provide the levels of modelling accuracy necessary to describe the complex gas flow in the helical separator. The results from this modelling approach provide sufficient levels of accuracy to capture the bulk gas flow field within the separator although there are some local regions which are not accurately represented.

3. The use of laser sheeting allows the bulk flow field to be examined and provide further evidence that the flow phenomenon, such as the presence of the PVC at the entrance to the centre tube, which have been captured by the LDA and CFD do in fact exist.

7.2 Two Phase Flow Investigation

To allow the separation efficiency and pressure drop across the separator to be measured a test facility had to be designed, constructed and commissioned. As separators are highly dependent on the flow conditions at the inlet a series of investigations were carried out to assess how varying these conditions impacts on the separation efficiency of the unit. This was achieved by varying the following parameters; gas and liquid flowrate, system operating pressure and inlet flow regime. In doing so the separation efficiency of the separator was measured subject to a stratified liquid film plus droplet mist and a droplet only inlet condition. The findings from the two phase flow investigation are summarised as follows;

1. The overall separation efficiency increases as the system pressure and gas flowrate increase.

2. Quantified data in the form of a Grade Efficiency Curve has been obtained for the droplet performance of the separator indicating that the separation efficiency is independent of liquid loading.

3. The maximum droplet diameter which escapes the no mesh separator is smaller than for the standard unit indicating that the internal meshes are detrimental to the overall performance of the separator.

4. The separator can separate droplet diameter greater than 20 microns with a high level of efficiency however droplet diameters below 10 microns are frequently found to pass through the separator.

5. The pressure drop across the separator increases as the liquid load increases and the standard unit is found to have a significant increase in pressure drop due to the presence of oil on the internal meshes reducing the flow area.

Combining the data obtained from the experimental two phase flow investigation with the validated single phase flow model the ability of the DPM model was assessed to determine the droplet separation efficiency of the helical separator. Having assessed the different solution approaches and modelling options the following conclusions were discovered;

1. The average realization approach of Derksen has been proven to reduce the required CPU time for droplet efficiency determination by 96.5% when compared with the concurrent simulation approach.

2. The careful selection of the appropriate wall model allows the prediction of the separation efficiency for the 100% discharge flowrate case for droplet diameters greater than 5 microns; however diameters below this size are over predicted when compared with the experimental data. For the 50% discharge flowrate case the models are able to predict the droplet separation efficiency for diameters greater than 10 microns however below this the models significantly over predict the separation efficiency. This over prediction indicates there are underlying physical phenomenon within the models which require further investigation to allow the separation efficiency predictions to be captured for the sub 10 micron droplet diameters.

3. The GEC's produced from the validation of the DPM approach indicate that the models provide a sufficient level of detail necessary to indicate whether a proposed design change will result in improved separation efficiency.

7.3 Separator Design

Using the data obtained from the complete assessment of the performance of the existing helical separator and the information presented within the literature with regards to enhancing droplet separation efficiency a number of design improvements were proposed and evaluated. In doing so some of the proposed improvements were simulated using the refined DPM modelling approach to determine whether an increase in separation efficiency could be achieved, the resulting design was then tested experimentally. Other design improvements were trialled based on the results from theoretical calculations and also tested experimentally. The results from this study are thus summarised;

1. By increasing the gas flowrate through the separator from 50%-400% discharge volume flowrate the maximum droplet diameter which is not removed by the separator is reduced from 25 microns to 8 microns with the d_{50} being reduced from 11.5 microns to 2.5 microns indicating that a significant improvement in performance of the unit can be achieved simply by increasing the inlet gas velocity. This improvement in efficiency was indicated by simulating the 200% discharge flowrate case and comparing the GEC with the 100% and 50% discharge data.

2. Based on the recommendations in the literature for separators a tangential entry unit with compressed helix was simulated for the 100% discharge flowrate condition and the results indicated a reduction in the cut size diameter to 3 microns which is half the value of the no mesh unit. Based on this evidence the tangential entry unit was manufactured and the performance tests confirmed the increase in separation efficiency up to 8% compared with the standard unit. The results from these studies confirm the ability of the modelling approach described in this investigation to be used as a separator design tool.

3. Two attachments, an inlet mesh screen and swirl tube generator in the centre tube, were designed using theoretical calculations and implemented into the separator for experimental testing. The inlet mesh screen increased the droplet separation efficiency by 20% and the swirl generator by 15%. However the inlet mesh screen also resulted in a significant increase in pressure drop by an order of magnitude whereas the swirl generator only resulted in the pressure drop being doubled compared to the no mesh unit with no attachments.

7.4 Future Recommendations

As this is the first time an investigation has been carried out to assess the performance of the helical oil separator the results from this study indicate that a significant step forward has been made in capturing the separation efficiency and pressure drop through both computational and experimental methods. Although this study has provided insight into both the single and two phase flow conditions which govern the performance of the helical separator further investigations are required to provide a more detailed understanding and refined computational model. Based on the evidence presented within this thesis the author suggests the following factors need to be explored in a further study;

1. To allow the performance of the separator to be determined under conditions which are in line with those which exist in an industrial refrigeration system the test facility needs to be operated at higher working pressures such that the flow regimes in the inlet pipe and main separation space replicate those which occur in practice.

2. From the data presented within this investigation it is clear that the droplet size dictates the performance of the separator, hence to allow this to be captured when operating at pressure a purge system needs to be implemented across the flow sight glass windows to prevent a liquid film build up and hence allowing the Spraytec apparatus to measure the droplet size and distribution within the flow at elevated system pressures.

3. Further investigations are required to refine the models such that the efficiency of the sub 10 micron droplet predictions are more in line with the efficiencies obtained from the experimental measurements. Local investigations of the droplet wall interactions using a high speed in the Perspex separator may indicate that not all interactions result in the droplets sticking to the walls and being removed from the flow.

4. Based on the design improvement recommendations further investigations need to be carried out to produce experimental GEC's for all the modifications assessed and from the data further refinement of the designs can be explored to further push the boundaries of the minimum droplet size which can be removed by the separator with 100% efficiency.

References

Abdujelala, M. & Lilley, D., 1984. Limitations and Empirical Extensions of the k-epsilon Model as Applied to Turbulent-Confined Swirling Flows. *Chem Eng Com,* Volume 31, pp. 223-236.

Abdullah, M., 1996. *Experimental Investigation and Computer Simulation of an Improved Cyclone Dust Separator.* PhD Thesis ed. University of Strathclyde.

Abernethy, R., Benedict, R. & Dpwdell, R., 1985. ASME Measurement Uncertainty. *ASME Journal of Fluids Engineering,* Volume 107, pp. 161-164.

Adbelghaffar, W., Elwardany, A. & Sazhin, S., 2011. Effects of Fuel Droplet Break-up, Heating and Evaporation in Diesel Engines. *Proceedings of the World Congress on Engineering,* Volume 3.

Albrecht, H., Damaschke, N., Borys, M. & Tropea, C., 2003. *Laser Doppler and Phase Doppler Measurement Techniques.* Springer.

Alexander, R., 1949. *Proceedings Aus. I.M.M,* pp. 152-153:203-228.

ANSYS, 2009. *ANSYS Fluent Documentation*.

Armenio, V., Piomelli, U. & Fiorotto, V., 1999. Effect of the Subgrid Scales on Particle Motion. *Physical Fluids,* 11(10), pp. 3030-3042.

ASHRAE, 1998. *Handbook of Fundamentals.* Atlanta GA.

Austrheim, T., 2006. *Experimental Characterization of High-Pressure Natural Gas Scrubbers.* University of Bergen: PhD Thesis.

Azzopardi, B., 1985. Drop Sizes in Annular Two-Phase Flow. *Experimental Fluids,* Volume 3, pp. 27-31.

B.V, S. G. S. I., 2002. Gas/Liquid Separator-Type Selection and Design Rules. *Design and Engineering Practice,* Volume DEP 31.22.05.11-Gen, pp. 1-52.

Bai, C., Rusche, H. & Gosman, A., 2002. Modelling of Gasoline Spray Impingement. *Atomization and Sprays,* 12(1), pp. 1-27.

Baker, O., 1954. Simultaneous Flow of Oil and Gas. *Oil Gas Journal,* Volume 53, p. 185.

Bhasker, C., 2002. Flow Simulation in Industrial Cyclone Separator. *Advances in Engineering Software,* Volume 12, pp. 1-27.

Bird, R., Stewart, W. & Lightfoot, E., 1960. *Transport Phenomenon.* New York: John Wiley and Sons.

Boysan, F., Ayers, W. & Switherbank, J., 1982. A Fundamental Mathematical Modelling Approach to Cyclone Design. *Trans IChemE,* Volume 60, pp. 222-230.

Brennan, M., Narasimha, M. & Holtham, P., 2007. Mulitphase Modelling of Hydrocyclones-Prediction of Cut-Size. *Minerals Engineering,* 20(4), pp. 395-406.

Brigadeau, 2007. *Modelling and Numerical Investigation of high Pressure Gas-Liquid Separation.* Norwegian University of Science and Technology: PhD Thesis.

Browne, J. & Strauss, W., 1977. Pressure Drop Reduction in Cyclones. *Atmospheric Environment,* Volume 12, pp. 1213-1221.

Brown, L., 2010. *Henry Technologies Oil Separator Sales Review,* University of Strathclyde.

Burkholz, A., 1989. *Droplet Separation.* VCH.

Cengel, Y. & Boles, M., 2010. *Thermodynamics:An Engineering Approach.* 7th ed. McGraw Hill.

Combellack, J. & Matthews, G., 1981. Droplet Spectra Measurements of Fan and Cone Atomisers using Laser Diffraction Technique. *Journal of Aerosol Science,* Volume 12, pp. 529-540.

Cortes, C. & Gil, A., 2007. Modelling the Gas and Particle Flow Inside Cyclone Separators. *Progress in Energy and Combustion Science,* Volume 33, pp. 409-452.

Cremaschi, L., Hwang, Y. & Radermacher, R., 2004. Investigation of Oil Retention in Residual Heat Pumps. *International Refrigeration and Air Conditioning Conference .*

Crowe, C., Sommerfeld, M. & Tsuji, Y., 1998. *Multiphase Flows with Droplets and Particles.* CRC Press.

De Schepper, S., Heynderickx, G. & Martin, G., 2008. CFD Modelling of all Gas-Liquid and Vapour-Liquid Flow Regimes Predicted by the Baker Chart. *Chemical Engineering Journal,* 138 (1-3), pp. 349-357.

De Souza, F., De Vasconcelos, R. & De Moro Martins, D., 2012. Large Eddy Simulation of the Gas-Particle Flow in Cyclone Separators. *Separation and Purification Technology,* Volume 94, pp. 61-70.

Delgadillo, J. & Rajamani, R., 2005. A Comparitive Study of Three Turbulence-Clkosure Models for the Hydrocyclone Problem. *International Journal of Mineral Processing,* 77(4), pp. 217-230.

Derksen, J., 2003. Separation Performance Prediction of a Stairmand High-Efficiency Cyclone. *AIChE Journal,* 49(6), pp. 1359-1371.

Dietz, P., 1981. Collection Efficiency of Cyclone Separators. *AIChE Journal,* 27(6), pp. 888-892.

Drain, L., 1980. *The Laser Doppler Technique.* John Wiley and Sons.

Elsayed, K. & Lacor, C., 2011. The Effect of Cyclone Vortex Finder Dimensions on the Flow Pattern and Performance using LES. *Computers and Fluids,* Volume 35, pp. 1952-1968.

Elsayed, K. & Lacor, C., 2013. The Effect of Cyclone Vortex Finder Dimensions on the Flow Pattern and Performance. *Applied Mathematical Modelling,* Volume 35, pp. 224-239.

Erdal, F. & Shirazi, S., 2004. Local Velocity Measurements and Computational Fluid Dynamics (CFD) Simulations of Swirling Flow in a Cylindrical Cyclone Separator. *Trans. ASME,* Volume 126, pp. 326-333.

Escudier, M., Bornstein, J. & Zehnder, N., 1980. Observations and LDA Measurements of Confined Turbulent Vortex Flow. *Journal of Fluid Mechanics,* 98(1), pp. 49-63.

Feng, J., Chang, Y., Peng, X. & Qu, Z., 2008. Investigation of the Oil-Gas Separation in a Horizontal Separator for Oil-Injected Compresssor Units. *Proceedings of the IMechE Journal of Power and Energy Part A,* Volume 222, pp. 403-412.

Fewel, K. & Kean, J., 1992. Computer Modelling Aids Separator Retrofit. *Oil and Gas Journal,* 90(27), pp. 76-80.

First, M., 1949. ASME Annual General Meeting. Volume 49A-127, pp. 1-25.

Fraser, S., Abdel Razek, A. & Abdullah, M., 1997. Computational and Experimental Investigations in a Cyclone Dust Separator. *Proceedings of the Institution of Mechanical Engineers,* Volume 211, pp. 247-257.

Gao, X. et al., 2012. The Research on the Performance of Oil-Gas Cyclone Separators in Oil Injected Compressor Systems with Considering the Breakup of Oil Droplets. *International Compressor Engineering Conference at Purdue.*

Gardner, N. & Owen, I., 1997. The Behaviour of Liquid Films and Drops in Relation to Liquid/Gas Separators. *Proceedings IMechE, 2011,* pp. 53-59.

Gil, A., Romeo, L. & Cortes, C., 2002. Effect of Solid Loading on a Pressurized Fluidized Bed Combustors Cyclone with Pneumatic Extraction of Solids. *Chem Eng Technology,* Volume 25, pp. 407-415.

Gimbun, J., Chuah, T., Fakhru'l-Razi, A. & Choong, T., 2005. The Influence of Temperature and Inlet Velocity of Cyclone Pressure Drop: A CFD Study. *Chemical Engineering and Processing ,* 44(1), pp. 7-12.

Gosman, A. & Ioannides, E., 1981. Aspects of Computer Simulations of Liquid-Fuelled Combustors. *AIAA 19th Aerospace Sciences Meeting,* pp. Paper AIAA-81-0323.

Griffiths, W. & Boysan, F., 1996. Computational Fluid Dynamics (CFD) and Empirical Modelling of the Performance of a Number of Cyclone Samplers. *Journal of Aerosol Science,* 27(2), pp. 281-304.

Gronald, G. & Derksen, J., 2011. Simulating Turbulent Swirling Flow in a Gas Cyclone: A Comparison of Various Modelling Approaches. *Powder Technology,* Volume 205, pp. 160-171.

Gupta, A., Lilley, D. & Syred, N., 1984. *Swirl Flows.* Abacus Press.

Hanjalic, K., 1999. Second-Moment Turbulence Closures for CFD: Needs and Prospects. *Journal of Computational Fluid Dynamics,* 12(1), pp. 67-97.

Hoekstra, A., Derksen, J. & Van Den Akker, H., 1999. An Experimental and Numerical Study of Turbulent Swirling Flow in Gas Cyclones. *Chemical Engineering Science,* Volume 54, pp. 2055-2065.

Hoffmann, A. et al., 2006. Effect of Pressure Recovery Vanes on the Performance of a Swirl Tube, with Emphasis on the Flow Pattern and Separation Efficiency. *Energy and Fuels,* Volume 20, pp. 1691-1697.

Hoffmann, A. & Stein, L., 2008. *Gas Cyclones and Swirl Tubes: Principles, Design and Operation.* Second Edition ed. Springer.

Hoffmann, A., Van Santen, A., Allen, R. & Clift, R., 1992. Effects of Geometry and Solid Loading on the Performance of Gas Cyclones. *Powder Technology,* Volume 70, pp. 83-91.

Hogg, S. & Leschziner, M., 1989. Computation of Highly Swirling Confined Flow with a Reynolds Stress Turbulence Model. *AIAA,* Volume 27, pp. 57-63.

Hsieh, K. & Rajamani, R., 1991. Mathematical Model of the Hydrocyclone based on Physics of Fluid Flow. *AIChE,* 37(5), pp. 735-746.

Ishii, M. & Grolmes, 1975. Inception Criteria for Droplet Entrainment in Two-Phase Concurrent Film Flow. *AIChE,* 21(2), pp. 308-318.

Jekel, T., Reindl, D. & Fisher, 2001. Gravity Separator Fundamentals and Design. *HAR Ammonia Refrigeration Convention and Exhibition,* pp. 1-23.

Jia, L., Suyi, H. & Xiaomo, W., 2007. Numerical Study of Steam-Water Separators with Wave-Type Vanes. *Chin. J. Chem. Eng,* 15(4), pp. 492-498.

Kegg, S., 2008. *A Numerical Investigation of Gas Cyclone Separation Efficiencywith Comparison to Experimental Data and Presentation of a Computer-Based Cyclone Design Methodology.* University of Akron: Masters Thesis.

Kline, S., 1985. The Purpose of Uncertainty Analysis. *ASME Journal of Fluids Engineering,* Volume 107, pp. 153-160.

Kumar, R. & Conover, T., 1993. Flow Visualization Studies of a Swirling Flow in a Cylinder. *Experimental Thermal and Fluid Science,* 7(3), pp. 254-262.

Launder, B. & Spalding, D., 1972. *Lectures in Mathematical Modelling of Turbulence.* London and New York: Academic Press.

Launder, B. & Spalding, D., 1974. The Numerical Computation of Turbulent Flows. *Computer Methods in Applied Mechanics and Engineering,* Volume 3, pp. 269-289.

Lefebvre, 1989. *Atomisation and Sprays.* Hemisphere.

Leith, D. & Mehta, D., 1967. Cyclone Performance and Design. *Atmospheric Environment,* Volume 7, pp. 527-549.

Mandhane, J., Gregory, G. & Aziz, K., 1974. A Flow Pattern Map for Gas-Liquid Flow in Horizontal Pipes. *International Journal of Multiphase Flows,* 1(4), pp. 537-553.

Marchetti, J. & Svendsen, H., 2011. Improvements on a Laser Scattering Technique for Droplet Size Measurements Applied to a Gas-Liquid Separation Equipment. *Measurement,* Volume 44, pp. 493-499.

McLaughlin, D. & Tiederman, W., 1973. Biasing Correction for the Individual Relization of Laser Anemometer Measurements in Turbulent Flows. *Physics Fluids,* 16(12), pp. 2083-2088.

Meier, H. & Mori, M., 1999. Anisotropic Behaviour of the Reynolds Stress in Gas and Gas-Solid Flows in Cyclones. *Powder Technology,* 101(2), pp. 108-119.

Meng, H. & van der Geld, C., 1991. Particle Trajectory Computations in Steady Non-Uniform Liquid Flows. *ASME-Liquid Solid Flows,* Volume 118, pp. 183-193.

Mothes, H. & Loffler, F., 1988. Prediction of Particle Removal in Cyclone Separators. *International Chemical Engineering,* Volume 28, pp. 231-240.

Mugele, R. & Evans, H., 1951. Droplet Size Distribution in Sprays. *Industrial and Engineering Chemistry,* Volume 43, pp. 1915-1931.

Mundo, C., Sommerfeld, M. & Tropea, C., 1995. Droplet-Wall Collisions: Experimental Studies of the Deformation and Breakup Process. *International Journal of Multiphase Flow,* 21(2), pp. 151-173.

Murphy, S. et al., 2007. Prediction of Strongly Swirling Flow within an Axial Hydrocyclone using Two Commercial CFD Codes. *Chemical Engineering Science,* 62(6), pp. 1619-1635.

Narasimha, M., Brennan, M., Holtham, P. & Napier-Munn, T., 2007. A Comprehensive CFD Model of Dense Medium Cyclone Performance. *Minerals Engineering,* 20(4), pp. 414-426.

Ogawa, A., 1984. *Separation of Particles from Air and Gases: Volume 1.* CRC Press.

O'Rourke, P. & Amsden, A., 1987. The TAB Method for Numerical Calculation of Spray Break-up. *SAE Report No. 872089.*

Patterson, M. & Reitz, R., 1987. Modelling the Effects of Fuel Spray Characteristics on Diesel Engine Combustion and Emission. *SAE Technical Paper 872089.*

Peng, W. et al., 2002. Flow Pattern in Reverse-Flow Centrifugal Separators. *Powder Technology,* 127(3), pp. 212-222.

Perry, R. & Green, D., 1984. *Chemical Engineers' Handbook.* 6th Edition ed. New York: McGraw-Hill.

Phyfe, N., 1999. CFD Modelling of Cyclone Separators. *Fluent Users Group Meeting.*

Ramachandran, G., Raynor, P. & Leith, D., 1994. Collection Efficiency and Pressure Drop for a Rotary-Flow Cyclone. *Filtration and Separation,* pp. 631-636.

Reydon, R. & Gauvin, W., 1981. The Canadian Journal of Chemical Engineering. p. 59.

Rudd, M., 1969. A New Theoretical Model for the Laser Dopplermeter. *Journal of Scientific Instruments (Journal of Physics E),* 2(2), pp. 55-58.

Sakai, T., Kito, M., Saito, M. & Kanbe, T., 1978. Characteristics of Internal Mixing Twin Fluid Atomizer. *1st International Conference on Liquid Atomization and Spray Systems,* pp. 235-241.

Shalaby, H., 2007. *On the Potential of Large Eddy Simulation to Simulate Cyclone Separators.* Chemnitz University of Technology: PhD Thesis.

Shalaby, H., Pachler, K., Wozniak, K. & Wozniak, G., 2005. Comparative Study of the Continuous Phase Flow in a Cyclone Separator Using Different Turbulence Models. *International Journal for Numerical Methods in Fluids,* 48(11), pp. 1175-1197.

Shepherd, C. & Lapple, C., 1939. Flow Pattern and Pressure Drop in Cyclone Dust Collectors. *Ind. Eng. Chem,* Volume 32, pp. 1246-1248.

Simmons, M. & Hanratty, T., 2001. Droplet Size Measurements in Horizontal Annular Gas-Liquid Flow. *International Journal of Multiphase Flow,* Volume 27, pp. 861-883.

Slack, M., Prasad, R., Bakker, A. & Boysan, F., 2000. Advances in Cyclone Modelling using Unstructured Grids. *Trans IChemE,* 78(Part A: Advances in Cyclone Modelling using Unstructured Grids), pp. 1098-1104.

Smagorinsky, J., 1963. General Circulation Experiments with the Primitive Equations. 1. The Basic Experiment. *Monthly Weather Review,* Volume 91, pp. 99-164.

Souders, M. & Brown, G., 1934. Design of Fractioning Columns: 1. Entrainment and Capacity. *Industrial and Engineering Chemistry,* Volume 26, pp. 98-103.

Stairmand, C., 1949. Pressure Drop in Cyclone Separators. *Engineering,* Volume 168, pp. 408-413.

Stairmand, C., 1951. The Design and Performance of Cyclone Separators. *Trans. Institution of Chemical Engineers,* Volume 29, pp. 356-383.

Taitel, Y. & Dukler, A., 1976. A Theoretical Approach to the Lockhart-Martinelli Correlation for Stratified Flow. *International Journal of Multiphase Flow,* Volume 2, pp. 519-595.

Temprite, 1999. *Temprite Product Catalogue*.

Ter Linden, A., 1949. Investigation into Cyclone Dust Collectors. *Proceedings of the Institution of Mechanical Engineers,* Volume 160, pp. 233-251.

Ter Linder, A., 1953. Cyclone Dust Collectors for Boilers. *Trans. of the ASME,* pp. 433-440.

Thome, J. R., 2004. Engineering Data Book III. *Laisanne, Switzerland: Wolverine Tubes Inc..*

Tu, J., Lee, B. & Fletcher, C., 1996. Eulerian Modelling of Particle-Wall Collisions in Confined Gas-Particle Flow via a Lagrangian Approach. *ASME, Fluids Engineering Division ,* 236(1), pp. 751-758.

Versteeg, H. & Malalasekera, W., 2007. *An Introduction to Computational Fluid Dynamics.* Essex, England: Pearson Education Limited.

Wang, L., Parnell, C., Shaw, B. & Lacey, R., 2003. Analysis of Cyclone Collection Efficiency. *ASAE Annual International Meeting.*

Yakhot, V. & Orszag, S., 1986. Renormalization Group Analysis of Turbulence. 1. Basic Theory. *Journal of Scientific Computing,* 1(1), pp. 3-51.

Yang, I., Shin, C., Kim, T.-H. & Kim, S., 2004. A Three-Dimensional Simulation of a Hydrocyclone for the Sludge Separation in Water Purifying Plants and Comparison with Experimental Data. *Minerals Engineering,* Volume 17, pp. 637-641.

Zhang, L., 2010. *Design and Numerical Simulation of the Real-Time Particle Charge and Size Analyser.* Faculty of Advanced Technology, University of Glamorgan: PhD Thesis.

Zhou, L. & Soo, S., 1990. *Powder Technology,* Volume 63, pp. 45-53.

Appendix 1

The acquisition of the experimental data necessary for the oil separator separation efficiency and pressure drop measurements was achieved through a National Instruments NI-6210 unit from which the signal was processed using a custom built programme in Labview.

Figure A.1.1: Experimental Data Acquisition Labview Setup

The numerical constants for the oil flowmeters were prescribed values of 0.158 and 0.5 for the low flowrate and high flowrate units respectively. One pulse signal corresponds to 0.158 mL and 0.5 mL of oil allowing the total volume of oil measured during the sample measurement to be directly displayed in the control front panel window of the software.

The vortex air flowrate meter was also calibrated such that the air flowrate was displayed on the front panel window. The differential pressure transducer was calibrated using an inclined manometer such that the numerical constants could be found and input into Labview. The pressure drop was recorded every 0.1 second and recorded for the duration of the sample such that the data could then be manipulated to produce the mean pressure loss for a particular test condition.

Appendix 2

Prior to commencing any test sequence the general integrity of the rig should be checked to ensure that there is no obvious signs of leaks, all electrical connections are in place and safe and the oil in the primary and secondary separators and supply vessel are at appropriate levels. This involves ensuring the oil levels in the separator collection chambers are at a level where any additional oil volume will cause the ball float to respond and return the liquid through the 3/8" flare connection; this is indicated by the liquid level in the sight glass occupying approximately 50% of the volume. If this is not the case the separator should be pre-charged by attaching the pump to the rotalock valve on the base of the unit and running the pump until the aforementioned oil level is obtained. If the oil in the supply tank is seen to be below the lower sight glass on the vessel then additional oil should be drained from the degassing vessel mounted atop of this. Once these initial checks have been done the following operations should be executed in succession.

1. Ensure that all air supply valves to the rig are closed, the throttle valve directly upstream and downstream of the coalescing separator is fully open. For all air flowrates the Sierra Innova-Mass Series 240 meter is used with the Omega FMA-A2323 being used to monitor the flowrate to the atomising nozzle.

2. Dependent on the oil flowrate to be injected the valves to the appropriate pump and flowmeter are opened along with the valve from the storage vessel. Again due to the issues with air entrainment in the oil the micro-annular gear pump was only used for the atmospheric pressure tests which have an oil flowrate range of 1-43 mL/min. For all other tests the Hydra Cell P200 metering pump was used.

3. The valves in the return lines from the primary and secondary separator are opened and the ones in the measurement lines are closed to allow all the oil to be returned to the supply vessel during start-up until a steady state is reached.

4. The differential pressure transducer is reset to zero ensuring the lines leading to the high and low pressure side of the rig are closed and the valve which isolates the high pressure line from the low pressure line is open such that both ports of the transducer can be pressurised at the same time.

5. The correct air mass flowrate, oil volume flowrate, air line pressure and atomising line pressure are then identified for the test to be conducted.

6. The valve upstream of the pressure regulator is cracked open and any leaks identified before it is then fully opened. The main supply valve to the rig can then be opened and the pressure regulator set to accommodate for the required test working pressure. The flowrate can then be set using the main supply valve to the rig and the needle valve opened to set the pressure differential for the atomiser which controls the rate of liquid atomisation and hence the droplet size/distribution for a particular test case-for each test case the atomisation pressure was 1 Bar above the system operating pressure.

7. The system pressure can then be set using the throttle valve downstream of the secondary separator until the pressure gauge at the inlet to the primary separator indicates the desired working pressure.

8. If the mzr-gear pump is to be used the software for this can then be launched through the PC and the required volume flowrate directly input. For the Hydra Cell pump the potentiometer on adjustable frequency AC drive is increased and adjusted to obtain the required flowrate which is monitored using Labview. The setup for Labview described in section 4.4.2 allows the oil flowrate, air flowrate, differential pressure and elapsed time to be monitored on the one screen. The run button on Labview allows the oil flowrate which is being delivered by the appropriate pump to be observed by monitoring the number of pulses being recorded from the corresponding oil flowmeter through Labview.

9. With the system running and all the flowrates and pressures fine-tuned to the desired operating condition for a particular test case the system has to be left for a period of 45-60 minutes to allow a steady state to be achieved. This is to allow the flow regimes in the pipes and separators to establish since the degree of surface "wetting" on their internal surfaces by the oil is governed by the corresponding air and oil flowrates which require a period of time to become established. Naturally larger changes in the operating conditions require a longer stabilisation period. During the 45-60 minute stabilisation time the separated oil is directed back to the oil supply tank therefore the system exists as a closed loop.

10. When the measurement process is ready to commence, the ball valve leading from the conventional separator to the oil supply tank is closed and the measurement line valve opened to allow the separated oil to be drained into the appropriate measuring cylinder. As soon as the measurement valve is opened a stop watch is started so that at the end of the test run the volumetric oil flowrate from the conventional separator and coalescing

cartridge can be obtained. Based on the injected oil flowrate a suitably sized measuring cylinder is chosen for the conventional separator measurement with the assumption that the flowrate from this secondary separator will be significantly less than the primary helical separator, high oil flowrates from the conventional would indicate the helical is not performing its function. (This measuring cylinder size should be suitable to capture the separated oil from the conventional separator for duration of the test run or with one change out).

11. A drain vessel can then be placed under the measurement line valve of the helical separator and the ball valve leading back to the supply vessel from this separator can be closed. When the measurement from the primary separator is ready to begin the appropriate measuring cylinder is presented to the measurement line, with a funnel in the measuring cylinder to assist in capturing the separated oil, at the same time as clicking the "run" button on the Labview software. The sample collection time is again dependent on the injected oil flowrate and the vessel size being used to measure the separated oil volume, but can range from 45-600 seconds. At the end of each sample measurement the measuring cylinder must be removed and the "stop" button clicked in Labview simultaneously, allowing the oil to again drain into a separate vessel.

12. The data from each sample measurement is then recorded in a custom developed excel spread sheet to allow the overall separation efficiency of each operating condition to be determined and displayed graphically. The input data for the spread sheet is as follows; prior to the start of each run the working conditions for the specific test case are entered along with the initial air and oil temperature, the sample measurement data is then input according to the data displayed through Labview which capture the number of pulses detected by the inlet line flowmeter, the elapsed time for the sample to be collected and the separated volume of oil collected in the measuring cylinder. The air flowrate to the atomiser was also entered into the spread sheet as measured by the Omega thermal mass flow meter. The excel spread sheet was the set up to calculate the inlet volume based on the number of pulses, the difference in volume injected from that separated by the helical, the inlet flowrate, outlet flowrate and sample separation efficiency.

13. When enough data has been gathered to ensure the transient nature of the oil return mechanism can be averaged without any bias the run can be terminated. The ball valves to return the separated oil to the supply tank are opened and the measurement line valves

from both separators are closed whilst simultaneously stopping the stop watch and recording the total run time and the volume of separated oil from the coalescing separator in the spread sheet. All separated oil is returned to the degassing vessel ensuring the drain valve to the storage vessel is closed.

14. The rig can then be shut down by firstly pressing "stop" on the mzr-gear pump software or stopping the adjustable AC frequency driver controlling the Hydra Cell pump, closing all the oil line ball valves then fully opening the throttle valve downstream of the coalescing separator so the system can depressurise. The air supply can then be shut down by closing the atomiser needle valve, main rig supply valve and upstream ball valve respectively.

15. To complete the spreadsheet the coalescing filter is emptied and the volume of collected oil measured allowing a mass balance to be obtained for the entire run by calculating the efficiency of each of the three separators and summing the values. Finally the air and oil temperatures at the end of the run are recorded.

16. With the system shut down the degassing process can take place. This involves opening the ball valves in the closed loop heating line with the Mirlees single speed positive displacement pump and filter-drier. The pump and heater are switched on and the oil is circulated until it reaches around 80°C, as this is the most effective temperature for removing the absorbed gases. At this temperature the pump and heater are switched off, all valves closed and the vacuum pump connected to the top of the oil storage/degassing vessel and switched on. The 24 V power supply to the vacuum feedthrough, mixer, and motor assembly is turned on and set to 12 V and run for the duration of the degassing process, approximately 20 minutes.

17. When the degassing is complete the power supply and vacuum pump respectively are turned off and the connection to the vacuum pump slowly removed allowing the vessel to re-pressurise ready for the next test run to be carried out.

Appendix 3

1. Prior to opening the main air flow supply valve to the rig the ball valve on the liquid film removal device should be opened to allow the film flow to drain into the liquid holdup vessel.

2. A temporary measurement vessel should be placed at the outlet of the solenoid valve to allow the returned liquid film volume to be collected.

3. The transformer which supplies the liquid level sensor and solenoid valve circuit should be turned on.

4. Once the system has reached a steady state, after 45-60 minutes from start-up of the rig, and the solenoid valve has just opened to return the build up of oil in the hold-up vessel then a beaker is placed at the outlet from the solenoid valve replacing the temporary vessel. Simultaneously a measuring cylinder is placed at the outlet of the helical separator and the start button on the Labview software is activated allowing the timer and inlet oil flowrate to be counted.

5. When the beaker used to collect the liquid film oil volume was almost full the sample measurement should be stopped after the next oil return from the solenoid valve. At the point when the solenoid valve closes the liquid film measurement beaker and separator return line measuring cylinder should be removed and the Labview programme stopped simultaneously. Temporary vessels should replace the measurement vessels, the liquid film oil volume should be transferred to an appropriate sized measuring cylinder and all data recorded in the spreadsheet.

6. Once the solenoid valve has opened and closed again a new sample measurement should be started and the process described in point 5 repeated until sufficient data has been obtained for statistically meaningful average values to be calculated for the respective collected oil volumes.

7. The data is recorded in a similar spreadsheet to that used for the liquid film and droplet separation efficiency measurements with the addition of a column for inputting the volume of oil removed as liquid film.

Appendix 4

1. The Spraytec apparatus was turned on and the Standard Operating Procedure (SOP) set up which allows the optical properties of the oil to be defined, including density (995 kg/m^3) and refractive index (1.45).

2. The apparatus then carried out a background check to assess the surrounding light levels and a beam alignment process which would indicate if the optical lenses were fouled or the equipment was not level.

3. The side channel blower is then turned on, the main airflow rate to the rig set and the atomising line pressure set and the pump started. With the system running the start button was selected on the Spraytec software activating the measurement of the droplet size and distribution.

4. The size history plot is continually updated as the apparatus measures the droplets in the spray allowing any significant changes to be quickly identified and any issues to be resolved. The main issues being fouling of the optical lenses which required the system to be shut down and the lenses cleaned with lens cleaning paper.

5. For each droplet size measurement the data was acquired over a 300 second time interval and averaged over this time duration allowing sample sizes containing billions of drops to be obtained, even for very low liquid flowrates. When the liquid flowrate was low the droplet concentration in the mist, particularly at the outlet, was very low therefore the beam transmission from emitter to receiver was very high, close to 100%. In this case the recorded data had to be altered such that the minimum scattering percentage was reduced to 1% to allow the measurements to be obtained.

6. Once the measurement time had elapsed the software was stopped, which closed the shutter on the laser. The pump was then stopped, the airflow rate to rig was turned off, including the atomising line, and finally the side channel blower was turned off.

Appendix 5

The design of the inlet wire mesh screen attachment was based on the approach of Burkholz as described in Chapter 2 of this thesis (Burkholz, 1989). The effects of varying the percentage closed area, wire diameter and number of mesh screen layers on the separation efficiency of a 5 microns droplet and pressure drop are shown in Table A.5.1.

Percentage Closed Area (%)	Wire Diameter (microns)	Number of Layers	Separation Efficiency (of a 5 micron droplet) (%)	Pressure Drop (Pa)
75	25	1	72.1	33.4
75	25	2	92.3	66.8
75	25	3	97.6	100.2
62	50	1	59.3	28.5
62	50	2	83.2	57.0
62	50	3	93.4	85.5
62	80	1	55.7	27.6
62	80	2	79.5	55.2
62	80	3	90.7	82.8
66	125	1	54.6	29.4
66	125	2	79.4	58.8
66	125	3	90.7	88.2
68	140	1	56	30.3
68	140	2	80.6	60.6
68	140	3	91.5	90.9
68	180	1	52.2	30.3
68	180	2	77.2	60.6
68	180	3	89.1	90.9

Table A.5.1: Inlet Wire Mesh Screen Attachment Selection Criteria

The design of the swirl generator attachment was based on the design criterion for a rotary flow cyclone which Ramachandran et al. applied to a rotary flow cyclone investigation. The effect of varying the pitch of the swirl generator on the separation efficiency, for a 5 micron droplet, and the pressure drop across the attachment are shown in Figure A.5.1.
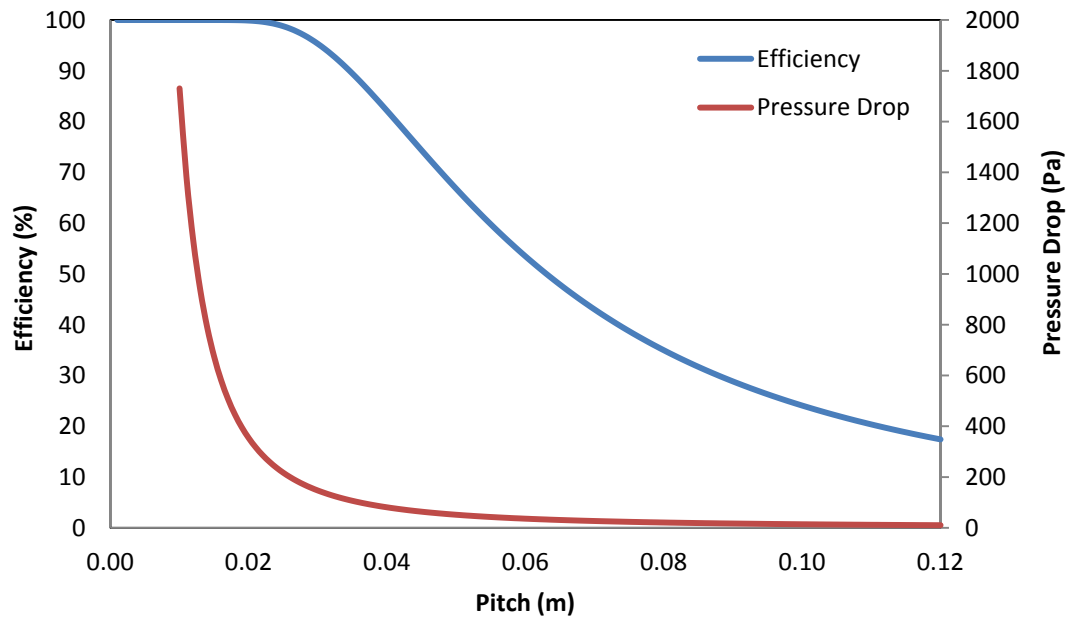
Figure A.5.1: Swirl Generator Effects of Varying Pitch

Appendix 6

Access to experimental data for the LDA measurements within the Perspex replica of the helical separator can be obtained from the digital files:- phD work>Flow Visualisation>LDA Results. All U and V velocity components at the locations within the separator discussed in Chapter 3 of this thesis can found by in this directory and are presented with respect to an x and y coordinate location as the z coordinate is 0 in the measurement plane. An example of the presentation of the data from the LDA measurements is given in Table A.6.1.

x (mm)	y (mm)	z (mm)	u (m/s)	v (m/s)	w (m/s)
-66	105	0	0	-0.0122	0.0010
-64	105	0	0	-0.0181	-1.4931
-62	105	0	0	-0.1301	-1.5672
-60	105	0	0	-0.3084	-1.3710
-58	105	0	0	-0.2476	-1.6456
-56	105	0	0	-0.2683	-1.6712
-54	105	0	0	-0.2757	-1.6982
-52	105	0	0	-0.2892	-1.7488
-50	105	0	0	-0.3059	-1.8178
-48	105	0	0	-0.3049	-1.8675
-46	105	0	0	-0.2978	-1.9279
-44	105	0	0	-0.4225	-1.9706
-42	105	0	0	-0.3843	-2.0451
-40	105	0	0	-0.3962	-2.0536
-38	105	0	0	-0.5034	-2.0695
-36	105	0	0	-0.5148	-2.0410
-34	105	0	0	-0.6563	-2.0272
-32	105	0	0	-0.7664	-0.6194
-30	105	0	0	0.0000	-0.0250

Table A.6.1: Example of LDA Raw Data

The separation efficiency and pressure drop data for all operating conditions and units tested can also be obtained from the digital files:- phD work>Experimental Rig>S-5190 Performance Data. Each spreadsheet containing the performance data states the configuration of the unit tested the operating pressure; gas discharge flowrate; oil mass fraction; air and oil temperatures at the start and end of the test. The data recorded includes then number of pulses recorded which corresponds to an oil volume, the time taken for the sample measurement and the volume of oil separated by the helical separator, and in the case of tests where the liquid film is extracted this volume is also recorded. An example of the data presentation is given in Figure A.6.1.

S-5190 Standard Unit

	Discharge Volume	100%	Operating Pressure	0BarG	Oil Mass Fraction	10%

Oil Temperature at start	20.2 °C				
Air Temperature at Start	18.76 °C				
Air Mass Flowrate	0.00636 kg/s		Oil Volume Flowrate	43mL/min
Density	1.206184454 kg/m³			
Inlet Pipe Cross-Sectional Area	0.000779311 m²		Air Flowrate to the Atomizer	30.8
Inlet Pipe Velocity	6.76871037 m/s		Oil Temperature at end	20.4 °C
Atomizing Pressure	1 Bar		Air Temperature at end	18.8 °C

Oil Inlet Pulses	Oil Inlet Volume (mL)	Helical Separated Oil Volume (mL)	Difference (Outlet-Inlet)(mL)	Time for Sample (s)	Inlet Oil Flowrate (mL/min)	Outlet Oil Flowrate (mL/min)	Separation Efficiency (%)
176	88	78	-10	118.2	44.67005076	39.59390863	88.63636364
201	100.5	96	-4.5	133.76	45.0807I4163	43.0622096	95.5238806
247	123.5	120	-3.5	163.34	45.36549529	44.07983348	97.1659919
203	101.5	99	-2.5	132.75	45.87570621	44.74576271	97.5369I4581
224	112	116	4	152.85	43.96467125	45.53483808	103.5714286
192	96	98	2	133.31	43.20756132	44.1077I885	102.0833333
202	101	100	-1	139.7	43.37866858	42.94917681	99.00990099
202	100	100	-1	138.51	43.75135369	43.31817197	99.00990099
223	111.5	122	10.5	152.2	43.95532194	48.09461235	109.4170404
204	102	102	0	139.87	43.75491528	43.75491528	100
	Total Difference(mL)		-6	**Average Flowrate (mL/min)**	44.3004486	43.92411391	99.19532937

Figure A.6.1: Sample Separation Efficiency Performance Data

The droplet size and distribution measurement data obtained from the Malvern Spraytec Laser Diffraction apparatus can be obtained from the digital files:- phD work>Experimental Data>Spraytec Droplet Measurements. The raw data from each operating condition can be exported to an excel file and used to produce a distribution curve for the droplets at the inlet and outlet of the separator. An example of the raw data is given in Figure A.6.2.

Size (µm)	% V <	% V	Size (µm)	% V <	% V	Size (µm)	% V <	% V
0.117	0.00	0.00	2.51	18.00	3.80	54.12	95.40	1.53
0.136	0.00	0.00	2.93	22.22	4.22	63.10	96.59	1.20
0.158	0.00	0.00	3.41	26.78	4.56	73.56	97.53	0.94
0.185	0.00	0.00	3.98	31.60	4.82	85.77	98.27	0.74
0.215	0.00	0.00	4.64	36.58	4.98	100.00	98.86	0.59
0.251	0.00	0.00	5.41	41.61	5.03	116.59	99.33	0.47
0.293	0.00	0.00	6.31	46.58	4.98	135.94	99.68	0.35
0.341	0.00	0.00	7.36	51.43	4.84	158.49	99.90	0.22
0.398	0.00	0.00	8.58	56.08	4.66	184.79	100.00	0.10
0.464	0.00	0.00	10.00	60.54	4.45	215.44	100.00	0.00
0.541	0.00	0.00	11.66	64.80	4.26	251.19	100.00	0.00
0.631	0.13	0.13	13.59	68.89	4.09	292.87	100.00	0.00
0.736	0.51	0.38	15.85	72.84	3.95	341.46	100.00	0.00
0.858	1.20	0.69	18.48	76.65	3.81	398.11	100.00	0.00
1.00	2.25	1.05	21.54	80.30	3.64	464.16	100.00	0.00
1.17	3.70	1.46	25.12	83.72	3.42	541.17	100.00	0.00
1.36	5.61	1.90	29.29	86.84	3.13	630.96	100.00	0.00
1.58	7.98	2.38	34.15	89.60	2.76	735.64	100.00	0.00
1.85	10.85	2.86	39.81	91.95	2.34	857.70	100.00	0.00
2.15	14.20	3.35	46.42	93.87	1.92	1000.00	100.00	0.00

Figure A.6.2: Sample Droplet Distribution Data